



SCHOOL OF MECHANICAL,  
INDUSTRIAL & AERONAUTICAL  
ENGINEERING

# Experimental and Numerical Characterization of Interlaminar Properties of SWCNTs Doped PAN Nano-mats Strengthened Multiscale Hybrid Composites

MECN9000 - Doctor of Philosophy

Muhammad Arif

926480

Supervisor: Prof. Jacob Muthu

A project report submitted to the Faculty of Engineering and the Built Environment, University of the Witwatersrand, Johannesburg, in partial fulfilment of the requirements for the degree of Doctor of Philosophy(PhD).

Date: 15th May 2019



UNIVERSITY OF THE  
WITWATERSRAND, JOHANNESBURG  
SCHOOL OF MECHANICAL,  
INDUSTRIAL & AERONAUTICAL  
ENGINEERING



**INDIVIDUAL DECLARATION WITH TASK  
SUBMITTED FOR ASSESSMENT**

I, the undersigned, am registered for the course MECN9000 - Doctor of Philosophy (PhD) which this is submitted in the year 2019. I herewith submit the following task “Experimental and Numerical Characterization of Interlaminar Properties of SWCNTs Doped PAN Nano-mats Strengthened Multiscale-Hybrid Composites” in partial fulfilment of the requirements of the above course.

I hereby declare the following:

- I am aware that plagiarism (the use of someone else’s work without their permission and / or without acknowledging the original source) is wrong;
- I confirm that the work submitted herewith for assessment in the above course is my own unaided work except where I have explicitly stated otherwise;
- This task has not been submitted before. either ly or jointly, for any course requirement, examination or degree at this or any other tertiary educational institution;
- I have followed the required conventions in referencing the thoughts and ideas of others;

- I understand that the University of the Witwatersrand may take disciplinary action against me if it can be shown that this task is not my own unaided work or that I failed to acknowledge the sources of the ideas or words in my writing in this task.

Signed this 15th day of May 2019

A handwritten signature in blue ink, appearing to read 'Muhammad Arif', written in a cursive style.

Muhammad Arif

## *Abstract*

Polymer composite reinforced with conventional macro size fibres have taken a major role in various modern engineering applications and their demand is ever increasing due to their light weight and design flexibility. Various improvements in manufacturing methods, fabrication techniques and composite constituents have been made over the years to produce better polymer composites. However, the major challenge of the conventional polymer composites is that failure at the matrix rich interlaminar region still remains and limits their performance resulting in unreliable usage of these composites. A number of research attempts had little success due to various limiting factors have been carried out to rectify this problem. One of the potential methods expected to improve the strength of the interlaminar region is the incorporation of nano-size fillers, such as electrospun Polyacrylonitrile (PAN) nanofibres mat as an interalia into the matrix rich interlaminar region of the conventional polymer composite. However, controlling the alignment and distribution of the PAN nanofibres during the chaotic electrospinning process is a major hurdle for improving the interlaminar regions. The random orientation of electrospun PAN nanofibres mat reduces their strengthening effect and also the required material properties.

Hence, the current study has focused on the design of electrospinning process for improving the orientation and distribution of the PAN nanofibre mats. The developed electrospinning process was used to produce random and aligned PAN nanofibres mat and also used for producing both pristine and functionalized single walled carbon nanotubes (SWCNTs) doped PAN nanofibres mat. These nanomats were then sandwiched with the glass fibre-epoxy matrix to produce nano strengthened multiscale hybrid composites.

As part of the electrospinning procedure, electric fields of general electrospinning technique were manipulated using two position adjustable auxiliary vertical electrodes (AVEs) to produce aligned nanofibres mat along with reduced diameter. So as to optimise the electrospinning parameters, the effect of AVEs on the PAN nanofibres mat orientation, distribution and diameter were experimentally matrixed and analysed. The fractographic study showed that

---

auxiliary vertical electrodes (AVEs) added to the electrospinning process reduced the diameter, enhanced the alignment of the nanofibres and improved molecular orientation. Among four different volume fractions of 0.1%, 0.2%, 0.5% and 1% randomly oriented PAN nanofibre mats, the volume fraction of 0.5% PAN polymer was selected to manufacture aligned PAN nanofibres mat strengthened hybrid composite based on the improved experimental randomly oriented PAN nanofibre mats strengthened hybrid composites.

A series of tests showed that glass fibre composites (GFC) reinforced with the volume fraction of 0.5% aligned nanofibre mats were better than those of 0.5% randomly distributed nanofibre mats. The aligned nanofibre mat with reduced diameter increased the tensile, flexural, and impact properties of glass fibre composite by 68.91%, 95.32% and 45.30% respectively.

Aligned nanofibres mat was further utilised to align and disperse the pristine and functionalized SWCNTs into the interlaminar region of fibreglass composite. Alignment and a nano-range diameter of nanofibres helped in improved distribution and alignment of pristine SWCNTs (p-SWCNTs), which was reflected in an increase in tensile, flexural and impact resistance by 89.30%, 105.48% and 107.17% respectively. A nondestructive functionalization method (Friedel craft alkylation) was used to improve the interface bonding of SWCNTs with the host PAN polymer nanofibre. PVA chains crafted to the surface of the SWCNTs without damaging the wall was confirmed using FTIR and Raman spectroscopy. The effect of functionalized SWCNTs (f-SWCNTs) doped aligned PAN nanofibre mats improved the properties of nano-hybrid multiscale composite up to 111.34%, 117.11% and 180.03% in tensile, flexural and impact resistance respectively.

A multiscale model was used to determine the properties of the multiscale nanohybrid composite strengthened with random and aligned PAN nanofibre mats, PAN doped with p-SWCNTs and f-SWCNTs aligned nanofibre mats. Three length scales, such as nano, micro and macro scales were modelled. At first, a numerical model was developed to determine the elastic properties of different carbon nanotubes (CNTs) i.e. Pristine and defective single wall (SWCNTs), double wall (DWCNTs), and multiwall (MWCNTs) for zigzag

and armchair configurations. CNTs atomic geometry was replicated with an equivalent space frame structure (SFS). Co-ordinates definition of SFS of CNTs was developed in MATLAB code and transferred to the finite element analysis (FEA) software 'ANSYS'. The basic entity of SFS, C-C chemical bond was designed as a circular beam of orthotropic properties. The properties were determined by linking the energy equation of molecular mechanics to structural mechanics along with the parametric study. The van der Waals forces between inter-shell of DWCNTs and MWCNTs were modelled as linear elastic springs in a simplified way. The simplified model avoided the problems due to the nonlinear behaviour of van der Waals forces and improved the performance of the FEA software by computational resources. The effect of chirality, vacancy defects, different diameters and numbers of walls on elastic properties of CNTs were calculated, tabulated and compared with each other. The result of the proposed SFS model with orthotropic properties was compared with others result. The SFS model is found better than the equivalent shell model as the defects can be placed at the exact location and a more realistic behaviour could be predicted. The SFS models could be developed with any type of defects, a number of walls, van der Waals and agglomerated forms with variable geometries.

Using the space frame structures (SFS) of SWCNTs, the nanoscale RVE of PAN nanofibre doped with SWCNTs was modelled. Simulated results of nanoscale RVEs were used to determine the equivalent properties of p-SWCNTs and f-SWCNTs doped nanofibres, which were further used in microscale RVE models. Four micro scale RVEs were developed to represent the random and aligned PAN nanofibres mats, PAN nanofibres mat doped with p-SWCNTs and f-SWCNTs aligned PAN nanofibres mat in epoxy matrix. Analysed micro scale RVEs provided equivalent properties of interlaminar regions developed with random and aligned PAN nanofibres mat, PAN doped with p-SWCNTs and f-SWCNTs aligned nanofibres mat. At the macro scale, MNHCs were developed with equivalent interlaminar regions and analysed. The results of the simulated MNHCs were compared with experimentally obtained results.

The results of the experimental study suggested that aligned nanofibres with reduced diameter improved the properties of interlaminar region noticeably

than the random nanofibres mat of the same volume fraction. Aligned nanofibres successfully placed the pristine and functionalized SWCNTs within the multiscale hybrid composites which significantly improved the properties of the multiscale hybrid composite. Results of the multiscale modelling were in line with the experimental results, which could be useful in extending the small-scale theoretical results to the real-life applications.

#### LIST OF PUBLICATIONS

The publications listed below have emanated from this research work so far:

1. Muhammad Arif, Jacob Muthu., “Characterization of CNT Properties using Space-frame Structure,” *Journal of Mechanics of Materials and Structures*, 2018, Vol. 13 (2018), No. 4, 443-461. DOI: 10.2140/jomms.2018.13.443, Status: Published.
2. Muhammad Arif, Mkhululi Ncube, Jacob Muthu., “Improvement of Interlaminar Region Properties of Fibre Glass Composite by Incorporating Electrospun Aligned Nanofibres Mats,” , Status: Under preparation
3. Muhammad Arif, Jacob Muthu., “Multiscale Modelling Analysis for Characterizing Multiscale Nanohybrid Composites,” Status: Under preparation

The paper abstracts are included in Appendix C.

## *Acknowledgements*

Immeasurable appreciation and sincere gratitude to the following persons for their guidance, help, and support in making this study possible.

My supervisor, Prof. Jacob Muthu, Mechanical, Industrial & Aeronautical Engineering, University of Witwatersrand, for his invaluable guidance in academic and financial support, trust and patience throughout the study, experiments and writing of this thesis.

Prof. Robert Reid, Head of the School, for his support during my study at the University of the Witwatersrand.

Prof Claudia Polese and Mr. Pietra Francesco for providing help and guidance in coding and numerical simulations,

S Riekert, M Coetzee, and P Radebe for their support during experiments, purchasing of materials, and trouble shooting of equipment.

H Jacobson, P Marks, M Rorane, and M Kubushi for their help in visa, registration and financial documentations.

Finally Dr Sarfraz Ali and Dr Tariq for their moral support and prayers.

# Contents

<b>Declaration of Authorship</b>	<b>i</b>
<b>Abstract</b>	<b>iii</b>
<b>Acknowledgements</b>	<b>vii</b>
<b>List of Figures</b>	<b>xiii</b>
<b>List of Tables</b>	<b>xxi</b>
<b>Abbreviations</b>	<b>xxiv</b>
<b>Physical Constants</b>	<b>xxvi</b>
<b>Symbols</b>	<b>xxvii</b>
<b>1 Introduction</b>	<b>1</b>
1.1 Background . . . . .	1
1.1.1 Agglomeration of CNTs . . . . .	4
1.1.2 Misalignment of the CNTs . . . . .	5
1.1.3 Poor Interface Region between CNTs and Matrix . . . . .	6
1.1.4 CNTs doped nanofibre mats . . . . .	8
1.1.5 Numerical modelling of CNTs and multiscale CNTs doped nanohybrid composites . . . . .	9
1.2 Research Motivation . . . . .	10
1.3 Problem Statement . . . . .	12
1.4 Research Objectives . . . . .	12
1.5 Thesis Layout . . . . .	14

---

<b>2</b>	<b>Literature Review</b>	<b>16</b>
2.1	Conventional Composites . . . . .	17
2.1.1	Ceramic matrix composite (CMC) . . . . .	17
2.1.2	Metal matrix composite . . . . .	18
2.1.3	Polymer matrix composite (PMC) . . . . .	18
2.2	Multiscale Nanohybrid Composites (MNHCs) . . . . .	21
2.3	Dispersion Processes of CNTs . . . . .	26
2.3.1	Physical methods . . . . .	28
2.3.2	Chemical dispersion methods . . . . .	30
2.4	Interface/interlaminar Region in the Composites . . . . .	31
2.4.1	Interface mechanism of CNTs with host materials . . . . .	35
2.5	Alignment of Carbon Nanotubes (CNTs) . . . . .	38
2.5.1	Electrospinning technique . . . . .	41
2.6	Multiscale Manufacturing of Composites . . . . .	48
2.7	Numerical Modelling of MNHCs . . . . .	49
2.7.1	Analytical methods . . . . .	50
2.7.2	Continuum mechanics . . . . .	51
2.7.3	Molecular dynamic simulations (MDS) . . . . .	53
2.7.4	Equivalent continuum model (ECM) . . . . .	54
2.8	Conclusion . . . . .	56
<b>3</b>	<b>Methodology</b>	<b>58</b>
3.1	Materials and Equipment . . . . .	61
3.2	Calculation for Volume Fractions . . . . .	63
3.3	SWCNTs Functionalization . . . . .	67
3.4	Dispersion of CNTs . . . . .	70
3.5	Testing Procedures . . . . .	73
3.5.1	Tensile test . . . . .	78
3.5.2	Flexural test . . . . .	81
3.5.3	Impact test . . . . .	83
3.6	Morphological Characterization . . . . .	85
3.6.1	Scanning electron microscopy (SEM) . . . . .	85
3.6.2	Raman spectroscopy . . . . .	87
3.6.3	Fourier transform infrared spectroscopy (FTIR) . . . . .	89
<b>4</b>	<b>Experimental Characterization of Multiscale Nanohybrid Composite</b>	<b>91</b>
4.1	Introduction . . . . .	91
4.1.1	Electrospinning for producing aligned PAN nanofibres mat . . . . .	93
4.1.2	Composites manufacturing process . . . . .	104

---

4.1.3	PAN nanomats strengthened hybrid composites . . . . .	106
4.2	Results and Dscussion . . . . .	107
4.2.1	Glass fibre composites . . . . .	107
4.2.2	Random PAN nanofibre mats strengthened hybrid composites . . . . .	109
4.2.3	Aligned and SWCNTs doped PAN nanofibre mat strengthened hybrid Composites . . . . .	116
<b>5</b>	<b>Space-frame Structure (SFS) Analysis with Orthotropic Responses of C-C bonds for characterizing CNTs Properties</b>	<b>136</b>
5.1	Introduction . . . . .	136
5.2	Modelling for Simulation . . . . .	139
5.2.1	SFS modelling of SWCNTs . . . . .	139
5.2.2	CNTs model development . . . . .	140
5.2.3	C-C chemical bond orthotropic properties . . . . .	145
5.2.4	Modelling of van der Waals forces . . . . .	150
5.2.5	Analysis procedure . . . . .	155
5.3	Results and Discussion . . . . .	156
5.3.1	Effect of chirality on the mechanical properties . . . . .	156
5.3.2	Effect of vacancy defects . . . . .	159
5.3.3	Effect of number of walls . . . . .	161
<b>6</b>	<b>Multiscale Modelling Analysis for Characterizing MNHCs</b>	<b>165</b>
6.1	Introduction . . . . .	165
6.2	Multiscale Modelling Procedure . . . . .	168
6.2.1	RVEs for SWCNT doped nanofibre . . . . .	168
6.2.2	Micro scale RVEs for random and aligned PAN nanofibre mats, p-SWCNTs and f-SWCNTs doped aligned nanofibres mats strengthened interlaminar region . . . . .	173
6.3	Macro Scale Modelling of 32% Glass Fibre Composite (GFC) . . . . .	177
6.3.1	Macro scale of modelling of MNHCs . . . . .	179
6.3.2	Boundary conditions . . . . .	181
6.4	Result and Discussions . . . . .	182
<b>7</b>	<b>Conclusion and Recommendations</b>	<b>191</b>
7.1	Conclusions: Experimental Study of MNHCs . . . . .	191
7.2	Conclusions: Numerical Study of MNHCs . . . . .	193
7.3	Recommendations . . . . .	196
7.3.1	Experimental recommendations . . . . .	196
7.3.2	Numerical recommendations . . . . .	197

---

<b>A</b>	<b>231</b>
A.1 Tensile Tests Details . . . . .	231
A.1.1 Neat glassfibre composite (32% Vol) . . . . .	231
A.1.2 Random nanofibres mat (0.1% Vol) strengthened hybrid composite . . . . .	233
A.1.3 Random nanofibres mat (0.2% Vol) strengthened hybrid composite . . . . .	234
A.1.4 Random nanofibres mat (0.5% Vol) strengthened hybrid composite . . . . .	236
A.1.5 Random nanofibres mat (1% Vol) strengthened hybrid composite . . . . .	237
A.1.6 Aligned nanofibres mat (0.5% Vol) strengthened hybrid composite . . . . .	239
A.1.7 (0.25% Vol) p-SWCNTs doped aligned nanofibres mat strengthened hybrid composite . . . . .	240
A.1.8 (0.25% Vol) f-SWCNTs doped aligned nanofibre mat strengthened hybrid composite . . . . .	242
A.2 Flexural Test Details . . . . .	243
A.2.1 Neat glassfibre composite 32% . . . . .	243
A.2.2 Random nanofibres mat (0.1%) strengthened hybrid composite . . . . .	245
A.2.3 Random nanofibres mat (0.2%) strengthened hybrid composite . . . . .	246
A.2.4 Random nanofibres mat (0.5%) strengthened hybrid composite . . . . .	248
A.2.5 Random nanofibres mat (1%) strengthened hybrid composite . . . . .	249
A.2.6 Aligned nanofibres mat (0.5%) strengthened hybrid composite . . . . .	251
A.2.7 0.25% vol p-SWCNTs doped aligned nanofibres mat (0.5%) strengthened hybrid composite . . . . .	252
A.2.8 0.25% vol f-SWCNTs doped aligned nanofibres mat (0.5%) strengthened hybrid composite . . . . .	254
A.3 Impact Test Details . . . . .	255
A.3.1 Neat glassfibre composite 32% . . . . .	255
A.3.2 Random nanofibres mat strengthened hybrid composite (0.1% Vol) . . . . .	256
A.3.3 Random nanofibres mat (0.2% Vol) strengthened hybrid composite . . . . .	257

---

A.3.4	Random nanofibres mat (0.5% Vol) strengthened hybrid composite . . . . .	258
A.3.5	Random nanofibres mat (1% Vol) strengthened hybrid composite . . . . .	259
A.3.6	0.5% (vol) aligned nanofibres mat strengthened hybrid composite . . . . .	260
A.3.7	0.25% Vol) p-SWCNTs doped aligned nanofibres mat strengthened hybrid composite . . . . .	261
A.3.8	(0.25% Vol) f-SWCNTs doped aligned nanofibres mat strengthened hybrid composite . . . . .	262
<b>B</b>		<b>264</b>
B.1	Matlab program, Armchair coordinate definitions . . . . .	264
B.2	Matlab program, Zigzag coordinate definitions . . . . .	286
B.3	Macro file (Pristine single wall zigzag) used as input to the ANSYS Mechanical APDL software . . . . .	304
B.4	Macro file (Defective single wall zigzag) used as input to the ANSYS Mechanical APDL software . . . . .	319
<b>C</b>		<b>341</b>
C.1	Paper1 . . . . .	341
C.2	Paper2 . . . . .	342

# List of Figures

1.1	Schematic of multiscale nanohybrid composite . . . . .	4
1.2	(a) agglomeration of CNTs and (b) nanovoids near agglomeration [22] . . . . .	5
1.3	Reinforcement-matrix interface/interphase region . . . . .	6
1.4	Schematic of different interface region bonding types (a) Mechanical interlocking (b) Physical bonding (c) Chemical bonding [33] . . . . .	7
1.5	Schematic of proposed study . . . . .	11
1.6	Schematic of thesis layout . . . . .	15
2.1	Type of composites . . . . .	17
2.2	Inter-laminar region in composite material [8] . . . . .	20
2.3	(a) CNT bridging (b) CNT pull outs (c) crack path deflection [68, 69] . . . . .	22
2.4	Graphene sheet (single layer) . . . . .	23
2.5	(a) TEM image of the cup stacked vapour grown CNF (b) Schematic representation of CNF [82] . . . . .	24
2.6	Carbon nanotubes arrangements a) Armchair b) Zigzag c) Chiral . . . . .	25
2.7	Carbon nanotube types a) SCNT b) Double wall CNT c) Multi wall CNT [83] . . . . .	26
2.8	(a) Schematic of calendaring machine (b) Extrusion mixer [23] . . . . .	28
2.9	(a) Magnetic stirring machine (b) Schematic of ball milling [96] (c) Sonicator . . . . .	29
2.10	Fibre-Matrix (a) Interface region (b) interlaminar region [106] . . . . .	32
2.11	Crack development at interface region in the composite (SEM image) [115] . . . . .	34
2.12	(a) Defective chemical functionalization, (b) Sidewall functionalization, (c,d,e) Physical functionalization (nan covalent) [124] . . . . .	37
2.13	(a) Model 1, (b) Model 2, (c) Model 3, and (d) Model 4 [129] . . . . .	39
2.14	Simple schematic of electrospinning technique . . . . .	42
2.15	Electrospun PAN nanofibres . . . . .	43

---

2.16	Electrospinning process . . . . .	47
2.17	(a) Thin drum collector, (b) Parallel plate collector, (c) Cylindrical collector [166] . . . . .	47
2.18	Vacuum assisted resin transfer method . . . . .	49
2.19	Representative volume element [181] . . . . .	52
3.1	Schematic of proposed methodology . . . . .	59
3.2	Manufacturing steps of the multiscale nano hybrid composite . . . . .	60
3.3	Friedal craft alkylation process . . . . .	68
3.4	Raman spectroscopy of the Pistine and functionalized SWCNTs . . . . .	69
3.5	IR spectra of (a) p-SWCNTs and (b) f-SWCNTs . . . . .	70
3.6	(a) Balance for weights (b) Magnetic stirrer (model MSH-300N) (c) Sonicator(model UD80SH-2L INTEGRAL SYSTEMS), (d) Mixing process of CNTs into the polymer solution . . . . .	72
3.7	Precipitation trends of SWCNTs in the two step dispersion . . . . .	73
3.8	Test sample dimensions (a) Tensile ASTM D638-08:2010 (b) Flexural ASTM D790- 07:2010 (c) Impact test specimens ASTM D256-06a:2010 . . . . .	74
3.9	Cutting layout for test specimens . . . . .	75
3.10	DoAll band saw . . . . .	76
3.11	TensilKut grinder and dog bone copy jig used to cut the tensile specimens . . . . .	77
3.12	(a) Tensile, (b) Flexural and (c) Impact test specimens . . . . .	78
3.13	SHIMADZU Universal testing machine (UTM) . . . . .	79
3.14	Dog bone specimen after test . . . . .	81
3.15	Flexural test specimen setup . . . . .	82
3.16	(a) Impact test machine 'Tinius Olsen Model impact pendulum' (b) Impact test specimen . . . . .	84
3.17	(a) SEM, FEI Nova 600, (b)FEI Quanta 400 FEG, USA . . . . .	86
3.18	Specimens coated for SEM (a and e) Tensile (b)Bending (c and d) Flexural test . . . . .	87
3.19	Working principle of the Raman spectroscopy . . . . .	88
3.20	Schematic of FTIR process . . . . .	90
4.1	Electrospun nanofibre jet path (a) [203], (b)[166] . . . . .	92
4.2	Electrospinning experimental matrix [206] . . . . .	95
4.3	(a)Electrospinning with AVEs, (b) Schematic of electrospinning with AVEs . . . . .	97
4.4	Effect of AVEs using electric field analysis . . . . .	99
4.5	Top view schematic of modified electrospinning process . . . . .	99
4.6	Span of PAN nanofibres vs AVEs position in negative X-direction	100

---

4.7	Span of PAN nanofibres vs AVEs position in Y-direction . . . . .	101
4.8	Spinneret-collector distance vs number of spinnerets maintaining simultaneously continuous jet issue from all six spinnerets . . . . .	101
4.9	Electrospun PAN nanofibre mats . . . . .	103
4.10	VARTM system . . . . .	105
4.11	Composite preform and testing specimens . . . . .	106
4.12	Properties of composites with different volume fraction of glass fibres23232 . . . . .	108
4.13	SEM image of 32% glass fibre composite fractured specimen . . . . .	109
4.14	Tensile properties of random nanofibre mats strengthened hybrid Composite . . . . .	110
4.15	Fracture behaviour of 0.5% volume fraction random PAN nanofibres mat (a) Nanofibres pullout and breakage (b) Nanofibres bridging . . . . .	111
4.16	Agglomerated PAN nanofibres in the fractured surface of 1% random PAN nanofibres mat strengthened hybrid composite . . . . .	112
4.17	Flexural properties of random PAN nanofibre mats strengthened hybrid composite . . . . .	113
4.18	SEM image of bending tested 0.5% random PAN nanofibre mats strengthened hybrid composite . . . . .	114
4.19	Impact resistance of random PAN nanofibre mats strengthened hybrid composites . . . . .	115
4.20	SEM image of fractured surface of impact tested of 0.5% random PAN nanofibre mats strengthened hybrid composites . . . . .	116
4.21	Tensile test results for aligned and doped PAN nanofibres mat strengthened hybrid composites . . . . .	117
4.22	Fracture surfaces obtained in tensile tests; (a) random PAN nanofibre strengthened hybrid composite, (b) aligned PAN nanofibre mat strengthened hybrid composite . . . . .	119
4.23	Broken PAN nanofibres in the fractured surface 0.5% aligned PAN nanofibres mat strengthened hybrid composite obtained in tensile tests . . . . .	120
4.24	Fracture surfaces p-SWCNTS doped aligned PAN nanofibre mat strengthened hybrid composite . . . . .	122
4.25	Fracture surfaces of f-SWCNTs doped aligned PAN nanofibre mat strengthened hybrid composite . . . . .	123
4.26	Nanocracks on the fractured surface of f-SWCNTs doped aligned PAN nanofibre mat strengthened hybrid composite . . . . .	124

4.27	Batch wise tensile test results; A: 32% glass fibre composite (GFC), B: 0.5% random PAN nanofibres mat strengthened GFC, C: 0.5% Aligned PAN nanofibre mat strengthened GFC, D: p-SWCNTs doped 0.5% aligned PAN nanofibre mat strengthened GFC, E: f-SWCNTs doped 0.5% aligned PAN nanofibre strengthened GFC . . . . .	125
4.28	Glass fibre fractured surfaces in the tensile tests (a) Neat Glass (b) random PAN nanofibres (c) aligned PAN nanofibres (d) p-SWCNTs doped (e) f-SWCNTs doped aligned PAN nanofibres mats strengthened hybrid composites . . . . .	127
4.29	Flexural test results for aligned and doped PAN nanofibres mat strengthened hybrid composites . . . . .	128
4.30	Fracture surfaces of 0.5% PAN nanofibre strengthened hybrid composites obtained in bending tests using (a) random PAN nanofibres mat (b) Aligned PAN nanofibre mat . . . . .	129
4.31	SEM fractographs of random and aligned PAN nanofibres mat strengthened hybrid composites. (a) broken fibres in bridging (b) elongated fibres in bridging . . . . .	130
4.32	SEM fractographs of random and aligned PAN nanofibres mat strengthened hybrid composites. (a) broken fibres in bridging (b) elongated fibres in bridging . . . . .	132
4.33	Impact test results for aligned and doped PAN nanofibres mat strengthened hybrid composites . . . . .	133
4.34	Fracture surfaces of PAN nanofibre strengthened hybrid composite obtained in impact test using (a) 0.5% random PAN nanofibres mat (b) Aligned PAN nanofibres mat . . . . .	134
4.35	Nanofibres bridging in the impact test specimen . . . . .	135
5.1	a. Hexagonal arrangement, b. Vacancy defect, c. Stone wales defect, d. Adatom in CNTs . . . . .	138
5.2	Equivalent SFS . . . . .	138
5.3	Rolling angle and chiral vector . . . . .	139
5.4	Modeling process of CNTs . . . . .	142
5.5	a) Armchair b) Zigzag CNTs modeling process . . . . .	143
5.6	DWCNT and MWCNTs modelling process a) SWCNT model, b) DWCNT model, c) MWCNT model . . . . .	143
5.7	CNTs with vacancy defects . . . . .	144
5.8	Equivalent SFS modelling process of CNTs . . . . .	144
5.9	Graphical representation of steric potential energy . . . . .	146
5.10	Equivalent beam model . . . . .	147
5.11	Radial test model . . . . .	149

---

5.12	Van der Waals forces interactions between different shells . . . .	151
5.13	Equivalent spring between shells . . . . .	151
5.14	End points of CNTs . . . . .	152
5.15	van der Waals forces trends . . . . .	154
5.16	DWCNTs under tension and torsion tests . . . . .	156
5.17	Elastic/shear modulus of pristine and defective SWCNTs Vs diameter . . . . .	158
5.18	The deformation pattern of hexagonal units (a) armchair and (b) zigzag -tensile load (c) armchair and (d) zigzag-applied moment	159
5.19	Percentage decrease in elastic/shear modulus due to vacancy defects in zigzag/armchair configuration (SWCNTs) as a function of diameter. . . . .	161
5.20	a) Elastic/shear modulus of pristine zigzag/armchair, b) Elastic/shear modulus of (DWCNTs/MWCNTs) obtained from tensile and torsion tests . . . . .	163
6.1	Modelling layout of multiscale nanohybrid composite . . . . .	167
6.2	Modelling details of SWCNTs doped PAN nanofibre RVE . . . .	168
6.3	Modelling details of SWCNTs doped PAN nanofibre RVE . . . .	169
6.4	Illustration of f-SWCNT doped RVE with covalent bonds . . . .	170
6.5	Modelling details of SWCNTs doped PAN nanofibre RVE . . . .	171
6.6	Details of random and aligned nanofibre-matrix RVEs . . . . .	173
6.7	Modelling process for p-SWCNTs and f-SWCNTs doped micro RVE . . . . .	174
6.8	Boundary conditions and tensile test results; (a) Epoxy RVE (control sample), (b) Matrix-random nanofibres RVE, (c) Matrix-aligned nanofibres RVE . . . . .	175
6.9	Composite model developing process . . . . .	177
6.10	Woven glass fibre mat development process . . . . .	178
6.11	Details of numerical model for 32% glass fibre composite . . . .	179
6.12	Equivalent interlaminar region MNHCs model . . . . .	180
6.13	(a) Numerical model boundary conditions and (b) Meshed model	181
6.14	Stress contours of Neat glass fibre composite under tensile load .	183
6.15	Maximum deflection within the interlaminar region of 32% glass fibre composite . . . . .	183
6.16	Theoretical vs experimental stress-strain curve for neat glass fibre composites . . . . .	184
6.17	Random nanofibre mat strengthened hybrid composites results (a) Deformation contours (b) Maximum deflection with in the interlaminar region (c) Theoretical vs experimental stress-strain curves . . . . .	185

---

6.18	Aligned nanofibres mat strengthened hybrid composites results (a) Deformation contours (b) Theoretical vs experimental stress-strain curves . . . . .	186
6.19	p-SWCNTs doped aligned nanofibres mat strengthened hybrid composites results (a) Deformation contours (b) Theoretical vs experimental stress-strain curves . . . . .	187
6.20	f-SWCNTs doped aligned nanofibres mat strengthened hybrid composites results (a) Deformation contours (b) Theoretical vs experimental stress-strain curves . . . . .	188
6.21	Comparison between experimental and theoretical elastic modulus of multiscale nanohybrid composites . . . . .	189
6.22	% Error-Theoretical vs Experimental elastic modulus . . . . .	190
A.1	Tensile strengths of glass fibre composite (32% vol) specimens . . . . .	232
A.2	Tested Tensile specimens of glass fibre composite (32% vol) . . . . .	232
A.3	Tensile strengths of random nanofibres mat (0.1% vol) strengthened hybrid composite specimens . . . . .	233
A.4	Tested Tensile specimens of random nanofibres mat (0.1% vol) strengthened hybrid composite . . . . .	234
A.5	Tensile strengths of random nanofibres mat (0.2% vol) strengthened hybrid composite specimens . . . . .	235
A.6	Tested Tensile specimens of random nanofibres mat (0.2% vol) strengthened hybrid composite . . . . .	235
A.7	Tensile strengths of random nanofibres mat (0.5% vol) strengthened hybrid composite specimens . . . . .	236
A.8	Tested Tensile specimens of random nanofibres mat (0.5% vol) strengthened hybrid composite . . . . .	237
A.9	Tensile strengths of random nanofibres mat (1% vol) strengthened hybrid composite specimens . . . . .	238
A.10	Tested Tensile specimens of random nanofibres mat (1% vol) strengthened hybrid composite . . . . .	238
A.11	Tensile strengths of aligned nanofibres mat (0.5% vol) strengthened hybrid composite specimens . . . . .	239
A.12	Tested Tensile specimens of aligned nanofibres mat (0.5% vol) strengthened hybrid composite . . . . .	240
A.13	Tensile strengths of p-SWCNTs (0.25% Vol) doped nanofibres mat (0.5% vol) strengthened hybrid composite specimens . . . . .	241
A.14	Tested Tensile specimens of p-SWCNTs (vol 0.25%) doped aligned nanofibres mat (0.5% vol) strengthened hybrid composite samples	241
A.15	Tensile strengths of f-SWCNTs (0.25% Vol) doped nanofibres mat (0.5% vol) strengthened hybrid composite specimens . . . . .	242

---

A.16 Tested Tensile specimens of f-SWCNTs doped aligned nanofibres mat (0.5% vol) strengthened hybrid composite . . . . .	243
A.17 Flexural strengths of glass fibre samples (32% Vol) . . . . .	244
A.18 Tested flexural specimens of glassfibre samples (32% Vol) . . . . .	244
A.19 Flexural strengths of Random nanofibres mat (0.1%) strengthened hybrid composite samples . . . . .	245
A.20 Tested specimens of random nanofibres mat (0.1%) strengthened hybrid composite . . . . .	246
A.21 Flexural strengths of Random nanofibres mat (0.2%) strengthened hybrid composite samples . . . . .	247
A.22 Tested flexural random nanofibres mat (0.2%) strengthened hybrid composite samples . . . . .	247
A.23 Flexural strengths of random nanofibres mat (0.5%) strengthened hybrid composite samples . . . . .	248
A.24 Tested specimens of random nanofibres mat (0.5%) strengthened hybrid composite . . . . .	249
A.25 Flexural strengths of random nanofibres mat (1%) strengthened hybrid composite samples . . . . .	250
A.26 Tested specimens of Flexural Random nanofibres mat (1%) strengthened hybrid composite . . . . .	250
A.27 Flexural strengths of aligned nanofibres mat (0.5%) strengthened hybrid composite samples . . . . .	251
A.28 Tested specimens of Aligned nanofibres mat (0.5%) strengthened hybrid composite samples . . . . .	252
A.29 Flexural strengths of 0.25% vol p-SWCNTs doped aligned nanofibres mat (0.5%) strengthened hybrid composite samples . . . . .	253
A.30 Tested specimens of 0.25% vol p-SWCNTs doped aligned nanofibres mat (0.5%) strengthened hybrid composite . . . . .	253
A.31 Flexural strengths of 0.25% vol f-SWCNTs doped aligned nanofibres mat (0.5%) strengthened hybrid composite samples . . . . .	254
A.32 Tested specimens 0.25% vol f-SWCNTs doped aligned nanofibres mat (0.5%) strengthened hybrid composite . . . . .	255
A.33 Tested impact specimens of glassfibre composite (32% vol) . . . . .	256
A.34 Tested specimens of Random nanofibres mat (0.1% Vol) strengthened hybrid composite samples . . . . .	257
A.35 Tested impact specimens of random nanofibres mat (0.2% Vol) strengthened hybrid composite . . . . .	258
A.36 Tested impact specimens of Random nanofibres mat (0.5% Vol) strengthened hybrid composite . . . . .	259
A.37 Tested impact specimens of Random nanofibres mat (1% Vol) strengthened hybrid composite . . . . .	260

---

A.38 Tested specimens of 0.5% aligned nanofibres mat glass fibre composite . . . . .	261
A.39 Tested specimens of (0.25% Vol) p-SWCNTs doped aligned nanofibres mat strengthened hybrid composite . . . . .	262
A.40 Tested Impact specimens of f-SWCNTs doped aligned nanofibres mat strengthened hybrid composite . . . . .	263

# List of Tables

1.1	Mechanical properties of CNTs [13, 14] . . . . .	3
2.1	Alignment methods of CNTs and their disadvantages . . . . .	40
3.1	Mechanical and physical properties of AMPREG 21 (resin-hardener) at 25°C [189] . . . . .	61
3.2	Standard mixing ratio of resin to hardener for Ampreg 21 [189] .	62
3.3	Woven E-glass properties [190] . . . . .	62
3.4	Parameters matrix for electrospinning process . . . . .	64
3.5	Volume Fraction values for different concentrations of PAN/DMF solution . . . . .	66
3.6	Proposed controlling factors and variables of dispersion process .	71
4.1	Electrospinning parameters range and optimized value along with AVEs . . . . .	96
5.1	Configuration properties . . . . .	141
5.2	Bond length and molecular mechanics constant values [225] . . .	148
5.3	Range of values for parametric study variables . . . . .	149
5.4	Orthotropic properties of CNTs . . . . .	150
5.5	Equivalent spring stiffness values . . . . .	154
5.6	Properties of pristine and vacancy defects SWCNTs (zigzag and armchair) . . . . .	157
5.7	Percentile decrease of elastic and shear modulus due to vacancy defects (zigzag and armchair) . . . . .	160
5.8	Properties of DWCNTs/MWCNTs of zigzag and armchair . . . .	162
5.9	CNTs elastic properties comparison between the current study and other researches . . . . .	164
6.1	Properties of the equivalent doped nanofibres materials . . . . .	172
6.2	Properties of the equivalent random and aligned doped-matrix RVE . . . . .	176

---

A.1	05 specimens batch tensile test results of neat glassfibre composite (32% Vol)	231
A.2	05 specimens batch tensile test results of random nanofibres mat (0.1% Vol) strengthened hybrid composite	233
A.3	05 specimens batch tensile test results of random nanofibres mat (0.2% Vol) strengthened hybrid composite	234
A.4	05 specimens batch tensile test results of random nanofibres mat (0.5% Vol) strengthened hybrid composite	236
A.5	05 specimens batch tensile test of random nanofibres mat (1% Vol) strengthened hybrid composite	237
A.6	05 specimens batch tensile test of aligned nanofibres mat (0.5% Vol) strengthened hybrid composite	239
A.7	05 specimens batch tensile test of (0.25% Vol) p-SWCNTs doped aligned nanofibres mat strengthened hybrid composite	240
A.8	05 specimens batch tensile test of (0.25% Vol) f-SWCNTs doped aligned nanofibre mat strengthened hybrid composite	242
A.9	Flexural strength details of neat glassfibre specimens (32% Vol)	243
A.10	Flexural strength details of Random nanofibres mat (0.1%) strengthened hybrid composite specimens	245
A.11	Flexural strength details of Random nanofibres mat (0.2%) strengthened hybrid composite specimens	246
A.12	Flexural strength details of random nanofibres mat (0.5%) strengthened hybrid composite specimens	248
A.13	Flexural strength of random nanofibres mat (1%) strengthened hybrid composite specimens	249
A.14	Flexural strength details of Aligned nanofibres mat (0.5%) strengthened hybrid composite	251
A.15	Flexural strength details of CNTs doped 0.5% aligned nanofibres mat	252
A.16	Flexural strength details of 0.25% vol f-SWCNTs doped aligned nanofibres mat (0.5%) strengthened hybrid composite	254
A.17	Impact test specimen results for neat glass fibre composite 32 %	255
A.18	Impact test specimen results for 0.1% Random nanofibres mat strengthened hybrid composite	256
A.19	Impact test specimens results for random nanofibres mat (0.2% Vol) strengthened hybrid composite	257
A.20	Impact test specimens results for Random nanofibres mat (0.5% Vol) strengthened hybrid composite	258
A.21	Impact test specimen results for (1% vol) random nanofibres mat glass fibre composite	259

---

A.22 Impact test specimen results for 0.5% volume fraction aligned nanofibres mat . . . . .	260
A.23 Impact test specimen results for (0.25% Vol) p-SWCNTs doped aligned nanofibre mat strengthened hybrid composite . . . . .	261
A.24 Impact test specimen results for 0.25% Vol) f-SWCNTs doped aligned nanofibres mat strengthened hybrid composite . . . . .	262
B.1 Properties of pristine and defective SWCNT of zigzag . . . . .	335
B.2 Properties of pristine DWCNT of zigzag . . . . .	336
B.3 Properties of MWCNT of zigzag . . . . .	337
B.4 Properties of pristine and defective SWCNT of zigzag . . . . .	338
B.5 Properties of DWCNT of Armchair . . . . .	339
B.6 Properties of MWCNT of Armchair . . . . .	340

# Abbreviations

<b>CNTs</b>	Carbon nano-tubes
<b>CNF</b>	Carbon nano-fibres
<b>CNPs</b>	Carbon nano-particles
<b>MNHCs</b>	Multi scale nano-hybrid composites
<b>PMCs</b>	Polymer matrix composites
<b>CMCs</b>	Ceramic matrix composites
<b>MDS</b>	Molecular dynamic simulations
<b>VARTM</b>	Vaccum assisted resin transfer moulding
<b>SWCNTs</b>	Single walled carbon Nano-tubes
<b>DWCNTs</b>	Double walled carbon Nano-tubes
<b>MWCNTs</b>	Multi walled carbon Nano-tubes
<b>SEM</b>	Scanning electron microscopy
<b>FTIR</b>	Fourier transform infrared spectroscopy
<b>AVEs</b>	Auxiliary vertical electrodes
<b>RVEs</b>	Representative volume element
<b>p-SWCNTs</b>	Pristine single wall carbon nanotubes
<b>f-SWCNTs</b>	Pristine single wall carbon nanotubes
<b>GFC</b>	Glass fibre composite
<b>NF</b>	Nanofibres
<b>PAN</b>	Polyacrylonitrile

---

<b>DMF</b>	Dimethylformamide
<b>TPa</b>	Tera pascal
<b>GPa</b>	Giga pascal
<b>CVD</b>	Chemical Vapour Decomposition
<b>MM</b>	Molecular mechanics
<b>FEA</b>	Finite element analysis
<b>MMCs</b>	Metal matrix composites
<b>FRCs</b>	Fibre reinforced composites
<b>l</b>	length
<b>d</b>	diameter
<b>OH</b>	Hydroxyl
<b>COOH</b>	carboxylic
<b>RTM</b>	Resin Transfer Moulding
<b>CM</b>	Continuum mechanics
<b>MDS</b>	Molecular Dynamic Simulations
<b>REBO</b>	Reactive empirical bond order
<b>AIREBO</b>	adaptive intermolecular reactive empirical
<b>LAMMPS</b>	Large-scale Atomic/Molecular Massively Parallel Simulator
<b>FCA</b>	Friedel-Crafts Alkylation
<b>PPE</b>	Personal protective equipment
<b>UTM</b>	universal testing machine
<b>MMU</b>	Microscopy and Microanalysis Unit
<b>RBM</b>	Radial breathing mode
<b>FTIR</b>	Fourier transform infrared spectroscopy
<b>CFCs</b>	Conventional fibre composites
<b>AVS</b>	Auxiliary voltage source

# Physical Constants

*Bond stretching force constant =  $k_r = 938 \text{ kcal.mol}^{-1}.\text{A}^{-2}$*

*Bond angle bending force constant =  $K_\theta = 126 \text{ kcal.mol}^{-1}.\text{A}^{-2}$*

*Torsional resistance force constant =  $K_\tau = 39.986 \text{ kcal.mol}^{-1}.\text{A}^{-2}$*

# Symbols

$\rho$	density	$g/cm^3$
$m_a$	mass per unit area	$g/cm^2$
$V_{gf}$	volume of the glass fibre	$cm^2$
$W_{nf}$	weight of nanofibres	$g$
$L_{CT}$	average of length of SWCNTs	$\mu m$
$d_{CT}$	average diameter of SWCNTs	$nm$
$E$	Young's Modulus	$GPa$
$\Delta L$	Change in length	$\mu m$
$\sigma$	Stress	$MPa$
$\sigma_f$	flexural stress	$MPa$
$L$	length between supports	$mm$
$b$	width of specimen measured at its centre	$mm$
$h$	thickness of specimen measured at its centre	$mm$
$\epsilon_f$	flexural strain of specimen	$mm/mm$
$E_f$	flexural modulus of elasticity	$MPa$
$K_I$	impact resistance	$KJ/m^2$
$e_I$	energy lost by pendulum due to impact	$KJ$
$A_I$	cross-sectional area of impact specimen	$m^2$
$\nu$	Poisson's ratio	
$V_f$	fibre volume fraction	

$V_m$  matrix volume fraction  
 $\epsilon$  strain

*DEDICATION*

*To my loving and caring parents, wife, adorable daughter, sons, sisters, brothers, and supportive lab staff.*

# Chapter 1

## Introduction

### 1.1 Background

Historically, men developed the first composite material out of mud and grass straws for fabricating bricks for construction [1]. Sticking of wood parts into diverse shapes has been used by the early Egyptians [2]. Concrete is another ancient composite made of aggregates, sand, and cement and is still in use for construction. Composite materials also exist in numerous natural forms such as bone, wood, and etc.

The increasing demand of highly functional composite materials in many engineering applications, such as aerospace, automobiles, ship buildings, submarine, nuclear, sporting goods, heat protecting cloths, vehicle tyres, and chemical facilities [3, 4] have forced the material scientists to develop new and innovative materials. The primary objective of these materials is to offer low weight and enhanced structural properties considering the environmental factors [3] and hence the development of composite materials has started. Besides weight reduction, the composite materials are also found to be the replacements for

the conventional materials, such as alloys, owing to their low cost, aesthetic look, and easy availability [5]. In addition, the mechanical properties of these composite materials can be tailored to the required design criterion by changing the ratio of reinforcements and matrix materials [2]. For example, a laminate can be manufactured from multiple laminae with desirable mechanical properties in different directions [6]. These advantages have escalated the use of fibre composites in various commercial and engineering applications.

A composite consists typically of binder and reinforcing material. The binder is commonly referred to as a matrix, which includes metals, ceramics, and polymers. The matrix holds the reinforcement, retains the composites shape, and protects the reinforcements from the environmental hazards. The reinforcements are geometrically controlled constituents found in different shapes such as fibres, particles or flakes, usually with high strength and modulus values. Various types of reinforcements, such as glass, aramid, carbon and natural fibres are used for manufacturing composites. Based on the types of matrices, the composites are commonly grouped into ceramic matrix, metal matrix and polymer matrix composites. Among the other composites, the polymer matrix reinforced with glass fibre composites are extensively used in various engineering applications due to their ease in manufacturing, lightweight, improved mechanical, and physical properties as explained before.

However, a number of factors limit their application as structural materials. One such critical issue is the failure at the matrix rich interlaminar regions. This is a common cause of catastrophic failure and is of critical concern in commercial applications where the stress transfer between the load bearing fibres and the matrix occurs [7]. Even, the composites with a higher volume fraction of more than 60% are prone to the interlaminar failures [8]. Another critical issue is the in-plane fibres orientation, which results in low resistance

to transverse loads (through thickness) [9]. The inferior through thickness strength is often the cause of delamination within the interlaminar region.

Hence, the researchers and engineers from industries have focused on using secondary reinforcements in the form of nanofillers (carbon nanoparticles and nanofibres) to strengthen the interlaminar regions. Kickelbick [10] suggested that reducing the length scale of the reinforcing fillers to the size of organic building blocks of polymer chains could improve the properties of the final composite materials. These nanoparticles benefit the composites by developing nanoscale straightened interface regions with their exceptional properties (Table 1.1) [11, 12]. The combination of carbon nanoparticles and macrofibre has a hierarchical structure (refer to Figure 1.1) ranging from nanoscales to macro scales and is termed as multiscale nanohybrid composites (MNHCs).

TABLE 1.1: Mechanical properties of CNTs [13, 14]

S.NO	Carbon nanoparticles (CNP <sub>s</sub> )	Young's Modulus	Tensile Strength
1	Graphene	1 TPa	130GPa
2	Carbon nanotubes (CNTs)	1.2 TPa	50-200 GPa
3	Carbon nanofibres (CNFs)	240 GPa	2.92GPa

The nanofillers of different types (nanoparticles and nanofibres) have been used to improve the interlaminar properties [15, 16]. These reinforcements include carbon nanotubes(CNTs) and nanofibres with dimensions in the range of nanometer and can prevent the premature failure at the weak inter-laminar region owing to their sizes [12]. Among these nanoreinforcements, carbon nanotubes (CNTs) provide the utmost scientific interest due to their large surface areas and extraordinary properties (refer to Table 1.1). However, the researchers could not manage to utilize the full potential of CNTs due to their inherent properties [9, 17], such as:

1. Agglomeration

2. Misalignment
3. Poor interfacial adhesion

These challenges in using CNTs as reinforcements are discussed below.

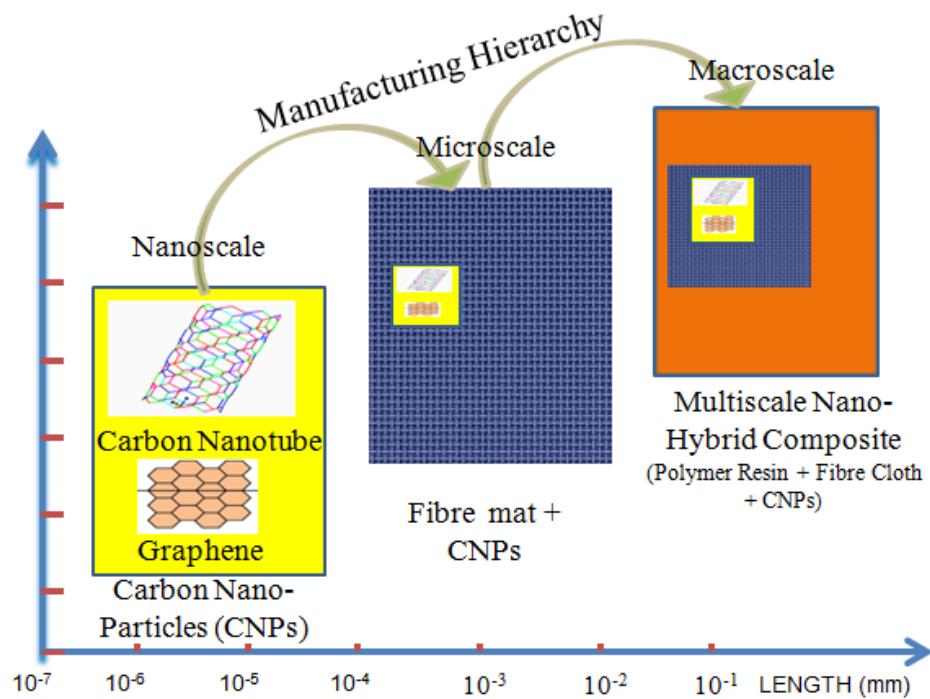


FIGURE 1.1: Schematic of multiscale nanohybrid composite

### 1.1.1 Agglomeration of CNTs

The uniform dispersion of CNTs within the matrix system is essential for strong interfaces between the matrix and CNTs. The CNTs have a strong tendency to form firm agglomerates (bundles) due to the electrostatic interaction and van der Waals forces, which lead to poor dispersion of the nanotubes into the matrix [18]. These agglomerations create micro and nano level cracks (voids) (refer to Figure 1.2) within the matrix (interlaminar region), which is the most

common cause of premature failure and results in inferior mechanical properties [19–22]. The general mechanical process used for removing agglomeration and improving the dispersion are magnetic stirring, calendaring, ball mill, extrusion, and sonication [23]. However, the mechanical stirring could not break the agglomerating bonds and are limited in capacity [24]. The sonication method uses high-frequency ultrasound waves and is capable of breaking the bonds with improved dispersion of CNTs [25]. However, longer duration of sonication destroys the CNTs, thereby reducing their aspect ratio and properties. Furthermore, the CNTs dispersed using these methods can agglomerate again with time and thus reduces the effectiveness of these techniques [26]. Therefore, there is a need for improving the dispersion of CNTs for improving the interlaminar properties of the multiscale hybrid composites.

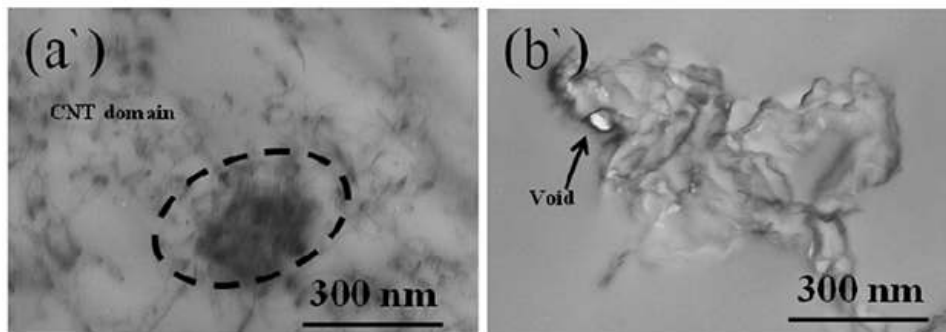


FIGURE 1.2: (a) agglomeration of CNTs and (b) nanovoids near agglomeration [22]

### 1.1.2 Misalignment of the CNTs

The alignment of reinforcement in composites is another important parameter and the composite properties depend on the degree of alignment [27]. Conventional dispersion methods such as solution blending, in-situ polymerisation and melt blending are unable to align the CNTs due to their nanosizes.

Hence, other techniques have been suggested by various researchers to improve the alignment such as Chemical Vapour Decomposition (CVD), Spinning Processes (melt spinning, solution spinning, emulsion spinning) and Electrical or Magnetic Field alignment. However, CVD causes damage to the host fibre surface [20] and creates voids and air gaps. Spinning process can only produce fibres having diameters in the range of micrometres [28]. The bigger diameter of the fibres as compared to CNTs cause misalignment where the desired improvement cannot be achieved. Electrical or magnetic fields are also prone to misalignment of CNTs due to field variation along the distance [29, 30]. Hence, the alignment of CNTs along the preferred direction still remains to be addressed and an effective method is required.

### 1.1.3 Poor Interface Region between CNTs and Matrix

The interface region is a boundary where reinforcements and matrix come into contact with each other as schematically shown in Figure 1.3. The load transfer from matrix to reinforcement takes place through the interface region, which has different properties as compared to the reinforcements and the matrix.

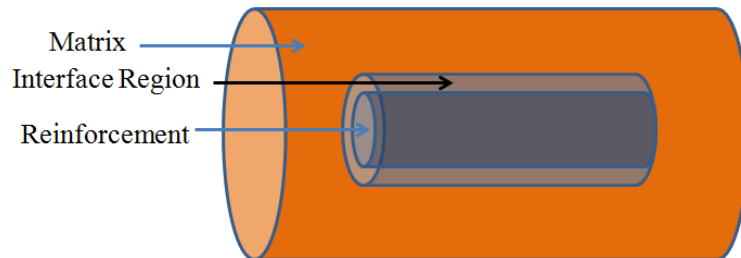


FIGURE 1.3: Reinforcement-matrix interface/interphase region

The interfacial bonding between the matrix and the reinforcements takes place mainly in one or more of the following ways (Figure 1.4) [31];

- Mechanical interlocking/bonding
- Physical bonding
- Chemical bonding

Mechanical bonding creates frictional contacts through keying or interlocking between the matrix and reinforcing materials. The frictional force due to interlocking assists in transferring the applied load from a matrix to reinforcements. The extent of the frictional force depends on the wettability of the matrix and roughness of reinforcements.

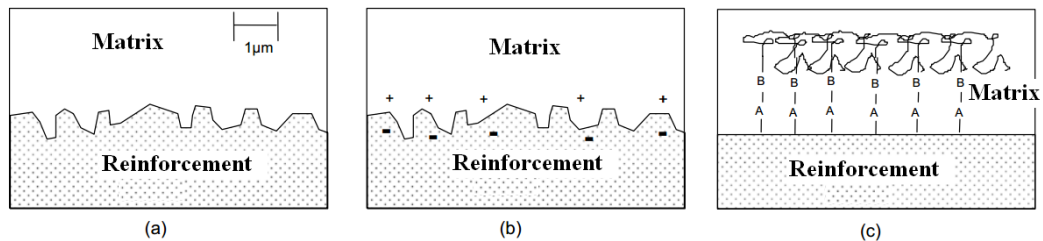


FIGURE 1.4: Schematic of different interface region bonding types (a) Mechanical interlocking (b) Physical bonding (c) Chemical bonding [33]

Physical bonding refers to the secondary(weak) or van der Waals forces, hydrogen bonding and dipole interactions. These are intermolecular forces caused by attraction or repulsion between molecules. Naturally, CNTs interact with the surrounding matrix through van der Waals forces due to their inert nature, which is insufficient for load transfer at the interface region [23]. Chemical bonding is created through covalent, non-covalent functionalization and surface modification of CNTs through surfactants and is considered more effective than the mechanical and physical bonding [8]. However, the disadvantage of the chemical functionalization process is that it creates defects in the structure of CNTs, which significantly reduces its mechanical properties [34]. Therefore,

an effective functionalization method is required for improving the interfacial adhesion.

#### **1.1.4 CNTs doped nanofibre mats**

As discussed before, the issues of misalignment, dispersion and interfacial adhesion could be improved by doping the functionalized CNTs within nanofibres and producing doped nanofiber mats. These CNTs doped nanofiber mats could provide added advantages, such as

- Easy insertion between conventional fabrics, thus the addition of them does not lead to a substantial increase in processing costs.
- Able to reduce the mismatch of ply properties between fibres and matrix due to their uniform thickness along the interlaminar regions.
- Act as bonding plies that join the adjacent fibre plies without increasing the thickness of the laminates.
- They are very thin, thus the addition of them does not add significant weight increase to the final composite material.
- The high percentage of porosity and irregular pores between the nanofibers can lead to an inter-penetrated structure when dispersed in the matrix and also increases the mechanical strength due to the mechanism of interlock.

Although researchers use a number of methods to produce CNTs doped nanofibre mats, the electrospinning process is versatile for incorporating new technologies in producing nanofibre mats. The whipping portion of electrospinning

jets have nanosize diameters and are vital for achieving nanofibres with improved mechanical properties [35]. However, the randomly aligned nanofibres mats produced by the conventional electrospinning process significantly reduce the desired mechanical properties of nanofibres [36]. Thus the currently used electrospinning process needs to be modified for producing aligned nanofibre mats and aligned CNTs doped nanofibre mats, which are expected to further improve the required mechanical properties.

### **1.1.5 Numerical modelling of CNTs and multiscale CNTs doped nanohybrid composites**

In addition to the experimental analysis, a number of numerical methods were also developed in predicting the mechanical properties of single, double and multiwalled carbon nanotubes. However, very limited research works were focused on understanding the effect of orthotropic behaviour and vacancies defect on the CNTs properties using molecular mechanics (MM) coupled with the conventional finite element analysis (FEA). The MM-FEA coupled numerical analysis might provide the benefit of both molecular and continuum scales for obtaining the CNTs properties, which will further assist in selecting suitable CNTs as a secondary reinforcement of multiscale hybrid composites.

Furthermore, it is also deemed necessary that the modelling of multiscale nanohybrid composites (MNHCs) using the predicted CNTs properties will benefit in validating the experimental results. This validation will provide opportunities for transferring the small-scale experimental results to the real-life applications. The currently available numerical models were based on the assumptions of perfect bonding between CNTs and matrix to ease the calculations and also ignored the effect of orthotropic behaviour and vacancies defect

of CNTs within the interlaminar region and the overall mechanical properties of MNHCs. Therefore, the numerical results may not be validated with the experimental results [37–39]. Therefore, the present work aimed at developing the numerical analysis of multiscale nanohybrid composites (MNHCs), which can reduce the mismatch between experimental results and numerical predictions. In this research, the numerical modelling of the multiscale nanohybrid composite will focus on the following issues which were expected to provide comparable results with low computation cost:

- Modelling the MNHCs interlaminar region with nano reinforcement.
- Using an equivalent true atomic structure of pristine and defected CNTs with orthotropic behaviour rather than assuming the SWCNTs as rod or cylinder in MNHCs.
- Modelling of the interface between SWCNTs and the surrounding polymer as van der Waals interaction and covalent bond.

## 1.2 Research Motivation

The recent research works have proposed that the carbon nanotubes (CNTs) could be used as secondary reinforcements for strengthening the interlaminar region of polymer composites due to their superior mechanical and geometrical (diameter and length) properties. However, there are a number of issues that need to be understood for achieving the full potential of nanofillers (nanofibres and CNTs) as an interlaminar strengthening mechanism. These factors are generally associated with agglomeration (poor dispersion) and misalignment of nanofillers and poor interfacial adhesion with the matrix. The above issues have emphasised more focused research analysis for understanding the effect of

nanoreinforcements for improving the interlaminar properties and the overall multiscale hybrid composites. Figure 1.5 shows the schematic of the proposed study;

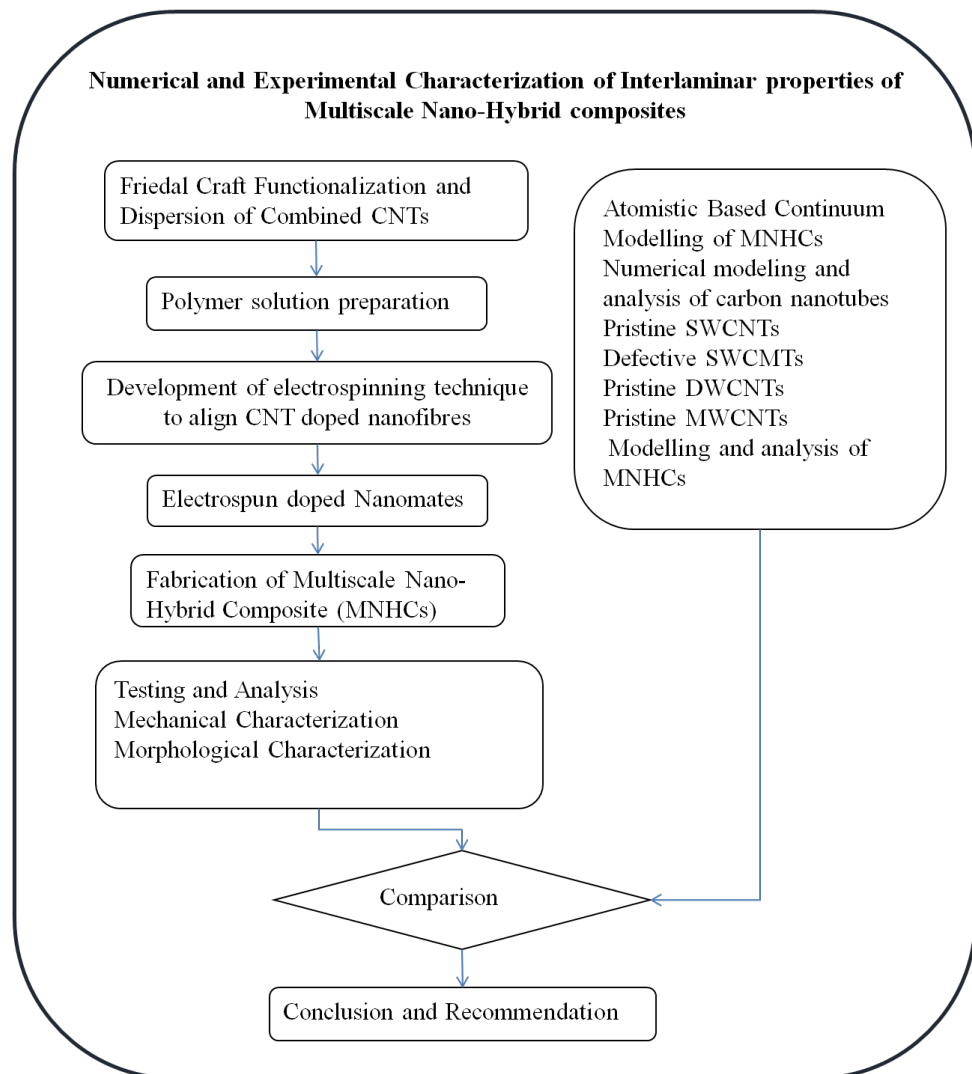


FIGURE 1.5: Schematic of proposed study

## 1.3 Problem Statement

In recent years significant efforts have gone into improving the interlaminar regions using secondary nanoreinforcements and also for developing improved multiscale nanohybrid composites (MNHCs). The nanoparticles, in particular, the CNTs have the potential to improve the interlaminar region properties and also expected to prevent the premature failure owing to their sizes [12]. These particles develop an interface area with surrounding polymers and could have much better properties than the bulk polymer [40]. The improvement of the properties of the interlaminar region depends on;

- The homogeneous dispersion of CNTs, which increases the interfacial area between CNTs and matrix as compared to entangled CNTs.
- The aligned CNTs, which offer more resistance to the applied load, thus improving the properties of the interlaminar region.
- The strong interfacial adhesion of CNTs with the matrix, which is expected to have improved mechanical properties.

However, current manufacturing techniques of MNHCs suffer from the disadvantages of agglomeration, misalignment, and poor interface bonding of CNTs with the matrix.

## 1.4 Research Objectives

It is understood from the recent research works [41, 42] that currently very limited attention was given for using CNTs doped electrospun nanofibres mats for strengthening the interlaminar properties. Moreover the dispersion, alignment

[43], and the interfacial adhesion of CNTs [38, 44] remain a challenge, which demands more innovative experimental and numerical methods [9, 18, 45]. Based on these requirements the following objectives are defined.

- Functionalization of CNTs using Friedel-Craft alkylation for improving the dispersion and the interfacial adhesion of CNTs within the matrix.
- Combination of mixing processes (Magnetic Stirrer and Sonication) for improving the dispersion of CNTs without destroying the aspect ratios.
- Improved alignment of the CNTs doped nanofibres using the modified electro-spinning technique to enhance the properties of the inter-laminar region.
- Manufacture a multiscale nanohybrid composite (MNHCs) consisting of CNTs doped nanofibres glass fibres.
- Experimental and morphological characterization of the MNHCs to determine the effect of the aligned CNTs doped nanofibres mats on improving the interlaminar properties of the multiscale hybrid composites.
- Develop a modelling technique to characterize the pristine, defective and multiwall CNTs.
- Based on the previous step, develop a numerical model for characterizing the multiscale hybrid composites strengthened with pristine and functionalized SWCNTs.
- Validate the numerical model with the experimental data.

## 1.5 Thesis Layout

This thesis is organised into seven chapters as shown in the schematic (Figure 1.6). A general introduction along with the motivation, problem statement and research objectives of the study are provided in Chapter 1. Chapter 2 includes a critical review of the interactive research of the interlaminar region, CNTs, electrospun nanofibres and the numerical characterization methods. Chapter 3 describes the manufacturing details of MNHCs. It includes the functionalization method, two-step optimised dispersion of CNTs, modification of the electrospinning method and vacuum assisted resin transfer moulding method.

Chapter 4 explains the manufacturing details of MNHCs along with the modified technique of electrospinning process and discusses the Mechanical and morphological characterization of the manufactured MNHCs. Chapter 5 presents the details of the newly developed SFS model of the CNTs with orthotropic material properties and compared with other studies.

Chapter 6 provides the details of the FEA model for MNHCs developed with realistic interfacial bonds with pristine and functionalized SWCNTs and compares the result of the experimental and numerical characterized MNHCs. In Chapter 7, the conclusions and recommendations are briefly mentioned along with future work.

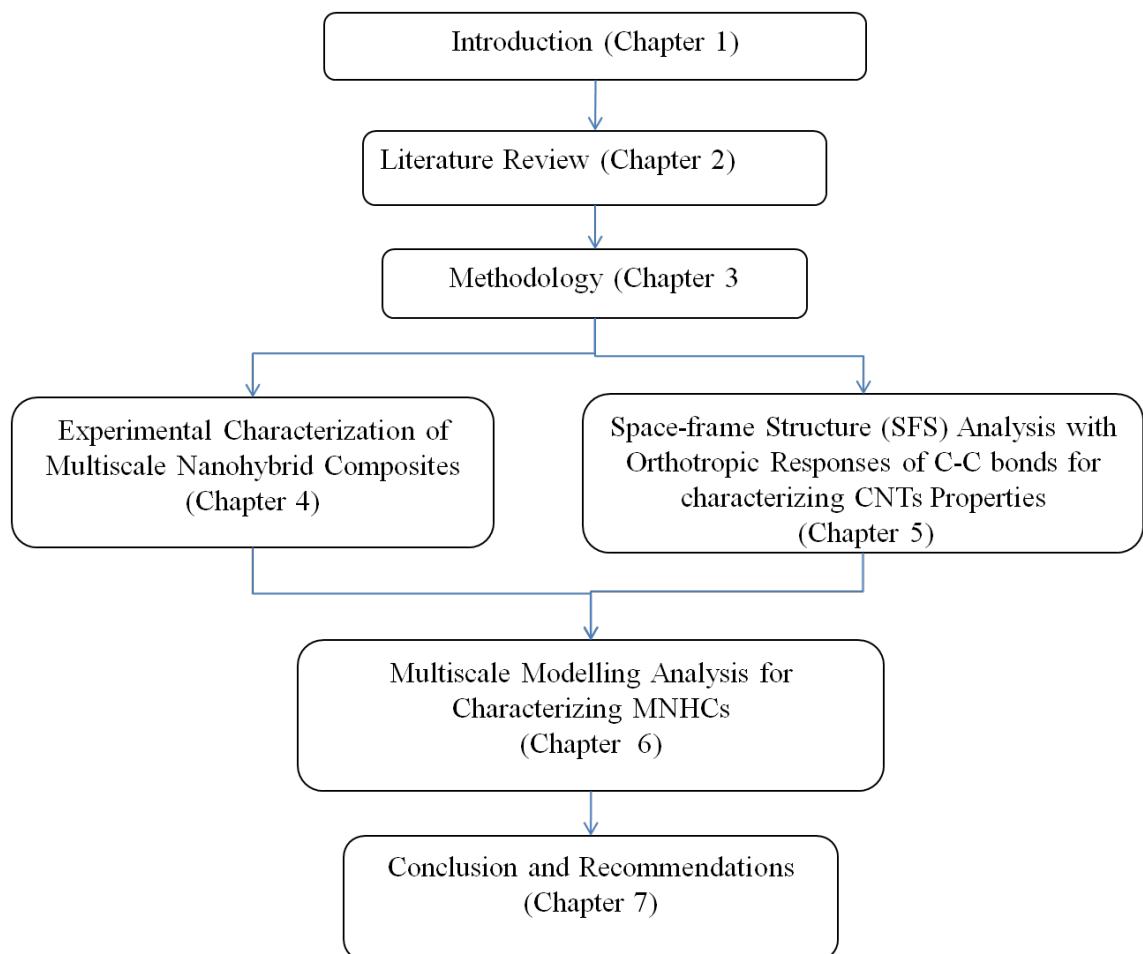


FIGURE 1.6: Schematic of thesis layout

# Chapter 2

## Literature Review

Composites are used in a wide range of engineering applications substituting the conventional materials for example steel [46, 47] and gained significance in different high tech research fields. Compared to conventional materials, ceramic, metallic and polymer composites possess high strength-to-weight ratio, high stiffness, good resistance to fatigue and corrosion [5]. Composites are developed by mixing two or more different materials. Constituents of the composites remain recognisable chemically and physically in the final product and interact with each other through the inevitable interface region. Because of interface regions, the final product has better or desirable mechanical and physical properties, which can not be achieved separately with each constituent alone. Wood is a naturally available composite made of lignin matrix holding cellulose fibres. The humans have been developing the composites, beginning from straw-mud composites to the latest metal and synthetic fibre composites.

Composite materials provide design flexibility depending upon the constituents ratio, geometry of reinforcements (particles, discontinuous, continuous) and orientations. For example, long fibres placed in a single direction into the

matrix provides strength in the same direction. While short discontinuous fibres exhibit equal properties in all directions. Manufacturing processes also impact the properties of composites. Composites developed with mouldings have different properties than hand lapping process. Figure 2.1 shows different types of composites, which are discussed in the ensuing paragraphs:

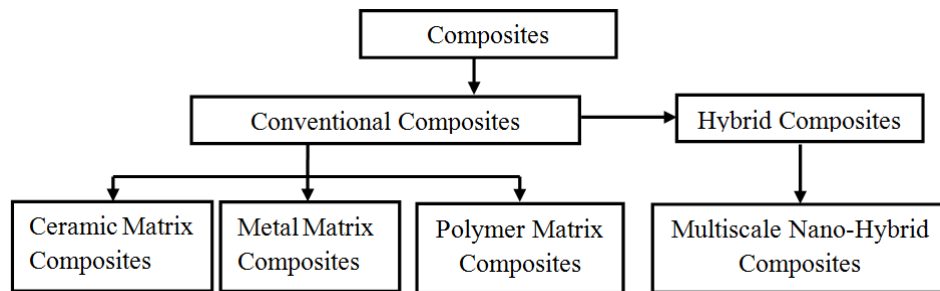


FIGURE 2.1: Type of composites

## 2.1 Conventional Composites

### 2.1.1 Ceramic matrix composite (CMC)

Ceramic matrix composite is the engineered combination of ceramic matrix with ceramic fibre. The ceramic matrix includes carbides (aluminium carbide, magnesium carbide, and beryllium carbide), nitride carbon, oxides (alumina, zirconia), silicon borides, glasses, and ceramic glasses. CMC reinforcements are graphite, nicalon and nextels. They are used in the form of continuous and discontinuous fibres, whiskers and particulates. They have an excellent chemical stability, good fracture toughness, and are also less brittle compared to the parent materials [53]. CMCs are used in aerospace, automobiles, turbines, jet engines and cutting tools. The disadvantages of CMCs include high cost and residual stresses during curing because of the different thermal coefficients of

matrix and reinforcement. In addition, the manufacturing of CMCs requires high temperatures, hence can only be manufactured with high-temperature reinforcements [54].

### **2.1.2 Metal matrix composite**

Metal matrix composite (MMC) is a mixture of the metal (aluminium, copper, titanium, and magnesium) reinforced with tungsten carbide, silicon carbide, and ceramic/carbon fibres [48]. Aluminium and titanium are commonly used metal matrices because of their low specific gravity and availability in different forms of alloys. Other matrices include Magnesium, Cobalt and Nickel and their alloys. Reinforcements are generally ceramics in the form of carbides, oxides, and nitrides, except metallic wires due to their high stiffness, specific strength at ambient and elevated temperatures. Since, the MMCs have high specific strength, specific modulus, toughness, surface durability and impact resistance at elevated temperature [49], they are particularly used in space industry (prototyping of space vehicle), commercial airlines [50], automotive disk brakes and drill bits [51, 52]. The major disadvantages of MMCs are the poor compatibility of the matrix with reinforcements which result in poor interfacial properties and residual stress. In addition, these materials also have a higher cost of manufacturing, high processing temperature, and complex manufacturing methods.

### **2.1.3 Polymer matrix composite (PMC)**

Polymer matrix composite (PMC) is made of polymer reinforced with fibres. The advantages of PMCs are high specific strength and stiffness, vibration

damping properties [55], lower manufacturing costs and lightweight as compared to metal and ceramic composites. PMCs are commonly used for building ships and submarines, automobile and aircraft structures, sports equipment, protecting armour and heat protecting cloths [56]. The properties of PMCs depend on the type of matrix, reinforcements and aspect ratio of fibres (length to diameter ratio) [57].

The polymer matrix can be classified as thermoset, thermoplastic and elastomers [58]. Thermoset polymer matrices are insoluble in solvents and have higher mechanical and physical properties than thermoplastics or elastomers. These are liquid at room temperature before curing and are irreversible once cured. They have low molecular weight and viscosity. These qualities promote easy penetration of the matrix into the reinforcements and create a very strong bond. Thermoset polymer composites are generally used in corrosive and moisture environments due to their noncorrosive behaviour. Other advantages include fatigue resistance, design flexibility, strong adhesion and good surface finish. The generally used thermoplastics are Acrylates, Cyanoacrylates and Epoxy.

On the other hand, thermoplastics polymers are high molecular weight matrices and have advantages, such as low cost, long shelf life, and easy handling. These matrices are recyclable on heating and weldable with other composites. However, recovery of reinforcement from the thermoplastic polymer composites is difficult. Thermoplastic polymers include Polypropylene, Low and high density polyethylene, Polyamides and unsaturated Polyesters [59].

The elastomer has high elongation and good elastic properties [60]. The generally used elastomers are Natural rubber, Polybutadiene, Neoprene and Silicon.

The properties (strength and stiffness) of the polymer composites mostly depend on the reinforcements and the contribution of matrices is negligible. The reinforcements are generally available in continuous and discontinuous forms. Different types of fibre reinforcements, such as glass, boron, aramid, and carbon, are available. They are very small in diameters ranging from  $3\mu\text{ m}$  to  $25\mu\text{ m}$ . Due to very small sizes, these fibres are used in bundles as unidirectional, bidirectional, random or woven mats.

Glass fibre composites (GFC) are an important type of PMCs and have generally been used in a number of commercial and engineering industries expected to replace the conventional materials [61]. The GFC has superior mechanical properties compared to the individual constituents. Though the glass fibre composites are used in numerous engineering applications, a number of factors limit their application as structural materials. The most common issue is the emergence of the crack in certain areas of composites where low strength single constituent of composite dominates and leads to total failure [58]. These areas persist within the interlayers of reinforcing fibres and are termed as matrix rich interlaminar regions as shown in Figure 2.2.

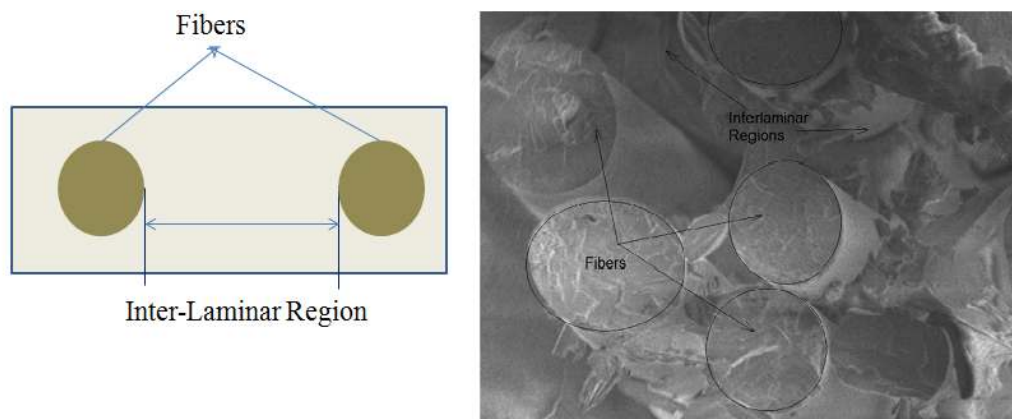


FIGURE 2.2: Inter-laminar region in composite material [8]

As the weak interlaminar region has no fibre reinforcement it leads to different kind of failures like crack development or delamination during the expected life of service [62]. Relatively weak interlaminar region limits the performance of these materials and make them precarious in commercial applications. Another important issue is the out of plane crack propagation which breaks the reinforcing fibres and results in low strength to transverse loads [64]. Lower through thickness resistance leads to the delamination of the reinforcing fibre layers.

The critical issue of PMCs can be improved by incorporating two or more different types of macro fibres into a single matrix termed as hybrid composites. The secondary fibre can overcome the weaknesses of the other which result in improved mechanical properties than the single fibre reinforced composites [65]. However, the macrofibres hybrid composites are also susceptible to failure due to the presence of inter-laminar regions between the macrofibres [66]. The weakness of the interlaminar region is attributed to the hierarchical material size gap between the matrix and macro fibres, which ranges from the molecular size to the macrosizes. Therefore, it is necessary to overcome the challenge of weak matrix-rich regions between the host material and reinforcing macrofibres.

## **2.2 Multiscale Nanohybrid Composites (MN-HCs)**

Macrosize of matrix rich region led the researchers to use nanosized fillers (nanofibres, carbon nanoparticles or both) to improve the strength of the interlaminar regions [16]. Nanofillers as secondary reinforcement can be promising to improve the properties of the interlaminar region within composites [67].

These particles benefit the composites not only by their intrinsic properties but mostly from its nanosizes (1-100 nanometer) which can significantly increase the properties of failure dominant interlaminar region [40]. Nanofillers, specifically carbon nanotubes (CNTs) develop nanoscale interface regions with matrix and resist the fracture within the interlaminar region by (i) crack bridging (ii) crack path deflection and (iii) pull out of interfaced CNTs (Figure 2.3) [68, 69]. Therefore, the MNHCs are expected to have improved mechanical properties as compared to the macrofibre composites due to improved interlaminar region [70, 71].

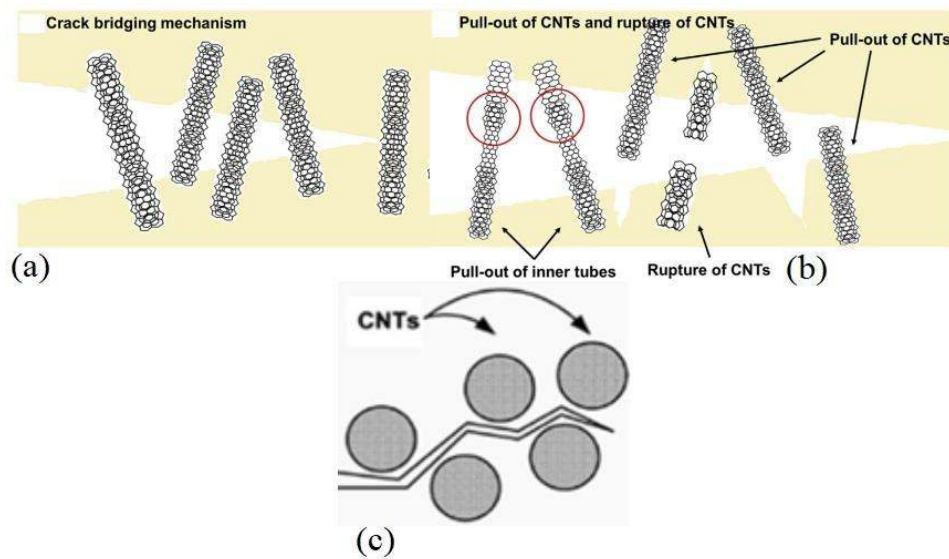


FIGURE 2.3: (a) CNT bridging (b) CNT pull outs (c) crack path deflection [68, 69]

Beside achieving better performance, the MNHCs can be tailored to the exact structural requirement at lower costs. Though the MNHCs can be produced with different kind of nanoparticles, carbon nanotubes (CNTs) processing with fibres, as secondary reinforcements are low cost and simple compared to hybrid composite of macrofibres. Such composites are coined as multiscale nanohybrid composites (MNCHs).

Several nanofillers of different types (nanoparticles and nanofibres) have been focused to improve the interlaminar properties [72]. These reinforcements include carbon nanoparticles (CNPs) and nanofibres which have dimensions in the range of nanometer. Generally, CNPs have the basic structure of graphene and has various distinct forms such as fullerenes, carbon nanofibre, carbon nanotubes and carbon nanobuds [73]. The size of nanoparticles varies between 1 to 100 nanometer. Graphene (Figure 2.4) is a two-dimensional material composed of carbon atoms arranged in periodic hexagonal shapes. The stacks of these sheets are commonly found in the form of graphite and are used in pencils. Single layer graphene sheets have remarkable mechanical, electrical, and thermal properties [74]. The reported strength of graphene sheet ranges from 0.7-7 Tpa [75, 76].

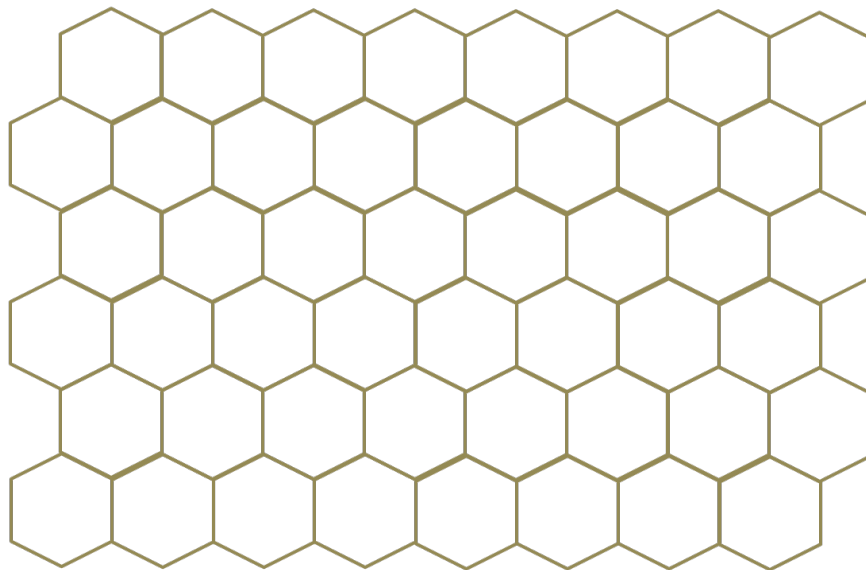


FIGURE 2.4: Graphene sheet (single layer)

Carbon nanofibres (CNF) are single or double graphene sheets rolled up helically about the fibre axis as shown in Figure 2.5. These fibres have been produced in the nanosize range of 100-500 nm with length up to 100  $\mu$  m [77]. CNFs are low-cost material as compare to the other CNPs like graphene and

carbon nanotubes. Generally, CNFs are manufactured using pyrolysis of hydrocarbons such as methane gas or acetylene. Electrospun nanofibres are used to produce the carbon nanofibres by the processes of stabilisation, carbonization and graphitization [78]. These processes are low cost and can yield mass production of CNF [79]. The mechanical properties of CNF depend on their diameters and its tensile strength vary from 1.77 to 2.2 GPa [14]. Hammel and his co-workers [80] have reported improved effect of CNTs on the mechanical properties of composites.

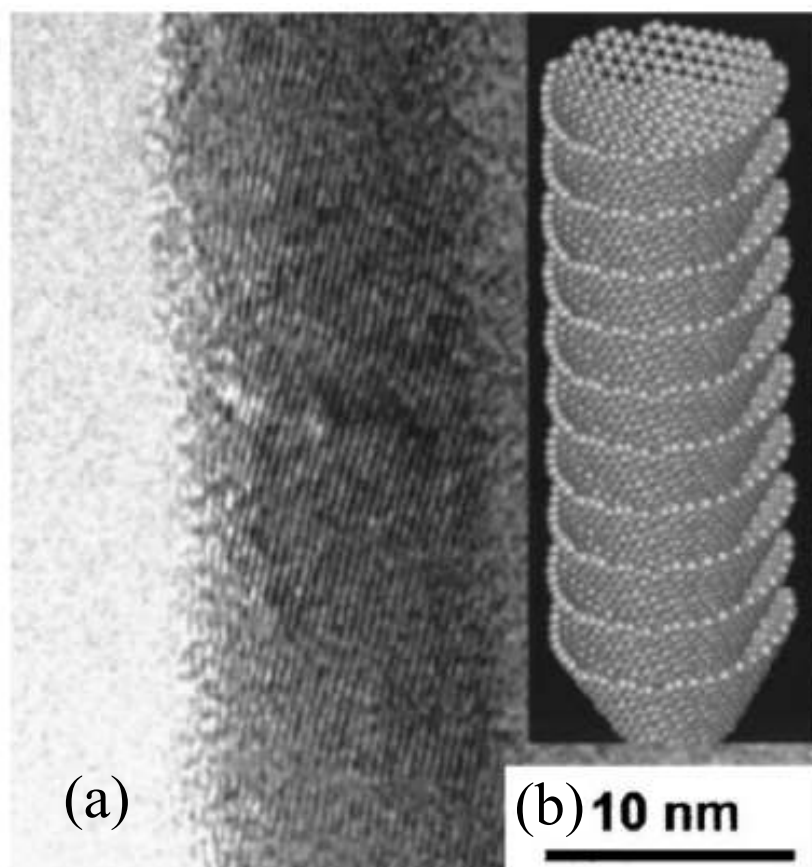


FIGURE 2.5: (a) TEM image of the cup stacked vapour grown CNF (b) Schematic representation of CNF [82]

Carbon nanotubes (CNTs), a seamless cylindrical form of graphene were first noticed by Iijima [81]. These tubes are found with open ends and sometimes

capped with half fullerene molecules. CNTs have diameters in few nanometers with different lengths. Generally, these tubes have significantly large aspect ratios ( $l/d$ ). These tubes are categorised in two different ways; (i) according to the roll-up angle of the graphene sheets which are described as Armchair, Zigzag and Chiral as illustrated in Figure 2.6 (ii) and according to the number of walls; single, double and multi-walled carbon nanotubes. A single-walled CNTs is a rolled up cylinder of single graphene sheet; a double-walled CNT is made of two concentric graphene sheets and a multi-walled CNTs contains more than two concentrically rolled up graphene sheets (Figure 2.7).

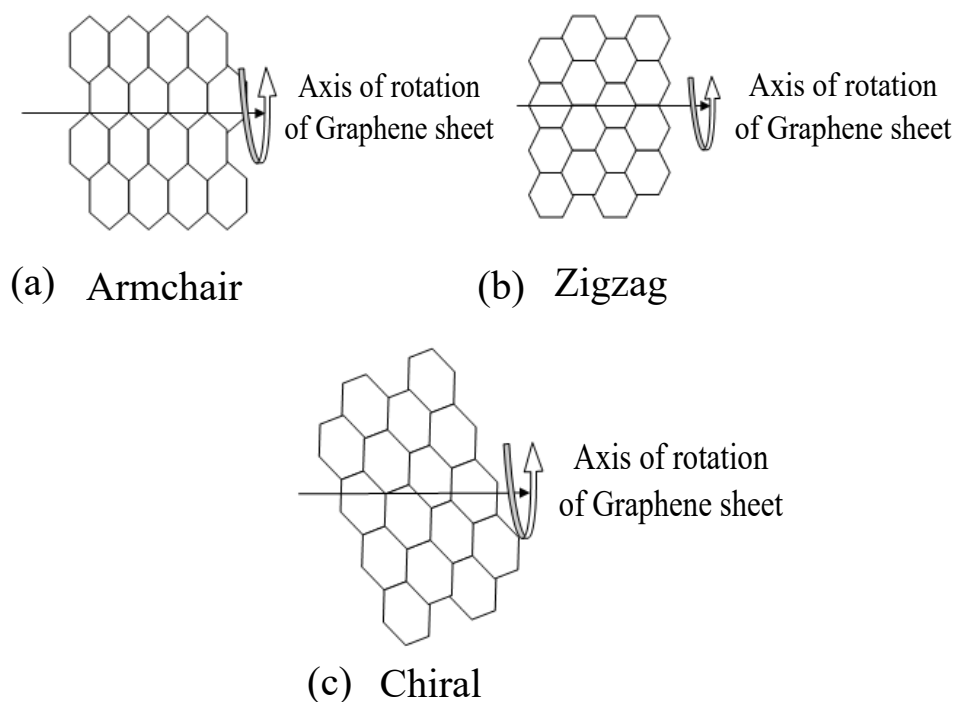


FIGURE 2.6: Carbon nanotubes arrangements a) Armchair b) Zigzag c) Chiral

CNTs exhibit excellent mechanical properties. These better physical and mechanical properties make CNTs highly desirable candidates as reinforcements for MNHCs. Though several studies have been conducted on using carbon

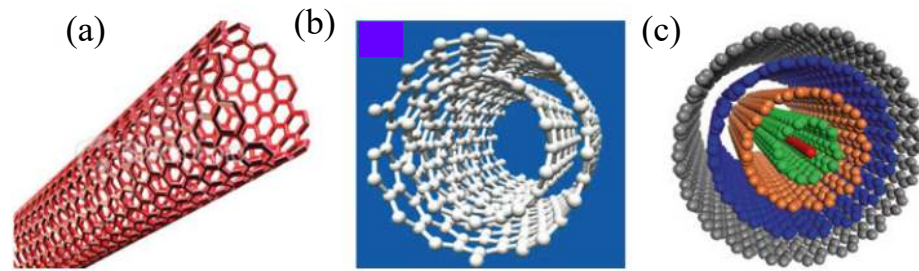


FIGURE 2.7: Carbon nanotube types a) SCNT b) Double wall CNT c) Multi wall CNT[83]

nanoparticles as a strengthening reinforcement for polymer matrix [84], but still many practical challenges concerning their fabrication need to be addressed before the realisation of their full potential.

The challenges are [8, 18, 45, 85, 86]

- Uniform dispersion of carbon nanoparticles into the polymer matrix
- Insufficient interfacial adhesion between the matrix and the carbon nanoparticles
- Misalignment of CNPs within the polymer matrix
- Control and fabrication of aligned CNPs-doped nanofibres

## 2.3 Dispersion Processes of CNTs

High mechanical properties of CNTs make them desirable nanofillers to achieve high-performance materials. However, nanotubes have the inherent nature of attraction to each other due to van der Waals forces and hydrophobic behaviour which results in the aggregation of these nanotubes and leads to the poor

dispersion of the carbon nanotubes [87]. The agglomerated state of the CNTs greatly reduces their highly expected performance in the engineering and other research fields [88]. The agglomerated CNTs cause voids and act as focal points for the stress concentrations which result in under performances [86].

Fraczek et al. [89] practically examined the distribution effect of MWCNTs in the PAN-composites. They found that the PAN nanocomposite prepared with ill distributed MWCNTs lead to the agglomeration of the nanotubes and caused the significant reduction in the mechanical properties (54% decrease in Young's modulus) compared to the neat PAN composite. While the second sample with a better distribution of MWCNTs showed higher mechanical properties. Yancheng Zhang et al. [43] used molecular dynamics model to study how the agglomeration of graphene particles affect the strength of the nanohybrid composites. They found that the single graphene sheet gave more strength to the composite than the two agglomerated sheets. Further, they studied that two separated graphene sheets showed higher strength to the previous cases. FEA model of CNTs agglomeration in the polymers was carried out by Aggeliki et al. [90] for better understanding their effect. They observed that agglomeration of CNTs negatively effects the strength of polymers and this effect increases with the increase in the number of CNTs. It was also noted that the negative effect increased with the increase in the number of CNTs in the agglomeration. Hence, the intrinsic agglomeration of the CNTs is a major obstacle in its utilisation as secondary reinforcement.

Therefore, the degree of distribution of CNTs in the host materials is an important parameter which can strongly affect the properties of the final composite material [91]. Uniformly distributed CNPs offer more area to interact with the matrix, which can increase mechanical properties of MNHCs composites by enhancing the interface region strength [92]. Different techniques have

been used to disperse the CNPs. The main methods are (a) Physical and (b) Chemical process [12, 72, 93].

### 2.3.1 Physical methods

#### Calendering

Calendering technique uses three consecutive rollers to homogenise and mix the viscous materials (Figure 2.8a). The gap between the consecutive rollers decreases. First and third roller rotate opposite to the second roller. The viscous material is poured into feeding cup and passed to the roller combination. The rollers exert a shear force which disperses and homogenises the material to a certain level depending upon the size of gaps. Researchers [18] have used calendering process to disperse the CNTs in polymer matrices. However, the minimum gap so far achieved between the rollers is  $1\text{-}5\ \mu\text{m}$ , which is not sufficient to disentangle the agglomeration of size less than  $1\ \mu\text{m}$ . In addition, only viscous materials can be fed into rollers, which makes this process unsuitable for thermoplastic materials such as polypropylene and polystyrene, etc.

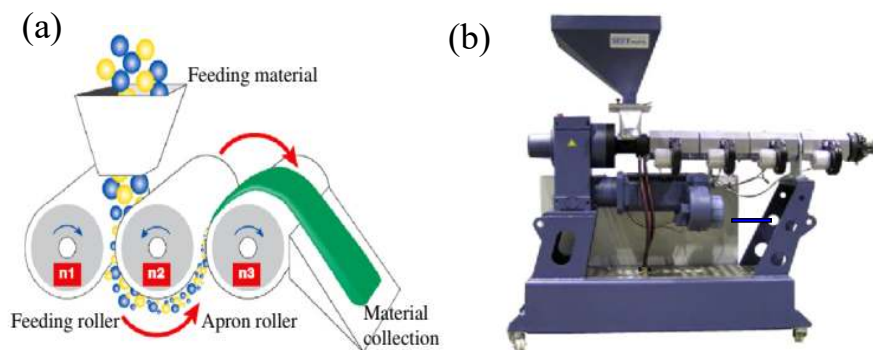


FIGURE 2.8: (a) Schematic of calendering machine (b) Extrusion mixer [23]

## Extrusion

Extrusion process uses a double screw extruder to mix CNPs with thermoplastic polymer (Figure 2.8b). The mixture is fed into a hopper and high speed rotating screws disperse the CNPs within the polymer. This technique partially disperses the CNPs within polymer matrix [94].

## Stirring

Mechanical stirring is a common and simple technique to disperse the CNPs within the polymer matrix (Figure 2.9a: magnetic stirrer). In this technique, mechanical or magnetic force rotates a propeller in a solution to disperse the CNPs. The degree of dispersion depends on the speed and size of the propeller. However, the mechanical stirring dispersion is less stable and tends to re-agglomerate due to frictional contacts and elastic interlocking mechanisms [95].

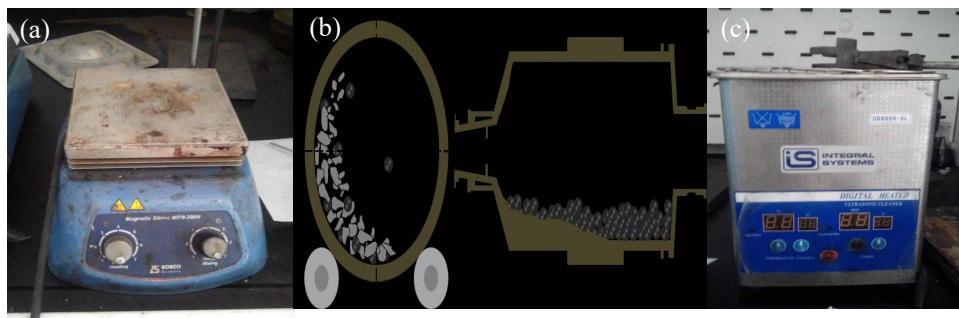


FIGURE 2.9: (a) Magnetic stirring machine (b) Schematic of ball milling [96]  
(c) Sonicator

## Milling

Ball milling is a grinding technique (Figure 2.9b), which is also used to disperse the CNPs within the matrix [97]. This process uses small rigid balls in a closed

container. On rotation of container, these tiny balls generate high pressure due to collision with each other which disperses the CNPs into the solvent. However, the ball mill process damages the structure of CNPs [23].

### **Sonication**

Sonication is the most common method, which uses sound energy to disperse the CNPs in host material (Figure 2.9 c). A source of high-frequency sound wave agitates the CNPs in the solution, which separates these particles from its bundles and disperses into the solvent. However, sonication time increases with high concentrations of CNPs, which shortens the length of CNPs and reduces the mechanical properties of composites [98].

### **2.3.2 Chemical dispersion methods**

Chemical dispersion methods involve chemical modification to the surface of the CNTs and addition of polymer chains to the CNTs called surfactants [99, 100]. The object of these methods is to restrict the mobility of CNTs and intra-CNT forces to prevent the agglomeration of the CNTs due to their hydrophobic nature.

Generally, chemical modification is done using acid treatments to graft the different functional groups through the covalent bond to the carbon atoms of the CNTs [101]. These functional groups potentially interact with the host materials and improve the dispersion of CNTs by restricting their movements and overcoming the van der Waals forces [102]. Acid treatment also helps to remove the carbon residues and catalytic materials used during the chemical process. Typically used acids are nitric, sulfuric and combination of halogen

groups with these acids. However chemical modification damage the surface of the CNTs due to covalent grafting of functional groups and most of these methods use long time sonication process which reduces the length of the CNTs. Because of the reduced length, aspect ratio reduces and result in degraded mechanical properties [103].

Noncovalent adherence of surfactants to the surface of the CNTs is a common and easiest dispersion method. This method increases the wettability of the CNTs and reduces the interaction between these particles [104]. Surfactants are mainly divided into four types a) cationic, b) amphoteric, c) non ionic, d) anionic [105]. These methods place the surfactant molecules between the CNTs which reduce the van der Waals forces between these tubes and improve their dispersion. However, the surfactant used for dispersion of CNTs are difficult to remove from the solution which limits the concentrations of CNTs into the polymers and significantly reduce their benefits [105].

## 2.4 Interface/interlaminar Region in the Composites

In the polymer fibre composites, both constituents; matrix and reinforcing fibres retain their chemical and physical properties. However, their combination produces a material with better mechanical properties due to the ineluctable interface regions between the two constituents [106]. The interface region is generated when the fibre is warped around by the matrix. The space between the two interface regions where the only matrix persists is defined as interlaminar regions. Figure 2.10 explains schematically the phenomena of interface and interlaminar regions. The properties of the interface region differ from its

constituents and define the properties of the composite materials. The interface region properties depend on the kind of interaction such as mechanical, physical and chemical [107].

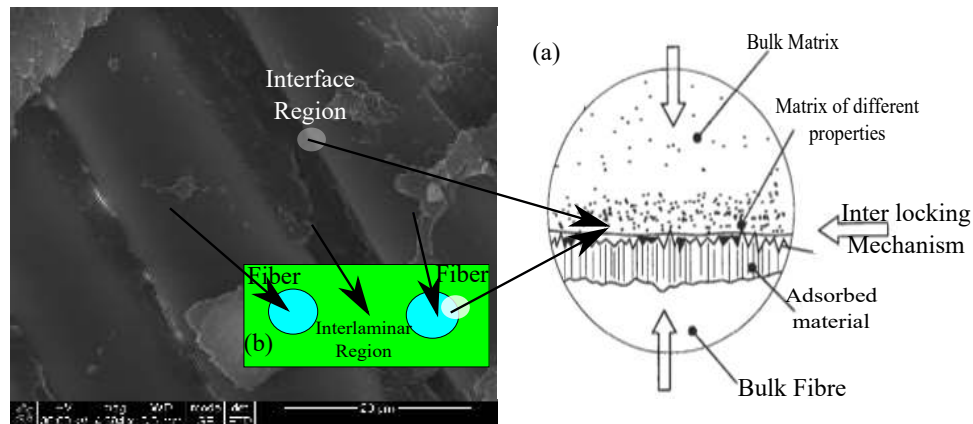


FIGURE 2.10: Fibre-Matrix (a) Interface region (b) interlaminar region [106]

Mechanical interaction occurs through the roughness of contacted surfaces which provides resistance against applied forces, but provides little resistance in transverse directions. Mostly, mechanical interface with the matrix is improved by introducing the corrugations and pits using surface treatments. Residual stresses during the curing and shrinkage process of fibre composites also improve the anchoring of the fibres into the matrix. The presence of temperature gradients during the moulding or manufacturing processes of composites also serve as clamping force between the reinforcement and matrix. De-fibrillation of the reinforcing fibres using beating process can also improve the interlocking strength at interface region due to increased contact surface area [108].

Physical interface mainly takes place through the electrostatic, van der Waals forces and by creating surface polarity at molecular levels [107]. van der Waals forces are generally attractive and arise due to interactions between different poles (induced or instantaneous dipoles) at the contacted surface. These poles are even generated between neutral atoms. Electrostatically charged particles

also serve as a binder between two mating surfaces. These charged particles are either defects or adsorbed particles and may have attractive or repulsive nature. Surface polarity can also be introduced through the addition of charged groups like the hydroxyl and carboxyl groups. Different approaches have been used to increase the physical bonding such as electron radiation heat treatment, ultraviolet and corona [109, 110].

Chemical bonding is considered as the most efficient and oldest method to improve interfacial properties. Generally, in this method, the surface of the reinforcing fibres are changed chemically to form a new compound. This reaction may change the surface roughness or may attach a functional group to the reinforcing fibre which can create better interlock with the matrix at interface regions. Chemical bonding includes a large number of methods like acetylene, silane coupling, surface oxidations, alkali, acryl, isocyanate, Methacrylate titanate, Methacrylate zirconate, benzyl, and chloropropyl treatments [111, 112].

Though all these natural or manufactured interlocking bond methods have specifically improved the properties of a interface region where the matrix polymer chain are tightly bound to the reinforcing fibres [113]. However, the mobility of the polymer chain at interlaminar regions (Figure 2.10) which are matrix rich, is substantially high as compared to the interface regions. In loading condition, stress concentrates on the matrix rich region provides an easy initiation to the cracks [114]. Yancheng Zhang et al. [43] have observed that the rupture starts in the polymer matrix rich region because its peak stress and strain values are less than the fibre/polymer interface region. A crack can be observed in the matrix rich region, initiated adjacent to the interface region of AL-composite as shown in SEM image Figure 2.11.

The increased demand for high-performance composites in the research and industrial areas have made the strength of the interlaminar region as the main

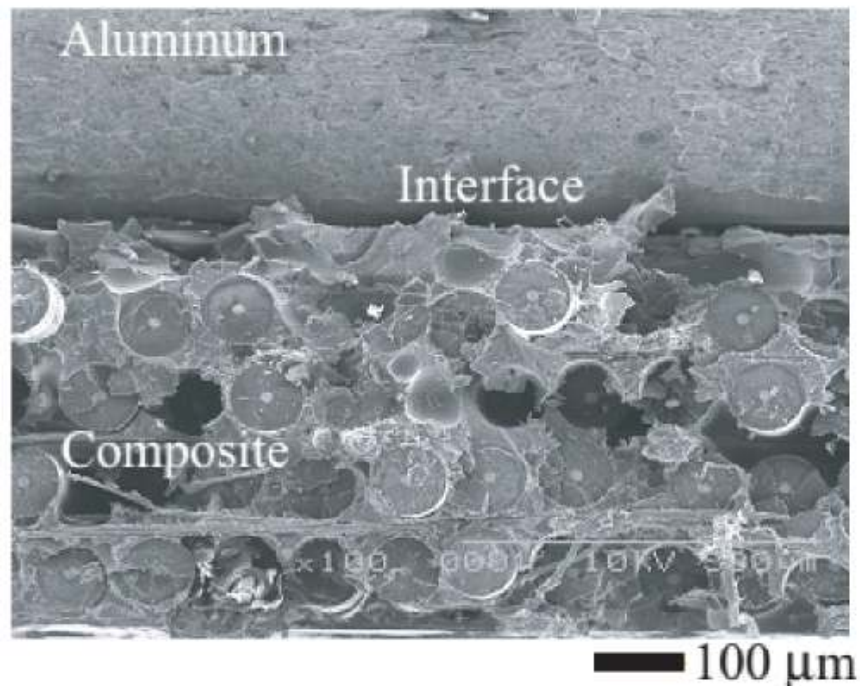


FIGURE 2.11: Crack development at interface region in the composite (SEM image) [115]

issue of interest. A possible solution to improve the interlaminar properties is the incorporation of nanofillers as secondary reinforcement [16, 116]. These nanofillers can resist the premature initiation of the crack in the interlaminar region due to their high aspect ratio, intrinsic properties and gap reduction in length scale between conventional fibre and matrix [10].

As discussed earlier, the carbon nanotube is the strongest nanoparticle and considered a most suitable candidate as nanofiller [117]. These nanotubes have two distinct properties; high aspect ratios ( $l/d$ ) and nano sizes. High surface area of CNTs results in a large interface region with the host material within the interlaminar region. Therefore, the higher aspect ratio of CNTs can transfer the load gradually and efficiently from the matrix to the stiffer macrofibres [113]. Nanosizes of this material can reduce the length scale mismatch between

the polymer chains and macrofibres, which will result in low imperfections in the interlaminar regions. These nanofillers are required in a very low mass, hence do not have a noticeable effect on the geometry and weight of the final composite along with the cost.

Although enormous efforts have been made to improve the interlaminar region properties using the CNTs as nanofiller in various polymer composites, however, mechanical properties corresponding to the high properties of the CNTs have still not been achieved [118]. One of the major issues is the poor interface mechanism between the CNTs and matrix which substantially reduces the reinforcing effect of CNTs [20]. The strength of the interface adhesion between the reinforcement and matrix determines the ability of load transfer from the matrix to CNTs. Therefore, better interfacial adhesion leads to better mechanical properties [72]. The interface mechanism of CNTs and its improving techniques are presented next.

### **2.4.1 Interface mechanism of CNTs with host materials**

Naturally, pristine CNTs are chemically inactive and form only physical contact through van der Waals forces with the matrix, which has a low mechanical strength and less efficient in load transfer [23]. Therefore, to develop composite material with high mechanical and physical properties, CNTs are required to have a strong connection with the matrix materials. Different methods have been utilized to improve the bonding of CNTs in the interlaminar region of the matrix to increase its resistance in loading conditions. These methods can be divided mainly into two types (i) physical bonding (ii) chemical bonding [24, 119].

Chemical bonding method uses two different approaches to increase the reactivity of CNTs with the matrix material. In the first method, it links different functional groups to the carbon atoms of the CNTs using a covalent bond. These groups can be attached to the surface or ends of the carbon nanotubes. CNTs can have defects like vacancy, stone wall, structure irregularities (pentagon or heptagon). These defects can be naturally or artificially generated through a chemical process. In the second method, these defect sites are attached to the hydroxyl (OH) or carboxylic groups (COOH). CNTs functionalized using covalent bonds can create a strong interlink with the polymer matrices. As a result, the interlaminar regions strengthened with chemically functionalized CNTs can have resistance to the applied loads. These methods include oxidization, functionalization through amine [120] chlorination, fluorination [121], hydrogenation [122] and carboxyl groups (-COOH) [123]. These processes reduce the inertness of CNTs and increase their reactivity with the matrix materials. Figure 2.12 shows carbon nanotube functionalization with different groups.

Covalent bond produced during chemical functionalization can provide improved interlaminar region and effective load transfer. However, this functionalization chemical reaction and its combination with sonication process cause damage to the structure of CNPs. These damages can not prevent and in some cases severely damage the large aspect ratio and turn CNTs into small lengths. The defects and low aspect ratio due to the chemical processes deteriorate the reinforcing properties of the CNTs.

In the physical bonding methods, the CNTs are warped around by the polymer chains or surfactants to functionalize [100, 125]. The researchers are concentrating on the physical functionalization methods due to their advantage over the chemical functionalization, as the CNT structure is either not damaged or

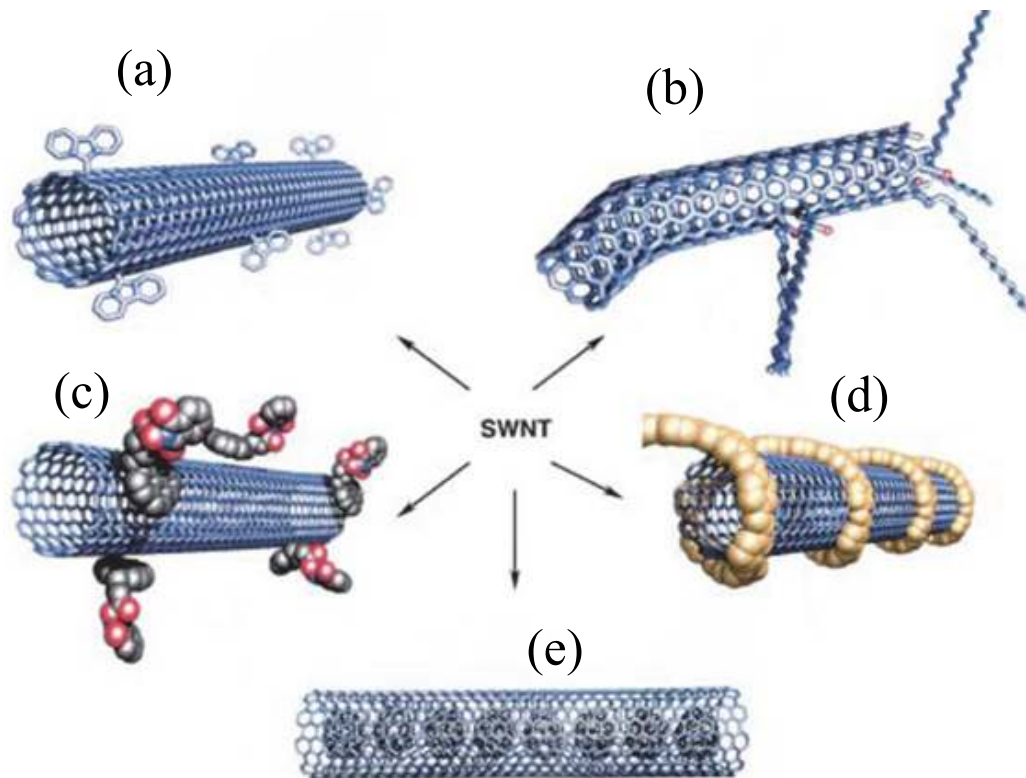


FIGURE 2.12: (a) Defective chemical functionalization, (b) Sidewall functionalization, (c,d,e) Physical functionalization (nanocovalent) [124]

is less damaged. Another method endohedral is also used in which a group of molecules is stored inside the CNTs[126]. Generally, physical bonding is noncovalent which is less stronger than covalent bonding. Despite large efforts in the area of the functionalization process, the structural damages still exist. The functionalization process is not mature due to the use of a large number of different materials and methods associated with different uncontrolled variables.

---

## 2.5 Alignment of Carbon Nanotubes (CNTs)

The geometrical orientation of CNTs within the composite material determines the mechanical properties of multiscale nanohybrid composites [127, 128]. CNTs possess high mechanical properties only in the direction of the length, therefore their intrinsic high strength can be utilized if they are incorporated in the preferred direction into the composites. The aligned CNPs can enhance the mechanical properties of composites in their direction and provide better control of mechanical properties as compared to random dispersion [122]. Zhou et al. [21] reported that the nanocomposite with aligned CNTs can have superior mechanical properties than the nanocomposites with randomly dispersed CNPs in a particular direction. Preeti Joshi et al. [129] analysed the orientation effect of the CNTs in nanocomposites. Among the four models, they observed highest Young's modulus for the nanocomposite with aligned CNTs. Figure 2.13 shows the strengths of different nanocomposites with respect to the CNT's orientations.

Simple mixing of CNTs with the polymer matrix or sprinkling can generate composites with random orientated CNTs. As the CNTs cannot be manufactured in larger lengths like the conventional fibre, this has made it difficult to align these particles using direct mechanical methods. Even higher concentrations of CNTs, which may seem desirable to achieve high strengths, reduce the degree of alignment of CNTs because of agglomeration and difficulty in motion [130]. All these difficulties have made the incorporation of CNTs with preferred orientation a challenging task.

The smaller diameter of CNTs has high existential flow which can help to align these nanoparticles. This means that if the CNTs are placed in a flowable liquid material having a high molecular chain system, then the alignment of host

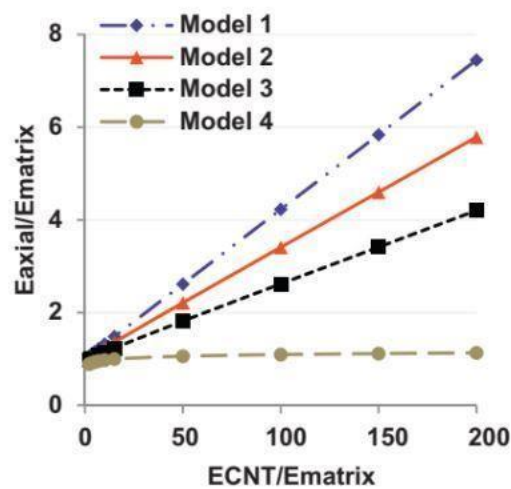
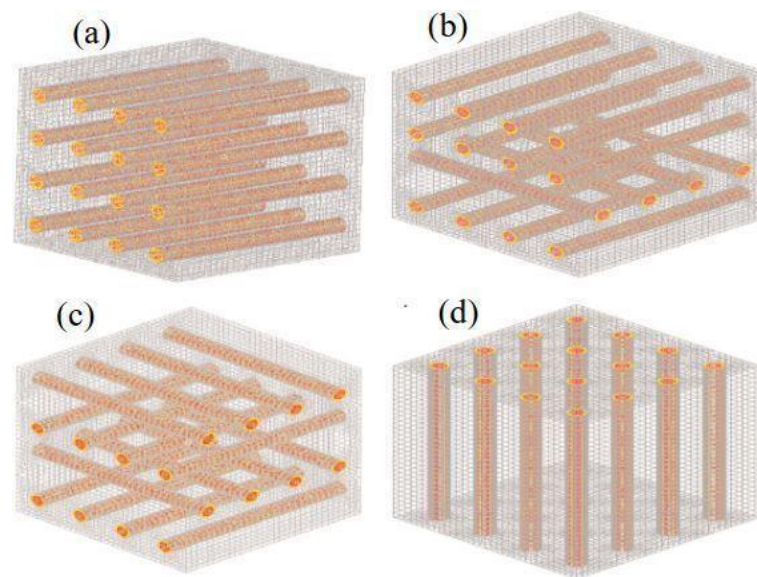


FIGURE 2.13: (a) Model 1, (b) Model 2, (c) Model 3, and (d) Model 4 [129]

material can provide a preferred direction of CNTs. However, to restrict the orientation and reagglomeration of these materials, the host material should have a size in the range of few nanometers with quick solidification property.

For this purpose, a number of techniques have been used to embed the CNPs

using polymeric macro and nanofibre into the composite. Conventional techniques include; melt spinning [131], solution blending, and in-situ polymerization [15]. Shear force using injection method can also help in the alignment of the CNTs within the composite structures [132]. These techniques are only capable of random dispersion of CNPs with low concentrations and can not align the CNPs in the matrix due to fibre diameter ( $2 \mu m$ ), which is much higher than the CNTs.

Other techniques have been developed to align the CNPs such as dry spinning, spinning process ( melt spinning, solution spinning, emulsion spinning), slicing, spray winding [133], and electrical or magnetic field [29] and growth of CNPs on fibre surface using catalytic thermal chemical vapour deposition technique [20]. However, these techniques have limitations shown in Table 2.1 [15, 30].

TABLE 2.1: Alignment methods of CNTs and their disadvantages

S.NO	Method	Limitations	Disadvantage
1	Dry spinning	Shortness of fibre array	Low mechanical Properties
2	Slicing method	Short array of CNPs	Same
3	Electrical and Magnetic field	Alignment varies with field strength	
4	Catalytic thermal chemical vapour deposition technique	Metal catalysts creates defects on fibre surfaces	

Owing to the limitation of these methods especially the alignment of CNTs over the small area only, their counterpart electro-spinning has attracted remarkable attention and offers several advantages. Electrospinning is the simplest method to create the fibres in nano sizes of a long polymer chain, which have the potential to align the CNTs over large area [134, 135]. It can also improve the dispersion of the CNTs which can increase interface region lengths within the composites. Moreover, the nanomates sizes are desirable with negligible weights and can be manufactured using different materials according to the requirement of the application. These nanomates can also reduce the mismatch

between CNTs/polymer chains and macrofibre, which will prevent the development of a sudden crack in the interlaminar regions. Ben et al. [136] observed that electrospun nanofibres doped with MWCNTs increased the strength of poly-phenylene isophthalamide. However, they also experienced a decrease in strength for high concentration (1% wt) of MWCNTs due to agglomeration and misalignment. Leonard's team [137] also experienced an increase in tensile strength and Young's modulus of electrospun polymer nano mat doped with MWCNTs, but they also pointed out the possibility of agglomeration and non-uniform dispersion of CNPs with increased concentration, which lowers the mechanical properties.

Zhiqiang Su's group [35] conducted a detailed study to determine the effect of the electrospinning process on alignment and dispersion of carbon nanotubes (CNTs). They inferred that the nanofibres doped with CNPs can be aligned with electrospinning techniques, which will improve the mechanical properties. However, they suggested further research to find how the diameter variation in nanofibres can be controlled and the effects of input parameters involved in the electrospinning process on the alignment of CNPs. Reneker et al. [138] observed that the optimization of the properties (elongation, diameter, and path) of the jet formed during electrospinning process and the concentration of the solution is required to achieve better alignment of CNTs.

### **2.5.1 Electrospinning technique**

Electrospinning of polymer solution is a simple technique to produce the fibres of different diameters ranging from micron size to the nano sizes. Generally, electrospinning technique comprises of a high voltage source, a polymer solution along with continuous feeding source, a conducting spinneret (needle) and a fibre collector plate or drum. Figure 2.14 shows the sketch of a fundamental

electrospinning technique. The terminals of high voltage source are connected to the spinneret and the collector.

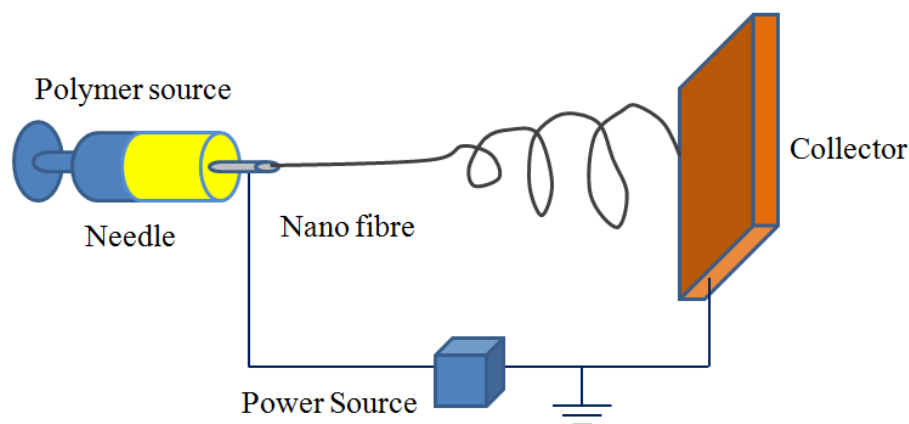


FIGURE 2.14: Simple schematic of electrospinning technique

A polymer solution is then fed to the spinneret through the feed pump. As the drop of the polymer solution appears at the tip of the spinneret, it gets charged and forms a cone shape pointed towards the collector plate due to electrostatic charge. When the electrostatic charge overcomes the surface tension of the polymer solution, it issues the jet. The solvent used to make the polymer solution starts evaporating as it travels towards the collector plate. As a result, continuous thinning polymeric fibre is formed. During the flight, polymer solution experiences different forces like electrostatic, rheological, aerodynamic, internal and gravitational [139]. Under these forces, the polymer jet starts whipping along complex spiral paths and random fibres are obtained as shown in Figure 2.15.

Historically the production of nanofibres using electrospinning apparatus was reported in 1934 by Formhals [140]. He used an electrical charge to develop artificial fibres. Later in the 1960s, Taylor studied the formation of the fibres using electrospinning. He found that polymer droplet changed to a cone shape,

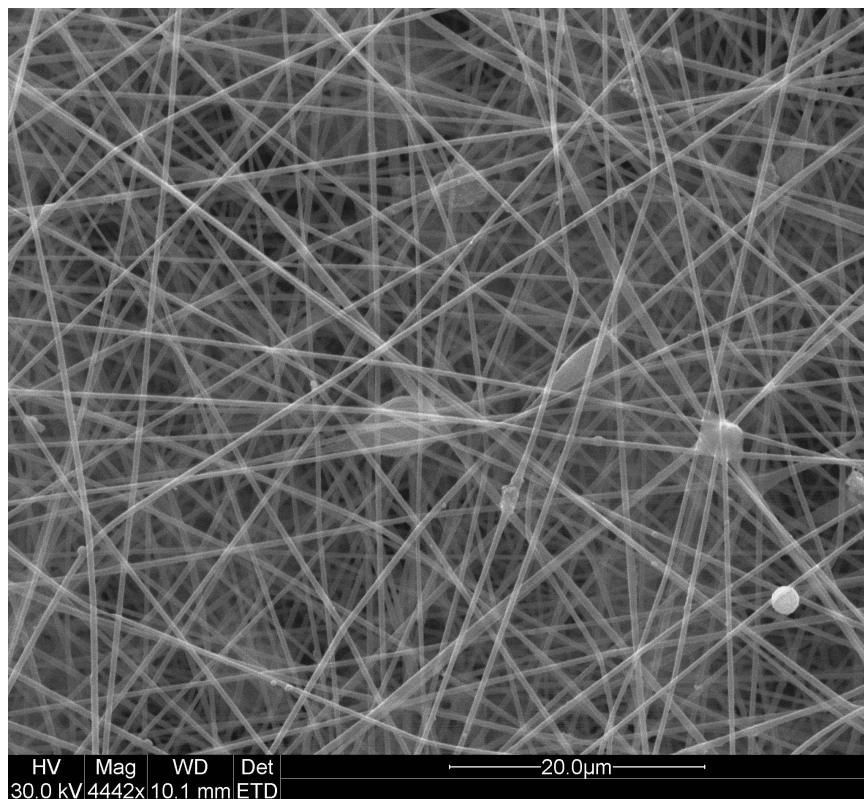


FIGURE 2.15: Electrospun PAN nanofibres

which was later converted into the jet under the electrostatic charge [141]. In the current literature, this cone shape is coined as 'Taylor cone'. This technique gained popularity in the research field after the publication by Doshi et al. [142].

In the last decades, the researchers have extensively explored the benefits of electrospun nanofibres in different fields like nanohybrid composites, tissue engineering, separation and filter membranes and nanoelectronic devices [35, 143–149]. Though the electrospinning process setup is easy to build, however, to generate a nanofibre with the desired diameter, orientation, and, controlled deposition is still a challenge being investigated. There is a number of parameters involved in the electrospinning which is interconnected to each

other [150]. The simultaneous optimisation of these parameters are very difficult and compel researchers to compromise on some of the aspects of the nanofibres like diameter, alignment, strength, and deposition etc. Electrospinning process has the following main parameters, which affect the strength, shape, diameter, and, quality of the produced fibres :

- Polymer material: Nanofibre properties depend on the type of material and its molecular weight used in the electrospinning process. Molecular weight directly affects the morphology and diameter of the electrospun nanofibres. Smaller diameter can be produced using lower molecular weights, however, at very low molecular weights, beaded fibres are produced [151]
- Concentration of polymer solution: Thickness of nanofibres is directly proportional to the density of the solution. The diameter of Electrospun fibres increases with the increase in polymer concentration due to increased polymer in the jet and less solvent to evaporate. However, a very high concentration of fibres reduce the polymer crystal structures which results in low mechanical properties [152]. Reduced polymer concentration can result in a smaller diameter which is considered good in mechanical strength. However, highly reduced polymer concentration produces fibres with beading or splashes [153].
- Spinneret-to-collector distance: Nanofibres thickness, density, homogeneity, and, distribution depends on the distance between spinneret-to-collector because they serve as the terminals of the battery (spinneret as anode and collector as a cathode). Usually, the distances vary between 8 cm to 30 cm. Some researchers [154] claim that distance variation affects the diameter while the others [155] suggested that diameter does not

change with distance and is rather more dependent on the concentration and another parameters like solution viscosity, applied voltage and rate of evaporation. Therefore, for each concentration of the solution, an optimum distance is required. Small distances between spinneret and collector will produce wet fibres due to low evaporation of solvent while too large distance produces splashes or beaded nanofibres [156, 157].

- **Flow rate:** Flow rate also affects the nanofibres thickness, density, homogeneity, and, distribution. Lower flow rates are more suitable to produce smaller diameter with uniform thickness. Solvents find more time to evaporate with lower flow rates along with stable Taylor cones which reduces the beads in the fibres [156]. While the higher flow rates destabilise the Taylor cone and more polymer at the spinneret tip cause increased diameter along with variation in the sizes of fibres [158].
- **Voltage:** The applied voltage between needle and collector plays a vital role in the production of nanofibres. A jet can be issued from the Taylor cone only if the value of applied voltage is more than the surface tension of the subjected polymer solution. Generally, the voltage for electrospinning is adjusted according to the flow rates with visual observation. High voltages relative to the flow rates create high-speed jets which result in wet fibres of variable size along with beads and unstable electrospinning process [159]. The effect of optimum voltage on the fibre diameter varies with the type of polymer solution and there is a difference of opinion regarding voltage effect [155, 156].
- **External factors:** Surrounding environment of electrospinning process affects the properties and structure of the fibres. The humidity of the environment is the most important factor which affects the morphology of the fibres [160]. Higher humidity negatively effects the electrospinning

process as the fibres start absorbing the water content which results in beaded fibres. Similarly, very low humidity breaks the nanofibres [161]. Temperature is another external parameter which can affect the fibres structure as the viscosity of polymers changes with temperature. However, these changes are considered small and ignored most of the time [162].

Briefly, to produce the uniform fibres with fine molecular chains requires the optimum values of the above-mentioned parameters.

### **Jet path description and alignment**

The electrospun polymer jet can be divided into two parts: near field and far field as shown in Figure 2.16. In the near field, the jet takes a straight path away from the spinneret and then starts whipping in a complex path due to electrical, gravitational and rheological forces [14, 15]. The far-field fibres attain the nano sizes which can align the CNTs along their length directions [27]. However, in the far field fibres travel along unstable helical paths which results in random fibres with the variable diameter at the time of collection [45]. The randomness of nanofibres results in a variable molecular orientation which reduces the mechanical properties [163].

This pragmatic issue was addressed by using different types of collectors such as static thin parallel collectors [164], and thin rotating collectors [165] (Figure 2.17a and b). But these methods are limited to producing a thin strip of aligned nano mat due to geometrical constraints and are unable to cover larger widths with aligned nanofibres [166]. In addition, aligned nanofibres produced through above-mentioned methods, can not be transferred without damage to the substrate of application. Nanofibre mats with larger width can be

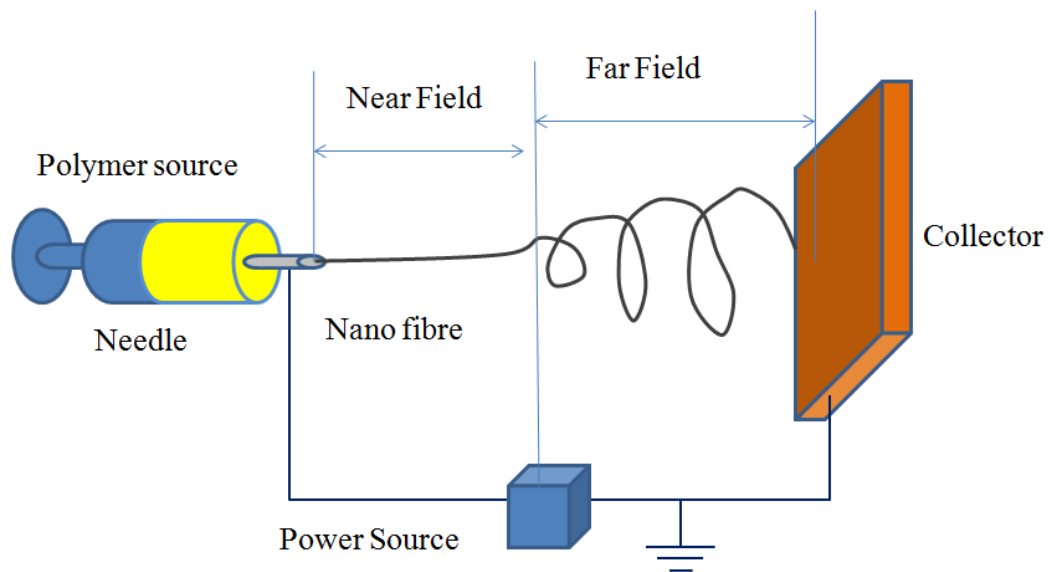


FIGURE 2.16: Electrospinning process

produced using cylindrical drum collectors (Figure 2.17 c). However, with this method, only random fibres can be collected [167] and these path variations cause randomly oriented nanofibre mats over the collector.

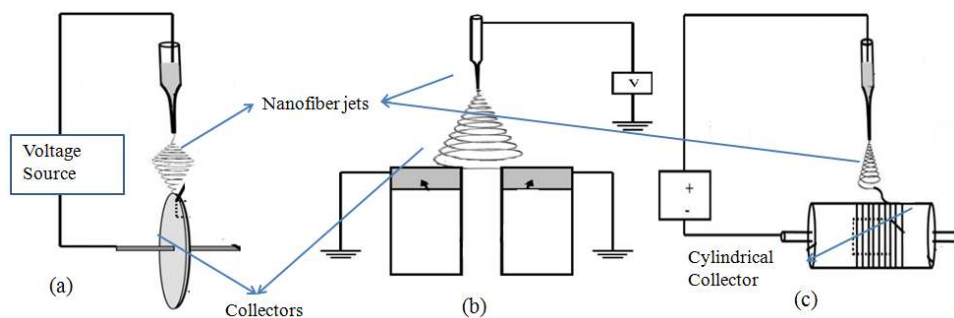


FIGURE 2.17: (a) Thin drum collector, (b) Parallel plate collector, (c) Cylindrical collector [166]

Some researchers have achieved controlled deposition of electrospun fibres in the near field using cylindrical drum but fibres were of large diameter which lowers their mechanical properties due to low aspect ratios [168]. Researchers [169] have used auxiliary electrodes with an auxiliary field to align the fibres

over the rotating collector. These methods [168–170] have reduced the target area and whipping instability but increased the complexity of the system by using auxiliary electric fields. Moreover, these systems avoid multi-spinneret systems due to clogging phenomena, hence they have limited nanofibres yield, which makes them unfit for commercial use. Multi-spinneret electrospinning systems increase the yield of nanofibres, however, each spinneret of this system acts as an auxiliary electrode for the other spinnerets and causes clogging and variable diameter due to self-repulsion between the jets [171]. Despite all efforts like general electrospinning, centrifugal spinning, electrospinning with a thin collector, parallel collectors, auxiliary field, none of the method has achieved aligned and controlled deposition of CNT-doped nanofibres mat over the large areas which can be used as strengthening mechanism within the interlaminar region.

## 2.6 Multiscale Manufacturing of Composites

A number of techniques are used to manufacture the multi-scale nanohybrid composites at the higher scale of lengths. Among the various manufacturing techniques, liquid composite moulding has gained popularity due to low equipment cost, simplicity and relatively short cycle time. Liquid composite moulding technique includes resin transfer moulding (RTM) and vacuum assisted resin transfer moulding (VARTM) [172].

RTM process uses fibre preform, which is packed into a bottom mould cavity of the desired shape. The mould is then assembled and fixed with clamps. The mixture of hardener and resin is then pumped into the mould cavity, evacuating the air through the edges till complete filling. This process has a good control of resin content, produces high quality of composites and is

suitable for mass production [173]. Vacuum assisted resin transfer moulding (VARTM) is a one-step advance closed moulding process as shown in Figure 2.18. This method uses a vacuum pump attached at the corner of upper die plate to suck the air from the cavity. The vacuum causes the resin to flow through the dry fabrics via an inlet pipe attached to the opposite corner of the die. The process continues until the resin begins to enter into the vacuum cylinder. The VARTM method requires less injection pressure as compared to RTM, which reduces the cost of equipment. Hence, it is more suitable for complex/large shapes components [174].

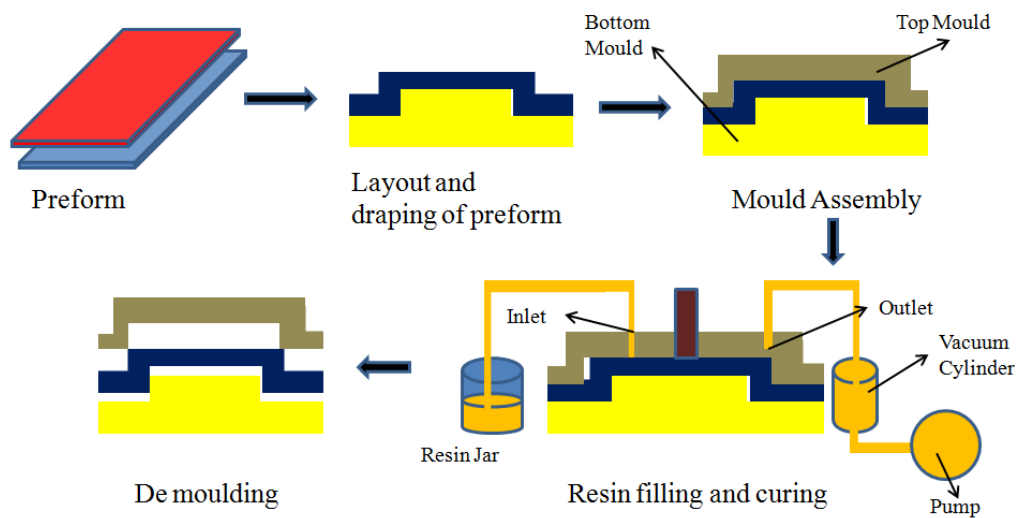


FIGURE 2.18: Vacuum assisted resin transfer method

## 2.7 Numerical Modelling of MNHCs

Experimental and theoretical approaches are used to optimise, characterize and analyse the nanohybrid composites [39]. Most of the literature show enormous experimental work going on to achieve the best results in the said field. Despite

tremendous experiments, results have shown variation in mechanical properties [32] and there is no standard method to evaluate these properties. From the viewpoint of the mechanical properties of composites, the determination of load transfer at CNPs-polymer/epoxy interface region is vital. Limitation factor such as nanoscale, cost and time associated with the experimental determination of the interface region led the researchers to develop the theoretical techniques to improve the prediction of properties. The following different approaches are reported in the literature to characterize the composite materials [175].

### 2.7.1 Analytical methods

Analytical methods use algebraic and calculus tools to solve elasticity equations for evaluating the approximate properties of composite materials. This method gives a quick solution and uses simple mathematical equations as compared to other methods [176]. Analytical methods include the following techniques [176];

- Rule of mixtures

$$E_c m = v_f E_f + (1 - v_f) E_m \quad \text{Equation of Young's moduli by Voigt [177]} \quad (2.1)$$

$$E_c = \frac{E_f E_m}{E_m v_f + E_f (1 - v_f)} \quad \text{Equation of Young's modulus by Reuss [177]} \quad (2.2)$$

- Effective field Models

$$C_{MAT} = \frac{C_m + [V_f \cdot (C_f - C_m) A_{Eshelby}]}{V_m \cdot I + V_f \cdot (A_{Eshelby})} \quad \text{Mori-Tanaka Model [178]} \quad (2.3)$$

where

$$A_{Eshelby} = \frac{1}{I + \frac{E}{C_m} (C_f - C_m)} \quad \text{Eshelby tensor [178]} \quad (2.4)$$

- Cox model

$$E_c = E_f v_f n_1 - v_m E_m \quad \text{Equation of Young's modulus by Cox [179]} \quad (2.5)$$

These models use different parameters to analyse the nanocomposites e.g. orientation, aspect ratio, volume fraction and reinforcement efficiency. But these models deal only with some specific composites with simple geometry and global mechanical properties which can be easily approximated [38]. These models cannot evaluate the complex system of composites (random heterogeneous materials) and effects of small lengths e.g. orientation, and interface region in nanocomposites.

## 2.7.2 Continuum mechanics

Continuum mechanics (CM) predicts the mechanical behaviour of materials as continuous mass. The solution of CM problems is approximated through finite elements analysis (FEA). A representative volume of composite materials is analysed and the results are interpreted for whole composites [180]. Ehsan [181] used ANSYS software to model representative volume element (RVE) of composite material with randomly dispersed CNTs having variable length

and diameter. Three solid concentric tubes of properties equivalent to CNTs, interface region, and matrix respectively, were analysed through finite element analysis with different mesh sizes. Figure 2.19 shows the proposed RVE.

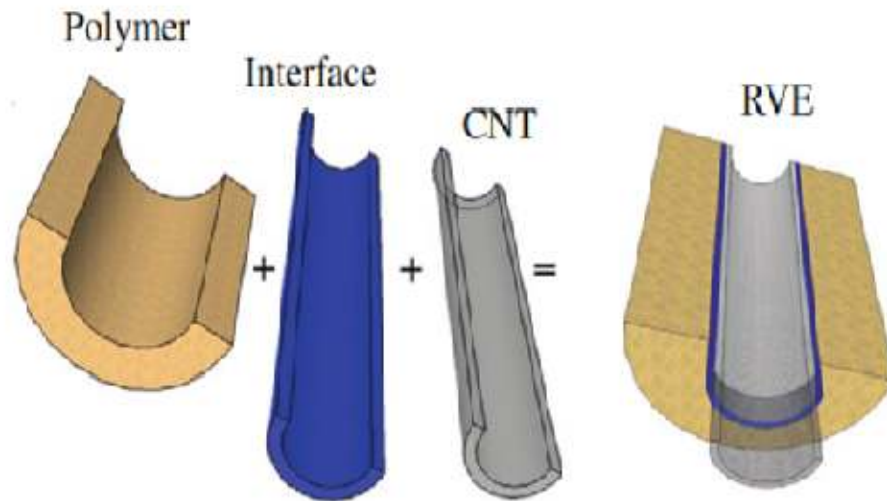


FIGURE 2.19: Representative volume element [181]

The research declared that the non-linear behaviour of the composite material is caused due to geometric effects of the model and the properties assigned to the RVE's at different sections. The strength of composites depends on the shearing strength of the interface region developed between CNTs and polymer. However, the simulations showed a higher strain rate at high stress as compared to experimental values since the FEA simulations ignore the voids. These voids are unbounded clusters made by agglomerated CNTs resulting from long range interactions [182]. These clusters decrease the mechanical properties of composites [133].

### 2.7.3 Molecular dynamic simulations (MDS)

MDS technique studies the behaviour of the composites materials at atomic/-molecular level [183]. These studies are based on mathematical expressions of Newtonian classical mechanics (laws of motion, conservation of energy, mass, linear momentum and angular momentum) and can provide more details regarding inter-atomic interactions. Inter-atomic forces are calculated by derivation of energy functions (potential fields) [184]. Mathematically;

$$F = -dU(r)/dt \quad \text{Force (where U is energy function)} \quad (2.6)$$

$$U(r) = U_{covalent} + U_{non-covalent} \quad \text{Energy function (potential Field)} \quad (2.7)$$

$$U(r) = U_{bond} + U_{angle} + U_{dedral} + U_{electrostatic} + U_{vanderWaals} \quad (2.8)$$

Potential fields are the mathematical representation of potential energies of the system of particles, which depend on the type of atoms to be simulated. Some of the potential fields are Tersoff, REBO (Reactive empirical bond order), Morse potential field and AIREBO (adaptive intermolecular reactive empirical bond order). However, MD simulations can handle simple atomic structure and a limited number of atoms in simulation, which reduces its capability to predict the behaviour of complex structure and a bigger system [46].

Researchers [183, 185] have used Molecular dynamics simulation software (LAMMPS) to characterize the triple-walled CNTs based composites. A representative box of the composite at the nanoscale within infinite replicas was examined by applying force in the single direction through MD software. Different volume fractions and dispersion configurations were used in simulation to determine the effects of interface region on macroscale elastic properties. But the research showed higher modulus values than actual values. The cause

of this error may be the use of single direction analysis, fixed arrangement and, the orientation of CNTs within the polymer.

#### **2.7.4 Equivalent continuum model (ECM)**

Majority of techniques currently employed to determine the CNT-doped polymer nanocomposite properties are indirect inferring of strength by applying above mentioned techniques. To overcome the limitation of MD, MM, and conventional CM methods, an equivalent continuum model (ECM) of atomic structure was proposed to characterize the behaviour of CNT and its nanohybrid composites at the coarser end of length scale [186]. Usually a three dimension representative volume unit (RVE) is developed which composed of matrix material and the CNTs. The matrix material is modelled as continuous material while the CNTs are represented as continuous shell or beam.

The above mentioned techniques have been used in many recent researches to evaluate mechanical properties of nanohybrid composite materials at different scales. These include, 'Multi Scale Finite Element Approach', in which author claims to use heterogeneous approach first time [187]. The research shows that the load transfer in nano composite material is characterized by volume percentage, geometry of CNTs and the interface region between constituents. But the study only considered the long fibres aligned with matrix, ignored the details of structure of matrix and bonded/non bonded elements for reducing computer cost and simplicity. The non bonded elements (CNTs/Graphene) are empty spaces which have negative impact on the strength of composite materials [54].

In another study, nanocomposites are characterized and evaluated through 'Atomistic Based Continuum (ABC) Multiscale Modelling' technique [84]. The

representative volume element (RVE) of cylindrical shape composed of CNT surrounded by matrix is examined. CNTs were modelled like a structure, in which carbon atoms acted as node and C-C bond as solid beam, and the problem was treated as traditional FEA problem. The inter-atomic potentials, Modified Morse and Lennard Jones were used to create covalent bond within CNT and CNT matrix bonds (Van der Waals) respectively. This characterization was also based on assumptions e.g. non-bonded interactions, assumed density, simple polymer chains, fixed number of CNT bonds with matrix and negligible voids. All these assumptions are considered due to Molecular Dynamics software, limitations and for simplicity.

Qian jiang et al. [133] used molecular dynamics simulation LAMMPS to characterize the triple walled CNT base polyimide composite. A representative box of composite at nanoscale within infinite replicas was examined in NVT ensemble by applying force in single direction through MD software. Different volume fraction and dispersion configurations were used in simulation. But the research showed higher modulus values of polyimide and CNTs than actual values. This error may be the cause of single direction analysis, fixed arrangement and orientation of CNTs within polymer.

Various studies have applied different methods to characterize the properties of nanohybrid composites. A mismatch of theoretical and experimental results exists in all the studies and the reasons may be the approximation and assumption in theoretical methods, and limitation of computational power etc. Hence new and accurate modelling techniques are required, which can overcome the existing gaps.

## 2.8 Conclusion

The literature review of previous studies and experimental works highlighted that the nanoparticle like CNT is a potential candidate as a secondary nanoreinforcement and can improve the matrix rich interlaminar properties. However, researchers are facing problems in the development of MNHCs using CNTs. These issues can be summarised as uniform dispersion, alignment and interfacial adhesion of CNTs within the polymer composites. The literature shows that if the CNTs are placed in the electrospun nanofibres having a high molecular chain system, then the alignment of host material can provide a preferred directions to the CNTs. However, the randomly oriented electrospun nanofibres do not align the host CNTs and reduce the mechanical properties. The randomness of the nanofibres make the general electrospinning technique unsuitable for producing CNTs doped aligned nanofibres.

The literature also shows different attempts to align the nanofibres using modified electrospinning technique which fell short due to limited area deposition and complexity of the systems. These methods include a different kind of collectors and use of auxiliary voltage sources. Recognising the shortcoming of the previous research in utilising the CNTs as a secondary nanofiller using a different kind of dispersion, functionalization and incorporation methods. This study aims to utilise the following steps to achieve the objectives set out by this study in Chapter No:1.

- Combination of different mixing processes (Magnetic Stirrer and Sonication) to disperse the SWCNTs within the polymer solution.
- Effect of Friedel-Craft functionalization of CNTs on the interlaminar region properties of MNHCs.

- Effect of nanofibres' orientations on the properties of the inter-laminar region.
- Experiments to understand the effect and optimisation of auxiliary vertical electrodes (AVEs) on the orientation of CNTs-doped nanofibres along with other parameters like polymer solution concentration, number of spinnerets, voltage, spinneret collector distance and humidity etc.
- Develop a modelling technique to characterize the pristine, defective and multi-walled CNTs along with van der Waals forces which can reduce the gap between experimental and numerical values.
- A realistic model of the interlaminar region within the MNHCs having pristine and functionalized SWCNTs.
- Evaluation of experimental and modelling analysis.

# Chapter 3

## Methodology

A detailed methodology including the experimental design, manufacturing method, and experimental analysis for improving the interlaminar properties of multiscale nanohybrid composites was presented in this chapter. The secondary reinforcements were used in the form of CNTs-doped PAN nanofibre mats. The experimental methodology is shown as a schematic in Figure 3.1. Different volume fractions (16%, 24%, 32% and 40%) of glass fibre and epoxy polymer matrix were selected for fabricating the glass fibre composites and were tested to obtain their properties. After optimization of the fibre glass composites, two types of secondary reinforcements were produced for improving the interlaminar regions;

- Randomly oriented PAN polymer nanofibres mats
- SWCNTs doped Aligned PAN polymer nanofibres mats

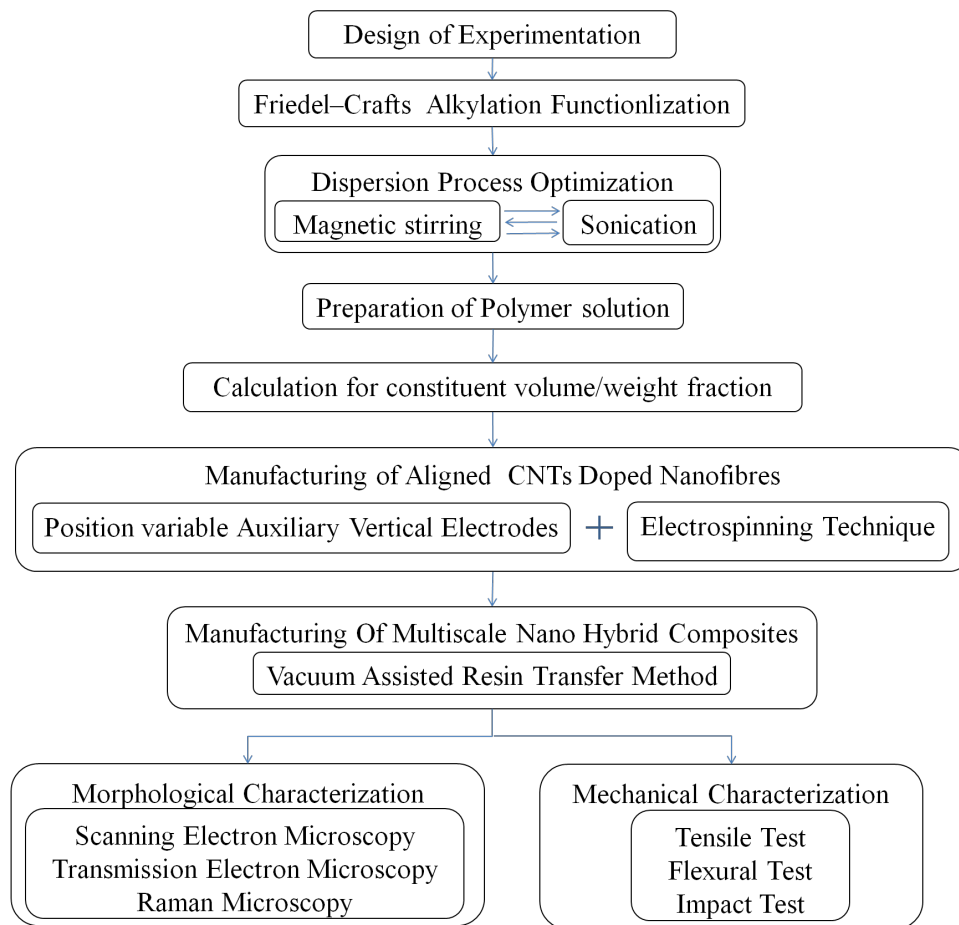


FIGURE 3.1: Schematic of proposed methodology

Four different volume fractions 0.1%, 0.2%, 0.5% and 1% of randomly oriented nanofibre mats were tested and the best combination of Randomly oriented PAN polymer nanofibres mats with 32% glass fibre multiscale nanohybrid composites were selected for producing aligned single-walled carbon nanotubes (SWCNTs) doped PAN polymer multiscale nanohybrid composites. However, for doping, only 0.25 vol% SWCNTs was selected. The reason behind selecting one volume fraction was based on the results from Pilehrood et al. [188]. Their results showed that the viscosity of the PAN/DMF solution (1.2 Pa. sec) was not altered by the additions of 0.25 vol % SWCNTs.

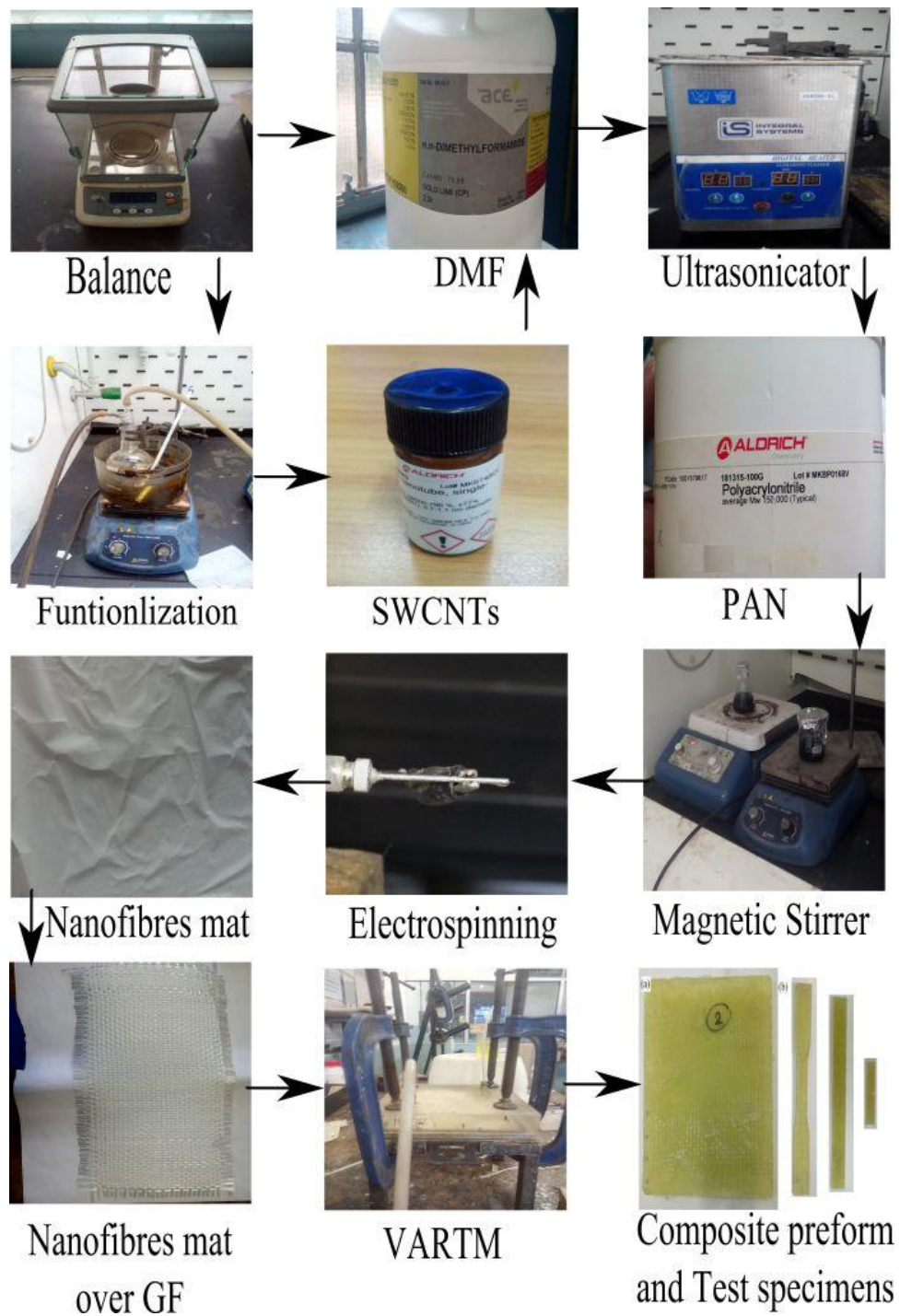


FIGURE 3.2: Manufacturing steps of the multiscale nano hybrid composite

However, for the increase in SWCNTs concentration to 0.5%, the solution viscosity was also increased from 1.2 to 51.9 Pa.sec and makes the solution difficult for electrospinning resulted in beaded fibres with larger diameters. Therefore, to achieve the desired nanosize PAN nanofibres and also for comparing with randomly aligned PAN fibre mats, the maximum amount of 0.25% volume fraction of SWCNTs was added to the PAN/DMF solution for manufacturing aligned CNTs doped PAN nanofibre mats. Both the pristine and functionalized SWCNTs were used for producing the CNTs doped PAN polymer nanofibres mats. Vacuum-assisted resin transfer moulding (VARTM) method was used to manufacture all the composites. Figure 3.2 shows the combined experimental process for manufacturing SWCNTs strengthened multiscale hybrid composites.

### 3.1 Materials and Equipment

AMPREG 21 resin and hardener (Bisphenol-A epoxy) were used as a base matrix and were purchased from AMT Composites Pty. Ltd. South Africa. The Ampreg 21 is used at room temperatures (18°C to 25° C) and has excellent thermal and mechanical properties when cured at an ambient temperature. Table 3.1 shows resin and hardener (AMPREG 21) properties used in this study.

TABLE 3.1: Mechanical and physical properties of AMPREG 21 (resin-hardener) at 25°C [189]

Standard Resin/ Hardener					
Initial Mixed Viscosity (cP)	Cured Density ( $g/cm^3$ )	Gel Time (minute)	Tensile strength (MPa)	Tensile Modulus (GPa)	De-mould Time (minute)
1194	1.148	21	72.7-81.3	3.3-4.3	143

As per the manufacture manual, the standard mixing ratio of resin and hardener is given in Table 3.2.

TABLE 3.2: Standard mixing ratio of resin to hardener for Ampreg 21 [189]

Standard Mix Ratio (Resin:Hardener)	
by volume	by Weight
100:38	100:33

The E-glass macro fibres mats (woven) were used as a macro scale reinforcing material and was resourced by the composite laboratory of the University of the Witwatersrand, Johannesburg. Table 3.3 shows the mechanical and physical properties of the woven E-glass fibres.

TABLE 3.3: Woven E-glass properties [190]

Property	Density ( $g/cm^3$ )	Tensile Elongation (%)	Young's Modulus (GPa)	Tensile Strength (GPa)
Value	2.6	2.4	81.3	1.72

The secondary reinforcements (randomly oriented nanomats) were manufactured from PAN/DMF polymer solution. Polyacrylonitrile (PAN) powder (molecular weight: 150 000, Density  $1.184g/cm^3$  at  $25^\circ C$ ) and the N, N-dimethylformamide (DMF solution-99% purity) were purchased from Sigma Aldrich, South Africa.

Pristine and functionalized single-walled carbon nanotubes (SWCNTs) were doped into PAN nanofibres mats for manufacturing the secondary nanoreinforcements. The single-wall carbon nanotubes (SWCNTs) (with median length:  $1 \mu m$ , average diameter: 0.83 nm) were purchased from Sigma Aldrich, South Africa. The chemicals used during functionalization were Polyvinyl alcohol

(PVA: , Molecular weight 30.00-70.00 amu), Aluminium chloride (AR: 77.8 - 81.8%, Formula Weight:133.34 g/mol) and dimethyl sulfoxide (DMSO: Formula weight:78.13 g/mol) purchased from Sigma Aldrich, South Africa. The testing equipment, such as universal testing machine, impact testing machine, metal bend saw, sheet metal cutter, grinder, and measuring tools were provided by the mechanical workshop of the department.

### 3.2 Calculation for Volume Fractions

Before manufacturing the glass fibre composites, the required number of glass fibre layers were calculated for obtaining the 32 volume % glass fibre in epoxy matrix. The dimensions of the single glass fibre layer was 19 cm  $\times$  19 cm according to the size of the VARTM mould cavity. The single layer was cut and weight was measured to be  $14.5 \pm 0.5$ g. Equation 3.1 was then used to calculate the required number of layers.

$$n_{layers} = \frac{\rho_{gf} \times t_m \times V_{gf}}{m_a} \quad (3.1)$$

where,

Glass fibre density ( $\rho_{gf}$ ) is  $2.58 \text{ g/cm}^3$

Thickness of the cavity of the mould ( $t_m$ ) was  $3.2 \pm 0.05$  mm

Volume fractions of the fibre glass mat ( $V_{gf}$ ) were 16%, 24%, 32%, and 40%

Glass fibre mass per unit area ( $m_a$ )  $\frac{14.5g}{19cm \times 19cm} = 0.04017 \text{ g/cm}^2$

The required number of fibreglass layer ( $n_{layers}$ ) were approximated to 3, 5, 7 and 9 for 16%, 24%, 32%, and 40% respectively. Secondly, the volume of PAN/DMF solution required for producing 0.1%, 0.2%, 0.5% and 1% volume fraction of PAN nanofibres mats using electrospinning process were calculated.

The PAN/DMF solution volume was obtained by,

$$V_{PAN/DMF} = \frac{V_{PAN}}{PAN_{conc}} \quad (3.2)$$

The PAN concentration ( $PAN_{conc}$ ) was obtained from our previous electrospinning experimental results and given in Table 3.4.

TABLE 3.4: Parameters matrix for electrospinning process

Spinneret - Collector Gap (cm)	10-35
Auxillary Vertical Electrodes	0-2
Applied Voltage DC (KV)	30-May
Number of Spinnerets	1-6
Flow Rates (ml/hr)	0.12-0.50
% Concentrations	8-8.8

Based on the results  $PAN_{conc}$  was 8.1%. The  $V_{PAN}$  was determined using

$$V_{PAN} = \rho_{PAN} \times m_{PAN}$$

where

$\rho_{PAN}$  was PAN density ( $1.184g/cm^3$ )

$m_{PAN}$  was the mass of PAN for 0.1%, 0.2%, 0.5% and 1% volume fractions and was determined by

$$m_{PAN} = m_{mf} \times m_M \quad (3.3)$$

Where,

$m_{mf}$  was the mass fraction of PAN

$m_M$  was the total mass of the multiscale nano hybrid composites

The mass fraction of PAN and the total mass of the multiscale nano hybrid composite were calculated using equations 3.4 and 3.5.

$$m_{mf} = \frac{\rho_{PAN} \times V_{PANVF}}{\rho_M} \quad (3.4)$$

$$m_M = \rho_M \times V_M \quad (3.5)$$

Where,

$V_{PANVF}$  was the PAN nanomats volume fraction

$V_M$  volume of the multiscale composite which was equal to  $115.52\text{cm}^3$  based on the mould size.

$\rho_M$  was the density of the multiscale nano hybrid composite and was calculated by equation 3.6.

$$\rho_M = V_{gf} \times \rho_{gf} + V_e \times \rho_e + V_{PANVF} \times \rho_{PAN} \quad (3.6)$$

Where,

$\rho_{gf}$  was the glass fibre density ( $2.58\text{ g/cm}^3$ )

$\rho_e$  was epoxy-resin density ( $1.14858\text{g/cm}^3$ )

$V_{gf}$  was the glass fibre volume fraction i.e. 32%

$V_e$  was the matrix volume fraction and was calculated by

$$V_e = 1 - V_{gf} - V_{PANVF}$$

Table 3.5 shows the calculated mass of PAN and volumes of PAN/DMF solution using equation 3.1 and 3.2 for producing the required nanomats volume fractions.

TABLE 3.5: Volume Fraction values for different concentrations of PAN/DMF solution

S.No.	Volume of fraction of Nano fibre (%)	Mass of PAN (gram)	Volume of PAN/DMF solution (ml, 8.1%)
1	0.1	0.172	1.793
2	0.2	0.344	3.587
3	0.5	0.860	8.967
4	1	1.720	17.935

Next step was to produce the SWCNTs doped nanomats. For the current analysis, only 0.25% SWCNTs volume fraction was selected and the procedure for calculating the required SWCNTs mass is given below:

$$m_{CNT} = \rho_{CNT} \times V_{CNT}$$

Where

$V_{CNT}$  was the volume of SWCNTs

$m_{CNT}$  was the mass of SWCNTs

$\rho_{CNT}$  was SWCNTs density ( $1.66 \text{ g/cm}^3$ )

Volume of SWCNTs were calculated by,  $V_{CNT} = V_{PAN/DMF} \times \%V_{CNT}$

Where

$V_{PAN/DMF}$  was the volume of PAN/DMF solution (12 ml)

$\%V_{CNT}$  was the SWCNTs volume fraction (% 0.25)

Based on the above calculation, the mass of SWCNTs for the 0.25% SWCNTs volume fraction was 51 mg which was then mixed with 12 ml PAN/DMF solution to produce the SWCNTs doped nanofibres mats.

### 3.3 SWCNTs Functionalization

As discussed before, the intrinsic behaviour of CNTs has resulted in agglomeration (van der Waals forces) and poor interfacial bonding with the matrix. Hence various functionalization processes were used to improve both the interfacial adhesion and dispersion. However, the conventional covalent functionalization using acid oxidation severely damages the surface of CNTs and reduces their aspect ratio [191]. These damages limit the CNTs strengthening capabilities and thus reduce their benefits as strengthening agents. Therefore, in this study, Friedel-Crafts Alkylation (FCA) functionalization process suggested by Pei was adopted [118].

The Friedel-Crafts Alkylation (FCA) process was started by mixing SWCNTs (0.4 g) and PVA (4 g) with DMSO (40 ml) solution in a 250 ml flask using a magnetic stirrer. The flask was then immersed in an oil bath for homogeneous heating and was gradually heated to 90°C in the presence of nitrogen. During the functionalization process, the nitrogen environment promotes the electrophilic reaction to the CNT benzene ring and thus improve the PVA grafting.

As the heating promotes the chemical process, a catalyst Aluminum Chloride ( $\text{AlCl}_3$ ) was added for grafting the PVA chains onto the surface of the SWCNTs. During the chemical process, the OH groups from PVA reacted with the catalyst ( $\text{AlCl}_3$ ) and produced positive carbocations ( $\text{CH}_3^+$ ) ions (electrophiles) and negative  $\text{AlCl}_2^-$  ions respectively. The positive ions electrophiles were then attracted towards the SWCNTs hexagonal ring due to the CNTs surface delocalized electron (nucleophilic) sites and thus attached the PVA chains on the SWCNTs. This process has improved the chemical bonding with the host polymeric material [192]. After 20 hours of the chemical process,

the chemical reaction was aborted by adding 100 ml of methanol/hydrochloric acid mixture (volumetric ratio 1:1). The solution was then centrifuged at 3500 rpm for 15 minutes to precipitate the functionalized SWCNTs (f-SWCNTs). The f-SWCNTs were washed, filtered, and dried in a furnace for 3 hours at 70°. Figure 3.3 shows the equipment used in the functionalization process.

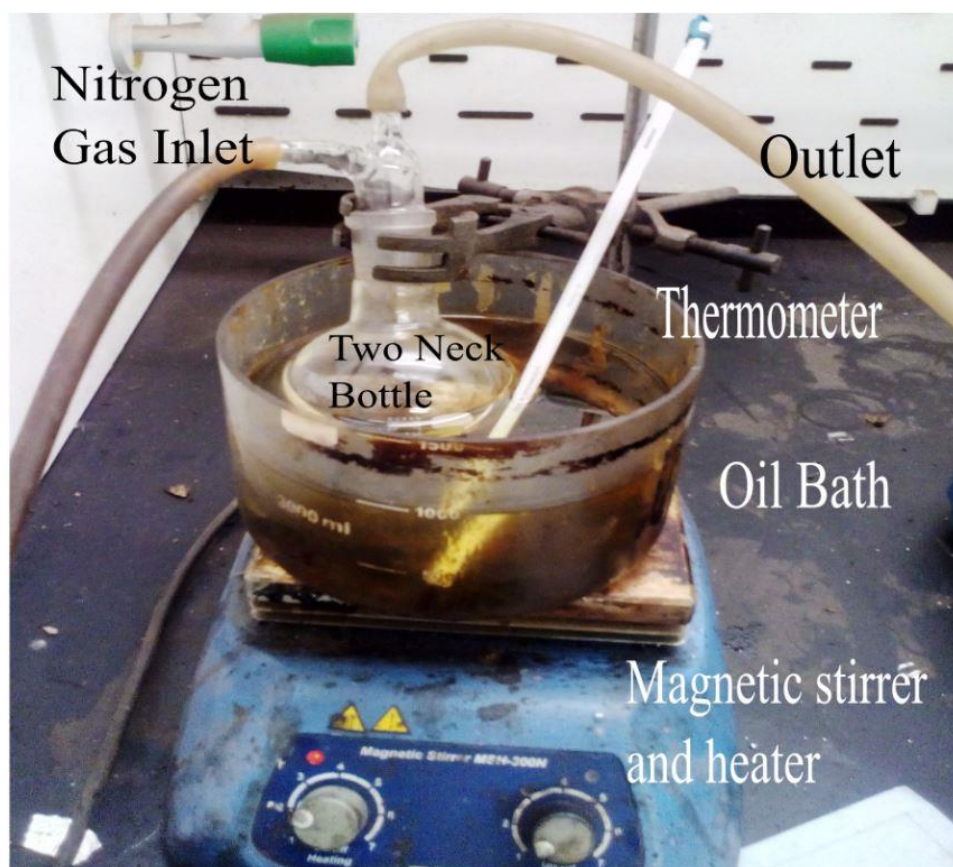


FIGURE 3.3: Friedal craft alkylation process

The Raman spectra were used to characterize both Pristine (p-SWCNTs), and functionalized SWCNTs (f-SWCNTs) and shown in Figure 3.4. The two peaks at the wavelengths of  $1280\text{-}1390\text{ cm}^{-1}$  and  $1480\text{-}1700\text{ cm}^{-1}$  were for the disorder (D band) and graphite band (G band) respectively. These bands represent two different vibrational modes of SWCNTs. The D band represents the crystal disorder, such as sidewall defects (pentagons or heptagons) or  $\text{Sp}^3$

carbon hybridization, and the G band was for the  $Sp^2$  carbon hybridization. The increased value of D-band to G-band ( $I_D/I_G$ ) ratio defines the structural changes of the SWCNTs wall due to functionalization process [193, 194]. In the current work, the  $I_D/I_G$  ratio was measured as 0.1025 and 0.1674 for p-SWCNTs and f-SWCNTs respectively. The higher ratio value of 0.1674 for f-SWCNTs was due to the carbocations attachment to the SWCNT walls as the  $Sp^2$  carbon hybridization was converted into  $Sp^3$  hybridized carbons. This confirmed the PVA grafting to the SWCNTs wall during FCA [192].

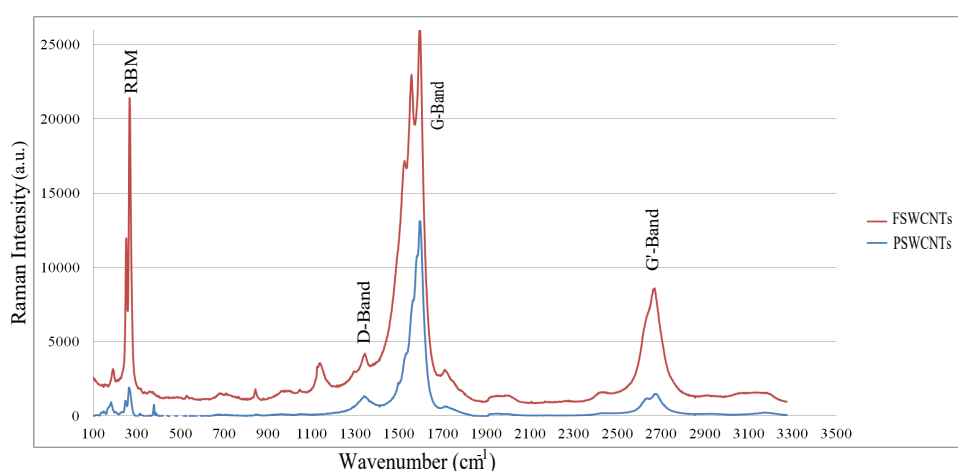


FIGURE 3.4: Raman spectroscopy of the Pistine and functionalized SWCNTs

Fourier transform infrared (FTIR) spectroscopy was used to analyze the functionalization of SWCNTs, and Figure 3.5 shows the FTIR spectrum of both pristine and Functionalized SWCNTs. IR spectra were obtained for the range of  $4000$  to  $500\text{ cm}^{-1}$ .

The peak at  $1027\text{ cm}^{-1}$  showed the C-O bond stretching while the peak from  $1100$  to  $1600\text{ cm}^{-1}$  confirmed the aromatic structures. The peaks corresponding to C-H and O-H bonds were obtained at  $2900\text{ cm}^{-1}$  and  $3200$ - $3400\text{ cm}^{-1}$  respectively. These peaks confirm that the PVA chains are attached to the surface of CNTs.

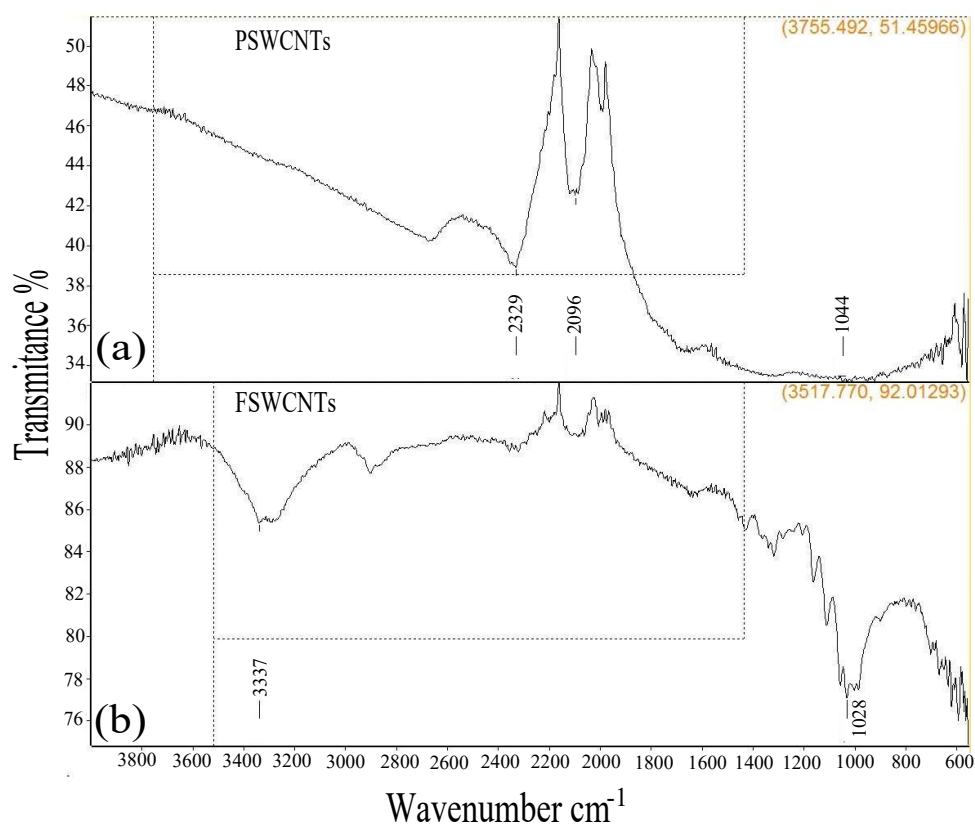


FIGURE 3.5: IR spectra of (a) p-SWCNTs and (b) f-SWCNTs

### 3.4 Dispersion of CNTs

Generally, the functionalized SWCNTs are dispersed within the PAN solution using ultrasonication or mechanical mixers before manufacturing CNTs doped PAN nanofibres mats. However, the dispersion of CNTs even after the functionalization is still a challenge due to their re-agglomeration. Longtime sonication is considered as the most suitable method for dispersion. However, it damages the structure of CNTs and reduces its aspect ratio which reduces their mechanical properties. Therefore, two-step dispersion was adopted in this study. Magnetic stirring and ultrasonication were used in sequence to reduce

the sonication time and to avoid the structural damage to the SWCNTs. Table 3.6 shows the range of input parameters used in the SWCNTs dispersion process.

TABLE 3.6: Proposed controlling factors and variables of dispersion process

Parameter	Step-1	Step-2	Step-3	Step-4	Step-5		Step-6
	Magnetic Stirring (time, minutes)	Sonication time (minutes)	Break time in sonication	Carbon nanotube ( Wt mg)	Concentration (%)		Final Mixing Mechanical Stirring (minute)
Variable	8	5	1 minute after 5 min sonication	50	10	17	45
		10					
		15					
	16	5					
		10					
		15					
	24	5					
		10					
		15					

The dispersion process was started by adding the functionalized SWCNTs (0.05g) into the solvent (11.03 ml, N, N-dimethylformamide (DMF), 99%) by magnetic stirring (model MSH-300N magnetic stir) and ultrasonication (model UD80SH-2L INTEGRAL SYSTEMS sonicator). Figure 3.6 shows the equipment used and schematic of the dispersion process. Before the sonication, the volume of solvent and weight of the SWCNT were measured using a graduated syringe and an electronic balance respectively. Nine samples, having the same amount of solvent and f-SWCNTs were mixed according to the matrix shown in the Table 3.6.

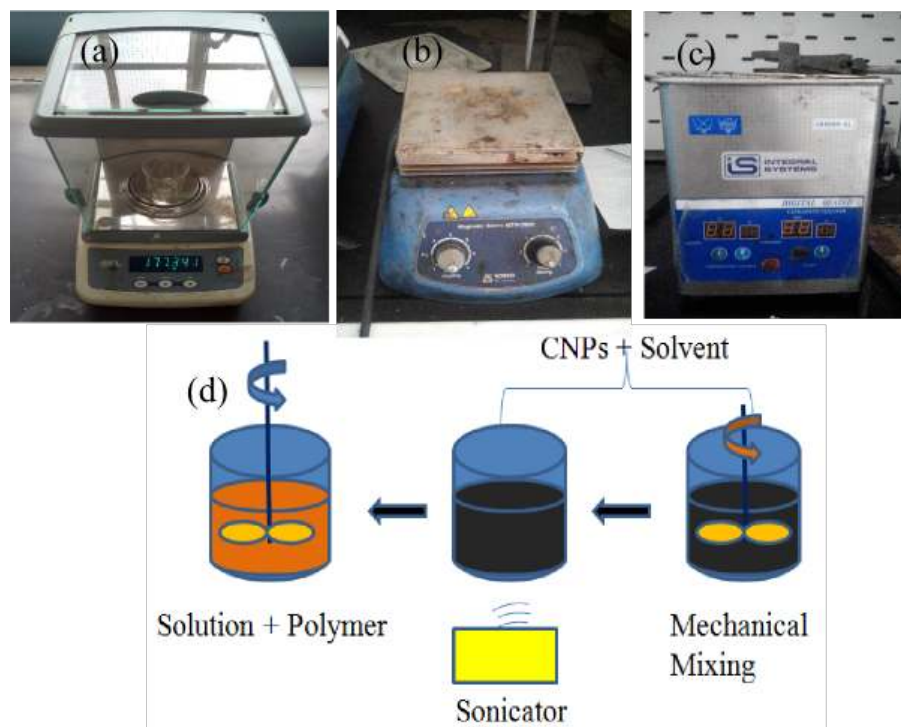


FIGURE 3.6: (a) Balance for weights (b) Magnetic stirrer (model MSH-300N) (c) Sonicator(model UD80SH-2L INTEGRAL SYSTEMS), (d) Mixing process of CNTs into the polymer solution

Figure 3.7 shows the trends of precipitation of the functionalized SWCNTs after mixing with the combination of magnetic stirring and sonication. It could be inferred that 24 minutes of magnetic stirring with 15-minute sonication including an interval of 1.5 min after every 5 minutes kept SWCNTs dissolved into the polymer solution for more than 96 hours. The dispersed SWCNTs were examined using Raman spectroscopy for structural defects which confirmed the absence of damage in f-SWCNTs after the two-step dispersion process. Based on the results of dispersion process, the SWCNTs-PAN solution which took maximum precipitation time (96 hours) was selected for electrospinning. The selected solution was electrospun within 48 hours to produce the doped CNTs nanomats to avoid precipitation of SWCNTs.

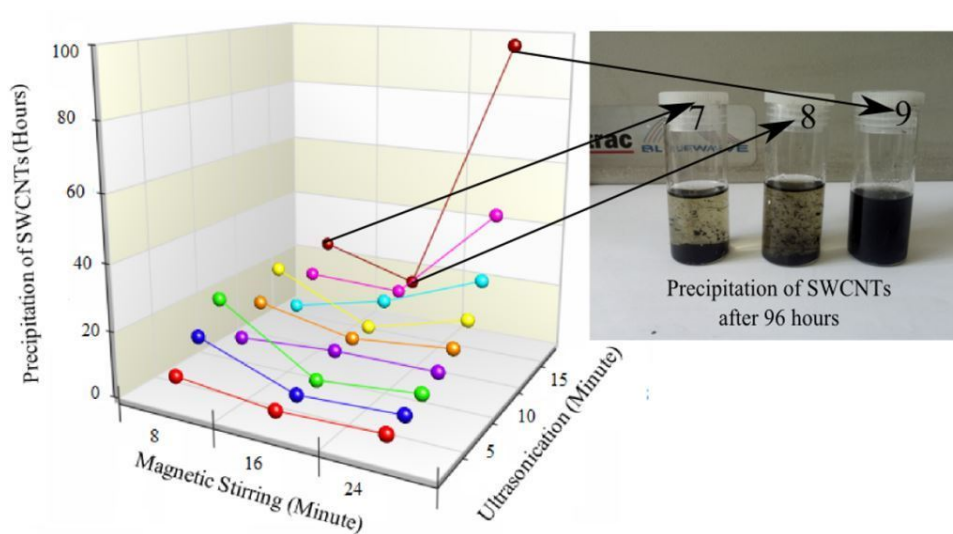


FIGURE 3.7: Precipitation trends of SWCNTs in the two step dispersion

### 3.5 Testing Procedures

The details of the manufacturing process of randomly oriented, aligned and SWCNTs doped nanofibres mat strengthened hybrid composites using electrospinning techniques and VARTM are presented in Chapter 4 for easy reading.

Before testing, the samples for the tensile, flexural and impact tests were prepared from the preform manufactured using VARTM. The tests were conducted according to the American Society for Testing and Materials (ASTM) standards. Five testing specimens of each tensile, flexural and impact test were machined and tested from the single VARTM composite preform respective to the ASTM D638:2010, ASTM D790:2010 and ASTM D256:2010 (Figure 3.8). The thickness of the specimens was kept at 3,2 mm in accordance with the ASTM standard. The bending test samples were manufactured at a span to thickness ratio of 16:1.

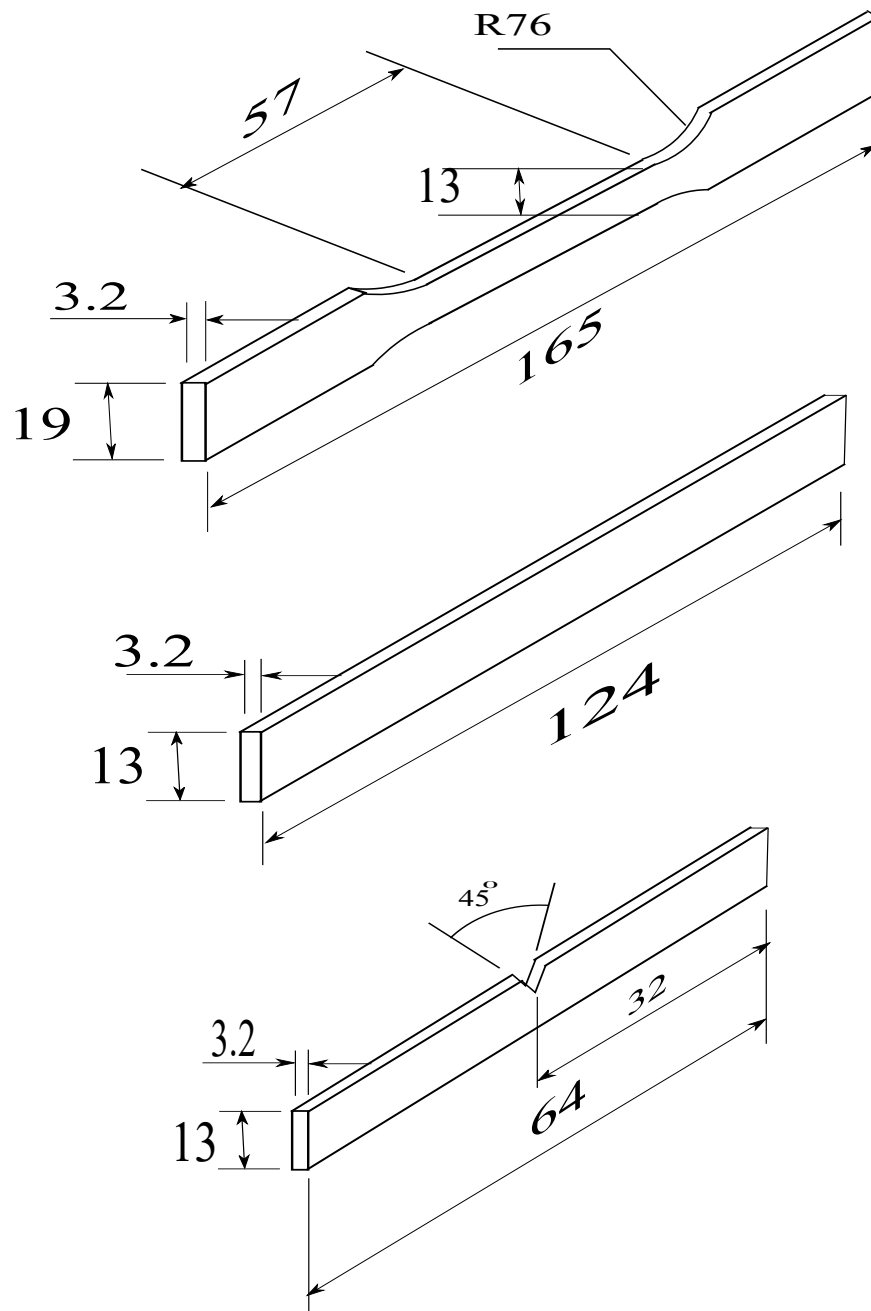


FIGURE 3.8: Test sample dimensions (a) Tensile ASTM D638-08:2010 (b) Flexural ASTM D790-07:2010 (c) Impact test specimens ASTM D256-06a:2010

The tensile and flexural tests were carried out with the universal tensile testing machine SHIMADZU. In accordance with DIN EN 527:1=2 and ISO 178, these tests were carried out at a crosshead speed of 2 mm / min. Impact tests have been performed on a Tinius Olsen impact pendulum in accordance with ISO 179- 1 standard. The recorded results were then used to obtain the tensile and flexural properties. The preform was marked using a steel ruler and thin marker as per the layout. The marking included the machine allowance of 1.5 mm for each specimen. The layout of the specimen is shown in Figure 3.9.

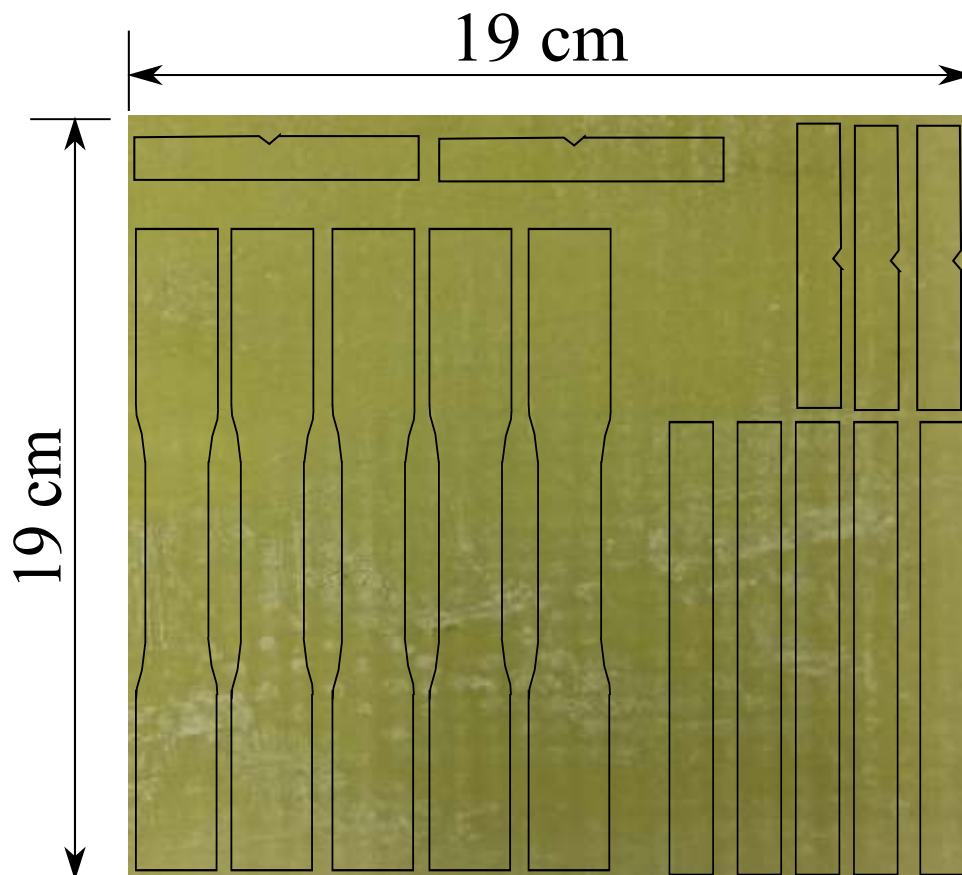


FIGURE 3.9: Cutting layout for test specimens

Five rectangular plates having dimensions of 165 mm  $\times$  19.5, 124 mm  $\times$  13

mm, and 64 mm × 10 mm for tensile, flexural and impact tests respectively were machined using a band saw (Figure 3.10).



FIGURE 3.10: DoAll band saw

Rectangular plates having a dimension of 165 mm × 19.5 mm were used as a preform for tensile dog bone specimen. These specimens were gripped tightly into the dog bone shaped steel jig (Figure 3.11). The steel jig was slid through

the guided path fixed on the table of the Tensilkut machine (Figure 3.11). A cylindrical grinder powered by pneumatic force was used to cut the specimen into the required dog bone shape and is shown in Figure 3.11.

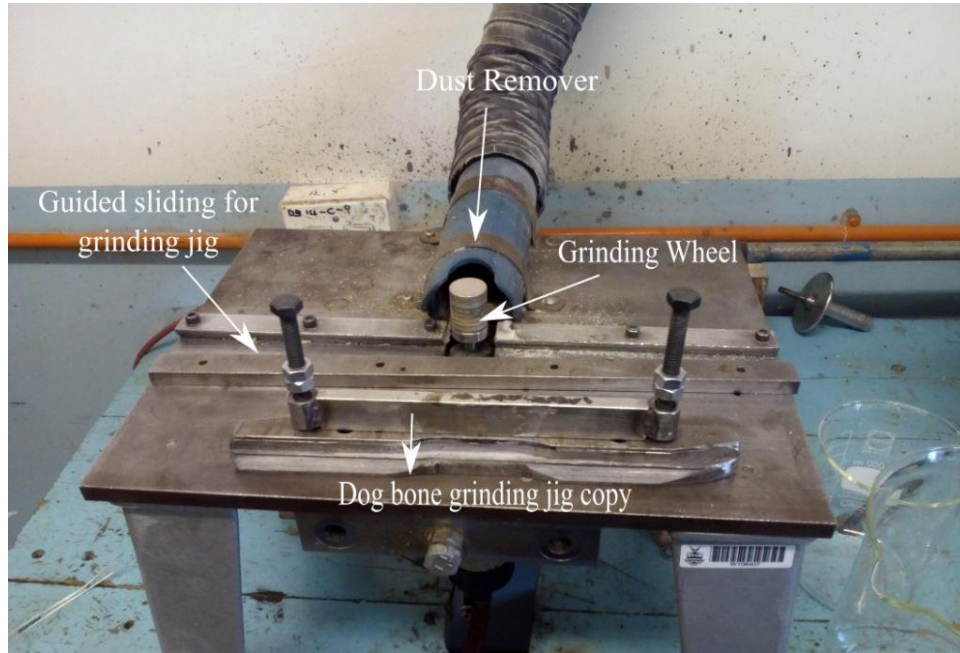


FIGURE 3.11: TensilKut grinder and dog bone copy jig used to cut the tensile specimens

Personal protective equipment (PPE) was used all the time during the machining operation to avoid accident and hazard (dust and flying debris). Moreover, a dust extractor was also used to eliminate the flying particles during machining. A notch of 2.5 mm depth was machined on the Impact test specimens. Finally, the cut specimens were cleaned using slow speed sandpaper grinder and then finally with fine sandpaper. Figure 3.12 shows the different testing specimens produced according to the ASTM standards.

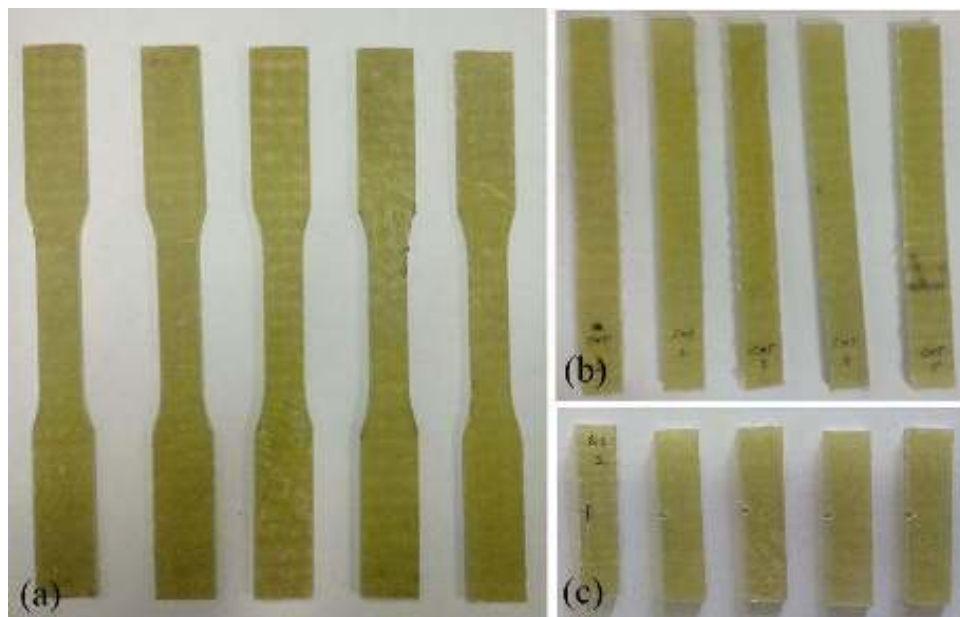


FIGURE 3.12: (a) Tensile, (b) Flexural and (c) Impact test specimens

### 3.5.1 Tensile test

The tensile test was carried out with a universal testing machine. (UTM, SHIMADZU AG-IS Autograph machine). The UTM machine was equipped with self-aligning clamps, a force indicator, a laser extensometer, and a set of vernier callipers. The recommended conditions adopted during the tests were; relative humidity:  $50 \pm 5 \%$ , and temperature:  $23 \pm 2 \text{ C}$ . A 20 kN load cell was used for testing. A laser extensometer (LE-05 Epsilon Technology laser) was interfaced with a SHIMADZU machine using an NI instruments data acquisition card (8 channel) to record the experimental data i.e linear extension and force. The UTM is shown in Figure 3.13.



FIGURE 3.13: SHIMADZU Universal testing machine (UTM)

The procedural guideline as explained in ASTM D638:2010 [195] was adopted for the tensile test. Firstly, the UTM machine was set for the tensile test and the clamps were attached to the machine (Figure 3.13). The lower clamps were stationary while the upper clamp was moveable with a predefined rate of loading. The thickness and width of the gauge length of each specimen were

measured and recorded at three points using Vernier Calipers before testing. A reflective tape was attached on the specimen surface for the gauge length of 50 mm.

The specimen was mounted tightly into the clamps to avoid slippage during the test. The distance between the clamps was  $115 \pm 5$  mm. The UTM integrated encoder was used to acquire the load and the displacement of the actuator. The laser extensometer values were recorded into the Desktop computer using LabVIEW software. The tests were performed at the speed of 2mm/min. Five tensile specimens of each composite were tested. All the specimens were failed within the gauge length which provided the validity of the tensile tests. Figure 3.14 shows a failed test piece within gauge length. The measured data of the specimens of each batch were averaged and used to calculate the tensile properties as given below.

$$Stress(\sigma) = \frac{Force}{Area} \quad (3.7)$$

$$Strain(\epsilon) = \frac{\Delta L}{L} \quad (3.8)$$

where:

$\Delta L$  was extensometer displacement, mm

$L$  was extensometer gauge length, mm

$$ElasticModulus = \frac{Stress}{Strain} \quad (3.9)$$

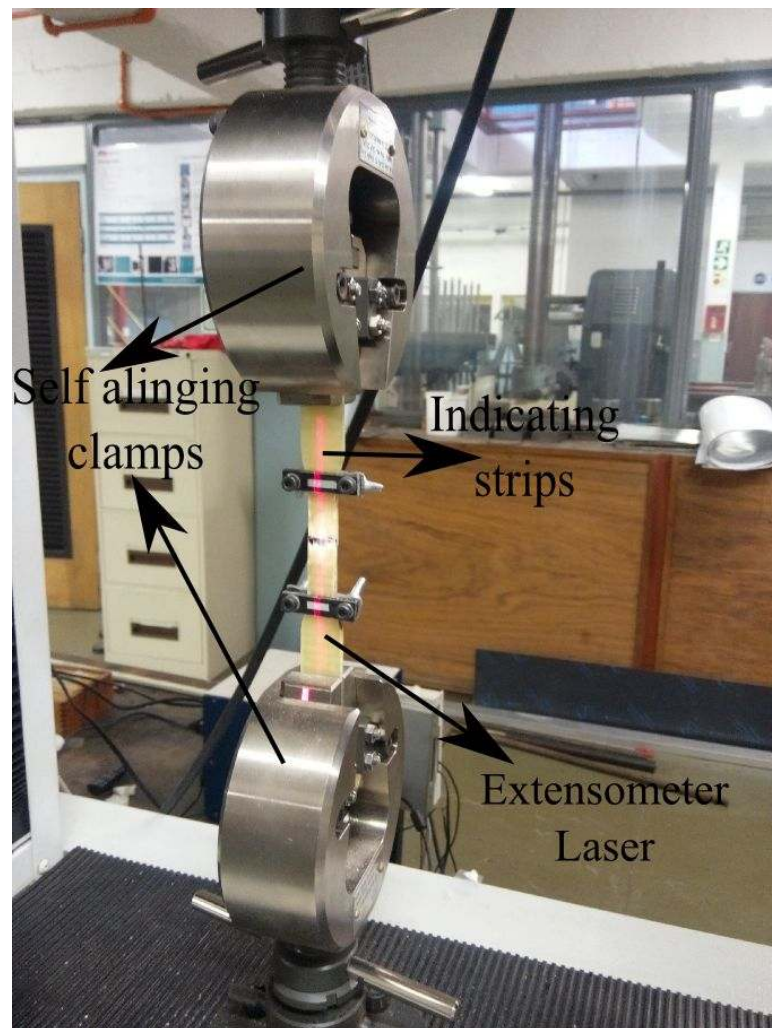


FIGURE 3.14: Dog bone specimen after test

### 3.5.2 Flexural test

The ASTM D790:2010 standard procedure and UTM (SHIMADZU) were used for the flexural test (3-point) of the polymer composites. The flexural test rig was mounted on the machine and then the test specimen was set as shown in Figure 3.15. The distance between the support was 63 mm. The load was

applied at the rate of 2mm/min until the fracture of the specimens. The force-displacement data was recorded by the built-in encoder. Before each test, the thickness and width of the specimens were recorded and a minimum of five specimens were tested. The flexural properties of specimens were determined using the equations 3.13, 3.11 and 3.12;

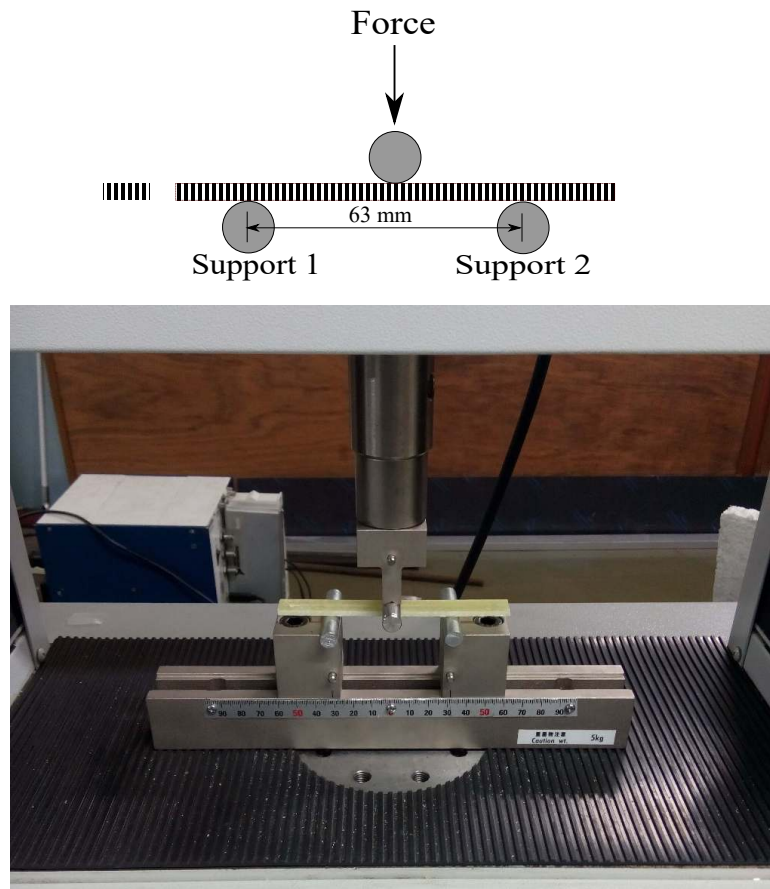


FIGURE 3.15: Flexural test specimen setup

$$\sigma_f = \frac{3F_{max}L}{2bh^2} \quad (3.10)$$

where:

$\sigma_f$  was specimen flexural stress, MPa

$F_{max}$  was applied load, N

$L$  was length between supports, mm

$b$  was width of specimen measured at its centre, mm

$h$  was thickness of specimen measured at its centre, mm

$$\epsilon_f = \frac{6hD}{L^2} \quad (3.11)$$

where:

$\epsilon_f$  was flexural strain of specimen, mm/mm

$D$  was the vertical deflection of the specimen at the point of load application, mm

$$E_f = \frac{\Delta\sigma_f}{\Delta\epsilon_f} \quad (3.12)$$

where:

$E_f$  was flexural modulus of elasticity, MPa

$\Delta\sigma_f$  was changed in the Flexural stress of specimen, MPa

$\Delta\epsilon_f$  was changed in the Flexural strain of specimen, mm/mm

### 3.5.3 Impact test

Notched impact tests were performed on a Tinius Olsen pendulum in accordance with ISO 179-1 standard. The machine has a static dial arm and can be moved and positioned manually before testing on the Joules mark 360°. First, the gauge correction factor for the machine was determined by releasing the

pendulum without any specimen. The specimen was then mounted on to the machine and the pendulum was manually released on to the specimen. Five specimens of each composite were measured and an average absorbed energy was recorded from the dial gauge to calculate the energy observed before failure by the specimens. The breaking energy was used to measure the impact resistance of all composites. The testing machine and the piece tested are shown in Figure 3.16

$$K_I = \frac{e_I}{A_I} \quad (3.13)$$

where:

$K_I$  was impact resistance  $\text{KJ/m}^2$

$e_I$  was energy lost by pendulum due to impact,  $\text{KJ}$

$A_I$  was crosssectional area of impact specimen  $\text{m}^2$

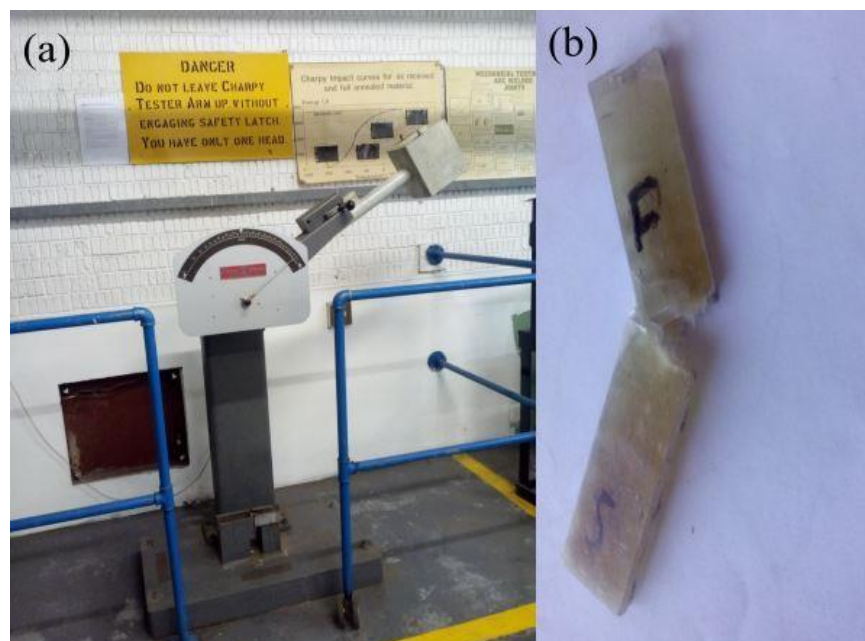


FIGURE 3.16: (a) Impact test machine 'Tinius Olsen Model impact pendulum' (b) Impact test specimen

---

## 3.6 Morphological Characterization

The electrospun nanomates, carbon nanotubes, and the tested glass fibre and the hybrid composites were morphologically analysed using Scanning Electron Microscopy, Raman spectroscopy, and Fourier transform infrared spectroscopy (FTIR).

### 3.6.1 Scanning electron microscopy (SEM)

Electron microscopy (SEM) scanning is the most commonly used high resolution image microscope. SEM produces the image by focusing the electron beam in a rectangular pattern over the surface of the sample. Once the SEM is calibrated and focused on the interested area, the image can be magnified with repeatable steps of focusing and calibration. The SEM imaging process is completed in a vacuum (low or high).

The nanofibres and all NGPCs were scanned using electron scanning microscopy (SEM, FEI Nova 600, FEI Quanta 400 FEG, USA Figure 3.17) at various voltages ranging from 5KV to 30KV. Before characterizing the nanofibres, the nanofibres and surfaces of the fractured specimens were mounted over an aluminium round post using double-sided carbon tape as shown in Figure 3.18. The specimens were coated with a thin carbon layer and a gold-palladium (Au / Pd) layer of 15 nm (60:40) with an EMITECH K950X evaporator and a sputter coater EMITECH K550X. The SEM analysis was performed at the University of Witwatersrand 's Unit for Microscopy and Microanalysis (MMU). The SEM has the capabilities of capturing images of non-conductive samples at resolutions as low as 0.8 nm due to the high voltages (30kV) and high vacuum.

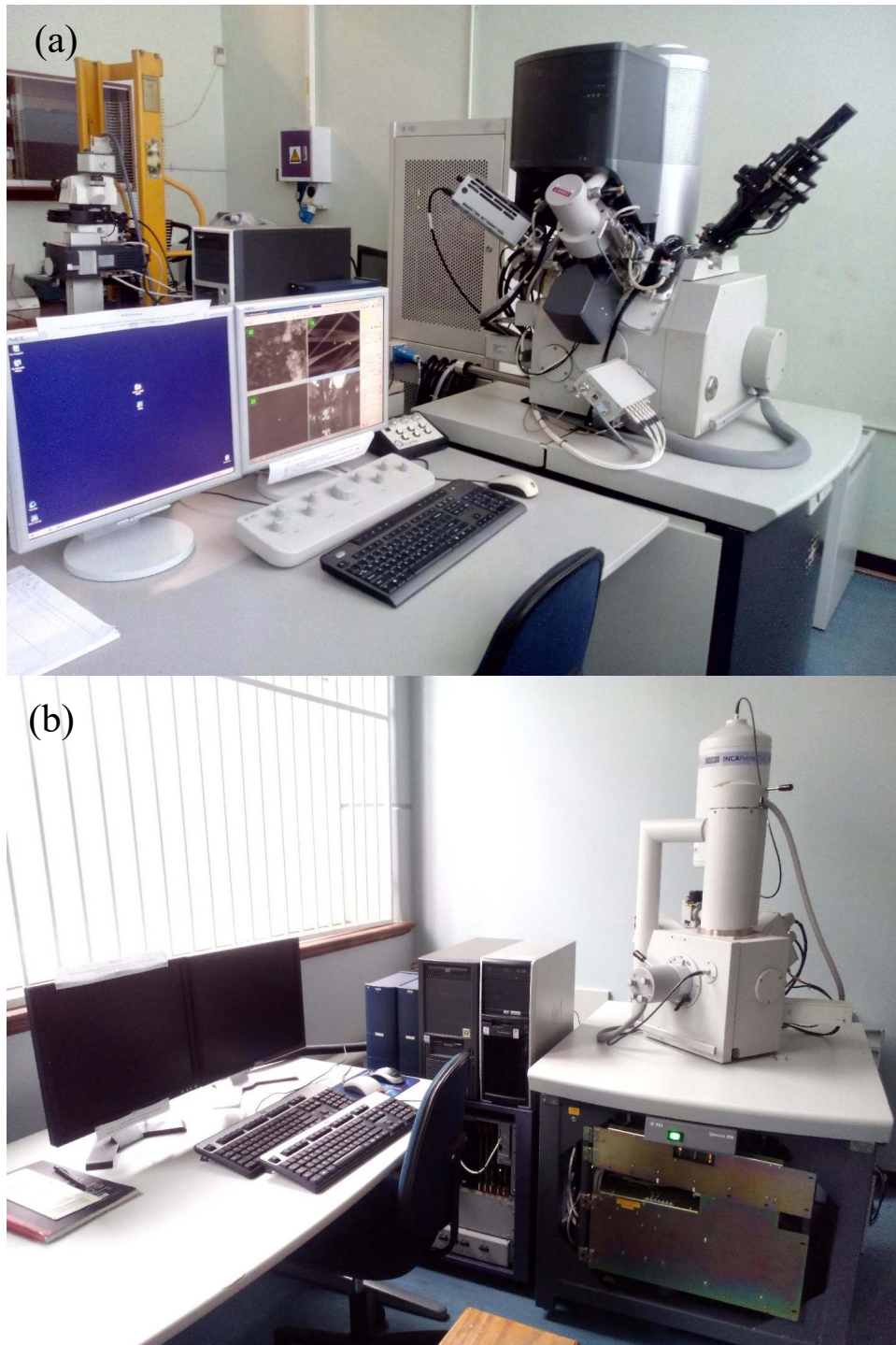


FIGURE 3.17: (a) SEM, FEI Nova 600, (b)FEI Quanta 400 FEG, USA

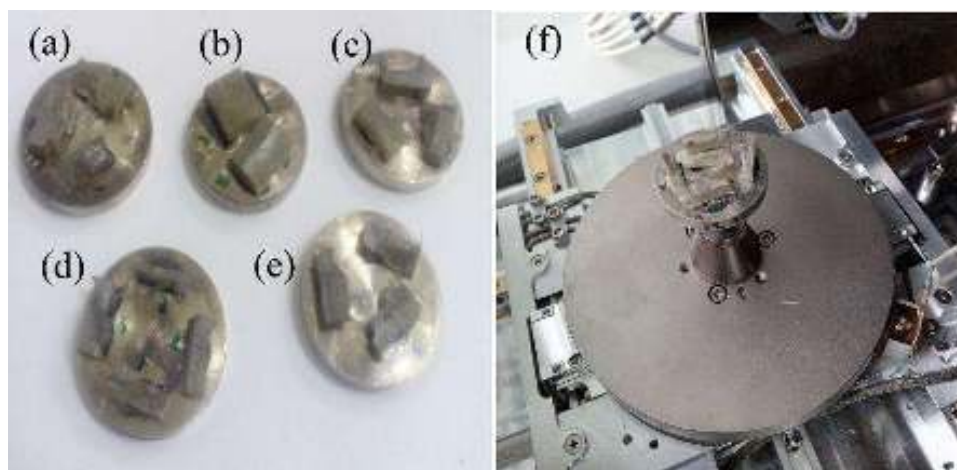


FIGURE 3.18: Specimens coated for SEM (a and e) Tensile (b) Bending (c and d) Flexural test (f)

### 3.6.2 Raman spectroscopy

The Raman spectroscopy was developed on the principle of Raman effect discovered by C.V. Raman in 1928 [196]. This technique analyses the materials using the vibrational modes of the molecular states. Monochromatic light source of known wavelength excites the electron cloud across the testing material. The incident light strikes back off the specimen with different wavelength due to an inelastic collision. The re-bounced light is measured as a function of wavelength and plotted against the wavelength before the collision. The change in the wavelength (upward or downward) is then compared to the library of materials to identify the nature of the chemical bonds within the specimen. Compared to the other analytical methods, Raman spectroscopy provides non-destructive, fast and easy analysis of the CNT samples. Raman analysis can probe the structure defects, diameter (SWCNTs), agglomerations and the structure kind (semiconducting or metallic) of CNTs along with the number of walls. Figure 3.19 shows the simplified principle sketch of the Raman spectroscopy.

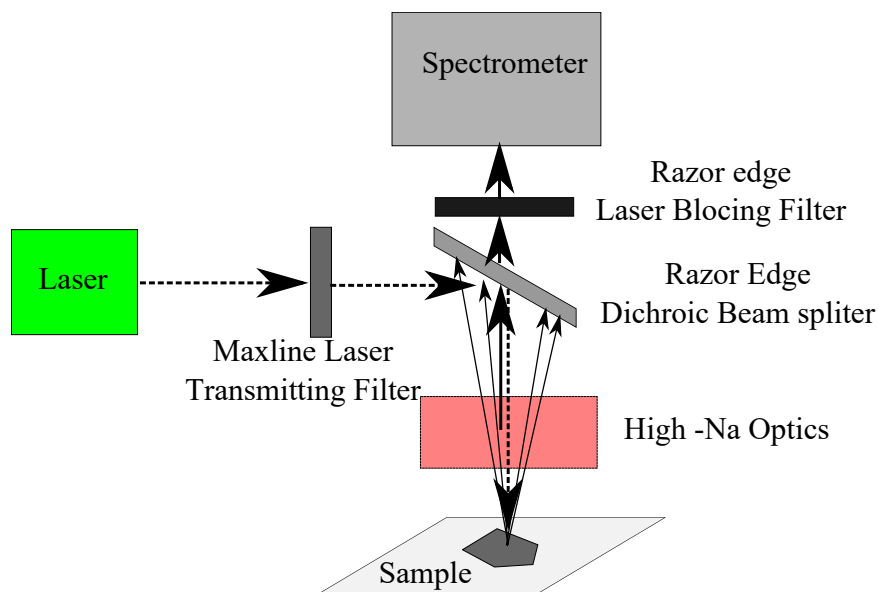


FIGURE 3.19: Working principle of the Raman spectroscopy

The Raman spectroscopy analysis was conducted in the Unit of Microscopy and Microanalysis (MMU) at Witwatersrand University, Johannesburg, South Africa. The Raman analysis was performed using the 514.5 nm green line of a Lexel argon ion laser and a Horiba LabRAM HR Raman spectrometer with an Olympus BX41 microscope fitting. A 100x target was used to collect the back-scattered light that was dispersed onto a liquid nitrogen-cooled CCD detector via a 600-line / mm grating. The sample's laser power was about 0.4 mW to prevent localized heating. LabSpec v4.18 software was used to collect acquired data.

In the Raman spectrum, Radial breathing mode (RBM) is the first region of the Raman spectrum for SWCNTs. The RBM contains a number of peaks showing the expansion and contraction of SWCNTs which depends on the diameters of the specimen. The RBM can be used to estimate the diameter of SWCNTs [197]. Generally, the RBM region is generated within  $100\text{-}500\text{ cm}^{-1}$ . The following two wavelengths were  $1300\text{-}1400\text{ cm}^{-1}$  and  $1500\text{-}1600\text{ cm}^{-1}$  for

---

the disorder (D band) and the graphite band (G band). These bands represent two different vibrational modes of SWCNTs. The D band represents the crystal disorder, such as sidewall defects (pentagons or heptagons) or carbon hybridization  $Sp^3$ , and the G band was used for carbon hybridization  $Sp^2$ . The G band is usually about  $1580 - 1620 \text{ cm}^{-1}$ . The G band is divided into two modes higher energy component (G+) and lower energy components (G-). G+ presents the vibration along the nanotube axis while G- presents the vibration along the girth of the tube [197]. The last peak seen in the Raman spectroscopy is called G' band. The G' band is an overtone of the D band (twice of the D band). These may be observed between  $2600\text{-}2800 \text{ cm}^{-1}$ .

### 3.6.3 Fourier transform infrared spectroscopy (FTIR)

FTIR is most helpful in the identification of organic or inorganic chemicals. It collects the data of the obscure mixture ingredients and develops a spectrum from the obtained interference pattern. It identifies the type of bonds in the molecules by generating an infrared spectrum against the wavelength of light.

Different molecules vibrate with certain frequencies according to the type of bond and material. FTIR uses the vibration characteristic of the functional molecules to identify their types in the unknown sample. Material molecules under FTIR process respond to the infrared light of specific wave number only which changes their excitation state (ground to higher energy) and cause bonds to bend, stretch or wagging. Different molecules respond to the specific wave number of light. This property of molecules is used to identify the type of molecules or functional groups in the sample.

Figure 3.20 shows the schematic of the FTIR equipment. IR beam from the source enters into the interferometer, which splits the incoming beam into two

rays using beam splitter prism. One ray directs towards stationary mirror while the other is received by the movable mirror. The reflected rays combine at the beam splitter due to interference phenomena and the resulted ray is called interferogram. A sample placed in the path of interferogram absorb the specific frequencies of light depending on its type of functional group. The interacted signal with sample has a unique feature measured by a detector. The final interferogram is decoded with Fourier transform and plotted as transmittance or absorbance against wave number. FTIR spectrum contains different types of peaks representing different bond types [199].

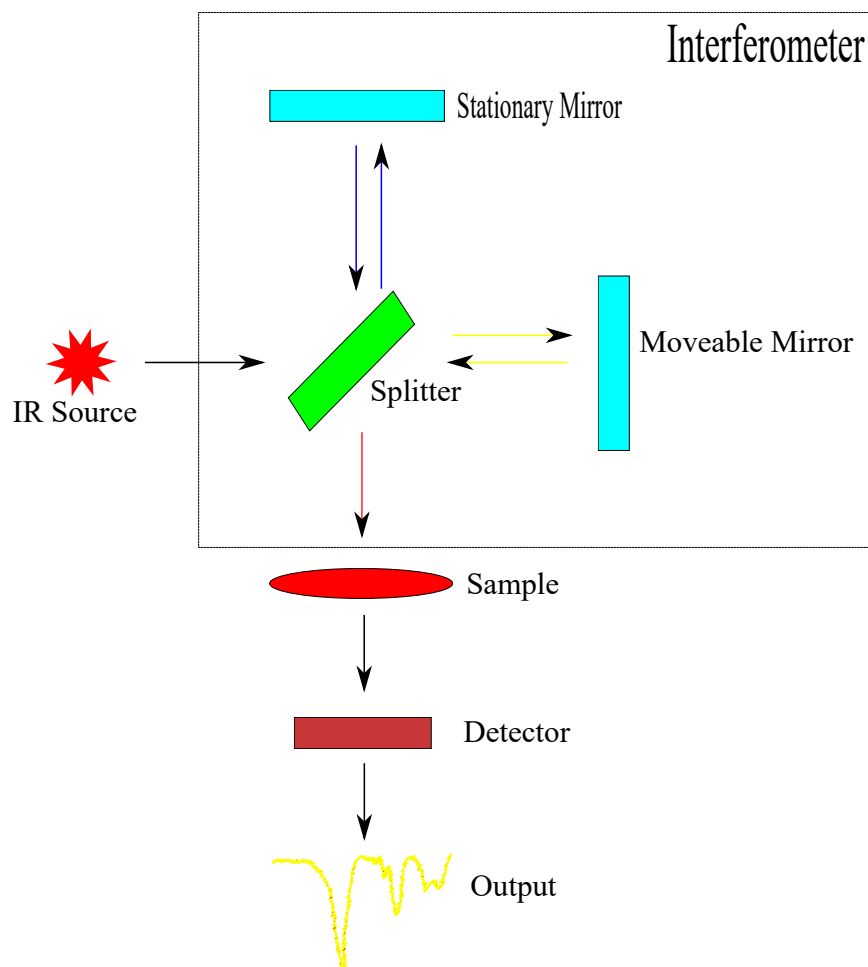


FIGURE 3.20: Schematic of FTIR process

# Chapter 4

## Experimental Characterization of Multiscale Nanohybrid Composite

### 4.1 Introduction

The major drawback with fibre composites is the matrix rich interlaminar regions, where the load transfer was expected to occur. Therefore, researchers were focusing on improving the interlaminar regions by adding nanofillers into the fibre composite system [16, 144]. The polymeric nanofibres have gained importance due to their ease of manufacturing in different sizes with unique mechanical properties. In addition, if these nanofibres could be manufactured in the form of mats (polymer nanofibres mats, PNMs), then the continuous nanofibre mats could be a suitable secondary nanoreinforcement for producing Multiscale Nano Strengthened Hybrid Composites (MNHCs).

The PNMs are thin, light in weight, and they do not increase the weight of the final composite. Moreover, they are expected to reduce the length scale mismatch between the macrofibres and the polymer matrix molecular chains. In addition, these nanomats could be collected directly over the fibre mats, therefore, they reduce the processing time/cost. In addition, the nano reinforcement such as carbon nanotubes (CNTs) could also be doped with polymeric nanofibres for improving the interlaminar regions. The doping of CNTs was expected to improve the CNTs inherent disadvantages, such as misalignment, poor interfacial adhesion, and distribution. Among several techniques, for producing the polymeric nanofibres mats and CNTs doped polymer nanofibre mats, the electrospinning is preferable due to their ease of manufacturing [148]. As discussed earlier, the electrospun polymer jet takes a straight path in near field, while in far field, it starts whipping into a complex path due to electrical, gravitational and rheological forces (Figure 4.1a) [139] thus in the far field, the path variations cause randomly oriented nanofibre mats (Figure 4.1b) [201]. The randomness of nanofibres results in a variable molecular orientation with poor mechanical properties [163, 202].

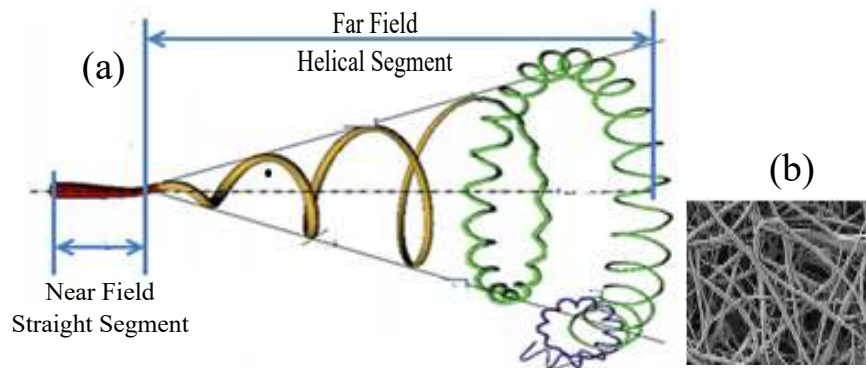


FIGURE 4.1: Electrospun nanofibre jet path (a) [203], (b)[166]

Based on the above factors, the objectives were defined as:

- Modifying the electrospinning process by adding adjustable auxiliary vertical electrodes (AVEs) and connected with the main DC power source
- Producing aligned PAN nanofibre mats and SWCNT's doped nanomats using a modified electrospinning process with multispinneret
- The effect of AVEs was analyzed to optimize the alignment, diameter, and morphology of PAN nanofibres.
- The effect of functionalization on the dispersion and the interfacial adhesion of the pristine and functionalized SWCNTs.
- Characterization of the mechanical properties of aligned nanomats and SWCNTs doped nanomats strengthened multiscale hybrid composites.

#### **4.1.1 Electrospinning for producing aligned PAN nanofibres mat**

Electrospinning was used to produce both PAN nanofibre mats and SWCNTs doped nanomats and was designed in our previous research work [204–206], which have contributed a deep understanding of the electrospinning parameters and their effects on producing the PAN nanofibre mats. The same set up with additional improvements was used for the current research work. The electrospinning facility consists of a variable high DC voltage power supply, NE-1600 syringe pump and a grounded rotating collector (diameter, 120mm and width, 210 mm) coupled with a variable high-speed DC motor. The two important electrospinning process (solution and operating) parameters were analyzed for producing the PAN nanofibre mats. The solution parameters including polymer concentration, viscosity, molecular weight, surface tension, and conductivity were analyzed.

1. Polymer concentration, viscosity, and molecular weight are directly related and were found to be critical in determining the fibre morphology.
2. Surface tension was controlled by the solvent composition
3. The conductivity was controlled by the polymer composition

Among the other solution parameters, the viscosity of the electrospinning solution plays an important role in producing smooth uniform PAN nanofibres, which could be varied by altering the polymer concentration.

The operating parameters such as volume flow rate, electric field strength, collector type, types of syringes and needle diameter were investigated to obtain an optimum operating value for the electrospinning process. The volume flow rate was closely controlled with the use of a syringe pump. The flow rates ranging from 0.5ml/hr up to 5ml/hr were experimented to find the ideal flow rate for the smooth uniform PAN nanofibre formation. The field strength was varied by changing either the applied voltage or the distance between the electrodes. Different types of needles and syringes also were used to find the optimum set-up to produce the best quality PAN nanofibres. Needles ranging from 32G to 18G (both 90 and 30 angled tips) were experimented with both glass and plastic syringes ranging from 5 to 50 ml volume. Based on the above observation, the major factors affecting the electrospinning process and the final quality of the PAN nanofibres were:

- Applied voltage
- Distance between electrodes
- PAN concentration

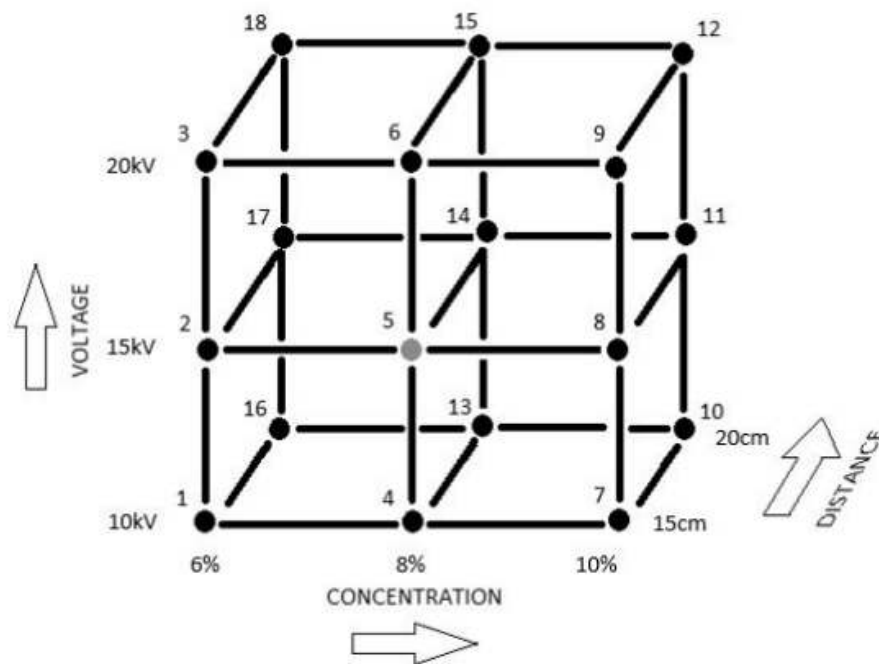


FIGURE 4.2: Electrospinning experimental matrix [206]

Since the above parameters are interlinked, an experimental matrix was developed for understanding their relationships with each other as shown in Figure 4.2. The results of the individual nodes of the experimental matrix are presented elsewhere [206] and the final optimized parameters from node 5 of the experimental matrix were taken for the current analysis. The values were:

- 8% of PAN Concentration
- Voltage of 15 KV
- Spinneret to collector distance of 15 cm

However, the previous research work could manage to produce non-aligned PAN nanofibre mats and an important parameter i.e alignment was not considered. Therefore the current research has focused on producing the aligned

TABLE 4.1: Electrospinning parameters range and optimized value along with AVEs

Electrospinning parameters	Range of values	Optimized values
Concentration (%)	8-8.8	8.1
Flow rate (ml/hr)	0.12-0.50	0.35
Applied voltage (DC-KV)	0-30	20
Collector to spinneret distance (cm)	5-35	25

PAN nanofibre mats and CNTs doped aligned PAN nanofibre mats by taking the previously optimized electrospinning parameters as a benchmark. For aligning the nanofibers, auxiliary vertical electrodes (AVEs) were introduced on both sides of spinnerets as shown in Figure 4.3a and a schematic of the entire electrospinning process is given in 4.3b. The AVEs shared the same main source voltages with spinnerets and no auxiliary voltage source was used. The AVEs could also be moved along X and Y-axis to analyze their effect on producing the aligned PAN nanofibres.

Since the addition of AVEs have changed the optimized values of the input parameters, such as voltage, flow rate, concentration and spinneret collector distance, the electrospinning input parameters were re-examined with AVEs to study their effect on alignment, diameter and morphology. The range of selected electrospinning parameters and optimized values are shown in Table 4.1. These parameters were varied for producing PAN nanofibre mats with the fibre diameter to the range of 120-150 nm.

### Effect of AVEs

During electrospinning, the electrostatic force pulled the polymer drop into fibre jet from the spinneret to the collector. The fibre jet moved along a highly whipped path and was collected randomly over the width of the collector. However, the positioned auxiliary vertical electrodes (AVEs) between spinneret

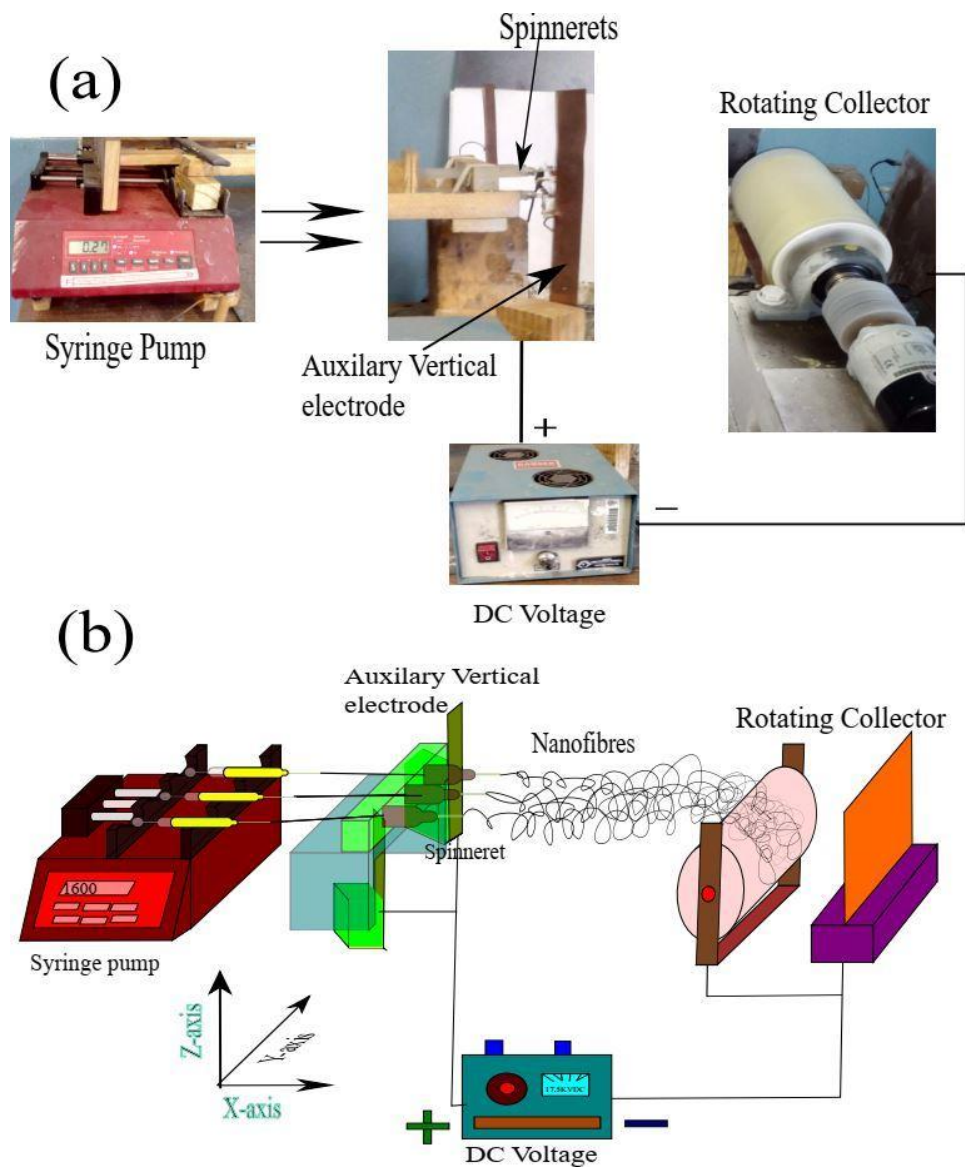


FIGURE 4.3: (a) Electrospinning with AVEs, (b) Schematic of electrospinning with AVEs

and collector in  $x - y$  plane (refer Figure 4.3) produced electrostatic force field, which reduced the PAN nanofibre whipping effect and produced more aligned PAN nanofibres mats.

In order to confirm the above phenomenon, an open source software, Electric Field was used to analyze the electrostatic force due to AVEs. The software developed electrostatic forces as electric field lines (green lines) between the spinneret and the collector. The whipping behaviour of the PAN nanofibre deposition schematically modelled using the Electric field software with AVEs are shown in Figure 4.4. The positive electrode at the spinneret is shown as a red colour, while the blue colour refers to the rotating collector as a negative electrode. The lines were directed from the spinneret to the entire width of the collector. As the electric field was not focused on the collector, the whipping effect deposited the PAN nanofibres randomly over the whole width of the rotating collector (Figure 4.4a).

However, after introducing the AVEs (Figure 4.4b), the polymer jet driving electrostatic forces between the spinneret and the collector was narrowed down towards the collector by the AVEs electric field. This phenomenon reduced the whipping effect and aligned the PAN nanofibres perpendicular to the collector axis. The AVEs position along the X and Y-axis added new parameters to the system as their position affected the PAN nanofibres production and its driving zone. The phenomenon of clogging was experienced when the auxiliary electrodes were placed between the spinnerets and the collector (forward of the line A'B') (Figure 4.5).

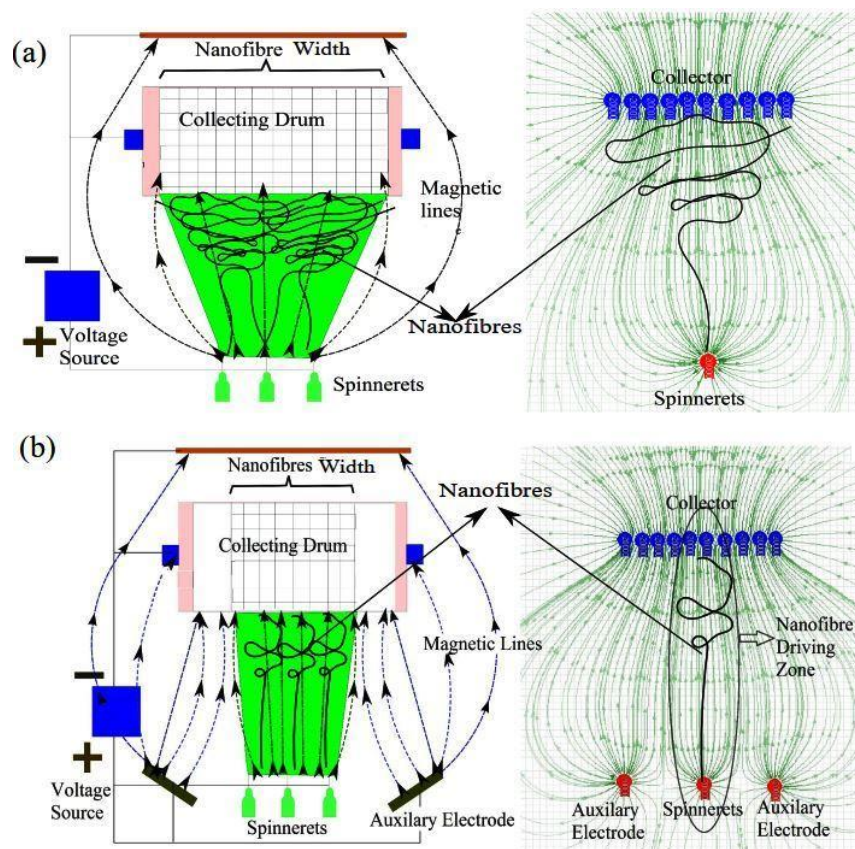


FIGURE 4.4: Effect of AVEs using electric field analysis

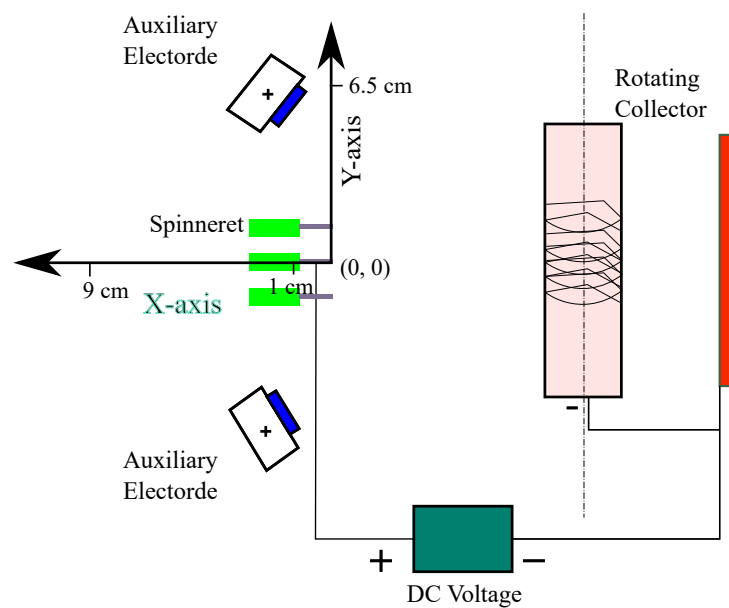


FIGURE 4.5: Top view schematic of modified electrospinning process

A Taylor cone was formed when the electrodes came in line with or behind the spinneret in the negative X direction. The driving zone became wider until the span became almost equal to the span generated in GES as the AVEs went behind the spinneret in the negative X direction. Figure 4.6 shows the span variation with the AVEs position along X-axis.

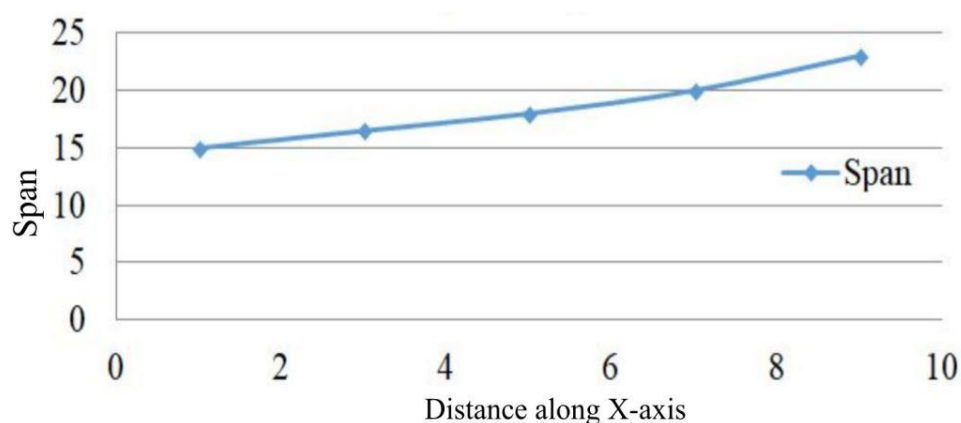


FIGURE 4.6: Span of PAN nanofibres vs AVEs position in negative X-direction

Similarly, the position of the AVEs along the Y-axis (Figure Figure 4.7) affected the span of the PAN nanofibres over the collecting drum. A minimum span of PAN nanofibres was observed at 6.5cm from the spinneret along Y-axis. When the distance between the AVEs and spinnerets along the Y-axis (Figure 4.5) reduced, the AVEs started acting as a single anode with spinnerets and the pattern of the electric fields gradually became similar to electrospinning without AVEs. Widening the positions of AVEs beyond 6.5cm along Y-axis caused a gradual increase in the span of PAN nanofibres over the collecting drum.

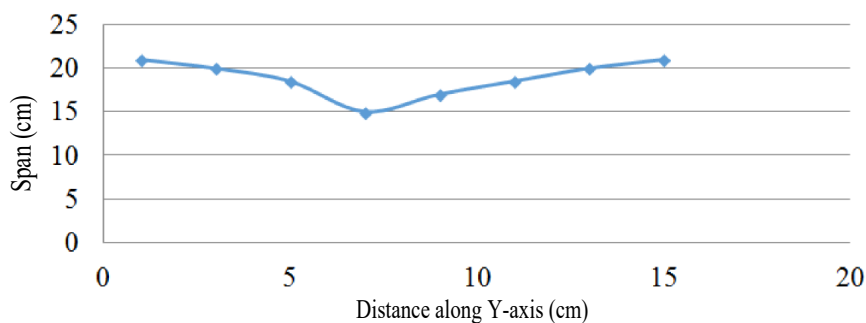


FIGURE 4.7: Span of PAN nanofibres vs AVEs position in Y-direction

It was observed that the distance and voltage of spinning also depend on the number of spinnerets. The fewer number of spinnerets, the higher the distance and lower the voltage. For the single spinneret, the spinning occurred at far distances of 35cm. When the second spinneret was added at the same distance, flow rate, and voltage, it disturbed continuous Taylor cone production and started dripping with slower rates. Voltage was raised to maintain the steady Taylor cone at a distance of 35cm. The addition of four more syringes required a very high voltage, which was unsafe for the supporting equipment; e.g. syringe pump and DC motors. The solution to this problem was found by decreasing the distance between the spinneret and the collector. Figure 4.8 shows the relation between the number of spinnerets and the distance of electrospinning.

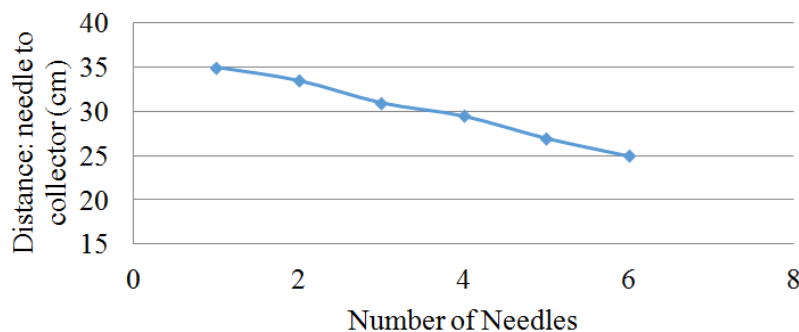


FIGURE 4.8: Spinneret-collector distance vs number of spinnerets maintaining simultaneously continuous jet issue from all six spinnerets

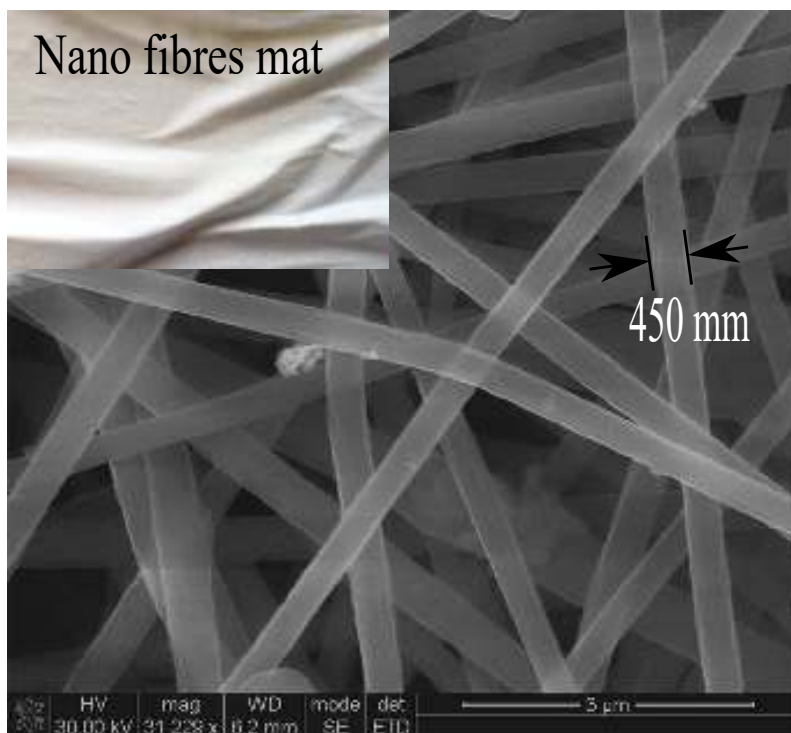
Another problem observed during the spinning process was the clogging of the polymer at the tip of the spinnerets due to misalignment. The positive charge of forwarding spinneret repulsed the polymer drop of the backward spinneret, which resulted in the non-emission of the jet from the backward spinneret. This problem was solved by aligning the tips of the spinnerets to each other and maintaining a minimum row distance of 2cm between spinnerets.

Figure 4.9 shows the camera images and scanning electron microscope (SEM) images of electrospun PAN nanofibre mats and the effect of AVEs could be seen from the SEM images (refer Figure 4.9b). Due to the AVEs electric field, the whipping effect of the PAN nanofibres was reduced and thus produced aligned PAN nanofibre mats. The smaller diameter and aligned PAN nanofibres have greater advantages as reinforcement in producing nano strengthened hybrid composites due to their high aspect ratio and orientation.

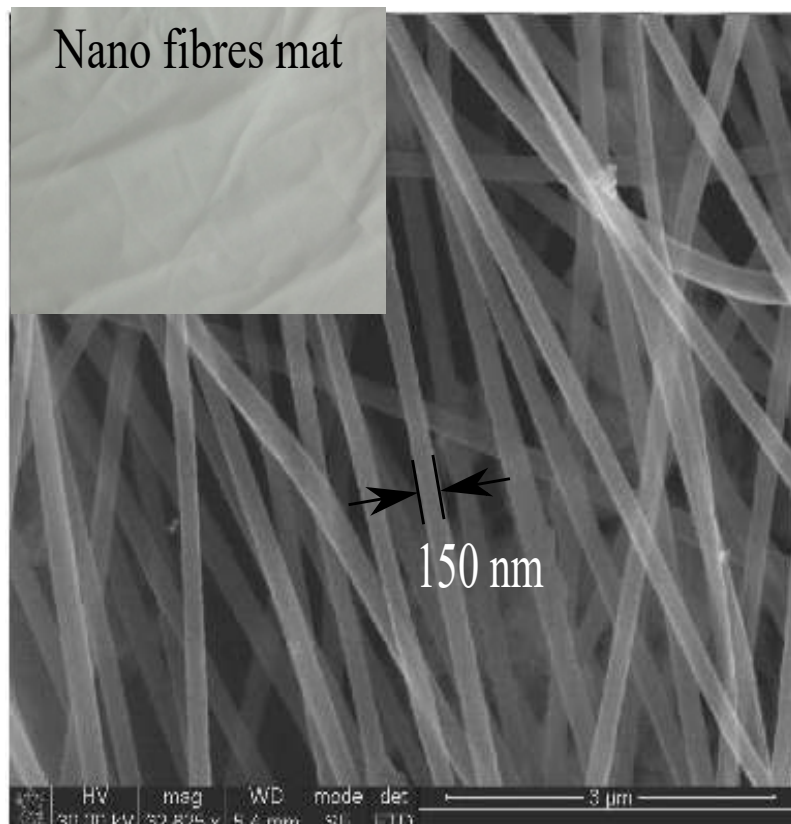
### **Manufacturing of PAN nanomats and SWCNTs doped nanomats**

As discussed, the PAN polymer solution was electrospun to produce nanofibers mat. The selected concentration of PAN-DMF solution (8.1%) was prepared by mixing the measured weight of PAN polymer to the same volume of solvent DMF. The solution was stirred mechanically along with heating for 24 hours. The electrospun syringe pump with six luer lock syringes (3 ml) was filled with the PAN-DMF solutions and the solution was electrospun into desired volume fractions (0.1%, 0.2%, 0.5% and 1%) over the glass fibre mats attached on to the collector drum.

For the doped nanofibers mat, the 0.25% volume fraction of pristine or functionalized SWCNTs were dispersed into the DMF solvent using magnetic stirrer and ultrasonication. Before sonication, the volume of solvent and weight of



(a) Random Nanofibres Mat



(b) Aligned Nanofibres Mat

FIGURE 4.9: Electrospun PAN nanofibre mats

the f-SWCNTs were measured corresponding to the volume fraction of 0.25%. Subsequently, the polymer (PAN) was poured into the SWCNTs/DMF solution and stirred mechanically along with heating for 24 hours. Thereafter, the doped PAN/DMF solution was electrospun over the glass fibre mats, which were used to manufacture the nanostrengthened hybrid composites.

### 4.1.2 Composites manufacturing process

The composites were fabricated using a vacuum assisted resin transfer moulding (VARTM) method (Figure 4.10). The fibre composites were manufactured using Bisphenol-A (AMPREG 21) epoxy resin with woven E-glass fibre volume fractions of 16%, 24%, 32% and 40%. The optimized 32% glass fibre composites were further strengthened using the following PAN nanofibre mats as discussed before for producing nanostrengthened hybrid composites:

1. 0.1, 0.2, 0.5, and 1% volume fractions of randomly distributed PAN nanofibre mats
2. 0.5% volume fractions of aligned PAN nanofibre mats
3. Pristine SWCNTs doped aligned PAN nanofibre mats
4. Functionalized SWCNTs doped aligned PAN nanofibre mats.

At the beginning of the manufacturing process, VARTM mould parts were cleaned with acetone and dried with a cloth. Several thin coats of releasing agent (NCA Waxol) were applied to the mould surfaces for easy removal of the cured products. Three pieces mould was used in the composite manufacturing; female square steel ring, upper and lower male plates. Male plates were provided with O-ring grooves to provide a stable vacuum during the process.

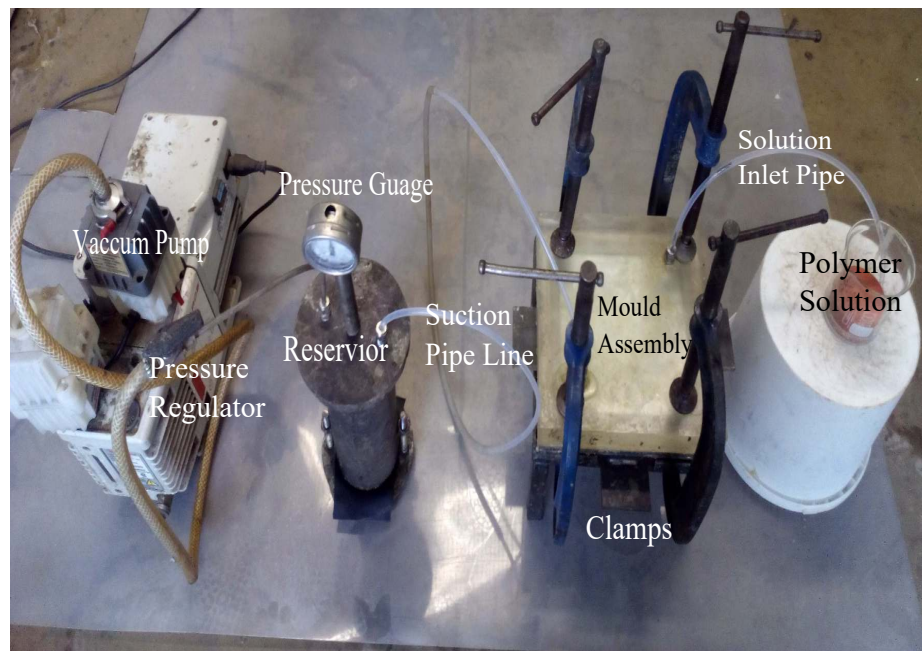


FIGURE 4.10: VARTM system

First, the lower male plate was positioned on a mould stand. After this, the female square steel ring was placed over the lower male plate and then before closing the mould with an upper male plate, seven fibreglass mats equivalent to the required fibre volume fraction were placed inside. The mould assembly was fastened using C-clamps to prevent vacuum break.

Suction and as riser port of the mould were connected through pipes to the resin reservoir and vacuum pump respectively. After setting up the VARTM assembly, the resin-hardener was mixed with a volume ratio of 100:38 and placed at the suction port. Then the vacuum pressure valve was opened slowly and a pressure of 80 psi was maintained until the resin fills the mould. Both suction and riser ports were closed after filling and then the resin was cured for 24 hours at room temperature. Figure 4.11a shows the manufactured preform which was machined into tensile, bending and impact test specimens (Figure 4.11b).

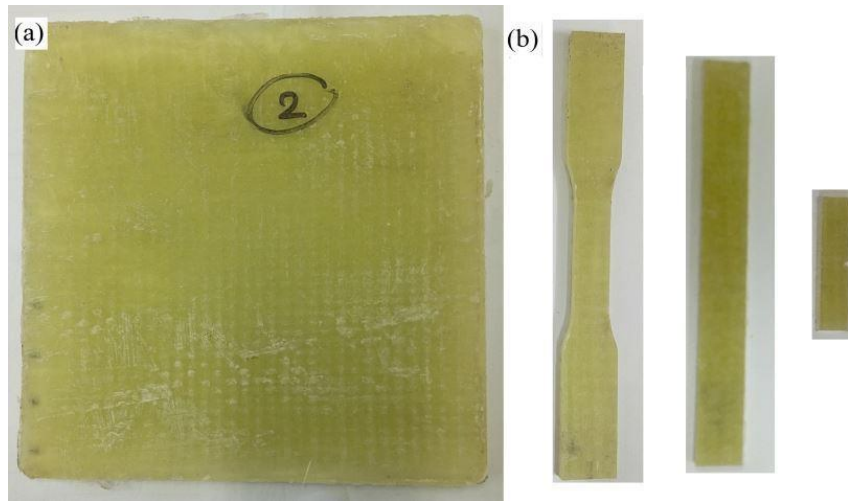


FIGURE 4.11: Composite preform and testing specimens

### 4.1.3 PAN nanomats strengthened hybrid composites

The similar procedure was followed for producing nanomats strengthened hybrid composites except that the alternative layers of glass fibre mats and electrospun nanofibers mats were placed. As discussed before, four different volume fractions, 0.1%, 0.2%, 0.5% and 1% of randomly oriented PAN polymer nanofibre mats were used with 32% glass fibre for manufacturing the PAN nanomats strengthened (random nanofibre) hybrid composites. Based on the mechanical properties of the random PAN nanofibres mat strengthened hybrid composites, the volume fraction of PAN polymer with better properties was selected to manufacture aligned and SWCNTs doped PAN nanofibre mats. For the current analysis, 0.5% volume fraction of PAN polymer was selected to produce the multiscale nano hybrid composites.

However, for doping, only 0.25 vol% SWCNTs was selected based on the results from Pilehrood et al. [188]. Their results showed that the addition of SWCNTs more than 0.25 vol% with the PAN/DMF solution (1.2 Pa. sec)

have drastically increased the viscosity of the PAN/DMF solution resulted in beaded electrospun fibres with larger diameters. Therefore, to achieve the doped PAN nanofibres diameter similar to the PAN nanofibre without SWCNTs, the maximum amount of 0.25% volume fraction of SWCNTs was added to the PAN/DMF solution for manufacturing SWCNTs doped aligned PAN nanofibre mats. Both the pristine and functionalized SWCNTs were used for producing the SWCNTs doped PAN nanofibre mats.

## 4.2 Results and Discussion

The glass fibre, randomly and aligned PAN nanofibre mats and SWCNTs doped aligned PAN nanofibre mats composites were experimentally characterized and only relevant results are presented below and details are presented in Appendix [A.1](#).

### 4.2.1 Glass fibre composites

Figure [4.12](#) shows the result of tensile strength and modulus, flexural strength and modulus, and impact resistance of the glass fibre composites. It is evident from the results that the increase of fibreglass volume fraction up to 32% have gradually increased the mechanical properties of the glass fibre composites. Further addition of fibre volume didn't show any appreciable increase in the composite properties. The addition of glass fibre mats improved the load resistance of the composite by transferring the load from resin to the glass fibres

A micrograph (Figure [4.13](#)) of 32% glass fibre composite shows the fractured surface of the tested specimen. The image further confirmed that there was a

load transfer from the matrix to the fibres which was confirmed by fibre pull-outs and breakage before the final fracture. Basically, the increase in volume fraction of glass fibres from 16% to 32% reduced the matrix rich regions gradually, which resulted in the improved mechanical properties of the composite. However, when the volume fraction of glass fibres was increased to 40%, there was not a noticeable increase in the mechanical properties. It could be related to the poor penetration of resin into the fibreglass mats and their agglomeration. For tensile, bending, and impact test, the similar trends were observed. Therefore, 32% volume fraction of glass fibre composite was chosen for further experimental study.

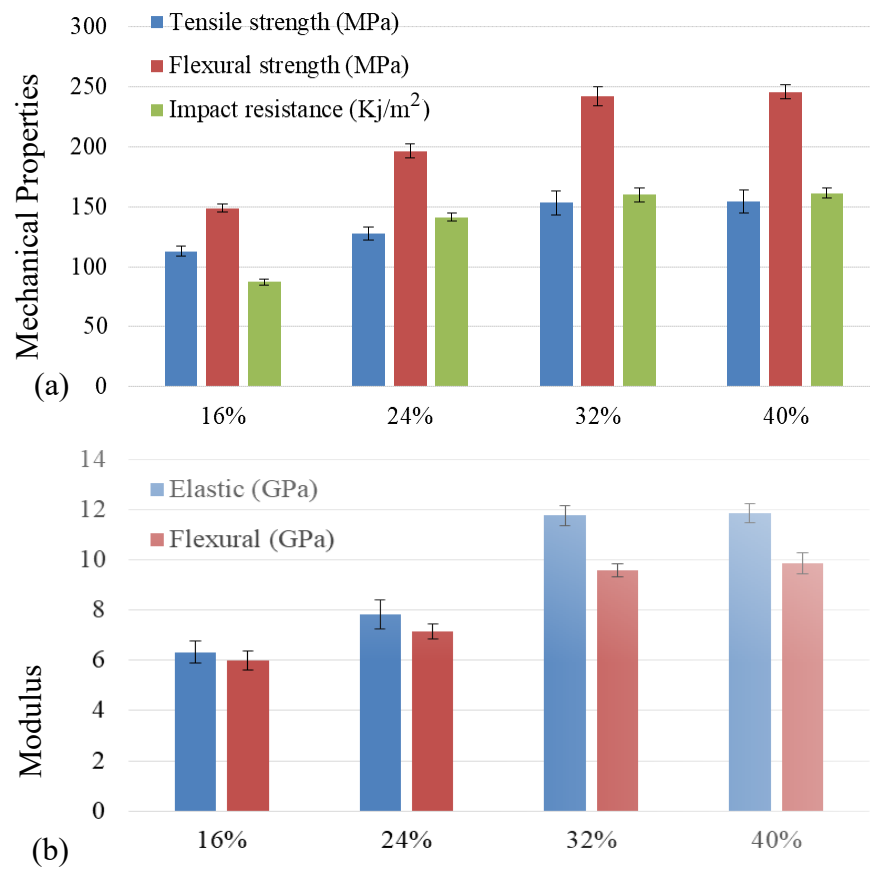


FIGURE 4.12: Properties of composites with different volume fraction of glass fibres

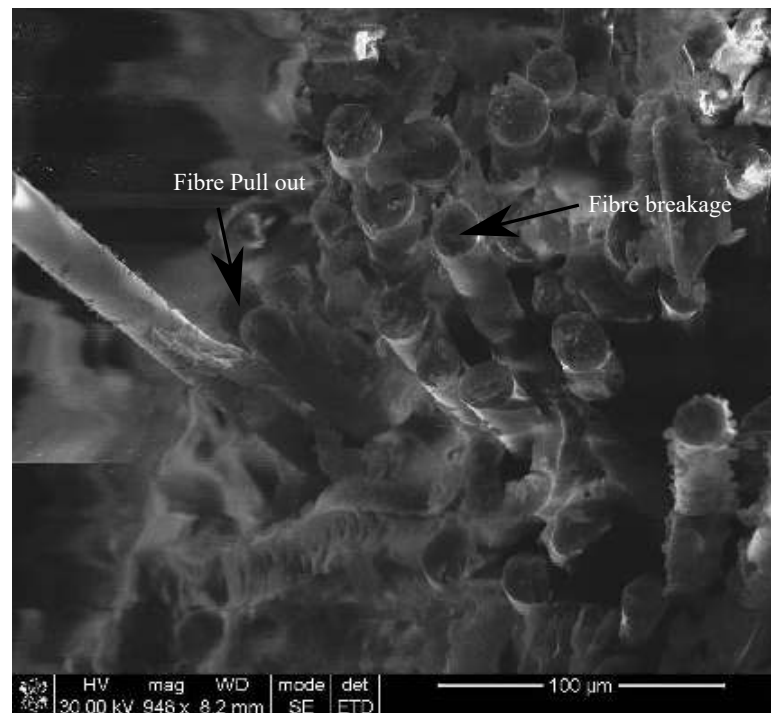


FIGURE 4.13: SEM image of 32% glass fibre composite fractured specimen

## 4.2.2 Random PAN nanofibre mats strengthened hybrid composites

### Tensile test results

The 32% glass fibre composite was then used as a reference to determine and optimize the effect of 0.1%, 0.2%, 0.5%, and 1% volume fractions of randomly oriented PAN nanofibre mats. Figure 4.14 shows tensile strength and elastic modulus of randomly oriented PAN nanofibre mats strengthened hybrid composites and the tensile properties were increased by the addition of randomly oriented PAN nanofibre mats. Though a very scanty increase in properties was seen for the initial addition of 0.1%, a phenomenal increase of 62.14% was observed for the addition of 0.5% random PAN nanofibre mats. The increase in

tensile properties could be attributed to the reinforcing effect of PAN nanofibre mats due to their nanosizes, improved molecular orientation during the electrospinning process and bridging effect within the interlaminar region.

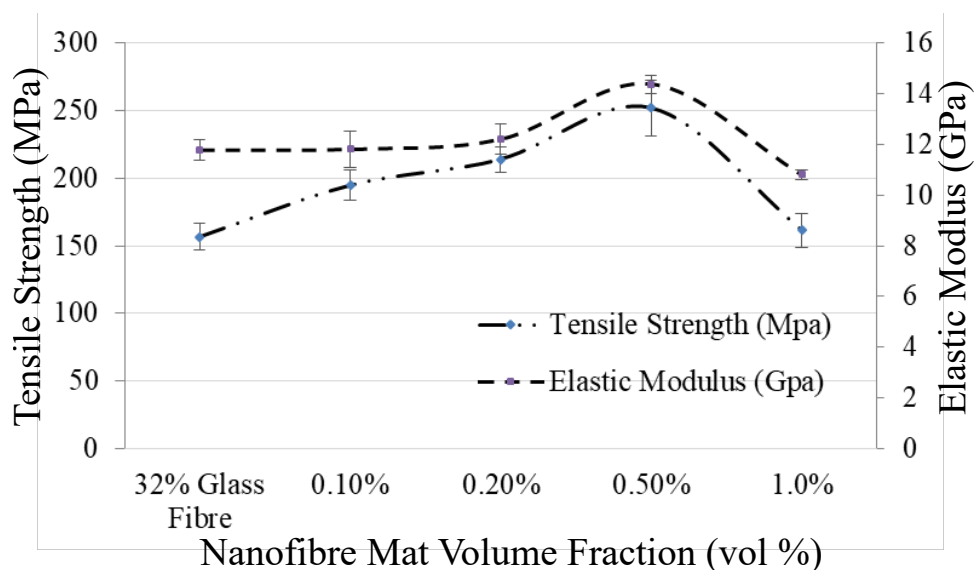


FIGURE 4.14: Tensile properties of random nanofibre mats strengthened hybrid Composite

Since the nanosized electrospun PAN fibres have the higher surface area, it has resulted in increased contact area within interlaminar regions. Thus the infused PAN nanofibre mats provided more resistance during PAN nanofibres breakage or pullout. This phenomenon has transferred the applied load from the matrix to the PAN nanofibres within the interlaminar regions before transferring the load to the macrofibres. Secondly, due to the improved molecular orientation during the electrospinning whipping process, the PAN nanofibres have obtained better tensile strength by which the PAN nanofibres provided more resistance during the relative slippage as the matrix delaminated over the PAN nanofibre mats by transferring the applied load (refer Figure 4.15a). In addition, the geometrical web network of PAN nanofibre mats within the matrix has provided bridging between the glass fibres to the matrix as shown

in Figure 4.15b and thus increased the resistance to the applied load and improved tensile properties.

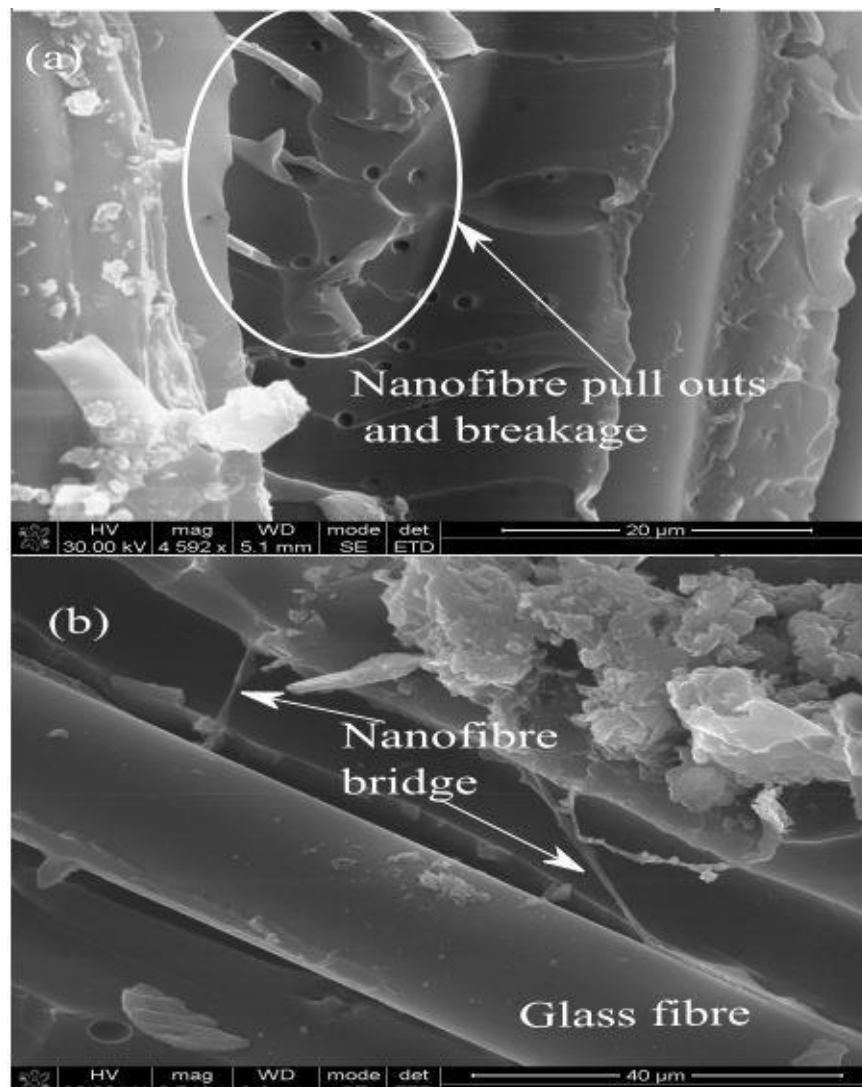


FIGURE 4.15: Fracture behaviour of 0.5% volume fraction random PAN nanofibres mat (a) Nanofibres pullout and breakage (b) Nanofibres bridging

However, a similar effect was not observed as the random PAN nanofibre volume fraction was increased from 0.5% to 1%. This may be associated with the PAN nanofibre agglomeration and poor penetration of resin into the PAN nanofibre mat which might have acted as stress concentration sites. Figure

4.16 provided evidence of agglomerated PAN nanofibres within the interlaminar regions.

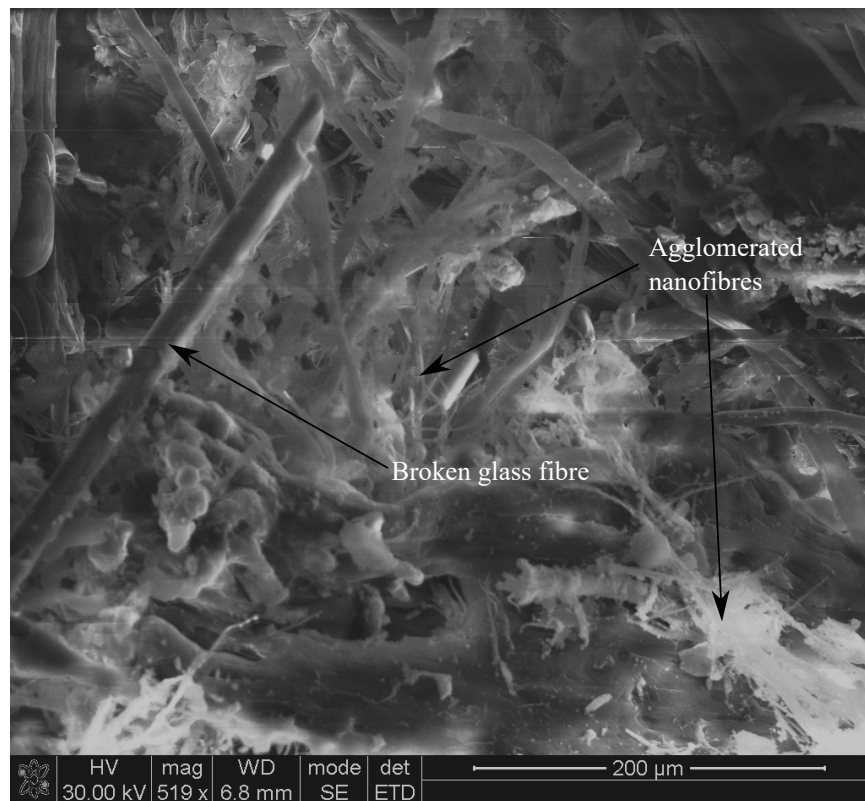


FIGURE 4.16: Agglomerated PAN nanofibres in the fractured surface of 1% random PAN nanofibres mat strengthened hybrid composite

### Flexural test results

Figure 4.17 shows the flexural properties of random PAN nanofibres mat strengthened glass fibre hybrid composites. It could be seen that the addition of randomly aligned PAN nanofibre mats has improved the flexural properties of 32% volume fraction of glass fibre composites. The addition of 0.1% volume fraction of nanomats has increased the flexural properties of the glass fibre composites to 13.073% and have gradually increased and reached a maximum of 67.199% for the addition of 0.5% volume fraction of random PAN nanofibre mats.

The improved flexural properties electrospun PAN nanofibres strengthened hybrid composite could be attributed to the interpenetrated network of PAN nanofibre mats into the rich matrix regions. The PAN nanofibres mat might have improved the bonding between the matrix and the glass fibre mat in such a way that the shearing interlaminar plane between the glass fibre and the polymer could have strengthened by the infused PAN nanomats. This phenomenon can be observed in Figure 4.18 which shows a pulled PAN nanofibre having a small piece of matrix. However, the increasing trend of the flexural properties was reversed for the addition of 1% volume fraction of random PAN nanofibre added. The reason behind the reduction may be associated with agglomeration of PAN nanofibres as explained before.

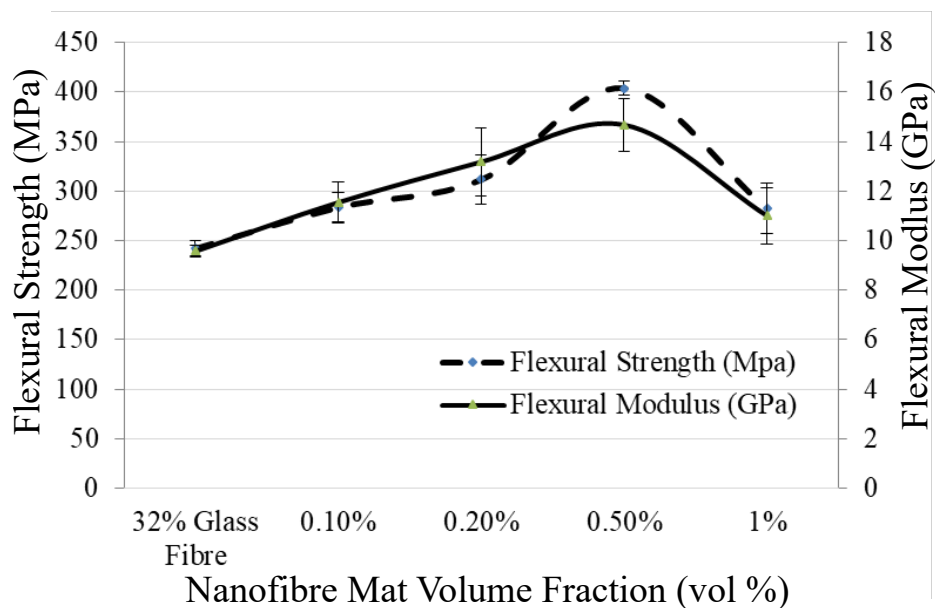


FIGURE 4.17: Flexural properties of random PAN nanofibre mats strengthened hybrid composite

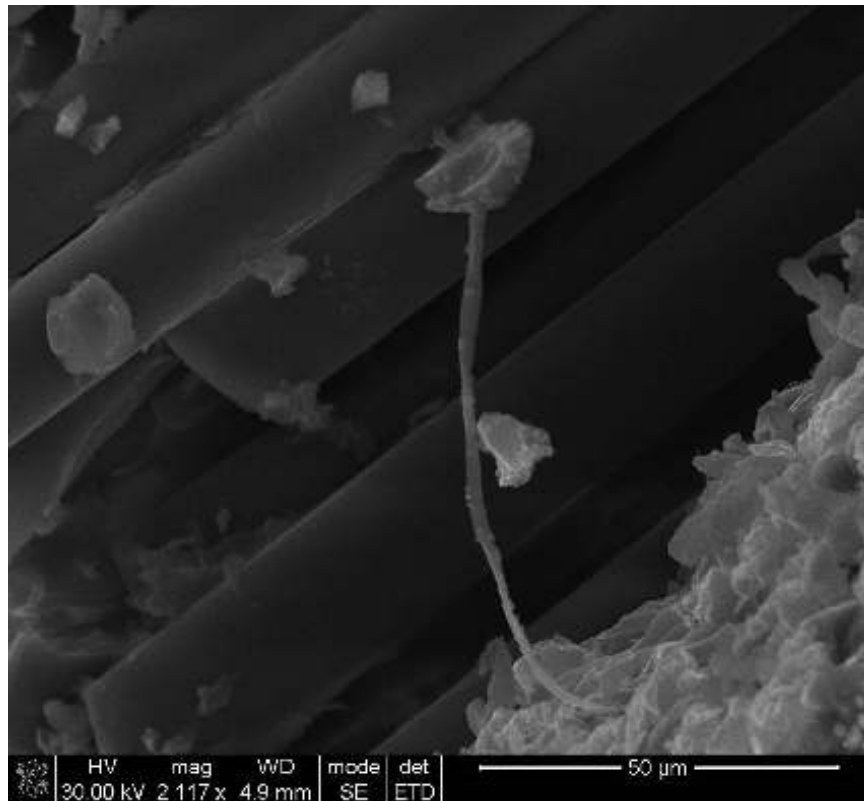


FIGURE 4.18: SEM image of bending tested 0.5% random PAN nanofibre mats strengthened hybrid composite

### Impact resistance

Figure 4.19 shows impact resistance of the PAN nano mats strengthened hybrid composite. The Impact resistance of 32% fibreglass composite was gradually increased with the addition of random PAN nanofibre mats. The 0.1% volume fraction random PAN nanofibre has increased the impact resistance to 5.391% and a further increase in random PAN nanofibre mats has gradually increased the impact resistance to a maximum value of  $193.112 \text{ KJ/m}^2$  for the addition of 0.5% random PAN nanofibre mats respectively.

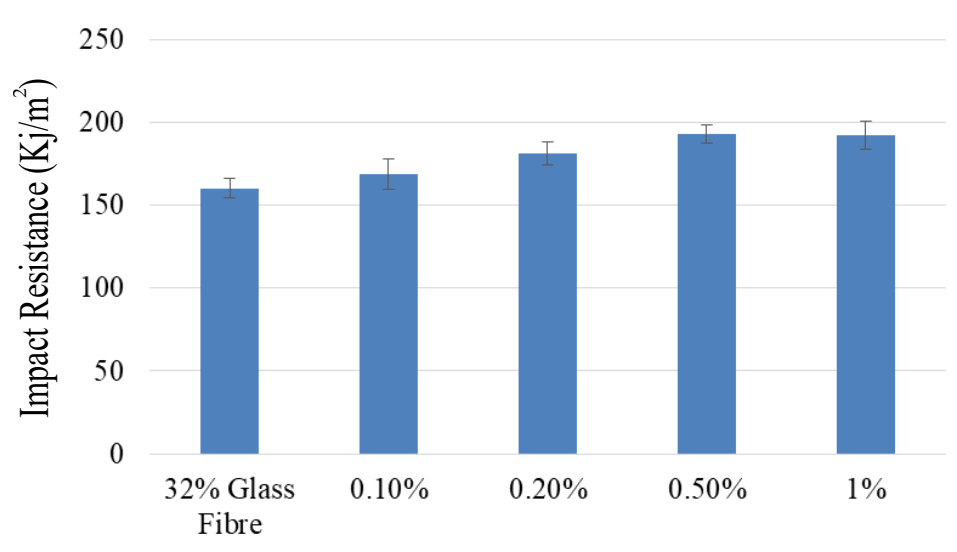


FIGURE 4.19: Impact resistance of random PAN nanofibre mats strengthened hybrid composites

Increased impact resistance could be the result of distributed PAN nanofibres network within the matrix interlaminar region, which held the matrix firmly and provided more resistance to the applied load. The elongated PAN nanofibres attached to the fractured glassfibres confirmed (Figure 4.20) that the applied load was transferred to the random PAN nanofibres mat nanofibre network from the matrix before moving to the glass fibres within the interlaminar region. However, a lower impact resistance was shown for 1% volume fraction of random PAN nanofibres which might be associated with poorly mixed matrix due to the agglomerated nanofibres.

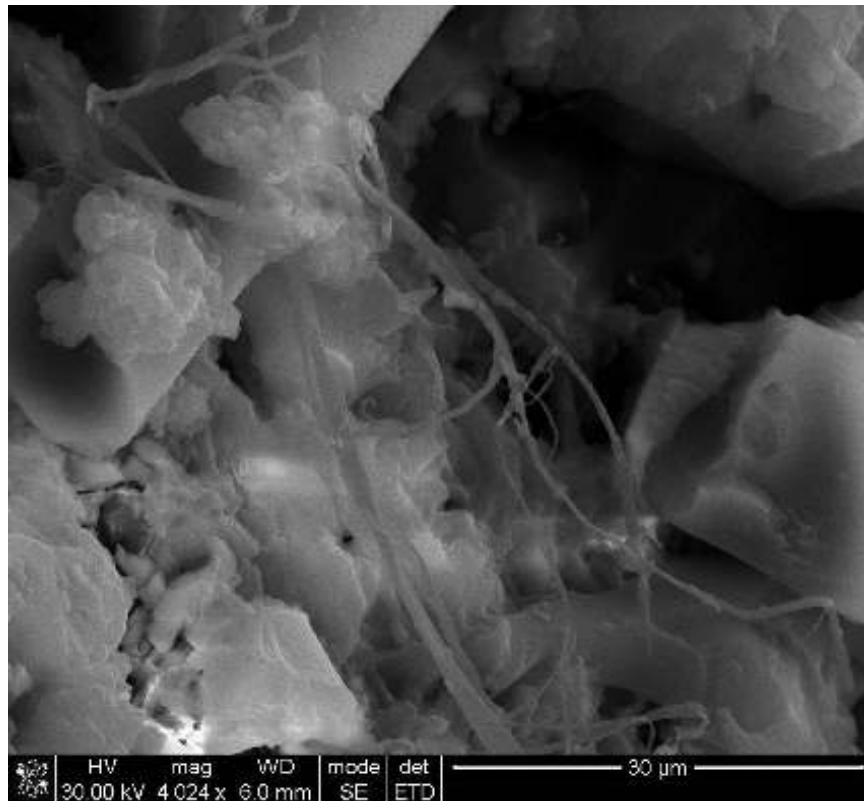


FIGURE 4.20: SEM image of fractured surface of impact tested of 0.5% random PAN nanofibre mats strengthened hybrid composites

### 4.2.3 Aligned and SWCNTs doped PAN nanofibre mat strengthened hybrid Composites

Based on the results from randomly oriented PAN nanofibre strengthened hybrid composites, 0.5% volume fraction of PAN nanofibre mats was selected for producing aligned PAN nanofibres mat, pristine-SWCNTs, and functionalized-SWCNTs doped PAN nanofibre mats. For doping, the volume fraction of 0.25% SWCNTs was selected for producing pristine-SWCNTs (p-SWCNTs) and functionalized-SWCNTs (f-SWCNTs) PAN nanomats.

## Tensile test results

The tensile properties of aligned PAN nanofibres mats, p-SWCNTs and f-SWCNTs doped PAN nanofibres mats are shown in Figure 4.21. The aligned PAN nanofibre mats have increased the tensile strength and elastic modulus of neat glass fibre composite by 68.91% and 32.78% respectively. Thus the aligned PAN nanofibre mats provided more strength to the neat glass fibre composites than randomly oriented PAN nanofibre mats by 6.77% (tensile strength) and 10.79% (elastic modulus). This increase can be attributed to the molecular orientations, reduction in PAN nanofibres diameter and uniform distribution due to AVEs.

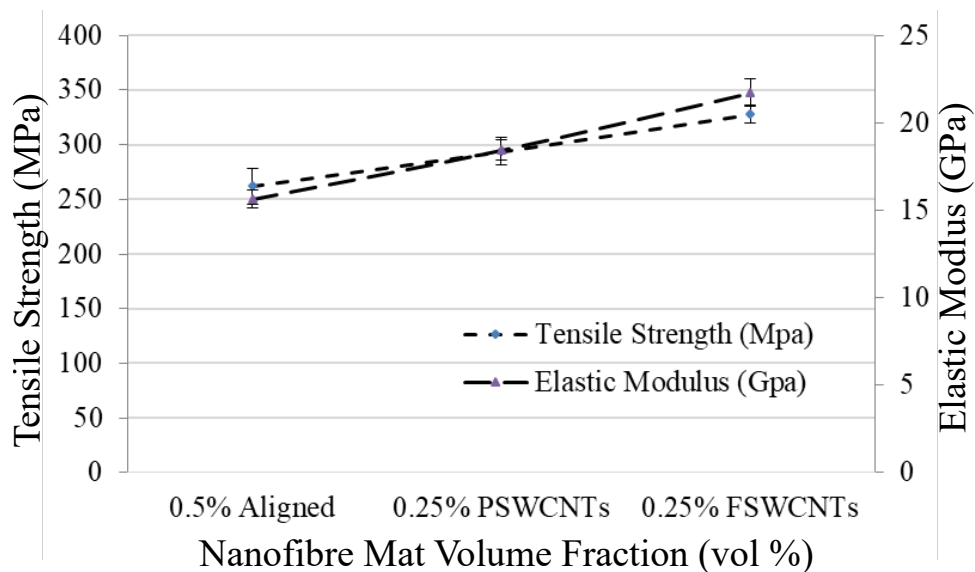


FIGURE 4.21: Tensile test results for aligned and doped PAN nanofibres mat strengthened hybrid composites

As discussed by Naraghi [207], the Molecular orientation of PAN nanofibres

depends on spinneret-collector distance and polymer viscosity. During electrospinning, the spinneret-collector distance was set at 25 cm, which has substantially reduced the solvent content and increased the polymer viscosity. Reduced solvent restricted the oriented PAN molecules from the relaxation and resulted in permanent molecular orientation. Rheologically, increased viscosity along with jet thinning under electrostatic force resulted in higher shear stresses which unwound and stretched the polymer molecules to produce higher molecular orientations. Better molecular orientation and smaller diameter of PAN nanofibres mat improved the tensile strength and modulus when infused into the interlaminar region.

Moreover, the increased spinneret-collector distance also reduced the diameter of the PAN nanofibre from 450 *nm* to the 150 *nm*. Thus, the three times reduction in diameter of aligned PAN nanofibres provided approximately three times larger network within the interlaminar region. Increased length of PAN nanofibres network provided more uniform distribution and resulted in improved tensile properties. Alignment of PAN nanofibres mat is another aspect which provided better strength to the interlaminar regions. By comparing both random and aligned PAN nanofibre mats strengthened hybrid composites fractured surfaces (refer Figure 4.22a & b), the agglomerated nanofibers from random PAN nanofibre (broken heads of PAN nanofibres) are clearly visible in Figure 4.22a. This phenomenon could be a result of uneven distribution (agglomerations) and random orientation of nanofibers which could have been the reason for lower strength of hybrid composites. On the other hand, the aligned PAN nanofibres mat with a reduced diameter and improved distribution have produced the hybrid composites with improved properties as seen in Figure 4.22b.

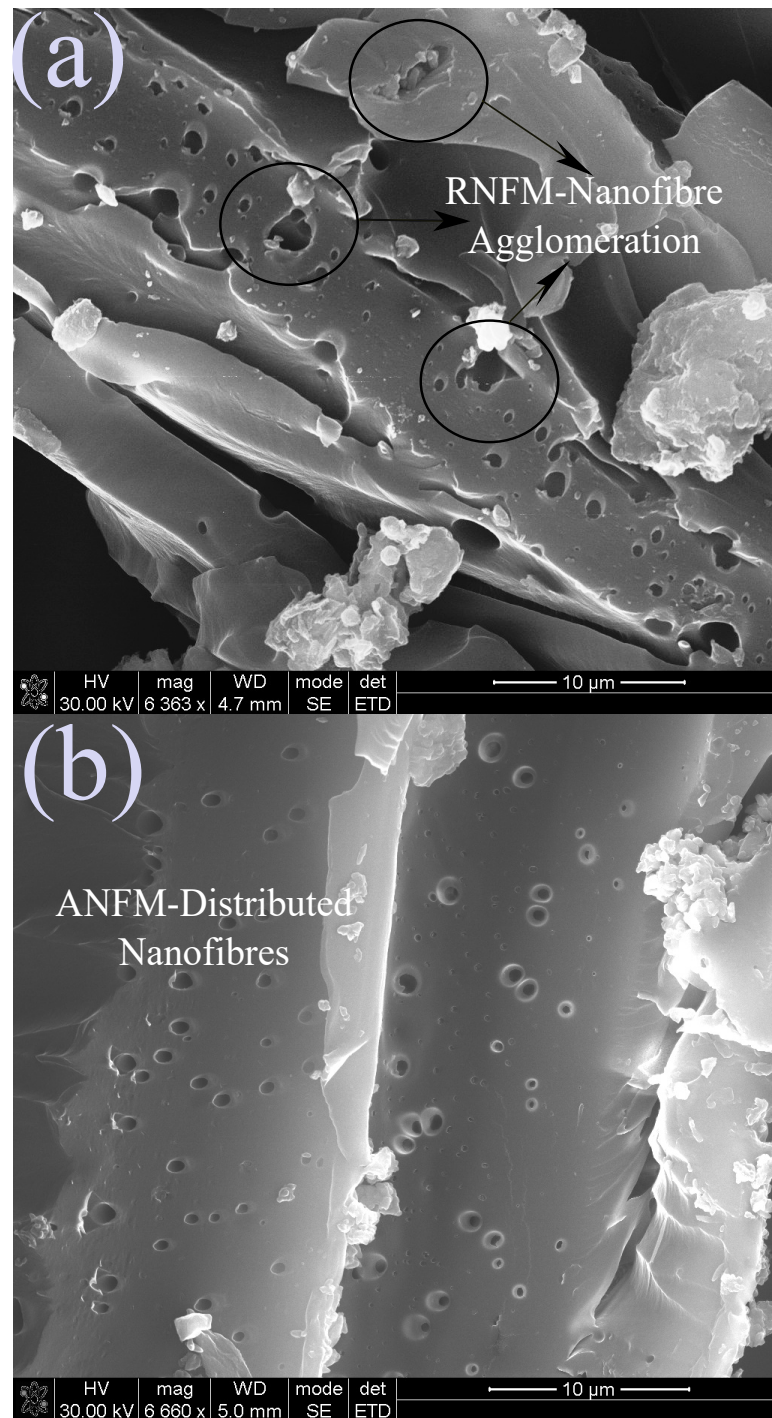


FIGURE 4.22: Fracture surfaces obtained in tensile tests; (a) random PAN nanofibre strengthened hybrid composite, (b) aligned PAN nanofibre mat strengthened hybrid composite

A more magnified image of a fractured surface (refer Figure 4.23) has shown the elongated broken heads of PAN nanofibres, which proved that the load transfer between the matrix to the PAN nanofibre mats has occurred before failure. A similar result was reported by Hannah [163], where a sheet of Poly(-caprolactone) (PCL) aligned PAN nanofibers was manufactured to mimic the human body tendons and ligaments which showed higher strength than the sheet developed from the random PAN nanofibres.

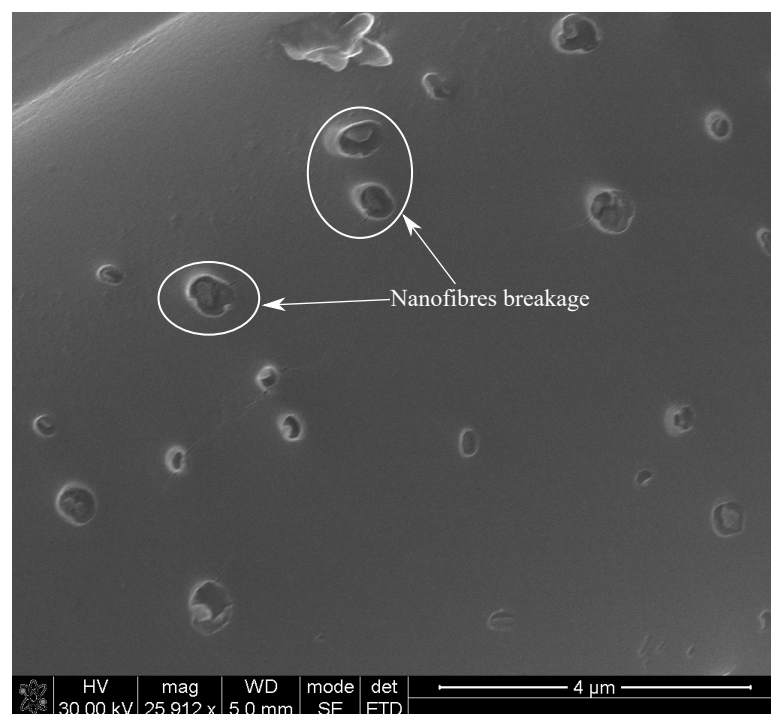


FIGURE 4.23: Broken PAN nanofibres in the fractured surface 0.5% aligned PAN nanofibres mat strengthened hybrid composite obtained in tensile tests

Aligned PAN nanofibres mat strengthened composite was manufactured using optimum volume fraction obtained from the random PAN nanofibres mat

---

strengthened hybrid composite which results were discussed previously. Further SWCNTs doped aligned PAN nanofibres mat with p-SWCNTs and f-SWCNTs with the volume fraction of 0.25% were used to fabricate the multiscale nanohybrid composite. A similar procedure of manufacturing was used as explained for the glass fibre composites. Volume fractions of 0.25% of pristine and functionalized SWCNTs were pre-dispersed into the polymer solution. The solutions were electrospun into aligned PAN nanofibre mats which were used to develop multiscale nanohybrid composites.

Previous studies [208, 209] have shown that the addition of pristine CNTs has reduced the strength of the interlaminar region rather than supporting. The cause of reduced properties were the agglomerated CNTs due to strong inter-atomic forces. Agglomerated bundles contained a large number of CNTs without any bonding with polymer and connected to each other through weak Van der Waals forces. These bundles served as a void in polymer where stresses concentrated and failure occurred at lower values of loads. Contrary to these studies, the alignment and the confinement of PAN nanofibre into the thinner diameter of PAN nanofibres helped in the better distribution of p-SWCNTs which is reflected as an increase in tensile strength (87.6%) and elastic modulus (56.6%) respectively.

In order to determine the strengthening mechanism of doped PAN nanofibres, SEM images of fractured surfaces of aligned, pristine and functionalized SWCNTs doped PAN nanofibres were compared. In case of aligned PAN nanofibres mat, the fractured surface was smooth along with the pull outs and broken heads which are seen in Figure 4.23. It indicated that the initiated crack took growth along a certain plan without any branched cracks and the growing crack was only resisted by the pullout and breakage of PAN nanofibres within the interlaminar region.

Whereas, the fractured surface (Figure 4.24) of the MNHC has the uniformly distributed array of the p-SWCNTs doped aligned PAN nanofibres along with several nano/microcracks. These cracks show the load distribution in the different directions and energy absorption during the crack initiation and growth. Therefore, it can be inferred that these nano/micro cracks were developed during the tensile test which provided a branched path to the applied load due to the resistive strength of doped PAN nanofibre mats. However, the five specimens of p-SWCNTs doped showed maximum variation (Figure 4.27) as compared to all other composites. This variation may be contributed to the pristine nature of SWCNTs and different rate of agglomeration in the five specimens.

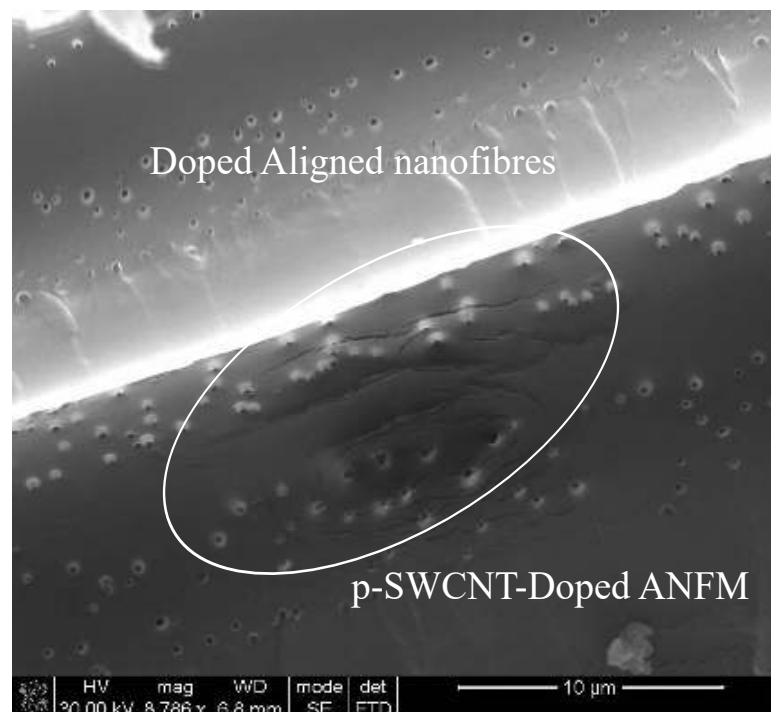


FIGURE 4.24: Fracture surfaces p-SWCNTS doped aligned PAN nanofibre mat strengthened hybrid composite

Figure 4.25 shows the SEM image of the fracture surface of f-SWCNTs doped

aligned PAN nanofibre mat composite. The f-SWCNTs doped aligned PAN nanofibre mat composite surface showed many time more cracks around the PAN nanofibres developed during the tensile tests. It can be seen that cracks were initiated within the matrix but the presence of f-SWCNTs PAN nanofibres branched the crack into many nanocracks. The f-SWCNTs doped PAN nanofibres mat not only prevent the matrix separation as big chunk by developing nano crack but it also stopped, reduced or diverted the propagation of cracks during the tensile test. This can be evident from the Figure 4.26. The cracks are ended or either diverted due to the PAN nanofibre as shown in Figure 4.26 (sites 1 and 2). While at site 3 the crack travelled across the empty hole after the pull out of the fibre. In all other cases (random and aligned PAN nanofibres mat, and p-SWCNT doped aligned PAN nanofibres mat) only smooth surface or few cracks were observed.

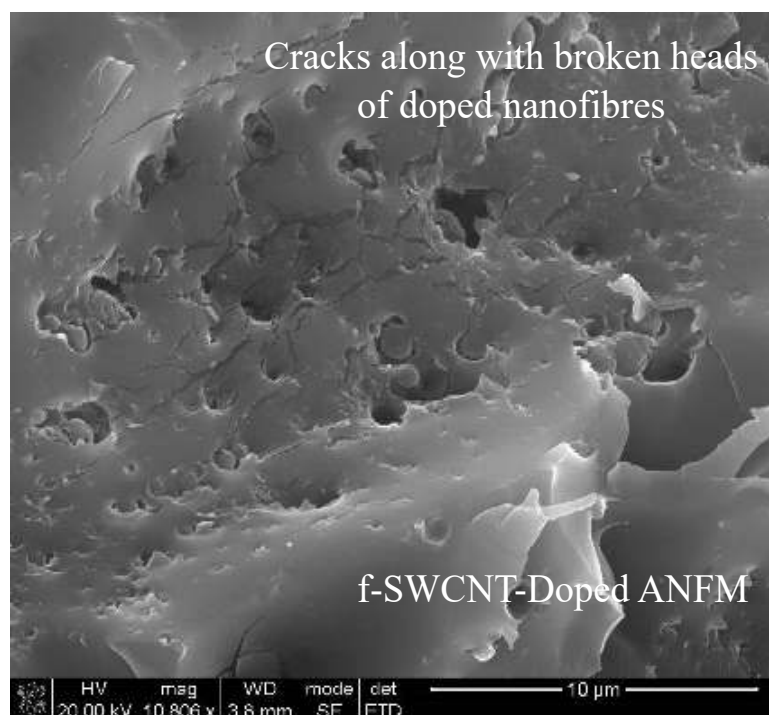


FIGURE 4.25: Fracture surfaces of f-SWCNTs doped aligned PAN nanofibre mat strengthened hybrid composite

Therefore, increased mechanical properties of hybrid composite strengthened with different PAN nanofibres mats can be described as a resistive network to the developing large cracks within the interlaminar regions. The effect of f-SWCNTs doped aligned PAN nanofibre mat was reflected as increase in tensile strength and elastic modulus up to 109.45% and 84.5% respectively. Tensile graphs obtained for the f-SWCNTs doped aligned PAN nanofibre mat composite were the most similar to each other with a minimum standard deviation of 15.66 MPa and 1.61 GPa in tensile strength and elastic modulus as compared to the other composites (Figure 4.27). This also confirmed the effectiveness of aligned PAN nanofibre mat as a carrier for SWCNTs and FC alkylation functionalization.

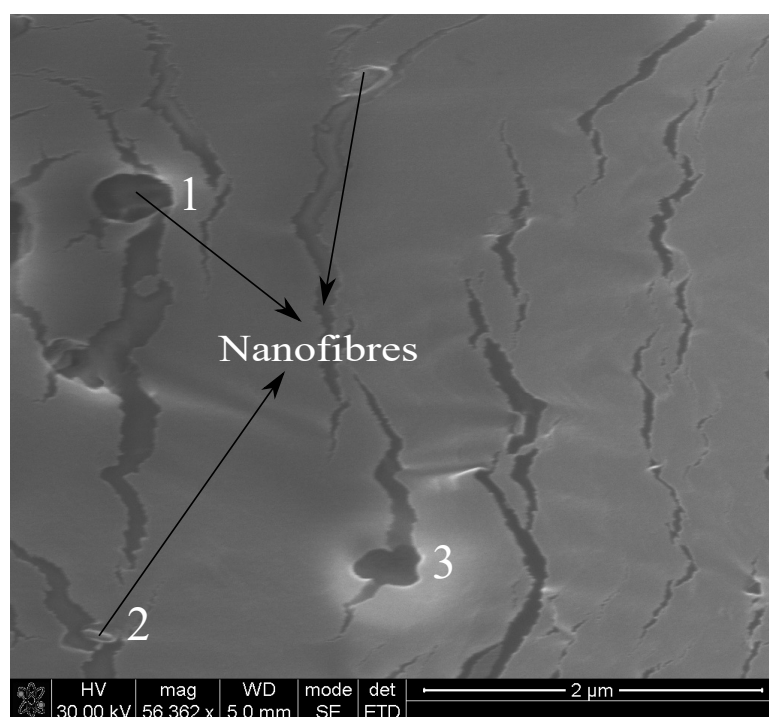


FIGURE 4.26: Nanocracks on the fractured surface of f-SWCNTs doped aligned PAN nanofibre mat strengthened hybrid composite

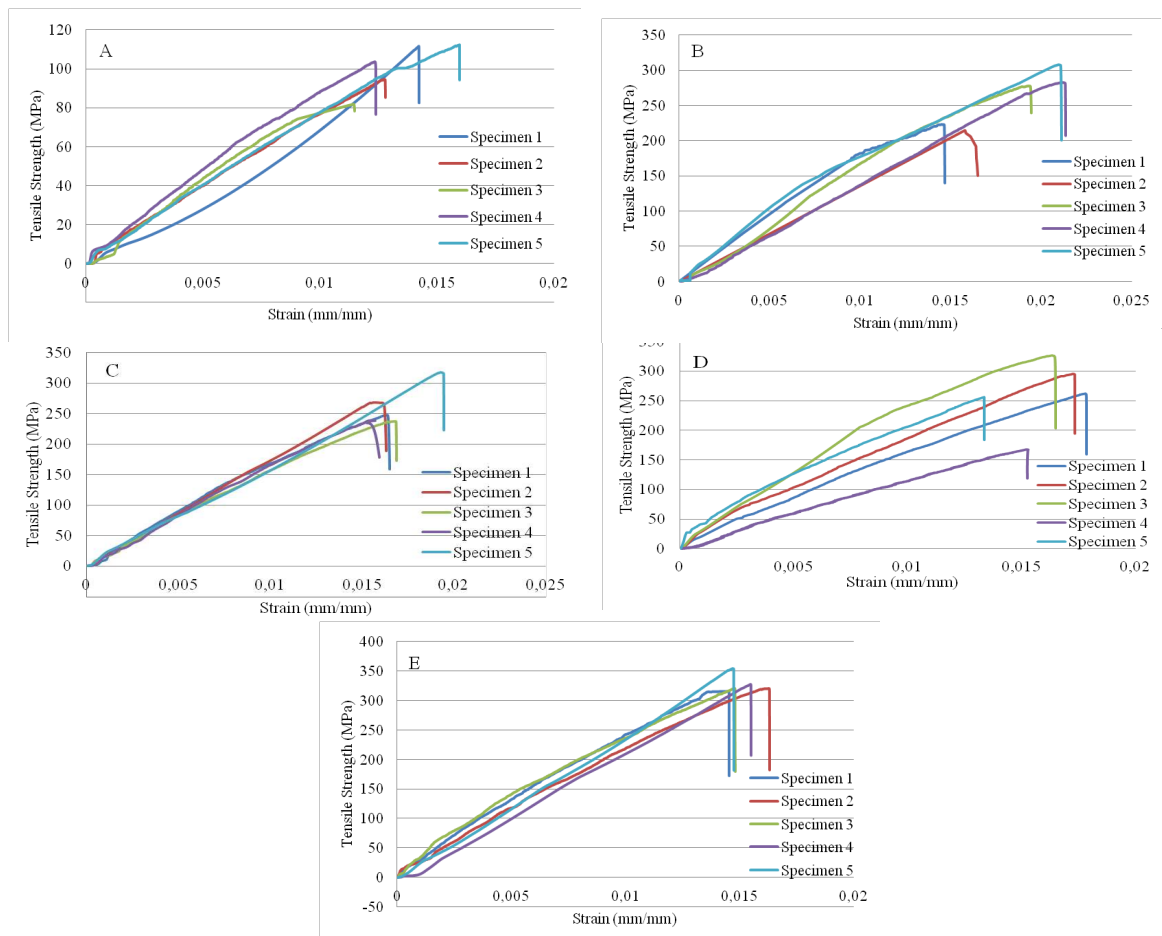


FIGURE 4.27: Batch wise tensile test results; A: 32% glass fibre composite (GFC), B: 0.5% random PAN nanofibres mat strengthened GFC, C: 0.5% Aligned PAN nanofibre mat strengthened GFC, D: p-SWCNTs doped 0.5% aligned PAN nanofibre mat strengthened GFC, E: f-SWCNTs doped 0.5% aligned PAN nanofibre strengthened GFC

Effect of different PAN nanofibres mats was also examined with the reference of the physical appearance of pulled out glass fibres after tests. Figure 4.28 shows the glass fibre surfaces in aligned PAN nanofibres mat and SWCNTs doped aligned PAN nanofibres mat strengthened hybrid composites. The fractured surface in tensile tests of neat glass fibre composite contained separated glass fibres from the matrix. Figure 4.28a shows the fractured surface of glass

---

fibres composite strengthened with the aligned PAN nanofibres mat. The morphology of glass fibres remained preserve during the pull-out and no damage was observed during pullouts. This indicates that the load was transferred to the glass fibres through PAN nanofibres bridging (Figure 4.28a) which prevented sudden separation of the matrix and improved the interlaminar region as compared to the neat and random nanofibre mat composites.

Figure 4.28 shows the glass fibre surfaces in all test composites. The fractured surface in tensile tests of neat glass fibre composite contained separated glass fibres from the matrix. There was no damage to glass fibre surface and morphology remained preserve (Figure 4.28a). In the case of random, only agglomerated PAN nanofibres can be seen in the interlaminar region (Figure 4.28b). The glass fibre separation was lower than the neat FGC. An improved interlaminar region was observed with aligned PAN nanofibre mat as some bridging through PAN nanofibres was observed (Figure 4.28c). The bridging through the PAN nanofibres reduced the sudden separation of glass fibres from the matrix, which resulted in higher mechanical properties as compared to neat and random PAN nanofibre mat composites.

Figure 4.28d confirmed the damaged morphology of glass fibres in the p-SWCNTs doped aligned PAN nanofibre mat strengthened hybrid composite due to the increased the bondage produced by p-SWCNTs doped PAN nanofibres mat. In the case of f-SWCNTs doped aligned PAN nanofibre mat composites, glass fibre was torn out into two branches along with the stretched/pulled out doped PAN nanofibres (Figure 4.28e). This suggested that the uniformly distributed doped aligned PAN nanofibre mat with functionalized SWCNTs wove the matrix rich regions more uniformly which provided better strength to the interlaminar region due to their enhanced strength and better bondage with matrix than any other PAN nanofibres mat.

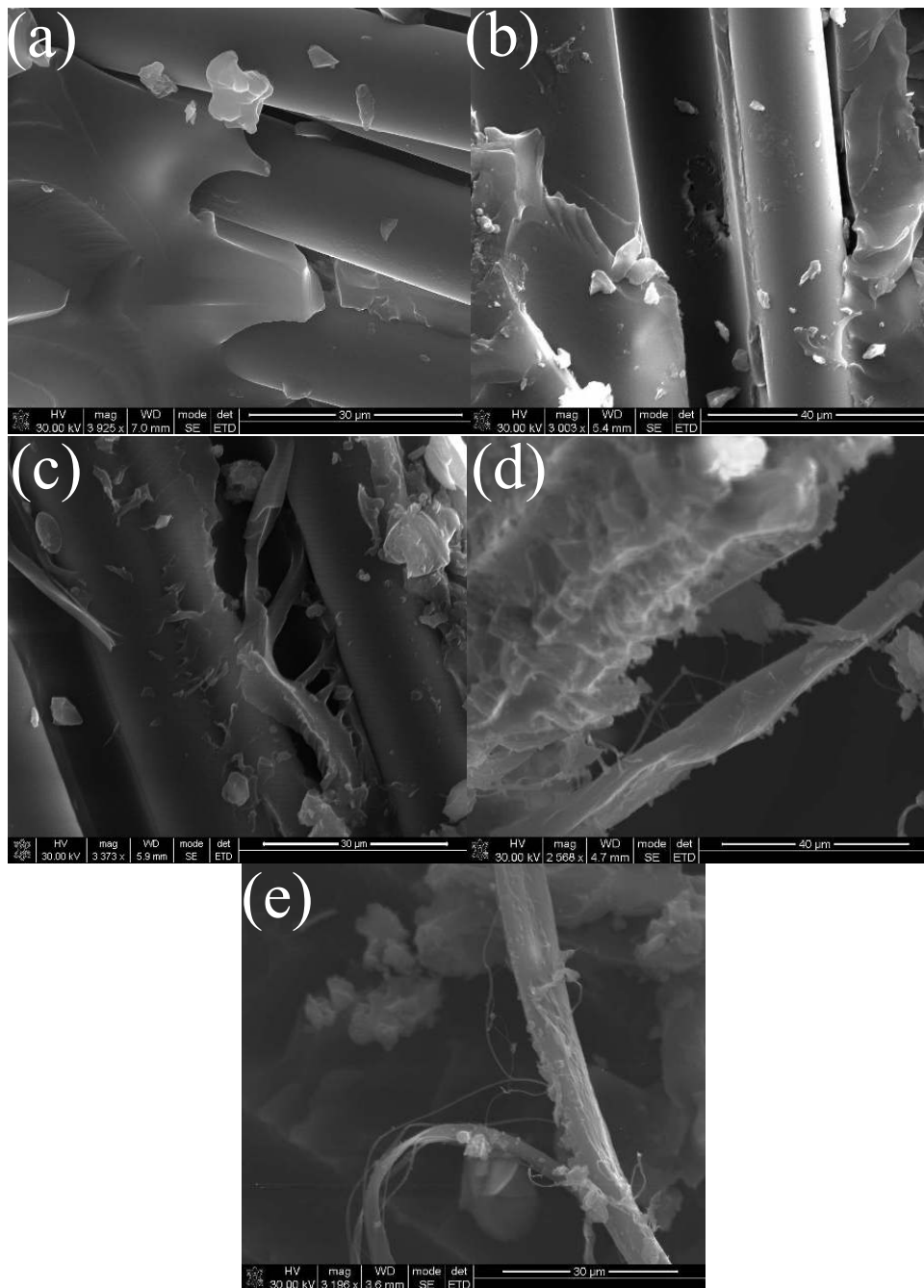


FIGURE 4.28: Glass fibre fractured surfaces in the tensile tests (a) Neat Glass (b) random PAN nanofibres (c) aligned PAN nanofibres (d) p-SWCNTs doped (e) f-SWCNTs doped aligned PAN nanofibres mats strengthened hybrid composites

### Flexural test results

Figure 4.29 shows the details of flexural properties of glass fibre composite reinforced with aligned PAN nanofibres mat, p-SWCNTs and f-SWCNTs doped aligned PAN nanofibre mats. The flexural properties of neat glass fibre composites were noticeably enhanced with aligned nanofibre mats and their doped variants, compared to the random nanofibre mats. Incorporation of random PAN nanofibres mat at the volume fraction of 0.5% into the neat glass fibre composite showed 67.11% increase, while the aligned PAN nanofibres mat results in 87.81%. Hence, the specimens manufactured using aligned nanofibre mat showed 30.980% greater resistance than the specimens prepared using random nanofibre mat.

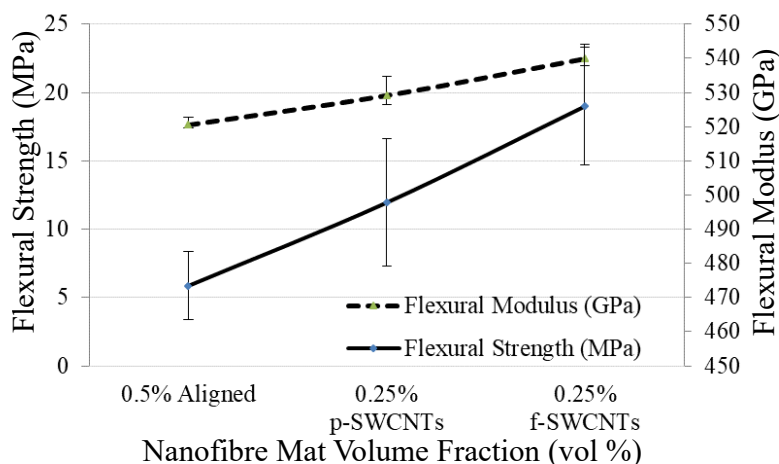


FIGURE 4.29: Flexural test results for aligned and doped PAN nanofibres mat strengthened hybrid composites

The reason for higher flexural properties for glass fibre composite reinforced with aligned PAN nanofibre mat can be explained in terms of alignment and the bridging of the PAN nanofibres within the interlaminar region due to the reduced diameter and better molecular orientations. The arrangement of PAN nanofibres mats in random and aligned mats is visible in Figure 4.30a and b.

Figure 4.30a shows an agglomerated PAN nanofibres within the fracture surface of random PAN nanofibres mat strengthened hybrid composite which was the main cause of lower mechanical properties. Whereas a uniformly distributed broken heads/breakage of PAN nanofibres can be seen on the fracture surface of the aligned PAN nanofibres mat strengthened hybrid composite as shown in Figure 4.30b.

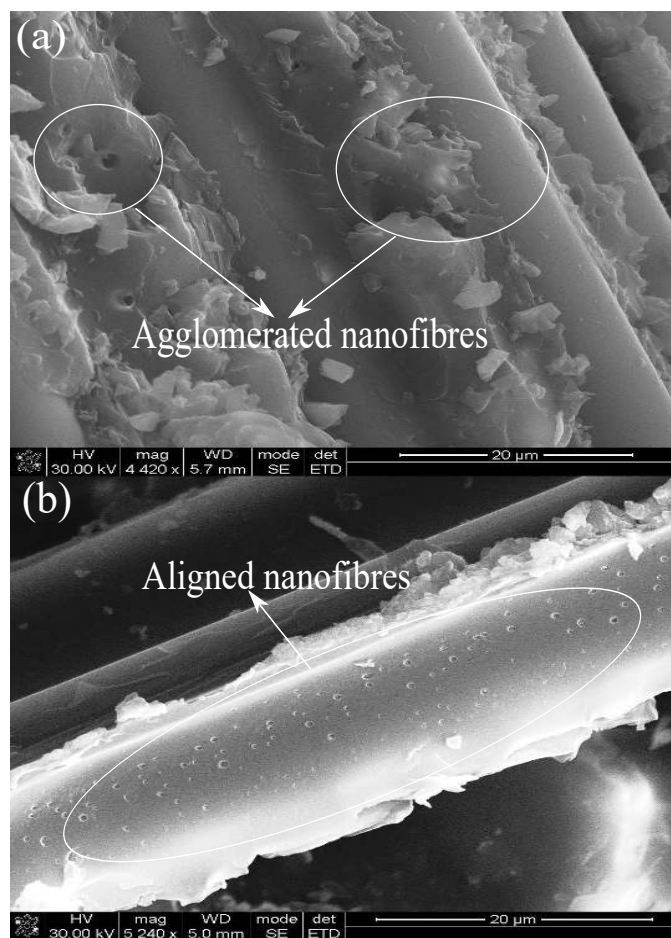


FIGURE 4.30: Fracture surfaces of 0.5% PAN nanofibre strengthened hybrid composites obtained in bending tests using (a) random PAN nanofibres mat (b) Aligned PAN nanofibre mat

SEM images were captured to evident the bridging phenomena within the different multiscale nanohybrid composites. Figure 4.31a and b show the bridging

of PAN nanofibres which resisted the crack propagation and absorbed the energy during their elongation or breakage. In case of randomly aligned PAN nanofibres, mat strengthened hybrid composite broken PAN nanofibres can be seen while in case of aligned PAN nanofibres only elongation of PAN nanofibres can be observed, which inferred that under the same strain rate breakage and elongation depends on the strength of PAN nanofibres and orientation. Less strong and random PAN nanofibres were broken (Figure 4.31a) while aligned PAN nanofibres with reduced diameter had more strength and remained intact within the interlaminar region (Figure 4.31b).

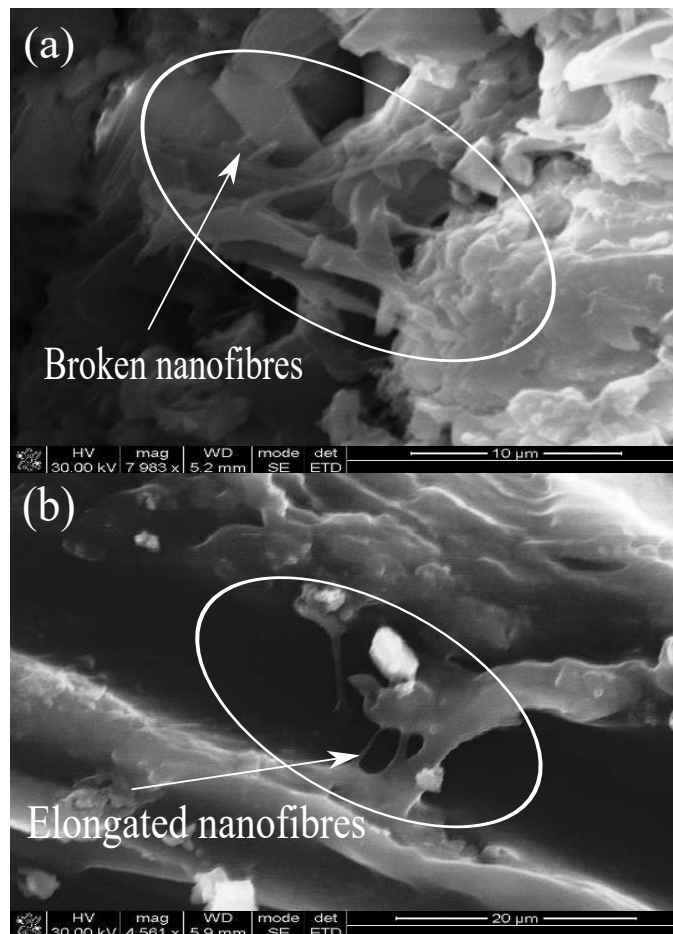


FIGURE 4.31: SEM fractographs of random and aligned PAN nanofibres mat strengthened hybrid composites. (a) broken fibres in bridging (b) elongated fibres in bridging

---

The bridging phenomena become more evident when SWCNTs doped PAN nanofibres mats were used as interlaminar to strengthen the interlaminar region. The figure shows the comparison of bridging developed during the test within the p-SWCNTs and f-SWCNTs doped PAN nanofibres mats strengthened hybrid composites. Both elongated and broken PAN nanofibres were found within the interlaminar region of p-SWCNTs doped PAN nanofibres mat strengthened hybrid composite. The network of doped PAN nanofibre restricted the crack propagation through their deformations which appeared as broken necked PAN nanofibres and bridging as shown in Figure 4.32a. It can be assumed that the p-SWCNTs doped PAN nanofibres obstructed the crack growth and ensured the high flexural properties. Therefore, p-SWCNTs doped PAN nanofibres provided more strength than the pristine aligned PAN nanofibres mat and resulted in overall improved flexural strength and modulus by 105.48% and 106.79% compared to the neat GFC, respectively.

Compared to the p-SWCNTs doped PAN nanofibres mat, f-SWCNTs PAN nanofibres provided better strength to the interlaminar region. It is evident from the Figure 4.32b that the elongation in the PAN nanofibre is lesser than the p-SWCNTs doped PAN nanofibres under the similar loading conditions. Moreover, the f-SWCNTs PAN nanofibres bridging has hindered the initiated crack as the crack was wider in the middle which was gradually restricted at the end. Thus the f-SWCNTs doped PAN nanofibres mat strengthened composite provided the highest flexural properties which were 117.11% and 134.8578% compared to the neat GFC, respectively. It can be inferred that the breakage or elongation of PAN nanofibres within the interlaminar region depends on the bondage strength between the SWCNTs and its host material i.e. PAN nanofibres mat. f-SWCNTs were anchored well into the PAN nanofibres due to FCA and showed more strength than the p-SWCNTs doped aligned PAN nanofibres.

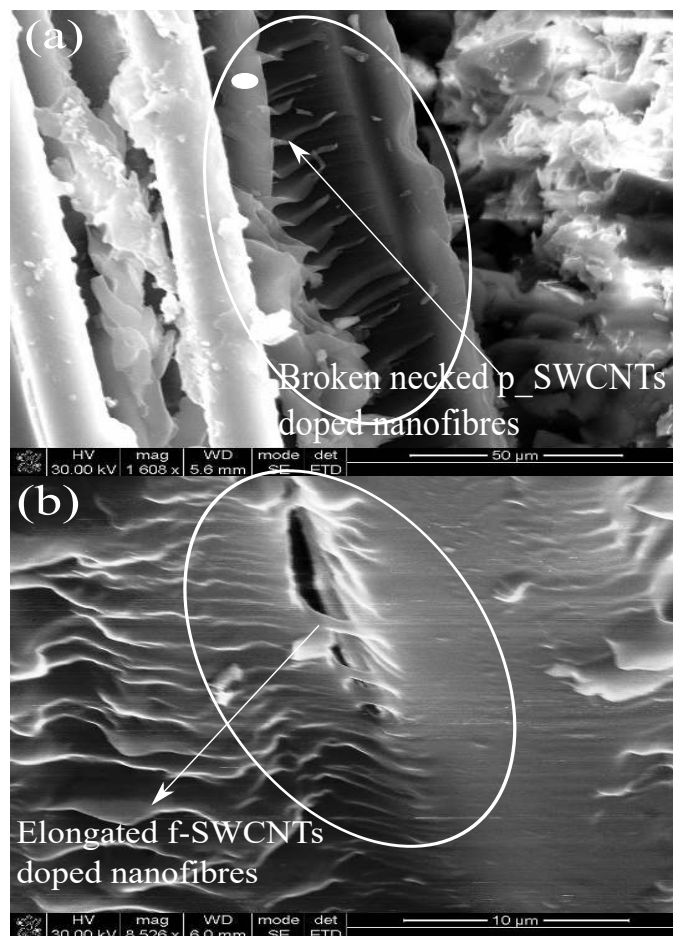


FIGURE 4.32: SEM fractographs of random and aligned PAN nanofibres mat strengthened hybrid composites. (a) broken fibres in bridging (b) elongated fibres in bridging

### Impact test results

Figure 4.33 shows the impact test results for 0.5% aligned and SWCNTs doped PAN nanofibre mats strengthened hybrid composite. For glass fibre composite with 0.5% random and aligned PAN nanofibres nanofibre mats, the impact resistance was  $193.11 \text{ KJ/m}^2$  and  $232.75 \text{ KJ/m}^2$  respectively. Hence, the respective improvements in the impact resistance were 20.55% and 45.3%. The result showed that the aligned PAN nanofibres mat gave a significant boost of

24.744% to the impact properties as compared to the random PAN nanofibres mat. The results concluded that the PAN nanofibres mat reduced the mismatch scale of matrix and macrofibres (glass fibre) by filling the interlaminar gap. However, aligned PAN nanofibres mat contributed more resistance to applied load as compared to the random PAN nanofibres mat due to their better distribution as shown in Figure 4.34. Random PAN nanofibres mat developed sites of agglomerated PAN nanofibres, which had low mechanical properties.

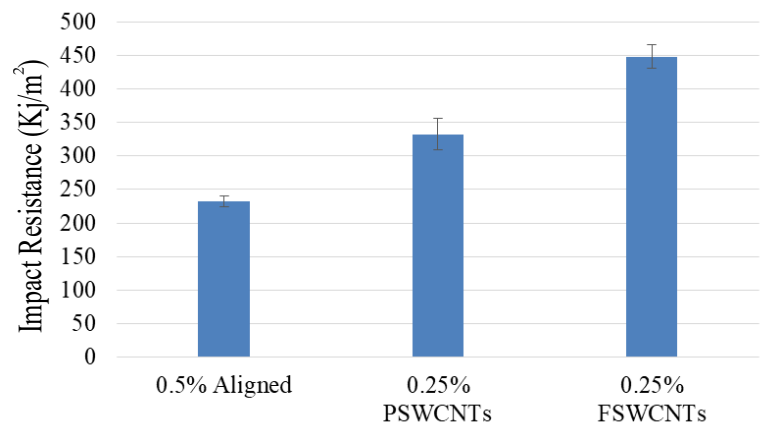


FIGURE 4.33: Impact test results for aligned and doped PAN nanofibres mat strengthened hybrid composites

Nanofibre mats strengthened hybrid composites manufactured from pristine and functionalized SWCNTs doped aligned PAN nanofibres mat were also investigated. As compared to the reference sample (neat glass fibre composite), pristine and functionalized SWCNTs doped PAN nanofibres mat improved impact resistance by 107.72% and 180.038% respectively. Functionalized SWCNTs doped aligned PAN nanofibres had the highest values of impact resistance; this may have the following reasons; (i) aligned PAN nanofibres have reduced the fibre agglomeration and improved alignment of SWCNTs along fibre axis;

(ii) functionalization improved the dispersion of SWCNTs and bonding between SWCNTs and PAN nanofibres mats which resulted in more strong network of doped nanofibre mats within the interlaminar regions. To identify the strengthening mechanism of doped PAN nanofibres, the fracture surface was examined using SEM. Figure 4.35 shows the bridging between the displaced glass fibres after the pendulum strike which restricted and prevented the crack propagation and resulted in high impact resistance.

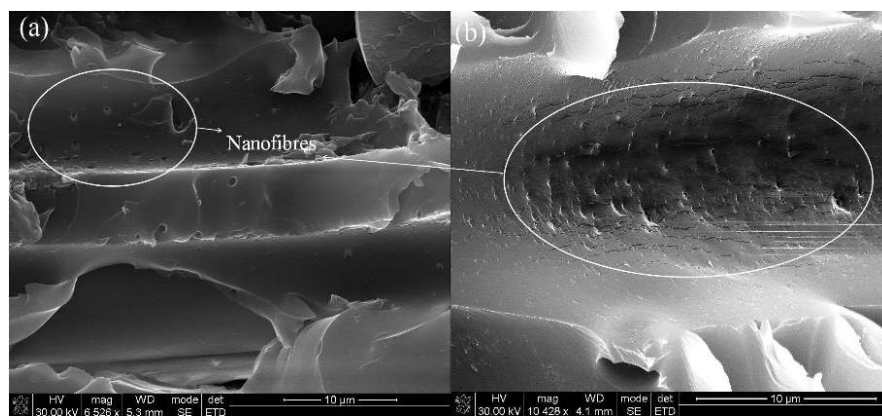


FIGURE 4.34: Fracture surfaces of PAN nanofibre strengthened hybrid composite obtained in impact test using (a) 0.5% random PAN nanofibres mat  
(b) Aligned PAN nanofibres mat

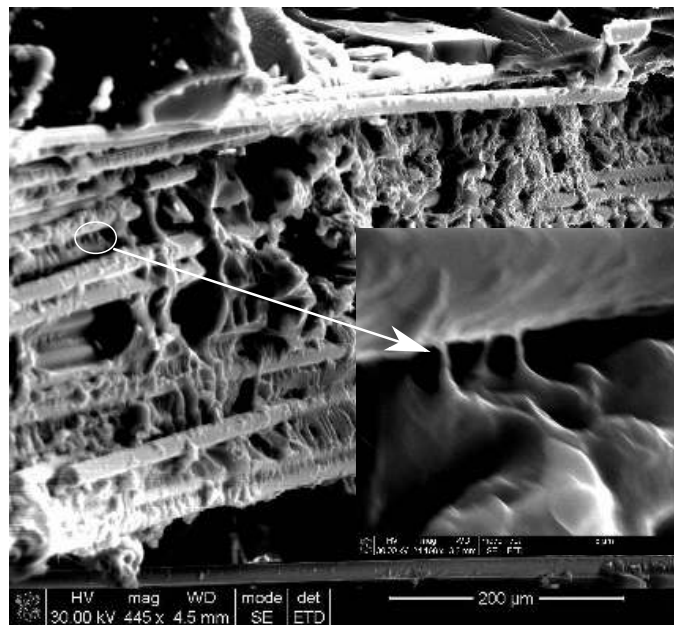


FIGURE 4.35: Nanofibres bridging in the impact test specimen

# Chapter 5

## Space-frame Structure (SFS) Analysis with Orthotropic Responses of C-C bonds for characterizing CNTs Properties

### 5.1 Introduction

The addition of a small number of CNTs to the polymer matrix improves the mechanical, thermal and electrical properties of the composites. However, the values of the properties measured experimentally are much lower than the theoretically determined/expected values [210]. The reasons/factors for this discrepancy have already been discussed in Chapter 2. Therefore, it is essential to understand the effect of these factors (diameter, chirality, number of

walls, vacancy defects and the orthotropic behaviour) on the CNTs mechanical properties, which will be further helpful in choosing suitable CNTs as a reinforcement.

Various experimental techniques such as Raman spectroscopy, scanning electron spectroscopy, transmission electron microscopy, nanoindentation and x-ray diffraction have been used to characterize the CNTs properties [211]. However, the main challenges faced with these experimental techniques are that they are either expensive or technically not feasible to obtain the nanoscale behaviour of CNTs. In addition, conventional theoretical models such as rule of mixtures [212], effective field models [213] and continuum mechanics models [214] also have limitations in predicting the behaviour of CNTs at nano length scales [212]. Hence, researchers have focused on developing molecular-scale models such as molecular dynamics (MD) and molecular mechanics (MM) methods. These methods are powerful and can provide details in molecular scale level. However, their limitations in analysing the number of atoms, length and time scales along with the computational cost have restricted their applications within the limited span [215].

To overcome these limitations in molecular models, an equivalent continuum model (ECM) was proposed [216]. In the ECM model, the individual carbon nanotube was modelled either as a shell or as a beam with isotropic properties [217, 218]. Moreover, in these models, the hexagonal atomic structure of a SWCNT was completely ignored [219] and thus resulted in exaggerated SWCNT properties. In addition, these models could not include the effects of vacancy defects (Figure 5.1), chirality and van der Waals forces between the walls. Hence, for including the atomic structure of CNTs, an SFS model was proposed [220]. In SFS model, the chemical bond between two carbon atoms (C-C) was modelled as a circular beam with isotropic properties in such a way

that one carbon molecule was modelled using six circular beams in a hexagonal shape as shown in Figure 5.2. The chemical bond properties were obtained from both solid and molecular mechanic analysis.

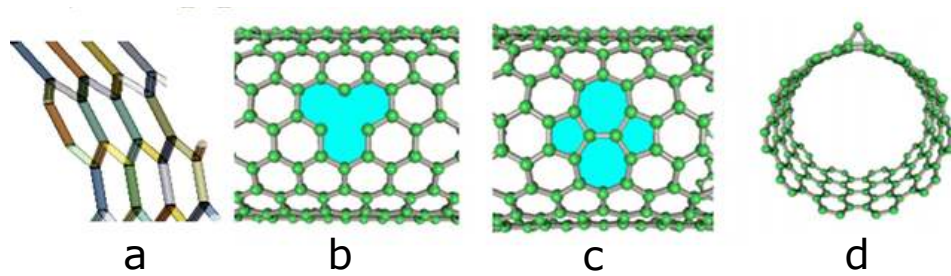


FIGURE 5.1: a. Hexagonal arrangement, b. Vacancy defect, c. Stone wales defect, d. Adatom in CNTs

However, CNTs have orthotropic properties [221], which was again ignored by the SFS model including the other important parameters as explained above. Hence the objectives of this paper were defined as to characterize the zigzag and armchair CNTs using SFS model by considering the effects of CNTs diameters, chirality, number of walls, vacancy defects and the van der Waals interactions between the walls (double and multi-walled). In addition, this research also focused on understanding the effect of the orthotropic behaviour of CNTs on their properties.

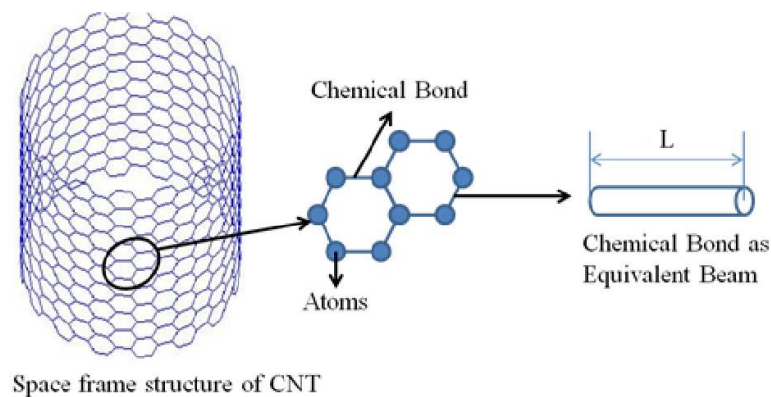


FIGURE 5.2: Equivalent SFS

## 5.2 Modelling for Simulation

### 5.2.1 SFS modelling of SWCNTs

Since CNTs are formed by rolling the graphene sheets, the parameters such as chiral angle ( $\theta$ ) and chiral vector ( $C_h$ ) define the types of CNTs such as zigzag and armchair. Figure 5.3 shows a schematic of chiral vector, chiral angle and the relevant geometrical parameters.

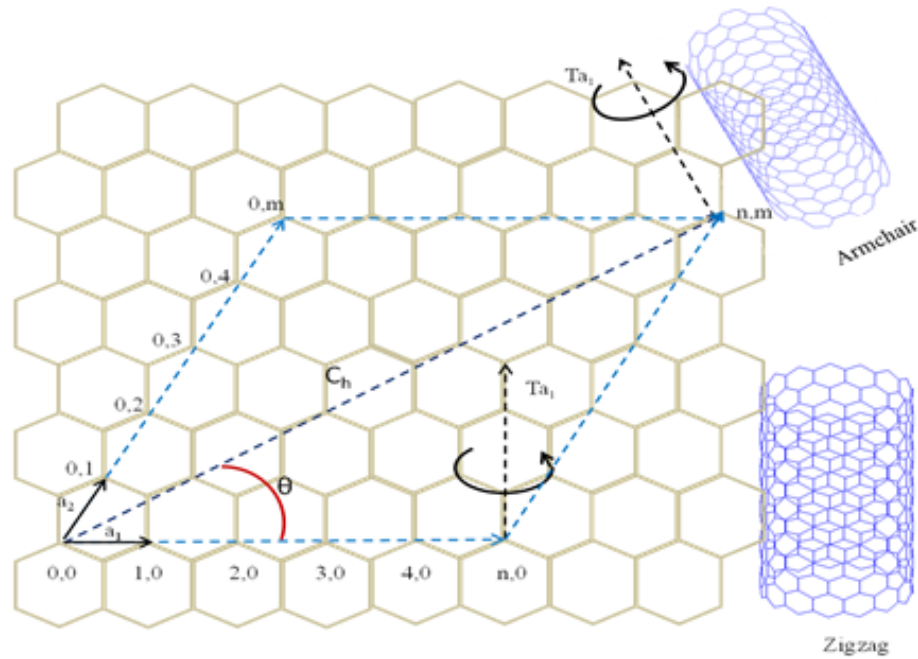


FIGURE 5.3: Rolling angle and chiral vector

The chiral vector ( $C_h$ ) is mathematically defined by the unit vectors  $a_1$  and  $a_2$ . The step integer  $n$  and  $m$  determine the chirality or twist of the nanotube.

$$\vec{C}_h = n\vec{a}_1 + m\vec{a}_2 \quad (5.1)$$

Different roll up directions of graphene (chiral angle,  $\theta$ ) give different configuration of CNTs as given in the equation.

$$\theta = \sin^{-1} \left[ \frac{\sqrt{3}m}{2(n^2 + nm + m^2)} \right] \quad (5.2)$$

Where

$\theta$  is the chiral angle.

If  $n \neq 0$  and  $m=0$  ( $\theta=0$ ) a zigzag tube is formed, while an armchair structure is generated if  $n=m$  ( $\theta=30^\circ$ ) [222].

The CNTs diameters are obtained using the step integers, which also defines both chiral vector and chiral angle.

$$d = 0.783\sqrt{n^2 + nm + m^2} \quad (5.3)$$

### 5.2.2 CNTs model development

For modelling a SWCNT, its coordinates were defined using a MATLAB code (Appendix B.1) for the different types of CNTs such as zigzag, armchair, single, defective, double and multiwall. The required chiral angle and chiral vector for the coordinates were obtained using the above equations and given in Table 5.1.

TABLE 5.1: Configuration properties

n	m	Diameters(Å)	$d_{s-s}$ (Å) (inter-shell distance)	Bond lengthL (Å) [29]	Number of walls		
					SWCNT	DWCNT	MWCNT
Zigzag							
7	0	5.481	3.4-3.8	1.41-1.42	1	2	3
11	0	8.61					
14	0	10.96					
20	0	15.657					
28	0	21.92					
Armchair							
4	4	5.424	3.4-3.8	1.41-1.42	1	2	3
6	6	8.13					
8	8	10.84					
11	11	14.916					
16	16	21.696					

A general methodology followed for producing both zigzag or armchair configuration was that a basic unit cell (a carbon molecule) was developed along the tube circumference. At first, a single carbon molecule was divided into 6 equivalent triangles. The height,  $h$  and the half of base,  $b$  of the individual triangle were used to draw the position of the individual carbon atoms and then the carbon molecule unit cell. The angle  $\psi$  defines the number of carbon molecules along the circumference based on the base length  $b$  with respect to the centre of the SWCNT. Figure 5.4 shows the schematic of the modelling process.

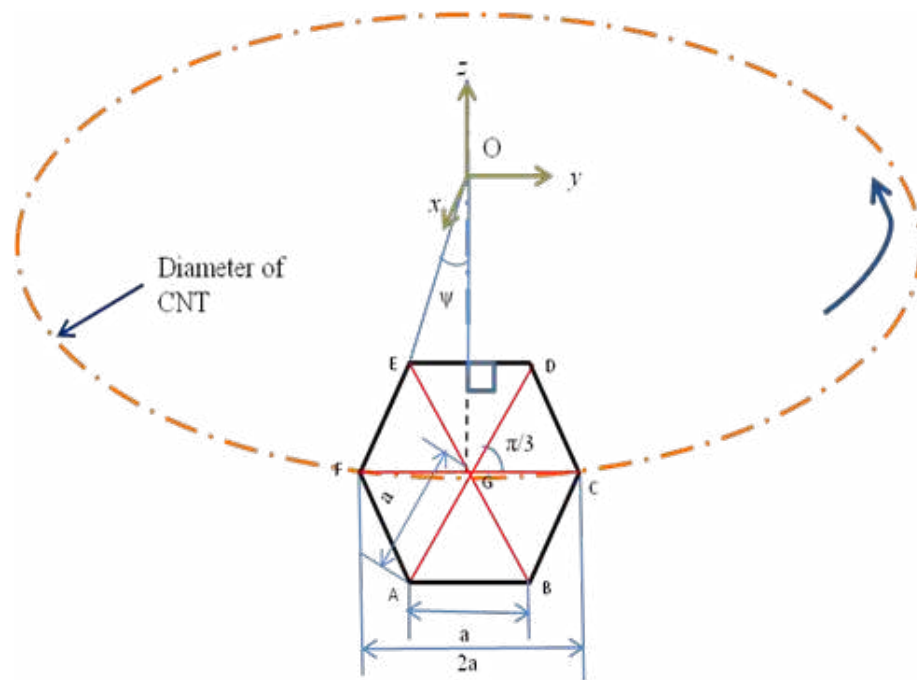


FIGURE 5.4: Modeling process of CNTs

The base unit cell was then extended further to obtain a base ring and then the full carbon nanotube (Figure 5.5). Double and multiwall CNTs were developed using the same procedure. The distance between the consecutive walls ( $d_{(s-s)}$ ) was kept at  $3.4 \sim 3.8 \text{ \AA}$  [220]. Figure 5.6 shows the double wall and multiwall CNTs modeled using the defined procedure.

The vacancy defects were randomly generated by removing a point (carbon atom) at three different places; top, centre and bottom of SWCNTs. These defects were approximately  $120^\circ$  apart from each other (Figure 5.7).

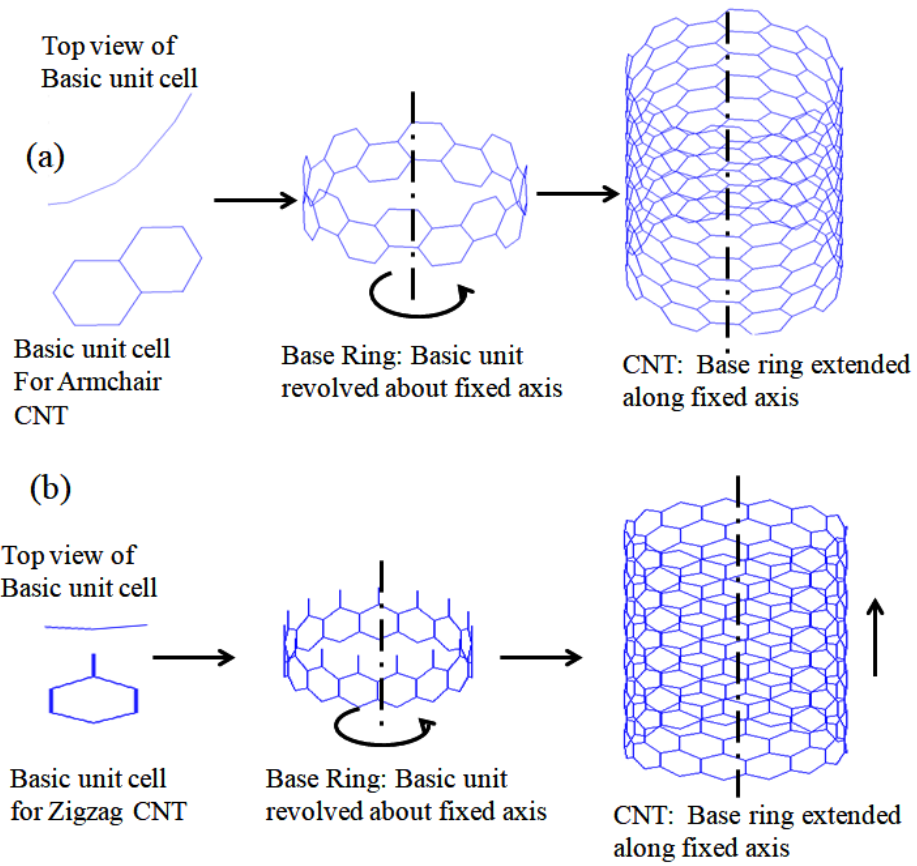


FIGURE 5.5: a) Armchair b) Zigzag CNTs modeling process

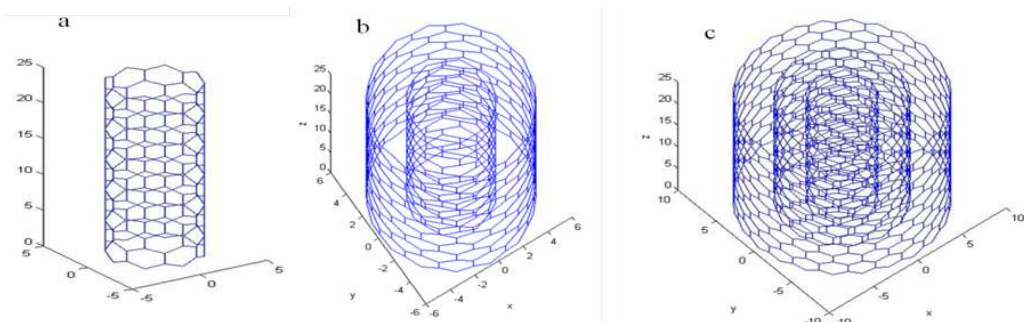


FIGURE 5.6: DWCNT and MWCNTs modelling process a) SWCNT model, b) DWCNT model, c) MWCNT model

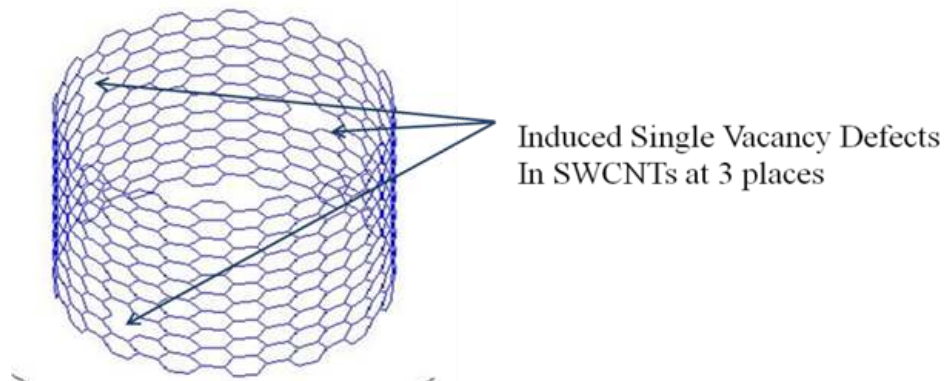


FIGURE 5.7: CNTs with vacancy defects

The macro files (Appendices B.2, B.3, B.4) containing the SWCNT coordinates were transferred to ANSYS for developing IGES/ANSYS workbench multibody SWCNT model. The in-built ANSYS workbench shared topology method was utilised to convert the multibody SWCNT SFS-model into a single part. This method joins each equivalent circular beam to the other beams through edge joints. Figure 5.8 shows the transferred ANSYS Workbench SWCNT model developed in MATLAB. Five different diameters were used for both the zigzag and armchair configurations. Pristine and defective single walled and pristine double and multi wall CNTs were considered for the analysis.

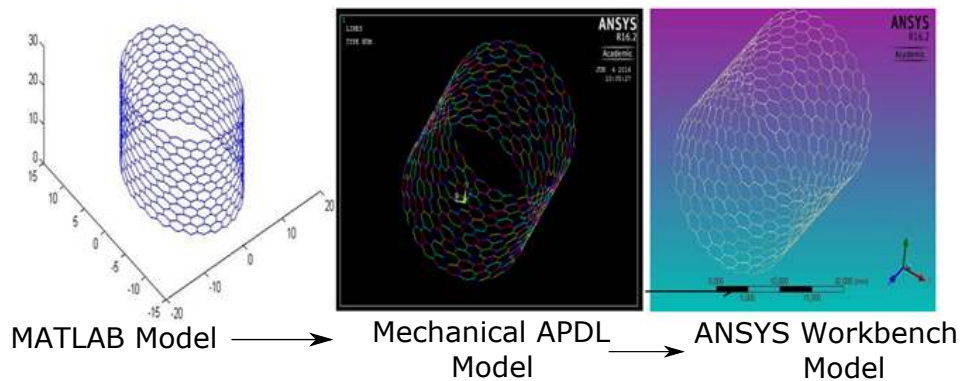


FIGURE 5.8: Equivalent SFS modelling process of CNTs

### 5.2.3 C-C chemical bond orthotropic properties

The next step is to define the C-C chemical bond properties. As briefly discussed before, most of the research works have considered CNTs as an isotropic material. However, theoretical studies [221] have shown that the CNTs behave like an orthotropic material. Hence, in this research, the orthotropic properties of CNTs were obtained by assuming orthotropic response from the individual C-C bond. Hence two individual methods were used to obtain both axial and transverse response of the C-C bonds.

#### C-C bond axial direction response

The axial direction response of C-C bond were obtained by equating the energy of the atomistic system (molecular mechanics) with the beam model (classical structural mechanics). Based on the Molecular mechanics, the C-C chemical bond could be expressed using steric potential energies, which gives the total potential energy ( $V_t$ ) [184] of the individual C-C bond as given in equation 5.4.

$$V_t = \sum V_r + \sum V_\theta + \sum V_\phi + \sum V_\omega + \sum V_{vdw} \quad (5.4)$$

Where

$V_r$ ,  $V_\theta$ ,  $V_\phi$ ,  $V_\omega$ ,  $V_{vdw}$  are the bond strength, bond angle variation, dihedral angle torsion, inversion, and interaction strain energies respectively (Figure 5.9).

Since the inversion and the interaction energies have very little influence on the total potential energy equation, hence the bond strength, bond angle variation, and dihedral angle torsion energies are only considered for the current analysis.

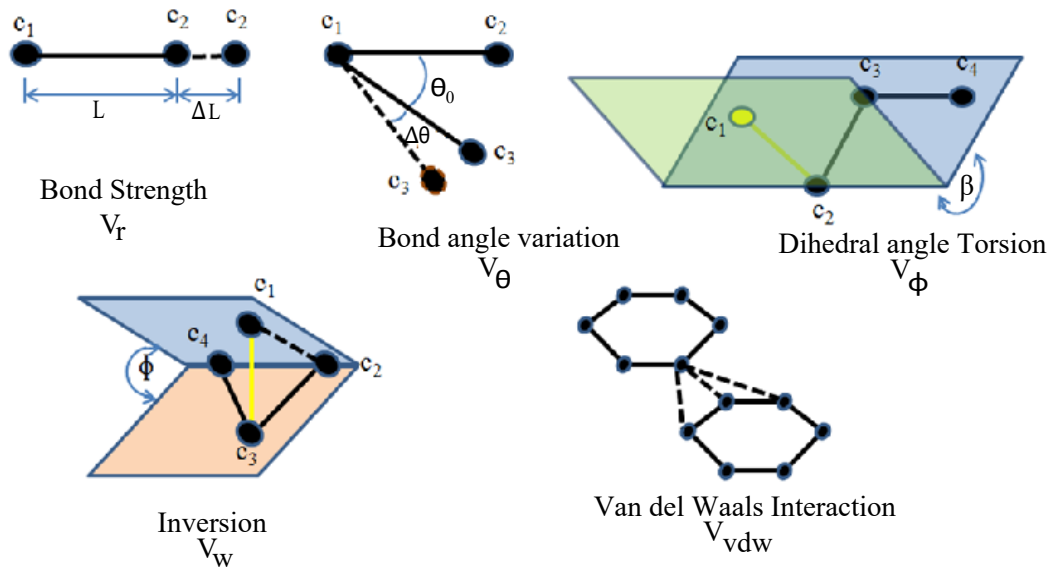


FIGURE 5.9: Graphical representation of steric potential energy

These energies are expressed as [223]:

$$V_r = \frac{1}{2}k_r(L - L_0)^2 = \frac{1}{2}k_r(\Delta L)^2 \quad (5.5)$$

$$V_\theta = \frac{1}{2}k_\theta(\theta - \theta_0)^2 = \frac{1}{2}k_\theta(\Delta\theta)^2 \quad (5.6)$$

$$V_\phi = V_w = \frac{1}{2}k_\tau(\Delta\Phi)^2 \quad (5.7)$$

Here,  $k_r$ ,  $k_\theta$ , and  $k_\tau$  are bond stretching, bond angle variation, and torsion resistance force constants respectively.  $\Delta L$ ,  $\Delta\theta$  and  $\Delta\beta$ , are bond stretching, bond angle variation and angle variation of bond twist respectively. The C-C chemical bond characteristics are assumed to be an analogue to a structural mechanics beam element (Figure 5.10). As such, the total deformation of carbon nanotube due to the external load is assumed to be the results of the individual bond interactions. Here, the carbon atoms act as joints of the connecting beam element and hence the stiffness equations associated with the structural mechanics of a beam element could be equated with the force

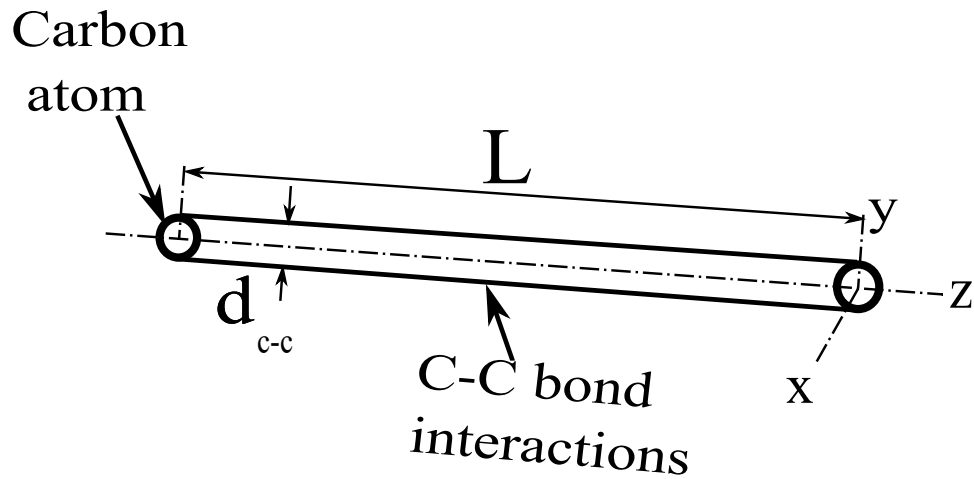


FIGURE 5.10: Equivalent beam model

constants of molecular mechanics to define the C-C chemical bond along the axial direction.

According to the classical structural mechanics, the strain energy equations of a beam under uniform axial, bending and torsional loads are given by

$$U_A = \frac{1}{2} \int_0^L \frac{F^2}{EA} dL = \frac{1}{2} \frac{F^2 L}{EA} = \frac{1}{2} \frac{EA}{L} \Delta L^2 \quad (5.8)$$

$$U_M = \frac{1}{2} \int_0^L \frac{M^2}{EI} dL = \frac{1}{2} \frac{M^2 L}{EI} = \frac{1}{2} \frac{EI}{L} \Delta \theta^2 \quad (5.9)$$

$$U_T = \frac{1}{2} \int_0^L \frac{T^2}{GJ} dL = \frac{1}{2} \frac{T^2 L}{GJ} = \frac{1}{2} \frac{GJ}{L} \Delta \beta^2 \quad (5.10)$$

Where

E is the elastic Modulus

A is the cross sectional area

L is the beam length

I is the moment of inertia

G is the polar moment of inertia

J is the polar moment of inertia

$\theta$  is rotational angle and

$\beta$  is relative rotation between the two ends.

By considering analogues and equating the corresponding energy equations, the relationship between the structural mechanics (EA, EI and GJ) and the molecular mechanics parameters ( $k_r$ ,  $k_\theta$ , and  $k_\tau$ ) are deduced and given below [224].

$$k_r = \frac{EA}{L}, \quad k_\theta = \frac{EI}{L}, \quad k_\tau = \frac{GJ}{L} \quad (5.11)$$

These above equations were used to obtain the C-C bond axial direction response. The parameters for calculating the C-C bond axial response are given in Table 5.2.

TABLE 5.2: Bond length and molecular mechanics constant values [225]

L	0.142nm
$k_r$	938 kcal.mol <sup>-1</sup> .Å <sup>-2</sup> = 6.52 × (10) <sup>-7</sup> N.nm <sup>-1</sup>
$K_\theta$	126 kcal.mol <sup>-1</sup> .Å <sup>-2</sup> = 8.76 × (10) <sup>-10</sup> N.nm <sup>-1</sup>
$K_\tau$	39.986 kcal.mol <sup>-1</sup> .Å <sup>-2</sup> = 2.780 × (10) <sup>-10</sup> N.nm <sup>-1</sup>

Using the above values, the C-C bond axial responses are obtained and given below.

$$d_{c-c} = 4\sqrt{\frac{K_\theta}{K_r}} = 0.14660 \text{ nm}$$

$$E_{zz} = \frac{(K_r)^2 L}{4\pi K_\theta} = 5.49 \text{ TPa}$$

$$G_{xy} = \frac{\left(\frac{K_r}{K_\theta}\right) K_\tau L}{8\pi} = 0.871 \text{ TPa}$$

## C-C bond Transverse Direction Response

The transverse direction responses of C-C bond were obtained using ANSYS parametric study. SFS model of single wall zigzag CNT with diameter 0.861 nm was chosen along with the C-C bond axial response values obtained before for this analysis. The parametric study was carried out by using the range of values of elastic modulus, shear modulus and poisson's ratio as given in Table 5.3. The analysis were repeated until the selected SFS model gave the radius modulus of 650 GPa Reich [226] and the corresponding orthotropic properties were selected to define the transverse response of the C-C bond interactions.

TABLE 5.3: Range of values for parametric study variables

Elastic Modulus (GPa)		Shear Modulus (GPa)		Poisson's ratio		
$E_{xx}$	$E_{yy}$	$G_{xy}$	$G_{yz}$	$\gamma_{xy}$	$\gamma_{yz}$	$\gamma_{xz}$
4.5-5.5	4.5-5.5	3-8.71	3-8.71	0.1- 0.25	0.1- 0.25	0.1- 0.25

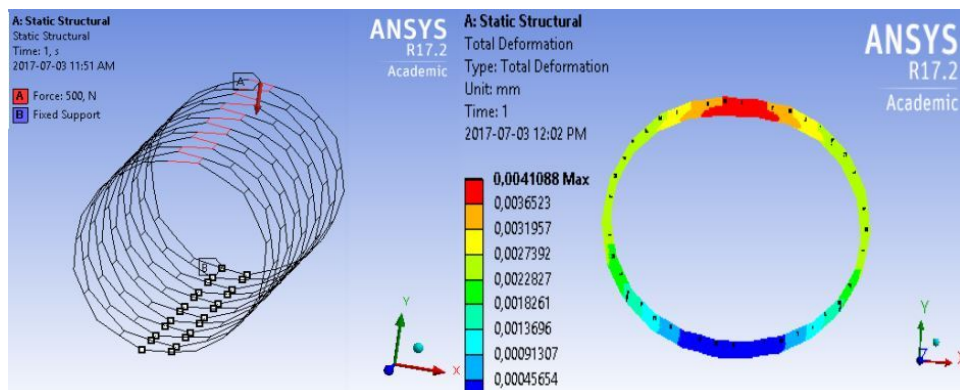


FIGURE 5.11: Radial test model

The overall orthotropic response of the C-C bond within a SFS SWCNT model is given in Table 5.4.

TABLE 5.4: Orthotropic properties of CNTs

	$E_{xx}$	523 GPa
Modulus	$E_{yy}$	523 GPa
	$E_{zz}$	5490 GPa
	$\gamma_{xy}$	0.1
Ratio	$\gamma_{yz}$	0.1
	$\gamma_{xz}$	0.1
	$G_{xy}$	409 GPa
Shear	$G_{yz}$	871 GPa
	$G_{xz}$	409 GPa

### 5.2.4 Modelling of van der Waals forces

DWCNTs and MWCNTs contain two or more concentric shells at distances 3.4 to 3.8 Å from each other and interact through the van der Waals ( $F_{vdw}$ ) forces. In addition, these forces are effective within 0.85 nm range [210] and the atoms which are not within the range will be coupled with the adjacent atoms. Based on the above assumption, a single carbon atom of one shell interacts with 58 atoms of adjacent shell (0.85 nm range) as shown in Figure 5.12. Generally, the van der Waals forces are calculated using Lennard-Jones potentials [227] as given in the equation 5.12.

$$F_{(vdw)} = 4\epsilon \left[ -12 \left( \frac{\sigma}{d_{s-s}} \right)^{12} + 6 \left( \frac{\sigma}{d_{s-s}} \right)^6 \right] \quad (5.12)$$

Ali and coworkers [220] modelled the van der Waals force ( $F_{vdw}$ ) interaction between two carbon atoms as a spring with a stiffness ( $K_{single\ C-C}$ ) of 0.24245 N/m. However with a large number of van der Waals interaction, modelling

of each interaction could lead to computational difficulties. Hence these inter shell interactions were modelled as an equivalent spring (Figure 5.13).

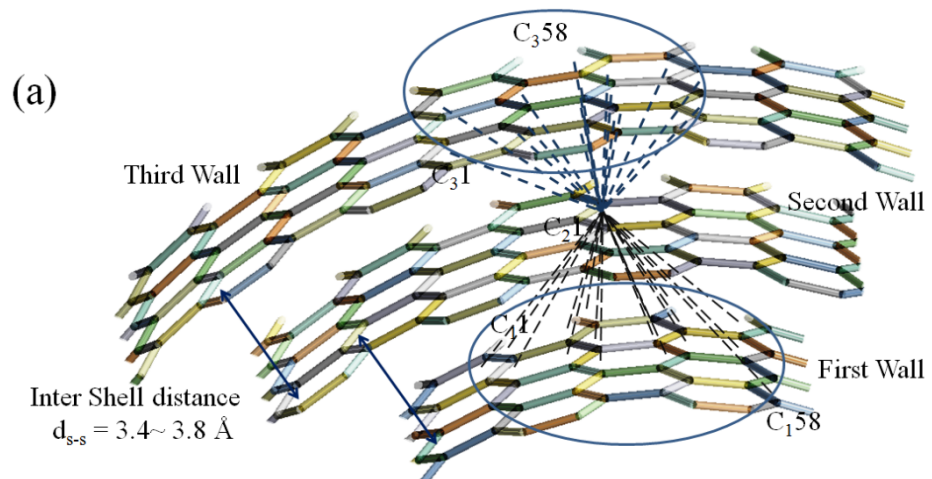


FIGURE 5.12: Van der Waals forces interactions between different shells

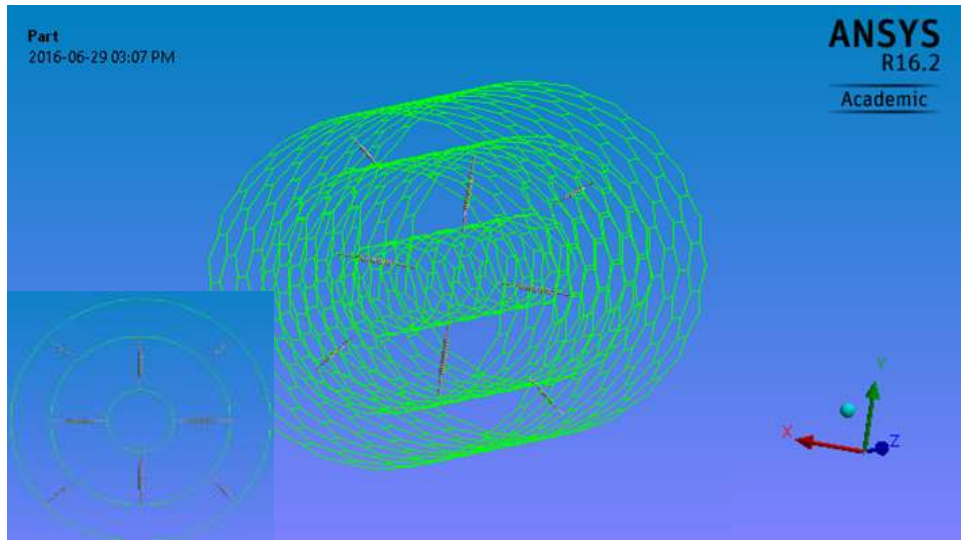


FIGURE 5.13: Equivalent spring between shells

Four equivalent springs at  $90^\circ$  interval inserted between two adjacent shells to model the total van der Waals forces interactions. The spring stiffness of a single equivalent spring ( $K_{eq}$ ) was calculated from the the total spring stiffness  $K_n$ . Here,

$$K_n = 58 \times K_{single(C-C)} \times (\text{Total number of interactions from first shell to the second shell} - (\text{TAI}))$$

Where

$n = (1stshell, 2ndshell...)$  The total atomic interactions (TAI) between one shell and the other were estimated by equation 5.13.

$$TAI = P_{total} - 0.5P_{end1} - 0.5P_{end2} - 0.875P_{2ndend1} - 0.875P_{2ndend2} \quad (5.13)$$

Where,

$P_{total}$  = total number of point in a single shell  $P_{end1}$  = number of points in end rows (Figure 5.14).  $P_{2ndend1}$  = number of points in 2nd end rows (Figure 5.14).

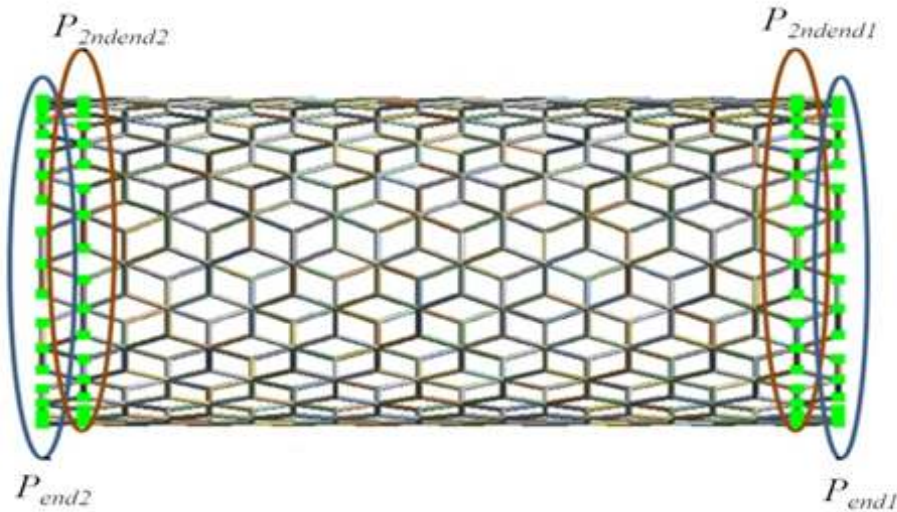


FIGURE 5.14: End points of CNTs

Since the atoms at the end points i.e  $P_{end1} = P_{end2}$  and  $P_{2ndend1} = P_{2ndend2}$ , the TAI equation becomes:

$$TAI = P_{total} - P_{end} - 1.75P_{2ndend} \quad (5.14)$$

Using the above TAI values, the total spring stiffness ( $K_n$ ) was obtained and then the  $K_{eq}$  for the individual spring was estimated using equation 5.15.

$$K_{eq} = \frac{K_{1stshell} + K_{2ndshell}}{S_0} \quad (5.15)$$

Where  $S_0$  is the number of springs to be inserted.

For simplicity and symmetry four springs were chosen between two consecutive walls. The values of equivalent springs constant  $K_{eq}$  obtained for all different CNTs are given in Table 5.5. Figure 5.15 shows that the van der Waals force become more effective with the increase in diameter and become more significant with higher number of walls and larger diameters. Therefore, these forces must be considered in theoretical analysis to reduce the mismatch with experiments.

TABLE 5.5: Equivalent spring stiffness values

Diameter ( $\text{\AA}$ )	Kc-c (N/m)	$P_{end}$	$P_{2ndend}$	Total points	Total working points	$P_{end}$	$P_{2ndend}$	Total points	Total working points	Keq (N/m)
Zigzag (DWCNTs)		1st Wall				2nd Wall				
5.481	0.24245	16	16	168	124	30	30	384	302	1498
8.613		22	22	264	204	40	40	480	370	2017
10.962		28	28	336	259	46	40	552	442	2465
15.66		40	40	480	370	58	58	696	537	3189
21.924		60	60	672	507	74	74	936	733	4360
Armchair (DWCNTs)		1st Wall				2nd Wall				
5.424	0.24245	16	16	161	117	36	36	359	260	1326
8.13		24	24	241	175	48	48	479	347	1836
10.84		32	32	321	233	52	52	519	376	2141
14.916		44	44	441	320	68	68	679	492	2855
21.696		64	64	641	465	84	84	839	608	3773
Zigzag (MWCNTs)		2nd Wall				3rd Wall				
5.481	0.24245	30	30	384	302	48	48	576	444	2623
8.613		40	40	480	370	58	58	696	537	3189
10.962		46	40	552	442	64	64	768	592	3579
15.66		58	58	696	537	76	76	912	703	4360
21.924		74	74	936	733	92	92	1104	851	5569
Armchair (MWCNTs)		2nd Wall				3rd Wall				
5.424	0.24245	36	36	359	260	56	56	560	406	2690
8.13		48	48	479	347	68	68	680	493	3418
10.84		52	52	519	376	72	72	720	522	3660
14.916		68	68	679	492	88	88	880	638	4630
21.696		84	84	839	608	104	104	1040	754	5601

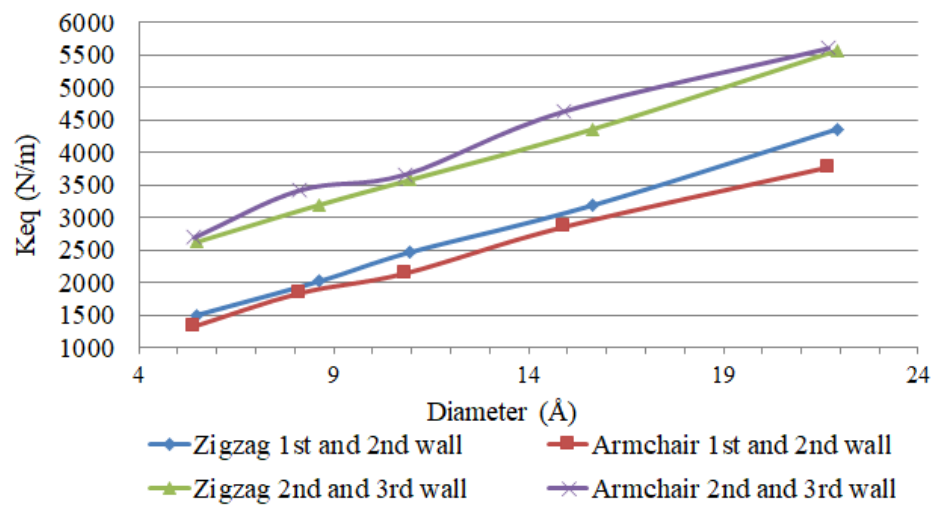


FIGURE 5.15: van der Waals forces trends

### 5.2.5 Analysis procedure

The proposed SFS model was analysed using equivalent properties (EP) method for determining the CNTs properties. The equivalent properties model was defined based on the assumption that the deformation could be equated for two SFS-models with an equal applied load, SWCNT length and area along with the varying C-C bond properties. Based on the above definition, the SFS model-SWCNT properties could be obtained from equation 5.16 and 5.17.

$$\frac{E_{SFS-SWCNT}}{E_{SFS-Ref}} = \frac{\Delta L_{SFS-SWCNT}}{\Delta L_{SFS-Ref}} \quad (5.16)$$

$$\frac{G_{SFS-SWCNT}}{G_{SFS-Ref}} = \frac{\Delta \theta_{SFS-SWCNT}}{\Delta \theta_{SFS-Ref}} \quad (5.17)$$

The proposed analysis was carried out by constraining the SWCNT model at one end and applying a load at other end (Figure 5.16). As explained in EP method, the C-C bond properties were assigned with a reference material and an orthotropic material individually. The first analysis was conducted with structured steel (reference material) properties of elastic modulus of 200 GPa and a Poisson's ratio of 0.3. A similar analysis was again carried out by using the orthotropic properties as explained in the previous section. The EP method was then used to obtain the overall properties of SFS SWCNT-model.

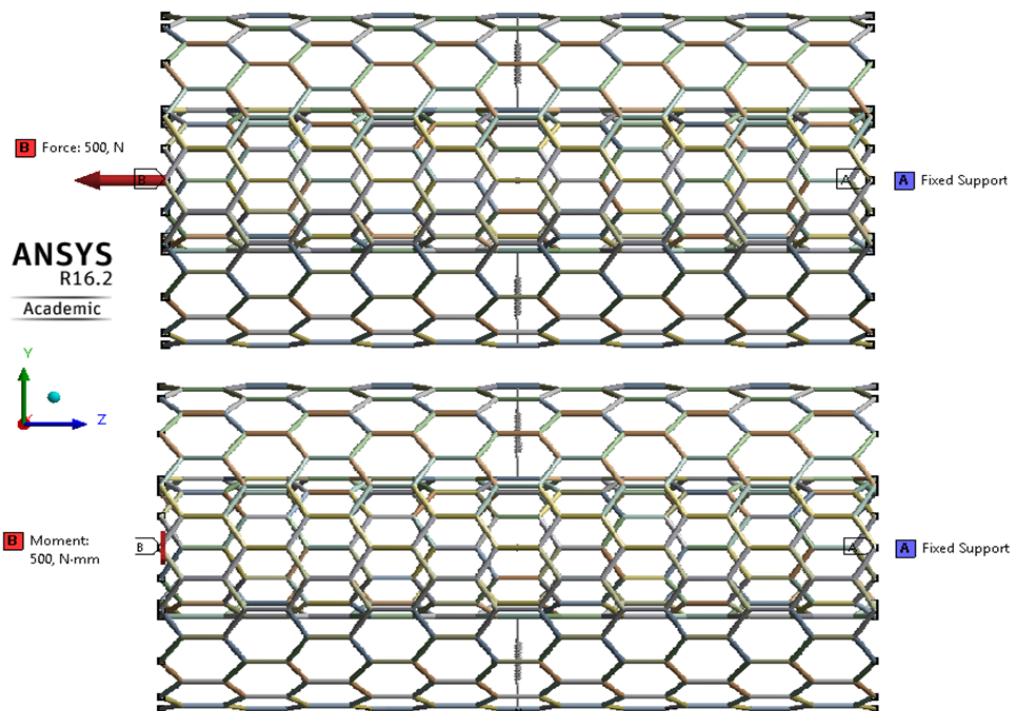


FIGURE 5.16: DWCNTs under tension and torsion tests

## 5.3 Results and Discussion

The analysis was carried out for obtaining the elastic properties of single, double and multiwall CNTs configurations. The results clearly showed the effect of chirality, defects, number of walls and the C-C bond orthotropic properties on the overall CNTs properties. The detailed results of the numerical analysis are given in Tables [B.1](#), [B.2](#), [B.3](#), [B.4](#), [B.5](#) and [B.6](#).

### 5.3.1 Effect of chirality on the mechanical properties

Since the chirality defines the types of SWCNT configurations, both zigzag and armchair were modelled and analysed. Table [5.6](#) shows the elastic and

shear modulus values of both zigzag and armchair configurations of a single wall carbon nanotube (SWCNT).

TABLE 5.6: Properties of pristine and vacancy defects SWCNTs (zigzag and armchair)

Diameter	Elastic Modulus		Shear Modulus	
(Å)	SWCNT- Pristine (GPa)	SWCNT- Vacancy Defects (GPa)	SWCNT- Pristine (GPa)	SWCNT- Vacancy Defects (GPa)
Zigzag (SWCNT)				
5.481	768.525	260.328	320.259	104.663
8.61	769.163	245.471	322.764	89.1
10.96	769.231	235.844	323.164	87.5
15.657	770.442	220.186	320.189	83.5
21.92	774.39	209.463	311.66	70.3
Armchair (SWCNT)				
5.424	755.213	257.637	362.658	97.8
8.13	755.149	240.937	360.011	92.9
10.84	755.659	231.113	359.075	89.0
14.916	759.881	221.317	358.563	85.0
21.696	765.583	228.005	358.125	84.0

It is evident that the elastic modulus of zigzag configuration is higher than the armchair as shown in Figure 5.17. The difference between the elastic modulus of the two configurations decreased with the increase in CNTs diameter. On the other hand, the armchair configuration has a higher shear modulus than

the zigzag. It is evident from these results that the chirality of the SWCNT-tube primarily affected the shear strength than the tensile strength.

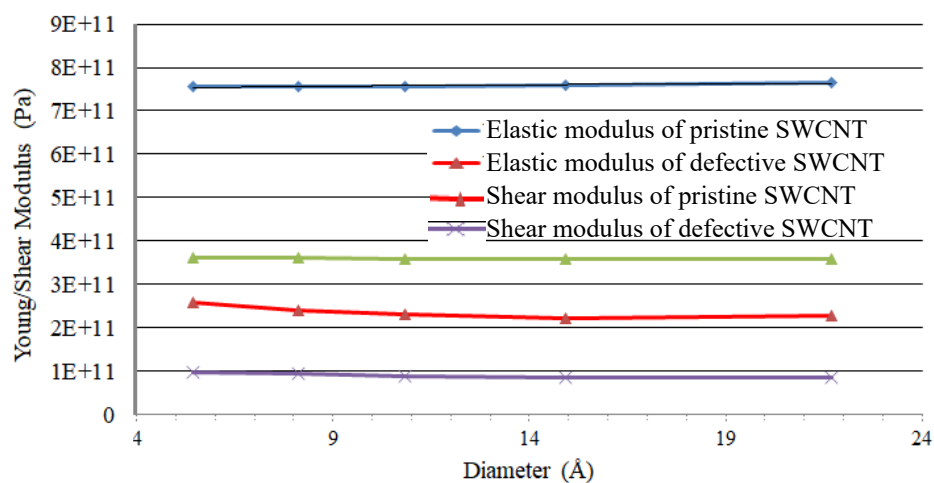


FIGURE 5.17: Elastic/shear modulus of pristine and defective SWCNTs Vs diameter

The variations in elastic and shear modulus for both configurations are attributed to the direction of hexagonal unit cell to the applied tensile and torsional loads. For the zigzag configuration, all six C-C bonds of a hexagonal unit have contributed towards carrying the applied load (Figure 5.18a), while the armchair unit cell have used only four C-C bonds for the similar types of loading (Figure 5.18b). Therefore the tensile strength of zigzag is higher than armchair. However, for the torsional loading, the reverse phenomenon could be seen as compared to the tensile loading (Figure 5.18c and d). The comparison based on chirality suggested that the zigzag SWCNTs of higher diameters could increase the properties of nanocomposites in axial direction. While for better transverse properties, armchair with smaller diameter would be a better choice as reinforcements.

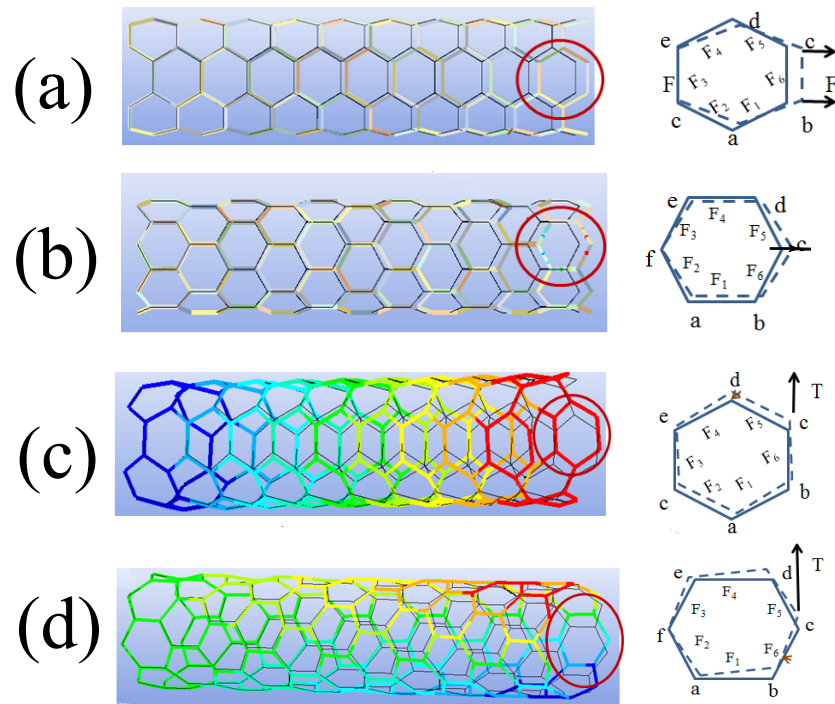


FIGURE 5.18: The deformation pattern of hexagonal units (a) armchair and (b) zigzag -tensile load (c) armchair and (d) zigzag-applied moment

The current analysis results align with the experimental values of 400 to 800 GPa as given by Treacy [228]. Further the results are also comparable with the other numerical analysis carried out by Mohammad [229], where they have used continuum mechanics method with non linear material properties and obtained the elastic properties of 881 GPa (elastic modulus) and 116 GPa (shear modulus). In addition, the molecular dynamics [230] results (elastic modulus 550 - 760 GPa for diameters in the range of 7-25 Å) for SWCNTs also align well with the SFS analysis results.

### 5.3.2 Effect of vacancy defects

The elastic properties of both zigzag and armchair configurations of SWCNTs with vacancy defects were analysed and their results were almost 70% lower

than the corresponding pristine configurations (Table 5.6). In addition, the vacancy defects have shown more influence on both elastic and shear modulus of both configurations as the diameter of CNTs was increased from 5.48 to 21.92 Å. The percentile decrease in SWCNT properties for the increase in diameter of a zigzag configuration was approximately 69.58% on elastic modulus and 72.79% on shear modulus. While for the armchair configuration, the percentile decrease was 68.9% on elastic modulus and 75.04% on shear modulus respectively (Table 5.7). It could be concluded from the Figure 5.19 that the SWCNTs with armchair configuration with vacancy defects have shown the better properties than the zigzag configuration. Moreover, the phenomenon was more significant for the diameter greater than 15 Å. From the above results, it could be pointed out that the armchair configuration with vacancy defects have shown improved properties than the zigzag configuration for the increase in CNTs diameter.

TABLE 5.7: Percentile decrease of elastic and shear modulus due to vacancy defects (zigzag and armchair)

Zigzag (SWCNT)		
Diameter (Å)	Elastic Modulus (%)	Shear Modulus (%)
5.481	66.13	67.32
8.61	68.09	72.38
10.96	69.34	72.91
15.657	71.42	73.89
21.92	72.95	77.43
Average	69.58	72.79
Armchair (SWCNT)		
Diameter (Å)	Elastic Modulus (%)	Shear Modulus (%)
5.424	65.89	73.01
8.13	68.09	74.19
10.84	69.42	75.19
14.916	70.87	76.29
21.696	70.22	76.53
Average	68.9	75.04

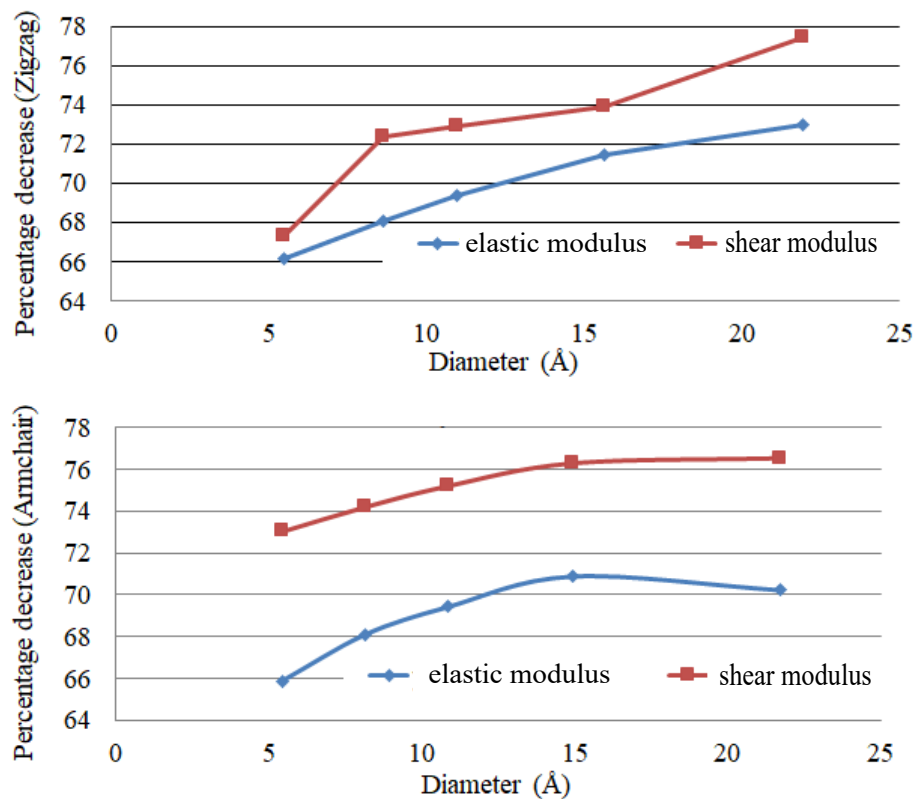


FIGURE 5.19: Percentage decrease in elastic/shear modulus due to vacancy defects in zigzag/armchair configuration (SWCNTs) as a function of diameter.

Ying et al. [231] have calculated the elastic modulus of 270 GPa for SWCNTs with defects. Sakhaee [232] showed that the elastic and shear modulus of defective SWCNTs were 470 GPa and 160 GPa respectively. The properties reported by these research works matched the values obtained by the current research work.

### 5.3.3 Effect of number of walls

The effect of the number of walls on the nanotube properties was also analysed using SFS models. The elastic and shear modulus of both DWCNTs and

MWCNTs approximately remain the same (Table 5.8 and Figure 5.20). For the individual cases, the elastic modulus of zigzag is higher than armchair and the armchair shear modulus is higher than the zigzag configurations. The elastic modulus varied inversely to the SWCNT's diameter until the value of 15.697 Å and then the variation of the elastic modulus became proportional to the SWCNT diameter. The elastic modulus of DWCNT was higher at lower diameter and was gradually reduced as the DWCNT diameter reached to 15.657 Å. Then for further increase in diameter, the elastic modulus started to increase again. For the MWCNT case, the elastic modulus values were increased proportional to the MWCNT number of walls and the diameter. However, the shear modulus of both DWCNTs and MWCNTs were increased as the diameter was increased up to 15.697 Å and then started to decrease with the increase in diameter.

TABLE 5.8: Properties of DWCNTs/MWCNTs of zigzag and armchair

Diameter (Å)	Elastic Modulus DWCNT (GPa)	Shear Modulus DWCNT (GPa)	Elastic Modulus MWCNT (GPa)	Shear Modulus MWCNT (GPa)
Zigzag				
	(Double)		(Multiple)	
5.481	794.199	320.235	769.884	318.893
8.61	783.311	322.752	779.365	322.767
10.96	770.318	323.312	777.732	323.208
15.657	761.661	328.514	783.622	321.879
21.92	782.353	311.379	794.376	310.314
Armchair				
5.424	757.671	366.795	664.844	301.52
8.13	753.1	359.754	653.188	297.13
10.84	75.9974	358.317	651.433	292.26
14.916	766.225	358.959	777.08	35.769
21.696	772.855	358.112	861.192	359.67

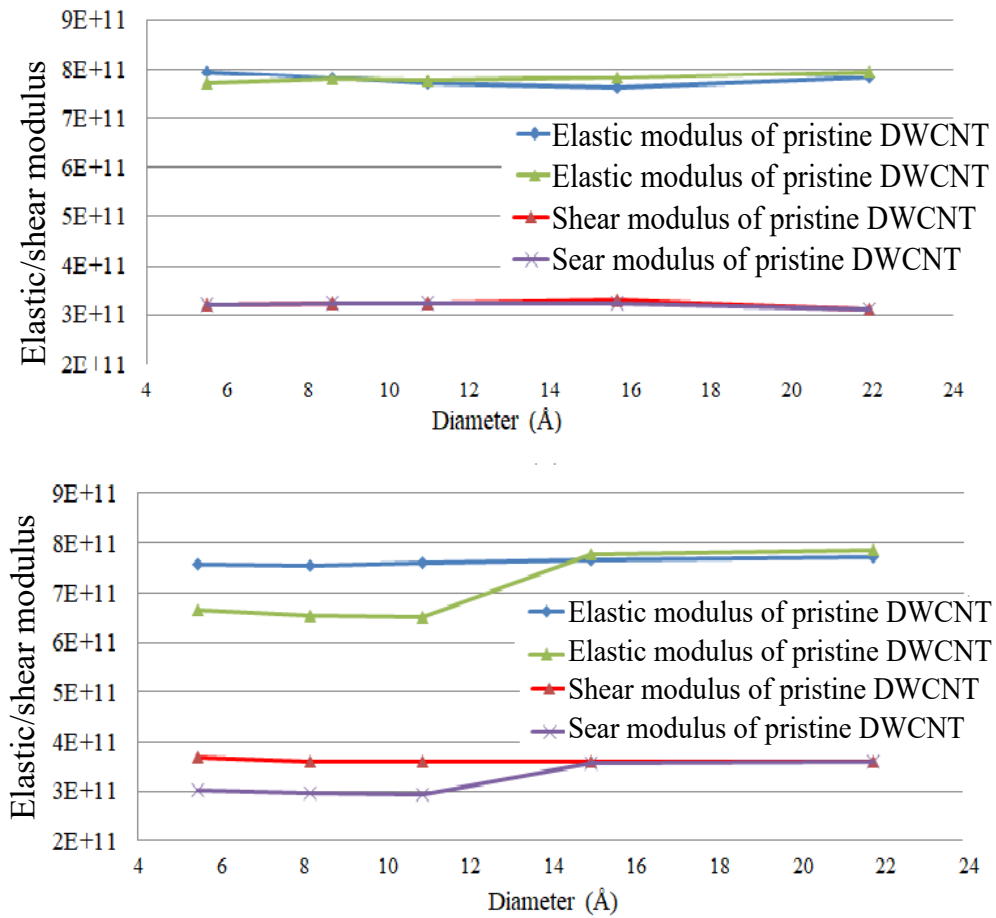


FIGURE 5.20: a) Elastic/shear modulus of pristine zigzag/armchair, b) Elastic/shear modulus of (DWCNTs/MWCNTs) obtained from tensile and torsion tests

Table 5.9 shows a comparative analysis of results from other research works along with the current SFS-Model research work. It could be concluded here that the SFS structure with orthotropic C-C chemical bond could provide accurate elastic properties of both zigzag and armchair configurations for both pristine and CNTs with vacancy defects.

TABLE 5.9: CNTs elastic properties comparison between the current study and other researches

Type of CNTs	Diameter (Å)	Elastic Modulus (GPa)	Shear Modulus (GPa)	Average percentage difference		Reference
				Elastic Modulus (%)	Shear Modulus (%)	
DWCNTs	10.0-30.0	1000-1100	400	-	-	[233]
DWCNTZigzag	5.41-21.92	761-794	311-323	32.173	21	Proposed SFS model
DWCNTArmchair	5.424-21.69	753-772	358-366	33.913	10	
MWCNTs	3.91-27.13	704	-	-	-	[234]
MWCNTs	5-8	990-1029	213-228	-	-	[232]
MWCNTZigzag	5.41-21.92	761-794	310-323	9.743	32.5	Proposed SFS model
MWCNTArmchair	5.424-21.69	651-786	292-360	8.571	30.909	

# Chapter 6

## Multiscale Modelling Analysis for Characterizing MNHCs

### 6.1 Introduction

Multiscale nanohybrid composites (MNHCs) are the combination of matrix with different types of reinforcements ranging from nano to macro length scales for producing materials with required properties. For example, the macrofibre composites with weak matrix-rich interlaminar regions are strengthened with nanofillers to produce various MNHCs. However, experimentally obtaining a suitable combination of different length scale reinforcements is time-consuming and expensive as presented in Chapter 4. Therefore, a multiscale analysis for analysing the effect of nanofillers on the macro-fibre composites is preferred and focus of this chapter. The numerical tools supplement the experimental analysis, which could be useful in extending the small-scale experimental results to the real-life applications.

Modelling the complete details of multiscale nanohybrid composites requires highly finer meshes along with higher computational resources. Therefore, researchers prefer working with representative volume elements (RVE) which contain all the constituents of the composite and are then analysed for obtaining the macro behaviour of polymer composite materials. Thus, the multiscale method would enhance the understating of the effect of the nanofillers (nanofibres and carbon nanotubes) within the interlaminar region of composites.

For this current research, multiscale modelling was used to predict the properties of the multiscale nanohybrid composite strengthened with random and aligned PAN nanofibre mats, PAN doped with p-SWCNTs and f-SWCNTs aligned nanofibres mats. Three length scales, such as nano, micro and macro scales were modelled. The nanoscale RVE of PAN nanofibre doped with SWCNTs was modelled first using the space frame structures (SFS) of SWCNTs and PAN polymer matrix. Simulated results of nanoscale RVEs were used to determine the equivalent properties of p-SWCNTs and f-SWCNTs doped nanofibres, which were further used in micro scale RVEs.

Four micro scale RVEs were developed to represent

- Epoxy embedded with random PAN nanofibre mats
- Epoxy embedded with aligned PAN nanofibre mats
- Epoxy embedded with PAN doped with p-SWCNTs aligned nanofibres mats
- Epoxy embedded with PAN doped with f-SWCNTs aligned nanofibres mats

These micro scale RVEs were analysed to obtain equivalent properties of the models which define the interlaminar regions. At the macro scale, MNHCs

were modelled as three layers of different constituents of the multiscale hybrid composites. Layer 1 and layer 3 were composed of epoxy embedded with macro glassfibres. Layer 2 was modelled as an equivalent constituent of nano strengthened interlaminar regions and the properties for this layer was obtained from the micro RVEs. The process of development at different scale is shown in Figure 6.1. The results of the simulated models were compared with experimental results.

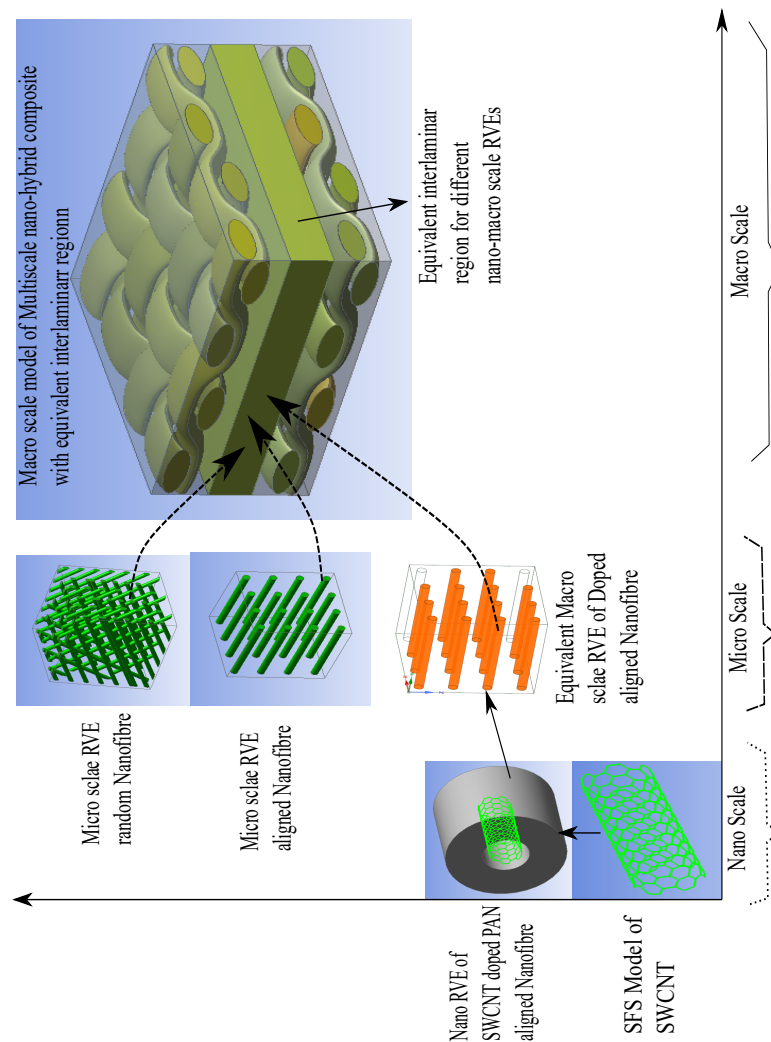


FIGURE 6.1: Modelling layout of multiscale nanohybrid composite

## 6.2 Multiscale Modelling Procedure

### 6.2.1 RVEs for SWCNT doped nanofibre

A circular three dimensional PAN nanofibre RVE was developed to analyse the SWCNTs doped PAN nanofibre properties. The RVE consisted of PAN polymer matrix, SWCNTs and interface bonding between SWCNTs and PAN polymer. The nanoscale SFS model of SWCNTs developed using the combination of molecular and structural mechanics presented in Chapter 5, was used for modelling the nanoscale RVE. The chosen model of SWCNTs had an armchair configuration with diameter 0.813 nm nearest to the purchased SWCNTs (diameter 0.83 nm). Dimensional details of the SWCNTs doped RVE are shown in Figure 6.2.

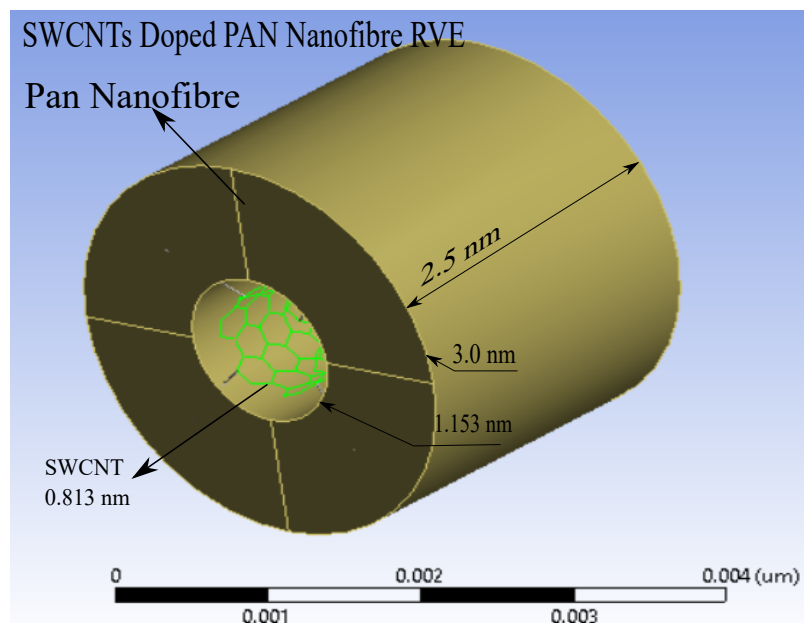


FIGURE 6.2: Modelling details of SWCNTs doped PAN nanofibre RVE

## Interface bonding modelling

The correct representation of SWCNTs-polymer interface is a challenging task due to length scale differences of SWCNTs and matrix. Therefore to reduce the length scale mismatch, multiscale modelling method was adapted. Interface bonding between SFS model of SWCNTs and surrounding polymer were defined as a Van der Waals (Vdw) and covalent bond (functionalization) interactions. These interactions were presented as a four equivalent mass less spring between the node of the SFS structure and PAN nanofibre cross-sectional area (Figure 6.3).

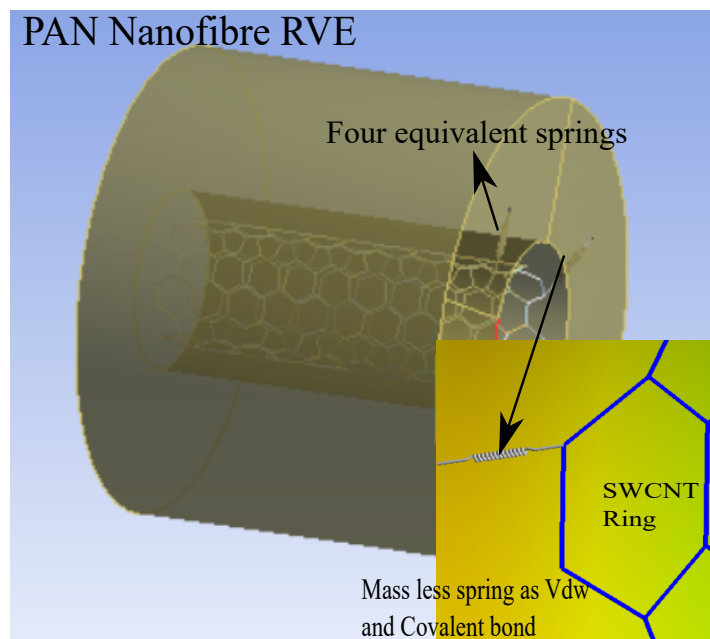


FIGURE 6.3: Modelling details of SWCNTs doped PAN nanofibre RVE

The equivalent spring constant for Vdw forces was defined as a sum of a single Vdw force spring constant ( $K_{single\ C-C} = 0.24245\text{ N/m}$ ) using the equation set in section 5.2.4, chapter 5. However, the sum of all interactions ( $K_{eq} = 1836\text{ N/m}$ , refer Table 5.5) was doubled ( $K_{Eq-Vdw} = 3672\text{ N/m}$ ), as the Vdw force about to double due to the surrounding polymer molecules [237].

Since the PVA chains were grafted to the SWCNT surface using FCA functionalization through covalent bonds (section 3.3, chapter 3). The number of covalent bonds produced by the FCA functionalization process on the surface of SWCNTs is extremely difficult to determine. Therefore, as suggested by Duan et.al. [238], 5% to 10% carbon atoms of SWCNTs were considered to be functional in doped PAN nanofibre RVE. A parametric study was carried out to determine the optimised percentage (8%) of functionalized carbon atoms for the range of 5% to 10% in the doped RVE. For the chosen length and diameter ( $d=0.8$  nm,  $l=2.34$  nm), 28 atoms (8% of 351) of the SFS structure were considered functionalized as shown in Figure 6.4. To present the 28 covalent bonds, four equivalent springs were used (Figure 6.3). The value of an equivalent spring constant for covalent bonds was obtained as given below;

$$K_{Eq-Covalent} = K_{Covalent} \times 28/4 \text{ where}$$

$$K_{Covalent} = K_r = 6.52 \times 10^{-7} \text{ N/nm [225]}$$

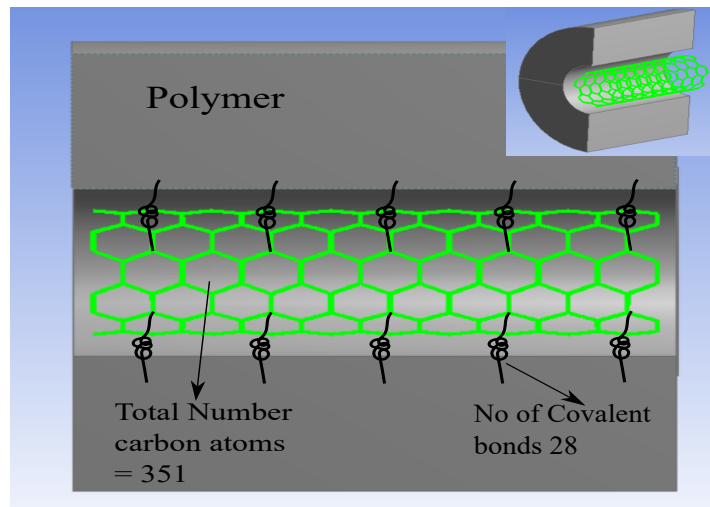


FIGURE 6.4: Illustration of f-SWCNT doped RVE with covalent bonds

One end of the RVE was fixed and tensile force was applied to the other end as shown in Figure 6.5a. Uniform mesh size was used and refined until FEA results

were converged. Tensile test result of SWCNT doped RVE was compared with the neat PAN RVE and properties of equivalent doped nanofibre were defined using the set of equations 6.1 - 6.4. Obtained properties of PAN nanofibre doped with pristine and functionalized SWCNTs are given in Table 6.1.

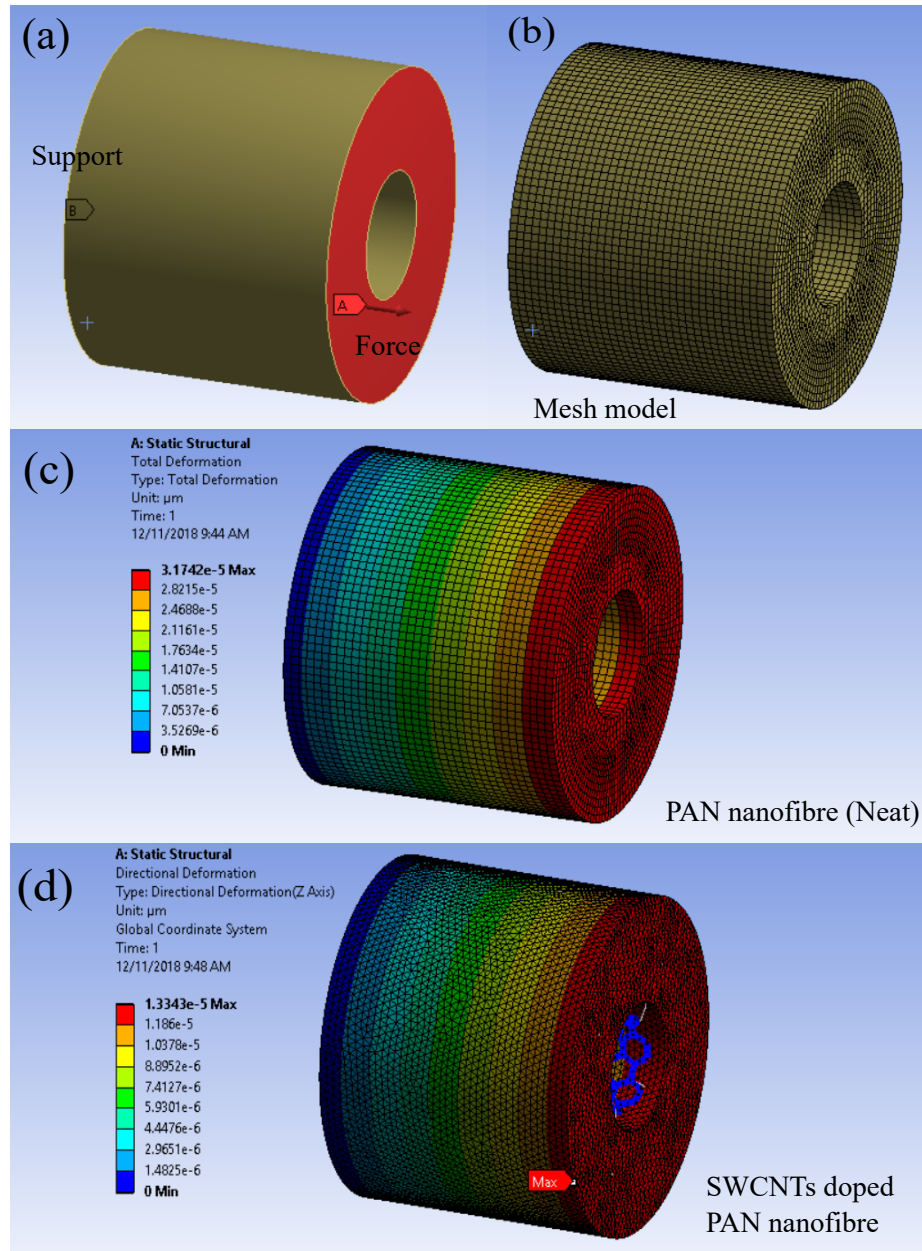


FIGURE 6.5: Modelling details of SWCNTs doped PAN nanofibre RVE

$$\frac{E_{Equivalent-RandomnanofibreRVE}}{E_{Neatepoxy}} = \frac{\Delta L_{Matrix-RandomnanofibreRVE}}{\Delta L_{Neatepoxy}} \quad (6.1)$$

$$\frac{E_{Equivalent-AlignednanofibreRVE}}{E_{Neatepoxy}} = \frac{\Delta L_{Matrix-AlignednanofibreRVE}}{\Delta L_{Neatepoxy}} \quad (6.2)$$

$$\rho_{Equivalent} = f \times \rho_f + \rho_m \times (1 - f) \quad (6.3)$$

$$\nu_{Equivalent} = \nu_f V_f + \nu_m V_m \quad (6.4)$$

Where

E = Elastic Modulus

$\Delta L$  = Change in length

$\rho$  = density

$\nu$  = Poisson's ratio

$V_f$  = Fibre volume fraction

$V_m$  = Matrix volume fraction

TABLE 6.1: Properties of the equivalent doped nanofibres materials

Material	Properties of materials		
	Elastic Moduls GPa	Poisson' s ratio	Density g/cm3
SWCNTs (0.813 nm, Armchair)	755.149	0.1	1.66
Aligned PAN nanofibre	130 [235]	0.3-0.35	1.184
p-SWCNTs doped nanofibre	307.026	0.324	1.185
f-SWCNT doped nanofibre	1084.36	0.324	1.185

### 6.2.2 Micro scale RVEs for random and aligned PAN nanofibre mats, p-SWCNTs and f-SWCNTs doped aligned nanofibres mats strengthened interlaminar region

Three-dimensional micro cubic RVEs were developed to present the matrix rich interlaminar region embedded with random and aligned PAN nanofibre mats. The volume fraction of the nanofibres used in the micro RVEs was kept approximately equal to 0.5% of the glass fibre composite. The diameter of the nanofibres was set as 450 nm for random and as 150 nm for aligned respectively based on the experimental results. Figure 6.8 shows the dimensions of the RVEs.

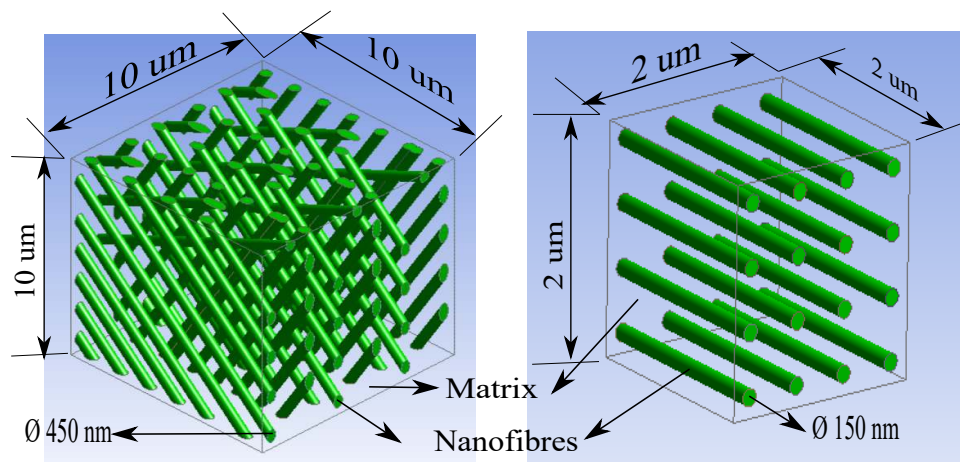


FIGURE 6.6: Details of random and aligned nanofibre-matrix RVEs

The nanoscale RVE of PAN nanofibre doped with SWCNTs was modelled first using the space frame structures (SFS) of SWCNTs and PAN polymer matrix. Simulated results of nanoscale RVEs were used to determine the equivalent properties of p-SWCNTs and f-SWCNTs doped nanofibres, which were further used in microscale RVEs. The properties of nanoscale RVE of PAN nanofibre

doped with p-SWCNTs and f-SWCNTs doped nanofibre found in Section 6.2.1 (Table 6.1) were assigned to the aligned nanofibres-matrix RVE. The modelling process for nano RVE to micro RVEs is shown in Figure 6.7.

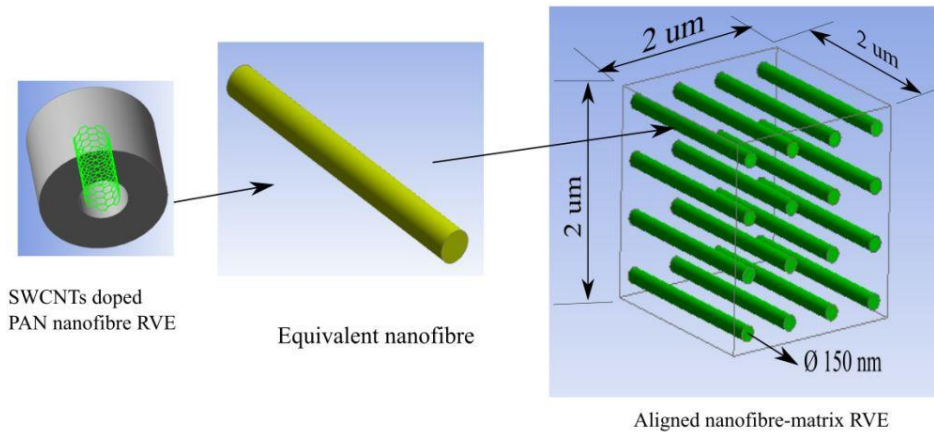
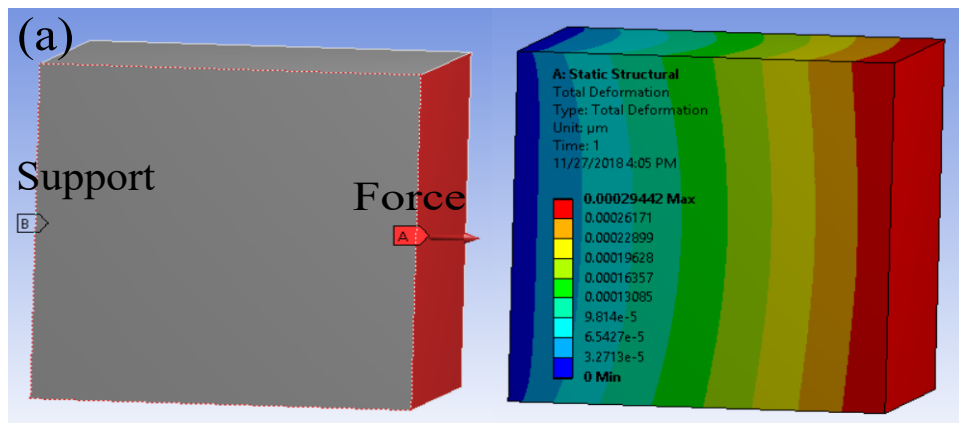


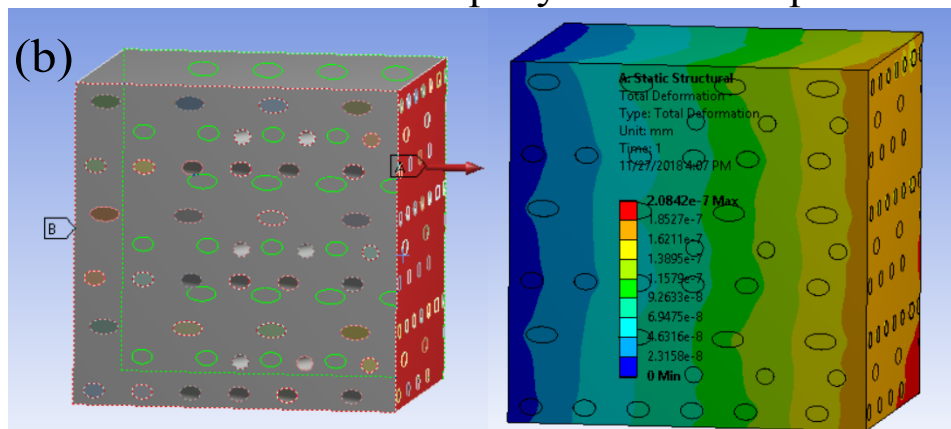
FIGURE 6.7: Modelling process for p-SWCNTs and f-SWCNTs doped micro RVE

The matrix-nanofibre interaction on matting surfaces was defined using the "bonded contact" option provided in the ANSYS software. Bonded contacts consider the surface of the mating glued or welded with each other. One end of the RVEs was fixed and the tensile force was applied to the other end as shown in Figure 6.8. Hexahedral mesh with uniform size was used and refined until the result was converged.

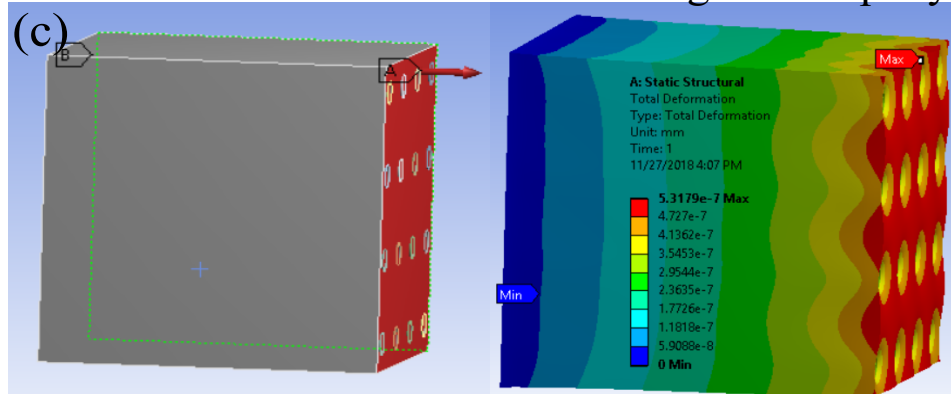
All four micro RVEs were simulated and results were compared with the neat matrix RVE (control sample) under same boundary conditions. The equivalent material properties of interlaminar regions embedded with random and aligned PAN nanofibre mats, PAN doped with p-SWCNTs and f-SWCNTs aligned nanofibre mats were obtained, as explained in the previous Section 6.2.1. Calculated equivalent properties of interlaminar regions are given in Table 6.2.



Micro RVE: Neat epoxy:Control sample



Micro RVE: Random nanofibres strengthened epoxy



Micro RVE: Aligned nanofibres strengthened epoxy

FIGURE 6.8: Boundary conditions and tensile test results; (a) Epoxy RVE (control sample), (b) Matrix-random nanofibres RVE, (c) Matrix-aligned nanofibres RVE

TABLE 6.2: Properties of the equivalent random and aligned doped-matrix RVE

Material	Properties		
	Elastic Modulus GPa	Poisson' s ratio	Density g/cm <sup>3</sup>
PAN random nanofibre	48	0.3-0.35	1.184
PAN aligned nanofibre	130 [236]	0.3-0.35	1.184
Neat Epoxy	4.3	0.3-0.35	1.148
Random nanofibre strengthened Epoxy/ Equivalent interlaminar region	6.16	0.3-0.35	1.14818
Aligned nanofibre strengthened Epoxy/Equivalent interlaminar region	9.41	0.3-0.35	1.14818
p-SWCNTs doped aligned nanofibre strengthened epoxy/ Equivalent interlaminar region	12.56	0.33	1.1482
f-SWCNTs doped aligned nanofibre strengthened epoxy/ Equivalent interlaminar region	16.356	0.325	1.1482

### 6.3 Macro Scale Modelling of 32% Glass Fibre Composite (GFC)

Construction of a woven glass fibre mat consisted of a repeated structures (basic unit cell, BUC) shown in Figure 6.9 which can be used to predict the properties of the fibreglass reinforced composite. The process is similar to the tensile test, where a part of the whole composite is tested to determine the tensile strength of the whole material.

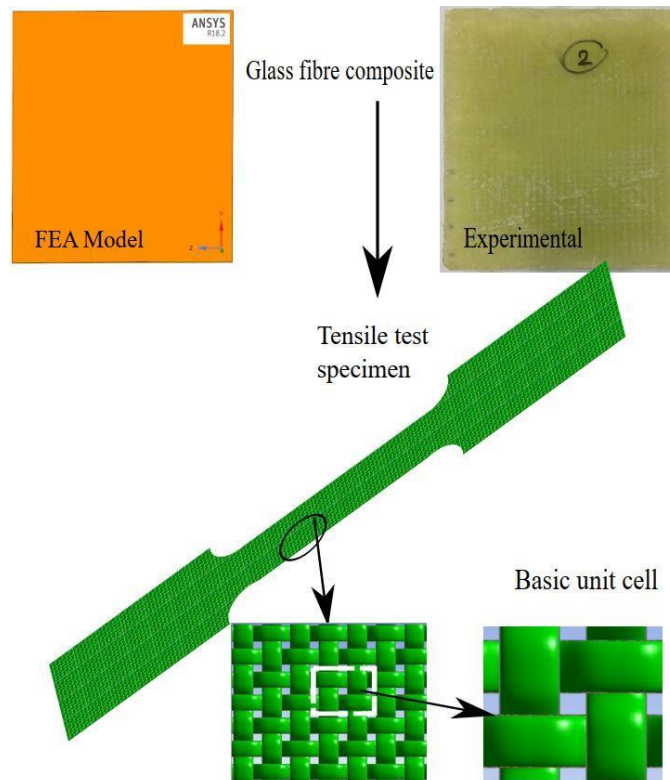


FIGURE 6.9: Composite model developing process

Initially, the geometry of the practically used glass fibre composite was modelled as a woven mat. Practically, tows of the glass fibre mats was consisted of elliptical tows having a number of circular strands as shown in Figure 6.10.

For simplicity, a single tow without circular strands was developed by sweeping an elliptical cross sectional area along the zigzag smooth path using design modeller of ANSYS 18.2. The tow was patterned to develop the woven glass fibre composites (Figure 6.10). The volume of the glass fibre mat was adjusted so that the glass fibre mats were 32% of the matrix in the Numerical model.

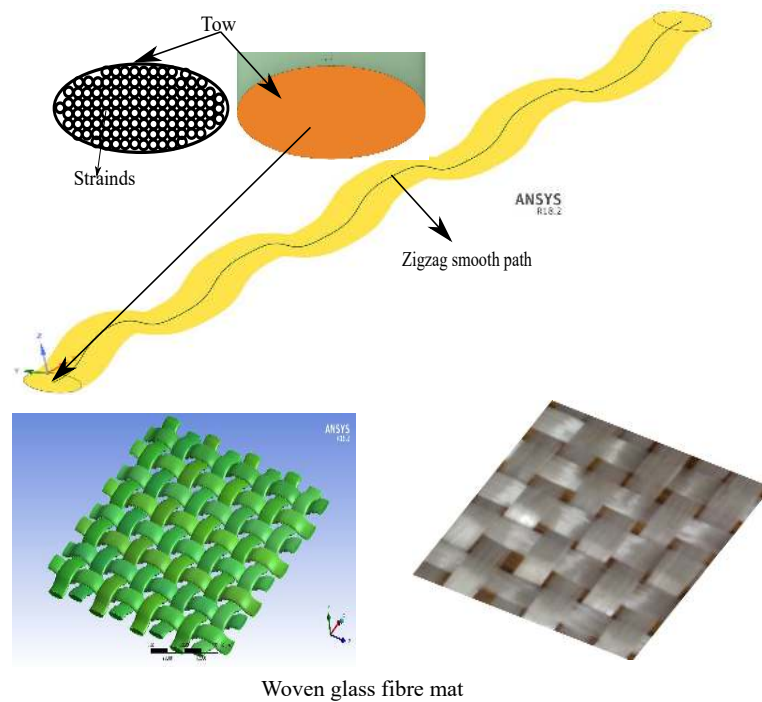


FIGURE 6.10: Woven glass fibre mat development process

Numerical model of a matrix having isotropic properties with dimensions  $2640 \text{ um} \times 2640 \text{ um} \times 3200 \text{ um}$  was developed to analyse the tensile properties of the composites. The practically used (refer Chapter 4) volume of seven woven glass fibre (32%) was embedded as a woven pattern of seven layers into the matrix. This study was intended to determine the effect of the different kinds of electrospun nanofibres mats within the interlaminar region. Therefore interlaminar region (Figure 6.11) was focused and Numerical model was reduced to two glass fibre layers Numerical model to minimise the computation cost.

The Numerical model consisted of a matrix and two layers of woven glass fibres mat as shown in Figure 6.11.

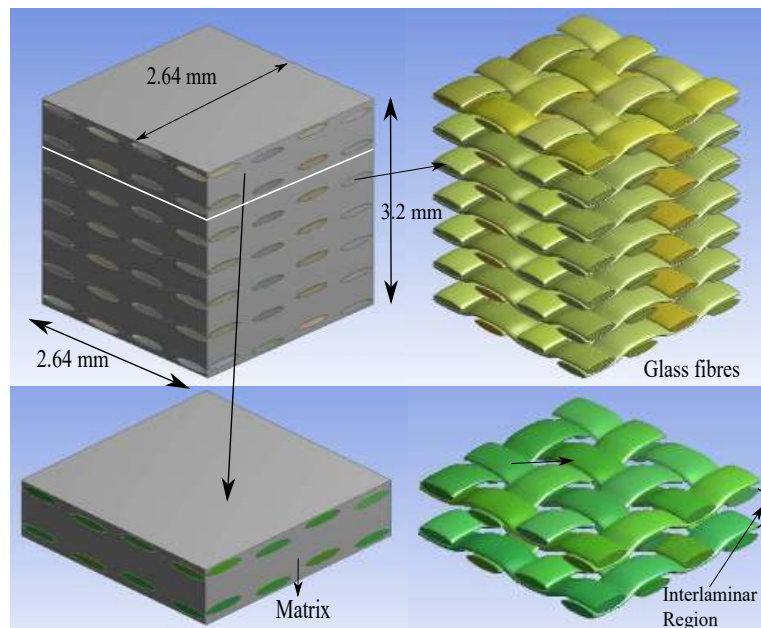


FIGURE 6.11: Details of numerical model for 32% glass fibre composite

### 6.3.1 Macro scale of modelling of MNHCs

The full - scale MNHCs model and its components require detailed models at different length scales, such as nano, micro and macro. Although the approach accurately determines the properties of the composite. However, due to nano-and micro-scale modelling, a very small discretization (mesh) leads to prohibitive computational resources and time. Therefore replacing smaller lengths constituents with an equivalent material having same properties, is cost effective in time and computation facility.

In this study, MNHCs were developed by replacing the matrix rich region of 32% glassfibre composite with an equivalent interlaminar regions as shown in Figure 6.12a and b. Layer 1 and layer 3 were modelled as a epoxy embedded

with macro glassfibres. while Layer 2 was considered as equivalent interlaminar regions. The properties of equivalent interlaminar regions were obtained from the analysis of nano and micro scale RVEs which are given in the Tables 6.1 and 6.2.

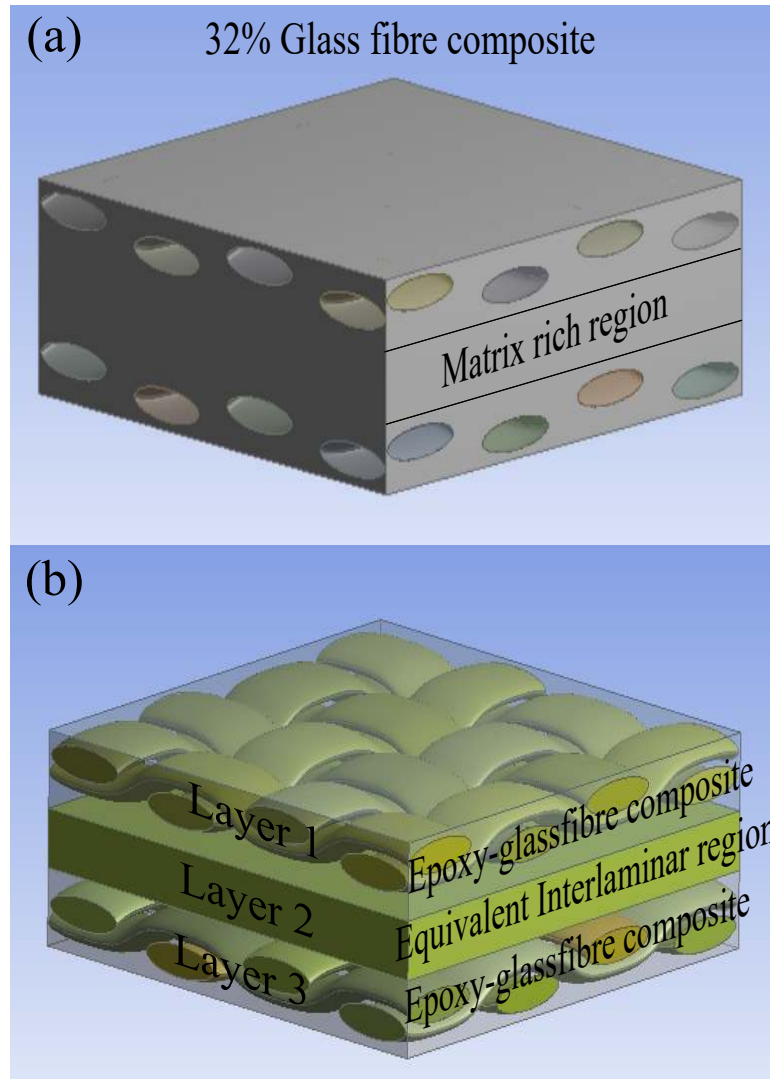


FIGURE 6.12: Equivalent interlaminar region MNHCs model

### 6.3.2 Boundary conditions

Models were analysed under axial force. One end of the model was constrained and force was applied to the other end as shown in Figure 6.13a. This supposition is compatible with the condition of experimental tensile tests in which one clamp was stationary and another clamp was moved in the opposite direction. In this study, uniform meshing technique along with element type SOLID186 for ANSYS simulation were generated. All nodes at the mating surface were made conformal by using node merge options. The mesh was refined until the convergence of the results. The mesh view of the Numerical model is shown in Figure 6.13b. Bonded contact regions were used between different types of materials i.e. glassfibres, nanofibres, equivalent interlaminar regions and epoxy matrix.

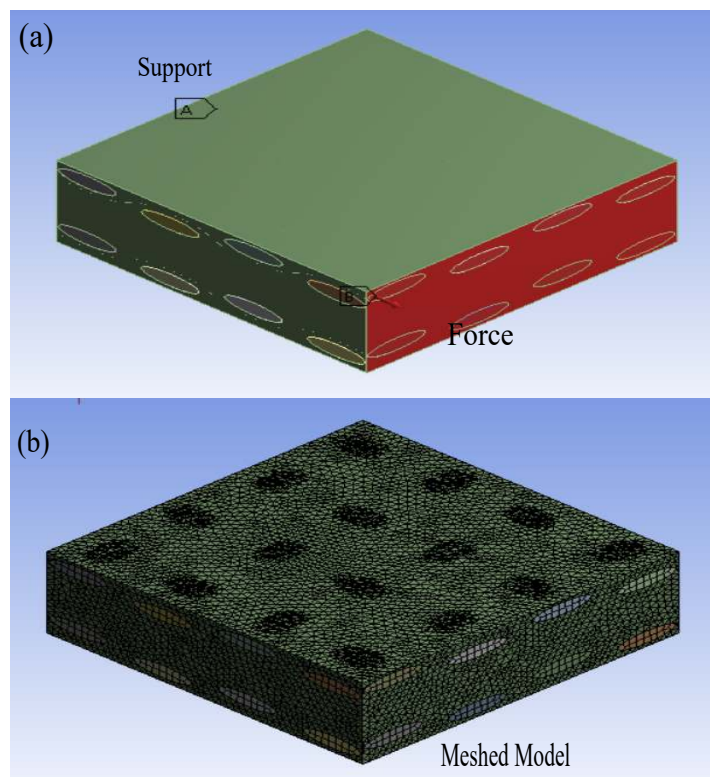


FIGURE 6.13: (a) Numerical model boundary conditions and (b) Meshed model

---

The boundary conditions and mesh were kept the same in all simulations to determine the effect of the different nanofibre mats on the strength of MNHCs. Following types of composites were analysed;

- Neat fibre glass composite (FGC)
- Random nanofibres mat strengthened hybrid composites
- Aligned nanofibres mat strengthened hybrid composites
- p-SWCNTs doped aligned nanofibre mat strengthened hybrid composites
- f-SWCNTs doped aligned nanofibre mat strengthened hybrid composites

## 6.4 Result and Discussions

Five different types of multiscale models consisting of 32% glass fibre composite, random and aligned PAN nanofibre mats, PAN doped with p-SWCNTs and f-SWCNTs aligned nanofibres mats strengthened hybrid composites were analysed. Only tensile tests were simulated and compared with the experimental values. Elastic modulus of all numerical models was determined using the equations 6.5 and 6.6.

$$E_{neat} = \sigma/\epsilon \quad (6.5)$$

$$E_{neat} = (F/A)/(\Delta L/L) \quad (6.6)$$

Figure 6.14 shows the deformation contours in the simulated 32% glass fibre composite model. Maximum elongation occurred within the matrix-rich inter-laminar region (Figure 6.15), which resulted in the crack being initiated first

into the subject region and the composite material failing. The result suggested that the interlaminar region was the weakest part of the composites due to the presence of single constituent (matrix).

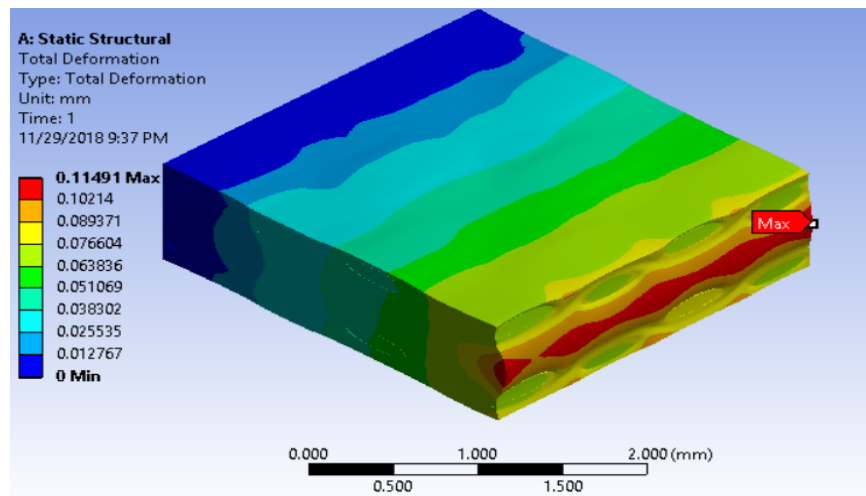


FIGURE 6.14: Stress contours of Neat glass fibre composite under tensile load

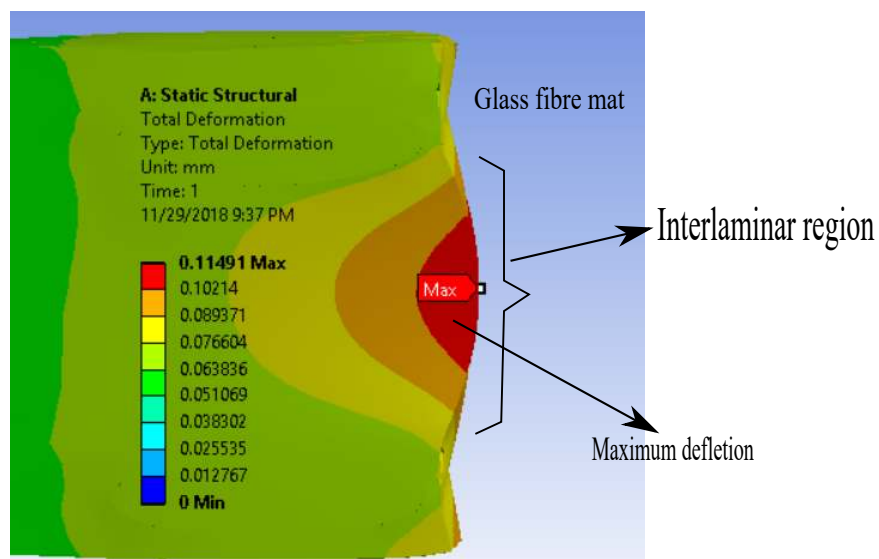


FIGURE 6.15: Maximum deflection within the interlaminar region of 32% glass fibre composite

The FEA simulation result was 8.91% higher than the experimental results (Figure 6.16). The difference can be attributed to manufacturing defects such as void generation and thickness variation due to pressure and temperature variation during the VARTM process. Another reason may be the micro notches development over the outer surfaces due to the machining process of tensile pieces.

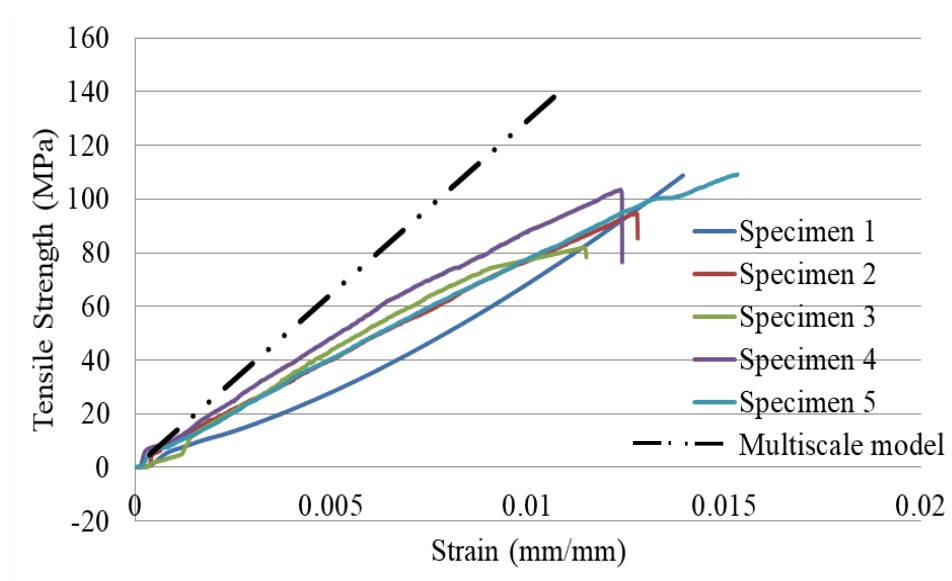


FIGURE 6.16: Theoretical vs experimental stress-strain curve for neat glass fibre composites

In the second simulation, the weak matrix rich region was strengthened with equivalent material of random nanofibres mat strengthened interlaminar region. The result of the model is shown in Figure 6.17a which described the deformation contours produced in the body. Figure 6.17b shows that the deformation in the interlaminar region was reduced by random nanofibers and the strength of the neat glass fibre composite was improved by 18.61%. Theoretical tensile test results were compared to experimental tensile test results (Figure 6.17c). The numerical results were found to be in accordance with the experimental data presented in Chapter 4. When the MNHCs model was developed

with equivalent randomly oriented nanofibre mats, the numerical modelling error of 8.91% for 32% glass fibre composite was reduced to 5.236%. Error gap reduction may be explained as the experimentally used random nanofibres mat filled the voids and reduced the mismatch with theoretical work.

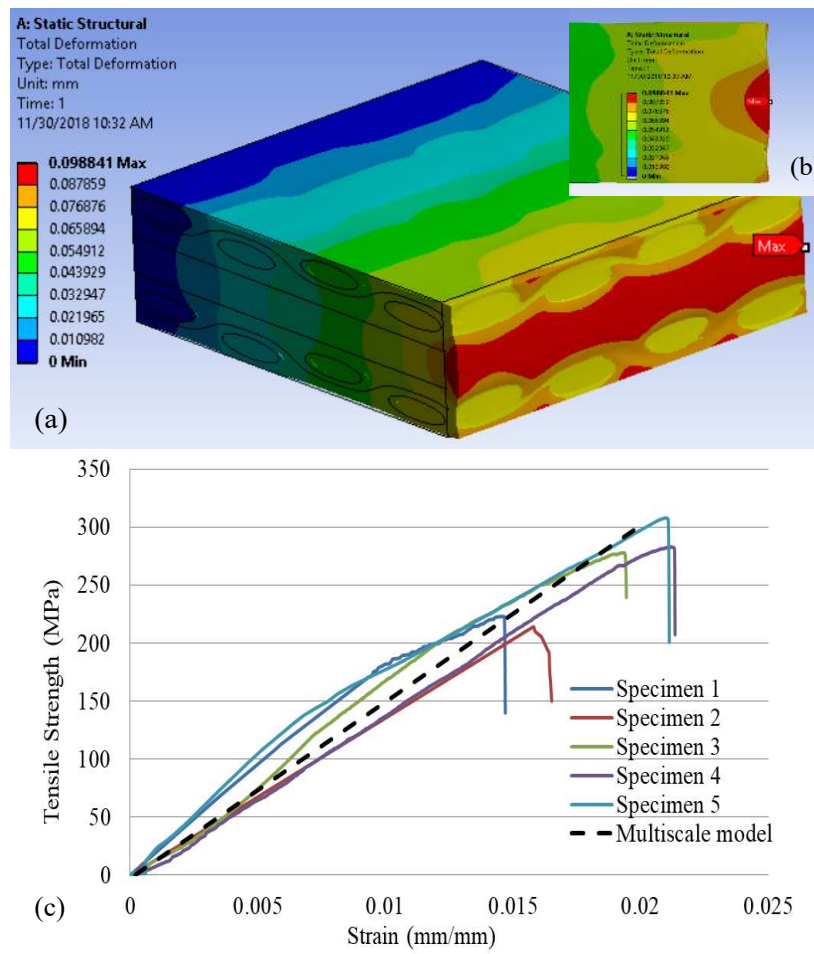


FIGURE 6.17: Random nanofibre mat strengthened hybrid composites results (a) Deformation contours (b) Maximum deflection with in the inter-laminar region (c) Theoretical vs experimental stress-strain curves

Thirdly, the layer 2 was assigned properties of equivalent matrix-aligned nanofibres mat RVE. The numerical result of the aligned nanofibres mat strengthened hybrid composite showed greater resistance to the applied load than the random nanofibres mat strengthened hybrid composite. Figure 6.18a shows that

deflection in the interlaminar region was reduced by 17% compared to 32% composite fibreglass. The reason for the higher elastic modulus can be concluded as (i) aligned nanofibres provided direct resistance due to the inline direction to the applied force; (ii) same volume fraction (0.5%) of nanofibres provided approximately nine times more length of nanofibres network within the interlaminar region due to the reduced diameter. A comparison between multiscale model analysis and experimental results of aligned nanofibre mat strengthened nano hybrid composite (Figure 6.18b) showed a consistency in the results.

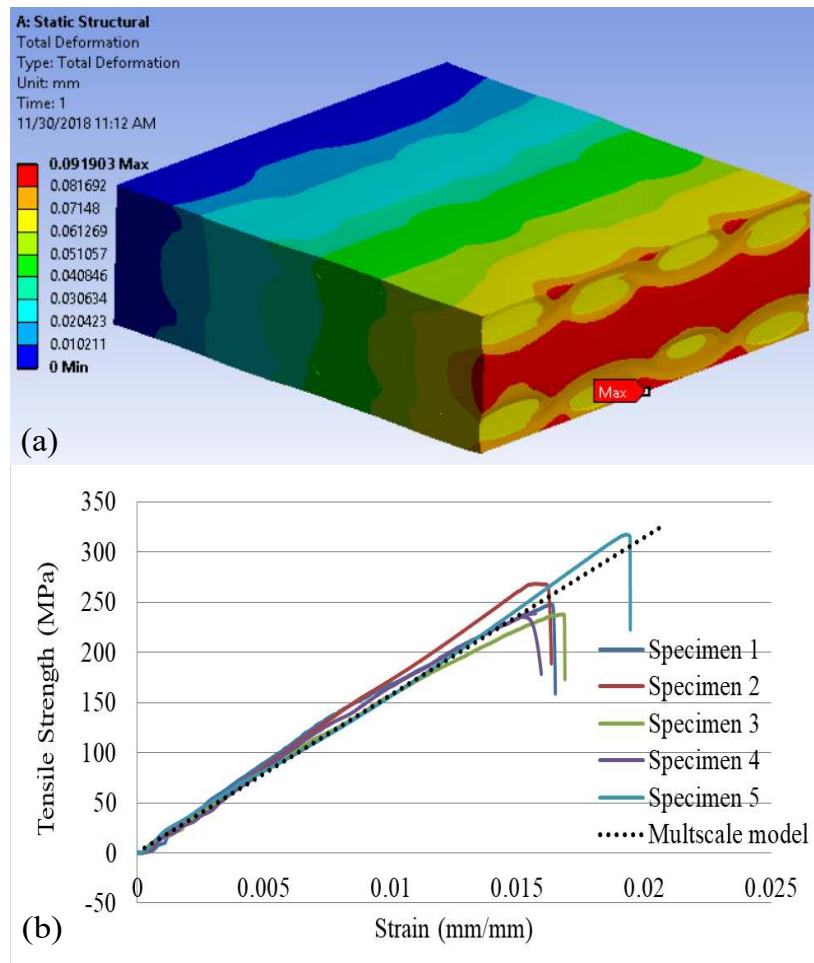


FIGURE 6.18: Aligned nanofibres mat strengthened hybrid composites results (a) Deformation contours (b) Theoretical vs experimental stress-strain curves

Further, response of multiscale model with equivalent interlaminar region composed of p-SWCNTs doped nanofibres mat and matrix was analysed. Compared to the previous MNHCs, it is evident from the Figure 6.19a that p-SWCNTs doped nanofibre mat provided more strength to the interlaminar region. The additional strength p-SWCNTs within the nanofibres mat produced stronger nanofibres mat and resulted in the higher modulus. Theoretical result obtained for p-SWCNTs doped aligned nanofibre mat were compared with the experimental results and were found in good agreement with each other as shown in Figure 6.19b.

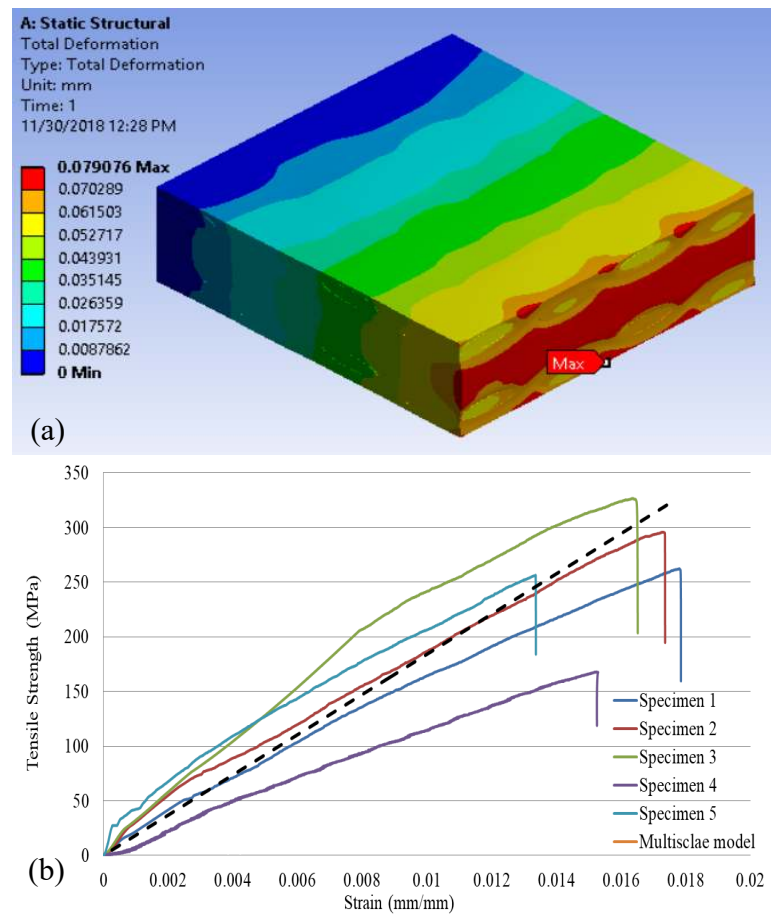


FIGURE 6.19: p-SWCNTs doped aligned nanofibres mat strengthened hybrid composites results (a) Deformation contours (b) Theoretical vs experimental stress-strain curves

In the fifth model, 32% fibre glass composite strengthened with f-SWCNTs doped aligned nanofibre mat was analysed. It was found (Figure 6.20a and b) that f-SWCNTs doped aligned nanofibres mat maximised the elastic modulus of the overall hybrid composite as compared to the other all nanofibre mats. It was because the covalent bond improved the bondage between the f-SWCNTs and nanofibres which enhanced the strength of the nanofibres mat. The strong nanofibre mat resulted in the improved properties of the interlaminar region, leading to the higher modulus.

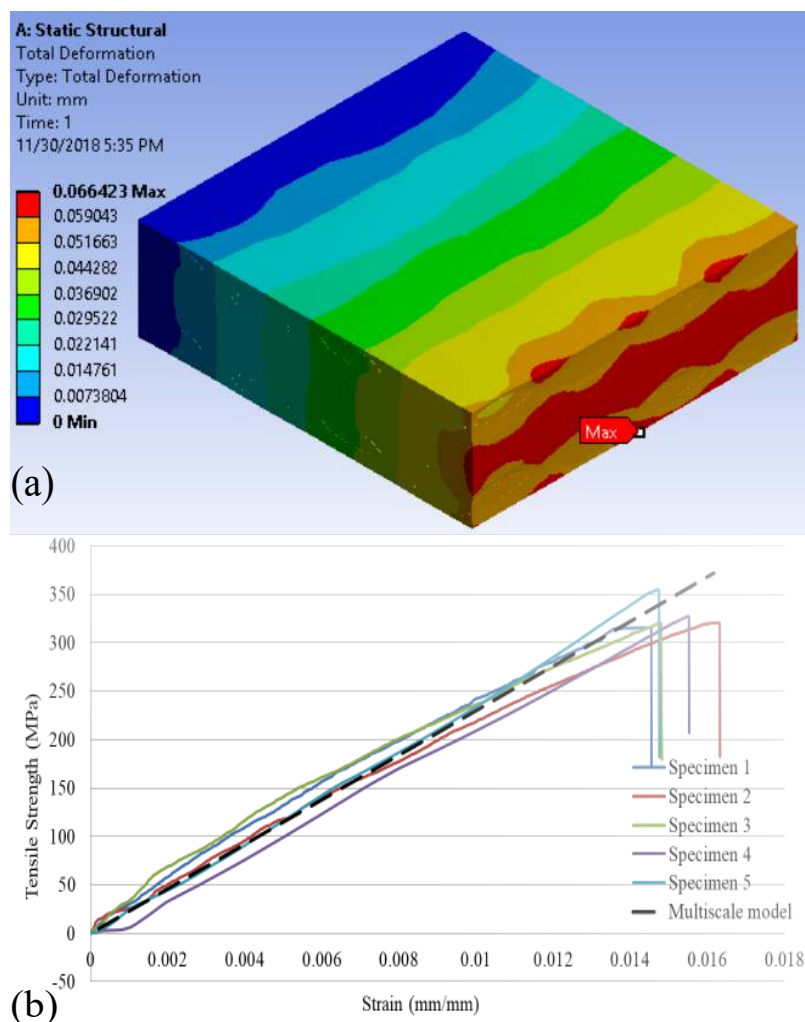


FIGURE 6.20: f-SWCNTs doped aligned nanofibres mat strengthened hybrid composites results (a) Deformation contours (b) Theoretical vs experimental stress-strain curves

The Figure 6.21 shows the overall results of the numerically modelled composites and their comparison with the experimental results. From the five different models, it is inferred that the glass fibres composites had the matrix rich regions which were the weakest in strength. Different nanofibres mat networks enhanced the strength of the weak interlaminar region and resulted in increased modulus. Among the models, a gradual increase in the elastic modulus of glass fibre composite with random and aligned PAN nanofibre mats, PAN doped with p-SWCNTs and f-SWCNTs aligned nanofibre mats was observed. Thus these observations recommended that the alignment, reduced diameter and uniform distribution along with f-SWCNTs doped nanofibres mat can enhance the properties of the interlaminar region.

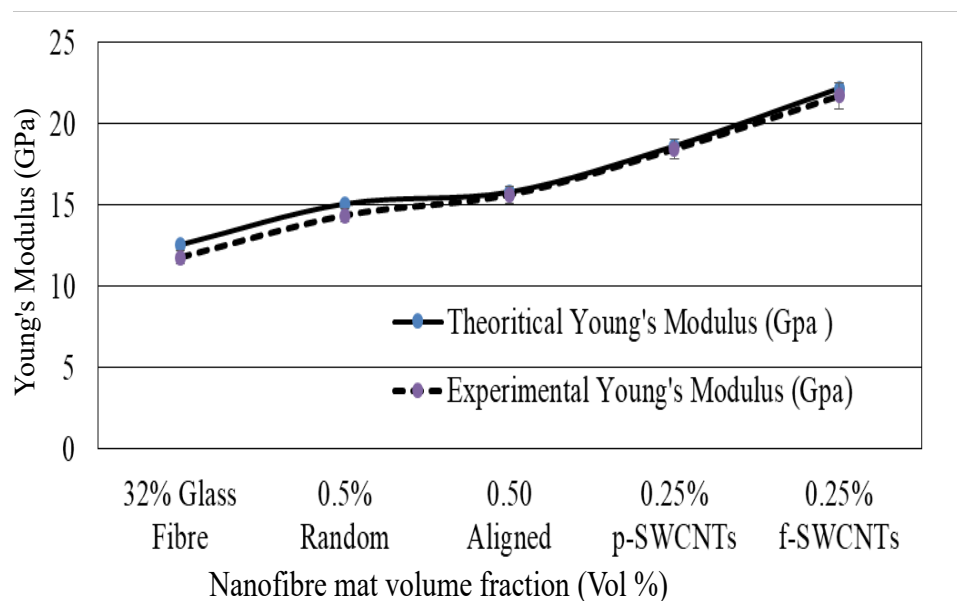


FIGURE 6.21: Comparison between experimental and theoretical elastic modulus of multiscale nanohybrid composites

Moreover, the comparison of the experimental and theoretical results concluded that FEA modelling can be used to design a composite without experimentation which will provide a fast and economical solution. Figure 6.22 shows

the percentage error between the experimental and theoretical work. It provided that the error was high initially which was reduced with the addition of different nanofibres mats. The error was minimum in the fourth model developed with p-SWCNTs doped aligned nanofibres mat and again become higher when analysed with f-SWCNTs doped nanofibres mat. The higher error for the neat glass fibre composite may be associated with voids, a variation in sample thickness due to the variable parameter of the VARTM process. While in the experimentally developed multiscale nanohybrid composites, the voids were reduced by PAN nanofibers mat and their variants. This led to a smaller error between experimental and theoretical results.

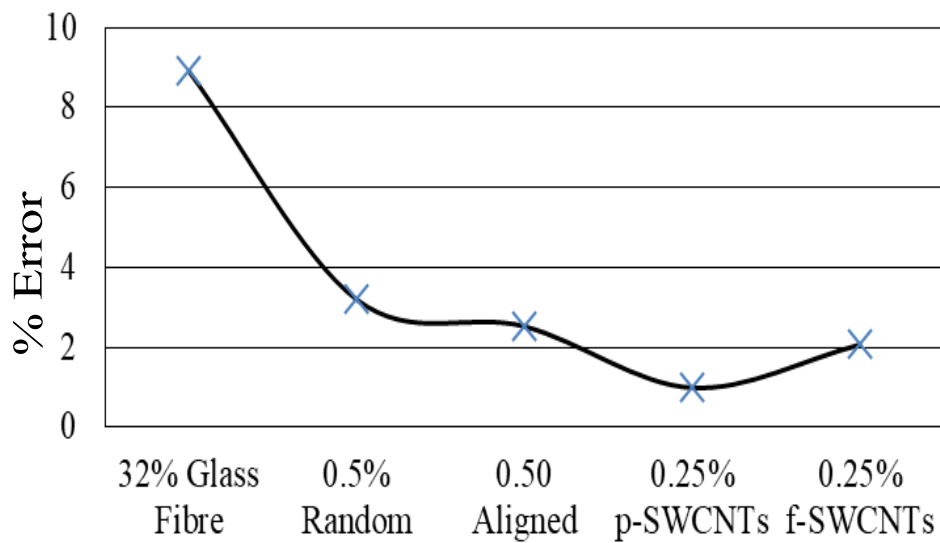


FIGURE 6.22: % Error-Theoretical vs Experimental elastic modulus

# Chapter 7

## Conclusion and Recommendations

### 7.1 Conclusions: Experimental Study of MN-HCs

In this study, multiscale nanohybrid composites were developed using a different kind of nanofibres mats. These were random, aligned, p-SWCNTs and f-SWCNTs doped nanofibres mat. The effect of the different volume fractions of glass fibres and random nanofibres were optimised. Electrospinning process was successfully modified to improve the molecular orientation and alignment along with reduced diameter. Further aligned nanofibre mats produced with AVEs were practically examined to determine their effect on the matrix rich interlaminar region of FGC. Aligned nanofibre mats were also doped with pristine and functionalized SWCNTs to utilise their high mechanical properties. Morphological (SEM, FTIR, Raman spectroscopy) and mechanical testing (Tensile, flexural, and bending tests) were used to investigate the improving effect of all

kinds of nanofibres mats on the interlaminar region. The following conclusions can be drawn from the results obtained:

- Different volume fractions of random nanofibres (0.1%, 0.2%, 0.5% and 1%) were produced using general electrospinning technique and used as interalia within the matrix rich interlaminar region of FGC. The hybrid composites were investigated and optimized.
- A conventional electrospinning process was modified using two vertical AVEs. The modified technique was simple and economical as it uses only one DC power supply and does not require any auxiliary voltage.
- The fractographic study confirmed that auxiliary vertical electrodes (AVEs) added to general electrospinning technique, reduced the diameter as low as 50 nm, enhanced the alignment of the nanofibres and improved molecular orientation.
- Optimised volume fraction (0.5%) volume fraction of random nanofibres mat was aligned using AVEs and was used to strengthen the matrix rich interlaminar region. Aligned nanofibres mat noticeably improved the tensile, flexural and impact resistance compared to the same volume fraction of random nanofibres mat.
- p-SWCNTs were functionalized using FCA. FTIR and Raman analysis confirmed the attachment of PVA to the surface of the SWCNTs without any noticeable damage.
- Compared to all the other composites, p-SWCNTs and f-SWCNTs doped nanofibre mats had higher strength and modulus. f-SWCNTs doped aligned nanofibre mats provided the highest increase in the tensile (111.34%),

---

flexural (117.11%) and impact resistance (180.03%). Matrix rich interlaminar region was the weakest region where failure was dominant without any nanoreinforcement. Different kinds of nanofibre mats strengthened the interlaminar region and enhanced the strength according to their geometry (diameter), orientation (random or aligned), molecular orientation, doping with f-SWCNTs/p-SWCNTs. Nanofibres mat developed a network which restricted/diverted the micro/nanocracks within the matrix interlaminar region through crack bridging.

- All kinds of composites were produced using VARTM method having similar manufacturing parameters. The parameters included; the volume of resin-hardener, glass fibre volume fractions, filling pressure and curing time. This provided the strengthening effect of the different kind of nanofibre mats within the interlaminar region.

## 7.2 Conclusions: Numerical Study of MNHCs

Zigzag and armchair configurations of SWCNTs along with vacancy defects and the number of walls, were modelled and characterized by the SFS method. The orthotropic properties of the C-C bond were calculated by comparing structural mechanics and molecular mechanics energy expressions along with the parametric study. A mathematical model of van der Waals equivalent springs between consecutive walls was developed to analyse their effect on DWCNTs and MWCNTs. The research showed that the SFS model elastic properties were in good agreement with the experimental and theoretical values found in the literature.

Multiscale model for experimentally produced MNHCs were developed and analysed. In multiscale modelling, three length scales, such as nano, micro

and macro scales were modelled. The nanoscale RVE of SWCNTs doped PAN nanofibre was modelled using space frame structures (SFS) of SWCNTs and PAN polymer matrix. Simulated results of nanoscale RVEs were used to determine the equivalent properties of p-SWCNTs and f-SWCNTs doped nanofibres which were further used in micro scale RVEs. Four micro scale RVEs were developed to represent the random, aligned, p-SWCNTs and f-SWCNTs doped aligned nanofibre mat in the epoxy matrix. Analysed micro scale RVEs provided equivalent properties of interlaminar regions developed with random, aligned, p-SWCNTs and f-SWCNTs doped aligned nanofibres mats. At the macro scale, MNHCs were developed with equivalent interlaminar regions. Comparison of the numerically obtained results with experimental results confirmed that the FEA models predicted the properties of multiscale nanohybrid composites in the acceptable range. The following key points were concluded from the numerical study:

- Different carbon nanotubes (CNTs) i.e. pristine and defective single wall (SWCNTs), double wall (DWCNTs), and multiwall (MWCNTs) for zigzag and armchair configurations were modelled. The orthotropic properties of the C-C bond were calculated by comparing structural mechanics and molecular mechanics energy expressions along with the parametric study. A mathematical model of van der Waals equivalent springs between consecutive walls was developed to analyse their effect on DWCNTs and MWCNTs
- It was found that zigzag elastic modulus is greater than the armchair configuration tubes for the similar CNT diameter.

- The shear modulus of armchair configuration is greater than the zigzag configuration. Vacancy defects significantly reduced the elastic properties of SWCNTs and the effect of the vacancy defects increased as the diameter was increased further.
- The rate of decrease in elastic and shear modulus of defective armchair become insignificant as the diameter increased further.
- Comparatively DWCNTs have higher elastic modulus and shear modulus (average) than SWCNTs and MWCNTs for the smaller CNTs diameter range.
- Numerical analysis of 32% fibreglass composite showed that maximum deflection occurred within the matrix rich interlaminar region. It confirmed that the region where cracks first took place was the matrix rich interlaminar region.
- Random nanofibre mat strengthened hybrid composite numerical results confirmed their strengthening effect within the interlaminar region which improved the modulus of the 32% fibreglass composite.
- Uniformly distributed aligned nanofibres mats with reduced diameter produced nine times increased network within the interlaminar region compared to the random nanofibres. It was observed, the reinforcing effect was enhanced substantially with the aligned nanofibres mat compared to the random nanofibres mat.
- p-SWCNTs and f-SWCNTs doped aligned nanofibres utilised the inherent strength of the SWCNTs and improved the tensile properties of the MNHCs. It was numerically proved that the functionalized SWCNTs provided the highest values of Young's modulus.

---

## 7.3 Recommendations

Throughout this study, numerous experimental and numerical investigations were carried out which concluded that the conventional glass fibre composites or similar macrofibre composites had limited strength due to weak matrix rich interlaminar regions. Nanofillers like the electrospun nanofibres mat and its variants, aligned and SWCNTs doped nanofibres mat strengthened the interlaminar region of the FGC and increased its mechanical properties. The methodology used to strengthen the interlaminar region of FGC provided a guide path to utilise the strength of the nanofibres mats and SWCNTs. There have been different research directions in the current study, that could be scientifically valuable and if used may provide more interesting results. Due to the certain limitation such as the scope of the study along with the time constraint; limited experimental and numerically resources, the research was focused only on the main objectives at hand. However, there are numerous areas which are connected to the current study, and could be the future extension to achieve the high-performance MNHCs using SWCNTs doped nanofibres mats. The possible future ideologies for the study could be as follows:

### 7.3.1 Experimental recommendations

- The current study was carried out in an open environment which may be further performed in a controlled environment. It will eliminate the effect of variable humidity at room temperature and could result in better performance.
- Introduction of two AVEs to electrospinning system acted as a new parameter into the system which changed the other input parameters as explained in chapter 4. During electrospinning, the symmetrical position of

the AVEs were maintained with respect to spinnerets which reduced the nanofibres deposition area. Therefore, the study can be further extended to the unsymmetrical position of AVEs which can shift the deposition area of nanofibres for specific applications. Moreover, different numbers and shapes of the AVEs can also be introduced into the system and their effect could be studied.

- Electric field produced by AVEs narrowed down the driving zone of the nanofibres which changed the natural whipping path. A detailed mathematical model of the modified electrospinning can be developed to predict the possible final geometry of the nanofibres mat.
- The current experimentation pattern could be performed with different polymer, nanoparticles and matrices to validate the results.
- Effect of different functionalization processes of the SWCNTs should be performed to focus the interfacial adhesion of nanofibres within the interlaminar region.
- In this study, only one volume fraction of SWCNTs, suggested by the previous study was used to confirm their strengthening effect along with functionalization. Further study should investigate the effect of the different volume fraction of f-SWCNTs.

### **7.3.2 Numerical recommendations**

- Since this work analysed the SWCNTs, DWCNTs and MWCNTs using orthotropic properties. Similar structures like buckyballs, graphene, and carbon nanofibres should be developed with the same strategy and analysed.

- Glass fibre composites and nanofibre mat strengthened composites were developed only with optimised glass fibre mats and random nanofibres mats. Future study should be extended to different kind of macro and nanofibres.
- Interfacial adhesion other than the Vdw and covalent could be explored. Single nanofibre and SWCNTs pullout test should be performed. Moreover, the study should also explore the bending and impact behaviour through FEA using same models.
- For the current models, different kinds of failure criteria should be explored using FEA simulations.

# Bibliography

- [1] Choo, V. K. S., *Fundamentals of composite materials*, “Dearborn, MI: Society of Manufacturing Engineers”, 1990, pp 2-4.
- [2] Kaw, A. K., *Mechanics of composite materials*, “Boca Raton: Taylor Francis”, 2006, pp 1-2.
- [3] Masuelli, M. A., *Introduction of Fibre-Reinforced Polymers - Polymers and Composites: Concepts, Properties and Processes*, “INTECH Open Access Publisher”, 2013, pp 1-2.
- [4] Grujicic, M., Arakere, G., He, T., Bell, W., Cheeseman, B., Yen, C.-F., and Scott, B., *A ballistic material model for cross-plyed unidirectional ultra-high molecular-weight polyethylene fiber-reinforced armor-grade composites*, “Materials Science and Engineering: A” 498, 2008, pp. 231-241.
- [5] Mallick, P., “Fiber-Reinforced Composites,” *Dekker Mechanical Engineering*, 2007, p. 1-11.
- [6] Armstrong, K. B., Cole, W. F., and Bevan, L. G. *Care and Repair of Advanced Composites (2nd Edition)*. “Society of Automotive Engineers, Inc.” 2005, pp 3-4.
- [7] Fan, Z., Santare, M. H., and Advani, S. G., “Interlaminar shear strength of glass fiber reinforced epoxy composites enhanced with multi-walled carbon

- 
- nanotubes,” *Composites Part A: Applied Science and Manufacturing* Vol 39, 2008, pp. 540-554.
- [8] Muthu, J., and Dendere, C., “Functionalized multiwall carbon nanotubes strengthened GRP hybrid composites: Improved properties with optimum fiber content,” *Composites Part B: Engineering* Vol 67, 2014, pp. 84-94.
- [9] Wicks, S. S., Wang, W., Williams, M. R., and Wardle, B. L., “Multi-scale interlaminar fracture mechanisms in woven composite laminates reinforced with aligned carbon nanotubes,” *Composites Science and Technology* Vol 100, 2014, pp. 128-135.
- [10] Kickelbick G. *Hybrid materials: synthesis, characterization and applications*, “Wiley-VCH Verlag GmbH & Co. KGaA”, 2007; 1-48.
- [11] Agarwal, S., Greiner, A., and Wendorff, J. H., “Electrospinning of Man-made and Biopolymer Nanofibers-Progress in Techniques, Materials, and Applications,” *Advanced Functional Materials* Vol 19, 2009, pp. 2863-2879.
- [12] Parveen, S., Rana, S., and Fangueiro, R., “A Review on Nanomaterial Dispersion, Microstructure, and Mechanical Properties of Carbon Nanotube and Nanofiber Reinforced Cementitious Composites,” *Journal of Nanomaterials* 2013, pp. 1-19.
- [13] Georgantzinou, S., Giannopoulos, G., Katsareas, D., Kakavas, P., and Anifantis, N., “Size-dependent non-linear mechanical properties of graphene nanoribbons,” *Computational Materials Science* Vol. 50, 2011, pp. 2057-2062.
- [14] Al-Saleh, M. H., and Sundararaj, U., “Review of the mechanical properties of carbon nanofiber/polymer composites,” *Composites Part A: Applied Science and Manufacturing* Vol. 42, 2011, pp. 2126-2142.

- 
- [15] Sun, X., Chen, T., Yang, Z., and Peng, H., "The Alignment of Carbon Nanotubes: An Effective Route To Extend Their Excellent Properties to Macroscopic Scale," *Accounts of Chemical Research* vol. 46, 2012, pp. 539-549.
- [16] Rahmanian, S., Thean, K., Suraya, A., Shazed, M., Salleh, M. M., and Yusoff, H., "Carbon and glass hierarchical fibers: Influence of carbon nanotubes on tensile, flexural and impact properties of short fiber reinforced composites," *Materials Design* Vol. 43, 2013, pp. 10-16.
- [17] Ghemes, A., Minami, Y., Muramatsu, J., Okada, M., Mimura, H., and Inoue, Y., "Fabrication and mechanical properties of carbon nanotube yarns spun from ultra-long multi-walled carbon nanotube arrays," *Carbon* Vol. 50, 2012, pp. 4579-4587.
- [18] Campo, M., Jimenez-Suarez, A., and Urena, A., "Effect of type, percentage and dispersion method of multi-walled carbon nanotubes on tribological properties of epoxy composites," *Wear* 324-325, 2015, pp. 100-108.
- [19] Coleman, J. N., Khan, U., Blau, W. J., and Gun'Ko, Y. K., "Small but strong: A review of the mechanical properties of carbon nanotube-polymer composites," *Carbon* vol. 44, 2006, pp. 1624-1652.
- [20] Sharma, S., and Lakkad, S., "Impact behavior and fractographic study of carbon nanotubes grafted carbon fiber-reinforced epoxy matrix multi-scale hybrid composites," *Composites Part A: Applied Science and Manufacturing* vol. 69, 2015, pp. 124-131.
- [21] Zhou, Z., Wang, X., Faraji, S., Bradford, P. D., Li, Q., and Zhu, Y., "Mechanical and electrical properties of aligned carbon nanotube/carbon matrix composites," *Carbon* vol. 75, 2014, pp. 307-313.

- 
- [22] Yue, L., Pircheraghi, G., Monemian, S. A., and Manas-Zloczower, I., “Epoxy composites with carbon nanotubes and graphene nanoplatelets - Dispersion and synergy effects,” *Carbon* vol. 78, 2014, pp. 268-278.
- [23] Ma, P.-C., Siddiqui, N. A., Marom, G., and Kim, J.-K., “Dispersion and functionalization of carbon nanotubes for polymer-based nanocomposites: A review,” *Composites Part A: Applied Science and Manufacturing* vol. 41, 2010, pp. 1345-1367.
- [24] Muthu, S. J., and Paskaramoorthy, R., “Double-wall carbon nanotube-reinforced polyester nanocomposites: Improved dispersion and mechanical properties,” *Polymer Composites* vol. 33, 2012, pp. 866-871.
- [25] Gopalakrishnan, K., Birgisson, B., Taylor, P., and Attoh-Okine, N. O., *Nanotechnology in Civil Infrastructure A Paradigm Shift*, Berlin: Springer Berlin, 2014, pp 103-130.
- [26] Liu, C.-X., and Choi, J.-W., “Improved Dispersion of Carbon Nanotubes in Polymers at High Concentrations,” *Nanomaterials* vol. 2, 2012, pp. 329-347.
- [27] Goh, P., Ismail, A., and Ng, B., “Directional alignment of carbon nanotubes in polymer matrices: Contemporary approaches and future advances,” *Composites Part A: Applied Science and Manufacturing*, vol. 56, 2014, pp. 103-126.
- [28] Zhou, F.-L., and Gong, R.-H., “Manufacturing technologies of polymeric nanofibres and nanofibre yarns,” *Polymer International* vol. 57, 2008, pp. 837-845.
- [29] Steinert, B. W., and Dean, D. R., “Magnetic field alignment and electrical properties of solution cast PET-carbon nanotube composite films,” *Polymer* vol. 50, 2009, pp. 898-904.

- [30] Romyen, N., Thongyai, S., and Prasertthdam, P., "Alignment of carbon nanotubes in polyimide under electric and magnetic fields," *Journal of Applied Polymer Science* vol. 123, 2011, pp. 3470-3475.
- [31] Chawla, K. K., "Processing of ceramic matrix composites," *Ceramic Matrix Composites*, 1993, pp. 126-161.
- [32] Goldsmith, M. B., Sankar, B. V., Haftka, R. T., and Goldberg, R. K., "Effects of microstructural variability on thermo-mechanical properties of a woven ceramic matrix composite," *Journal of Composite Materials* vol. 49, 2014, pp. 335-350.
- [33] Committee on High-Performance Structural Fibers for Advanced Polymer Matrix Composites, National Research Council, "High-Performance Structural Fibers for Advanced Polymer Matrix Composites", *The National Academies Press, Washington DC*. 2005.
- [34] Bose, S., Khare, R. A., and Moldenaers, P., "Assessing the strengths and weaknesses of various types of pre-treatments of carbon nanotubes on the properties of polymer/carbon nanotubes composites: A critical review," *Polymer* vol. 51, 2010, pp. 975-993.
- [35] Su, Z., Ding, J., and Wei, G., "Electrospinning: a facile technique for fabricating polymeric nanofibers doped with carbon nanotubes and metallic nanoparticles for sensor applications," *RSC Adv.* vol. 4, Sep. 2014, pp. 52598-52610.
- [36] Chou, T.-W., Gao, L., Thostenson, E. T., Zhang, Z., and Byun, J.-H., "An assessment of the science and technology of carbon nanotube-based fibers and composites," *Composites Science and Technology* vol. 70, 2010, pp. 1-19.

- 
- [37] Wernik, J., and Meguid, S., “Multiscale micromechanical modeling of the constitutive response of carbon nanotube-reinforced structural adhesives,” *International Journal of Solids and Structures* vol. 51, 2014, pp. 2575-2589.
- [38] Han, F., Cui, J., and Yu, Y., “The statistical second-order two-scale method for mechanical properties of statistically inhomogeneous materials,” *International Journal for Numerical Methods in Engineering* vol. 84, 2010, pp. 972-988.
- [39] Shokrieh, M. M., and Rafiee, R., “A review of the mechanical properties of isolated carbon nanotubes and carbon nanotube composites,” *Mechanics of Composite Materials* vol. 46, Nov. 2010, pp. 155-172.
- [40] Liu, Y., and Kumar, S., “Polymer/Carbon Nanotube Nano Composite Fibers-A Review,” *ACS Applied Materials Interfaces* vol. 6, Dec. 2014, pp. 6069-6087.
- [41] Chen, Q., Zhang, L., Zhao, Y., Wu, X.-F., and Fong, H., “Hybrid multi-scale composites developed from glass microfiber fabrics and nano-epoxy resins containing electrospun glass nanofibers,” *Composites Part B: Engineering* vol. 43, 2012, pp. 309-316.
- [42] Chen, Q., Zhang, L., Yoon, M.-K., Wu, X.-F., Arefin, R. H., and Fong, H., “Preparation and evaluation of nano-epoxy composite resins containing electrospun glass nanofibers,” *Journal of Applied Polymer Science* vol. 124, Apr. 2011, pp. 444-451
- [43] Zhang, Y., Zhuang, X., Muthu, J., Mabrouki, T., Fontaine, M., Gong, Y., and Rabczuk, T., “Load transfer of graphene/carbon nanotube/polyethylene hybrid nanocomposite by molecular dynamics simulation,” *Composites Part B: Engineering* vol. 63, 2014, pp. 27-33.

- 
- [44] Jia, J., Zhao, J., Xu, G., Di, J., Yong, Z., Tao, Y., Fang, C., Zhang, Z., Zhang, X., Zheng, L., and Li, Q., "A comparison of the mechanical properties of fibers spun from different carbon nanotubes," *Carbon* vol. 49, 2011, pp. 1333-1339.
- [45] Li, P., Liu, D., Zhu, B., Li, B., Jia, X., Wang, L., Li, G., and Yang, X., "Synchronous effects of multiscale reinforced and toughened CFRP composites by MWNTs-EP/PSF hybrid nanofibers with preferred orientation," *Composites Part A: Applied Science and Manufacturing* vol. 68, 2015, pp. 72-80.
- [46] Han, F., Azdoud, Y., and Lubineau, G., "Computational modeling of elastic properties of carbon nanotube/polymer composites with interphase regions. Part I: Micro-structural characterization and geometric modeling," *Computational Materials Science* vol. 81, 2014, pp. 641-651.
- [47] Peters, S. T., Handbook of composites, Estados Unidos: Chapman Hall, 1998, p. 25.
- [48] JJordan, J. L., Richards, D. W., Spowart, J. E., and White, B., Multifunctional Particulate Composites for Structural Applications (PREPRINT), United States: air force research lab eglin afb fl munitions directorate, 2008.
- [49] Bishop, J. E., and Kinra, V. K., "Analysis of elastothermodynamic damping in particle-reinforced metal-matrix composites," *Metallurgical and Materials Transactions A* vol. 26, 1995, pp. 2773-2783.
- [50] Hartaj Singh, Sarabjit, Nrip Jit, Anand K Tyagi, "An overview of metal matrix composite: processing and SiC based mechanical properties," *JER-S/Vol. II/ Issue IV/October-December*, 2011.pp. 72-78.

- 
- [51] Idusuyi, N., Babajide, I., Ajayi, O. K., and Olugasa, T. T., "A Computational Study on the Use of an Aluminium Metal Matrix Composite and Aramid as Alternative Brake Disc and Brake Pad Material," *Journal of Engineering* vol. 2014, 2014, pp. 1-6.
- [52] Smith, R.H., Stevens, J.H, Duggan, J.L., Lyons, N.J, Eason, J.W., Gladney, J.D, Oxford, J.A. and Chrest, B.J., "Earth-boring rotary drill bits and methods of manufacturing earth-boring rotary drill bits having particle-matrix composite bit bodies," patents/US8309018, March 29, 2011.
- [53] Beyerle, D. S., Spearing, S. M., Zok, F. W., and Evans, A. G., "Damage and Failure in Unidirectional Ceramic-Matrix Composites," *Journal of the American Ceramic Society* vol. 76, 1993, pp. 560-560.
- [54] Sommers, A., Wang, Q., Han, X., Tjoen, C., Park, Y., and Jacobi, A., "Ceramics and ceramic matrix composites for heat exchangers in advanced thermal systemsA review," *Applied Thermal Engineering* vol. 30, 2010, pp. 1277-1291.
- [55] Patrick Potter, "Surface Ships Put Composites to Work," *the AMPTIAC Quarterly*, Vol. 7, November 3, 2003, pp.37-40.
- [56] Barbero, E. J., "Introduction to composite materials design," *Boca Raton, FL: Taylor and Francis, an imprint of CRC Press*, 2010, pp 3, 29, 30, 36.
- [57] Campbell, F. C., "Structural composite materials, Materials Park," *OH: ASM International*, 2010, pp. 1-7.
- [58] Saba, N., Tahir, P., and Jawaid, M., "A Review on Potentiality of Nano Filler/Natural Fiber Filled Polymer Hybrid Composites," *Polymers* vol.6, 2014, pp. 2247-2273.

- [59] K Van de Velde, P Kiekens, “Thermoplastic polymers: overview of several properties and their consequences in flax fibre reinforced composites”, *Polymer Testing* Vol. 20, Issue 8, 2001, pp. 885-893,
- [60] Peng, W., and Riedl, B., “Thermosetting Resins,” *Journal of Chemical Education* 72, 1995, p. 587.
- [61] Mishnaevsky, L., and Dai, G., “Hybrid and hierarchical nanoreinforced polymer composites: Computational modelling of structure-properties relationships,” *Composite Structures* vol.117, 2014, pp. 156-168.
- [62] Wicks, S. S., Villoria, R. G. D., and Wardle, B. L., “Interlaminar and intralaminar reinforcement of composite laminates with aligned carbon nanotubes,” *Composites Science and Technology* vol.70, 2010, pp. 20-28.
- [63] Chung, D. D. L., *Composite materials: functional materials for modern technologies*, London: Springer, 2004.
- [64] Laffan, M., Pinho, S., Robinson, P., and Mcmillan, A., “Translaminar fracture toughness testing of composites: A review,” *Polymer Testing* vol.31, 2012, pp. 481-489.
- [65] Shahzad, A., “Impact and fatigue properties of hemp-glass fiber hybrid biocomposites,” *Journal of Reinforced Plastics and Composites* vol.30, 2011, pp. 1389-1398.
- [66] Ke Peng, Yan-Jun Wan, Dong-You Ren, Qing-Wen Zeng, and Long-Cheng Tang, “ Scalable Preparation of Multiscale Carbon Nanotube/Glass Fiber Reinforcements and Their Application in Polymer Composites,” *Fibers and Polymers* vol.15, 2014, No.6, 1242-1250.

- 
- [67] Karsli, N. G., Yesil, S., and Aytac, A., "Effect of hybrid carbon nanotube/short glass fiber reinforcement on the properties of polypropylene composites," *Composites Part B: Engineering* vol.63, 2014, pp. 154-160.
- [68] Cha, J., Jun, G. H., Park, J. K., Kim, J. C., Ryu, H. J., and Hong, S. H., "Improvement of modulus, strength and fracture toughness of CNT/Epoxy nanocomposites through the functionalization of carbon nanotubes," *Composites Part B: Engineering* vol.129, 2017, pp. 169-179.
- [69] Wernik, J. M., and Meguid, S. A., "Recent Developments in Multifunctional Nanocomposites Using Carbon Nanotubes," *Applied Mechanics Reviews* vol.63, 2010, pp. 050801-40.
- [70] Dzenis Y A, Reneker DH., Delamination resistant composites prepared by small diameter fiber reinforcement at ply interfaces. US6265333B1.
- [71] Rafiee, M. A., Rafiee, J., Srivastava, I., Wang, Z., Song, H., Yu, Z.-Z., and Koratkar, N., "Fracture and Fatigue in Graphene Nanocomposites," *Small* vol.6, 2010, pp. 179-183.
- [72] Salam, M. B. A., Hosur, M. V., Zainuddin, S., and Jeelani, S., "Improvement in Mechanical and Thermo-Mechanical Properties of Epoxy Composite Using Two Different Functionalized Multi-Walled Carbon Nanotubes," *Open Journal of Composite Materials* vol.03, 2013, pp. 1-9.
- [73] Geim, A. K., and Novoselov, K. S., "The rise of graphene," *Nature Materials* vol.6, 2007, pp. 183-191.
- [74] Lui, C. H., Liu, L., Mak, K. F., Flynn, G. W., and Heinz, T. F., "Ultraflat graphene," *Nature* vol.462, 2009, pp. 339-341.

- 
- [75] Rasuli, R., Zad, A. I., and Ahadian, M. M., "Mechanical properties of graphene cantilever from atomic force microscopy and density functional theory," *Nanotechnology* vol.21, 2010, p. 185503.
- [76] Hod, O., and Scuseria, G. E., "Electromechanical Properties of Suspended Graphene Nanoribbons," *Nano Letters* vol.9, Aug. 2009, pp. 2619-2622.
- [77] Arshad, S. N., Naraghi, M., and Chasiotis, I., "Strong carbon nanofibers from electrospun polyacrylonitrile," *Carbon* vol.49, 2011, pp. 1710-1719.
- [78] Rahaman, M., Ismail, A., and Mustafa, A., "A review of heat treatment on polyacrylonitrile fiber," *Polymer Degradation and Stability* vol.92, 2007, pp. 1421-1432.
- [79] Tibbetts, G., Lake, M., Strong, K., and Rice, B., "A review of the fabrication and properties of vapor-grown carbon nanofiber/polymer composites," *Composites Science and Technology* vol.67, 2007, pp. 1709-1718.
- [80] Hammel, E., Tang, X., Trampert, M., Schmitt, T., Mauthner, K., Eder, A., and Ptschke, P., "Carbon nanofibers for composite applications," *Carbon* vol.42, 2004, pp. 1153-1158.
- [81] Iijima, S., "Helical microtubules of graphitic carbon," *Nature* vol.354, 1991, pp. 56-58
- [82] Endo, M., Kim, Y. A., Hayashi, T., Fukai, Y., Oshida, K., Terrones, M., Yanagisawa, T., Higaki, S., and Dresselhaus, M. S., "Structural characterization of cup-stacked-type nanofibers with an entirely hollow core," *Applied Physics Letters* vol.80, 2002, pp. 1267-1269.
- [83] Kaushik, B. K., and Majumder, M. K., "Carbon Nanotube: Properties and Applications," *Carbon Nanotube Based VLSI Interconnects SpringerBriefs in Applied Sciences and Technology*, Feb. 2014, pp. 17-37.

- 
- [84] Wernik, J., and Meguid, S., “Multiscale modeling of the nonlinear response of nano-reinforced polymers,” *Acta Mechanica* vol.217, 2010, pp. 1-16.
- [85] Canton, G., Bisht, G., Kulinsky, L., and Madou, M., “Controlled Patterning and Dimensional Control of Suspended Carbon Nanofibers,” *Advanced Materials Research* vol.628, 2012, pp. 43-49.
- [86] Kathi, J., Rhee, K.-Y., and Lee, J. H., “Effect of chemical functionalization of multi-walled carbon nanotubes with 3-aminopropyltriethoxysilane on mechanical and morphological properties of epoxy nanocomposites,” *Composites Part A: Applied Science and Manufacturing* vol.40, 2009, pp. 800-809.
- [87] Matarredona, O., Rhoads, H., Li, Z., Harwell, J. H., Balzano, L., and Resasco, D. E., “Dispersion of Single-Walled Carbon Nanotubes in Aqueous Solutions of the Anionic Surfactant NaDDBS,” *The Journal of Physical Chemistry B* vol.107, 2003, pp. 13357-13367.
- [88] Yeh, M.-K., Hsieh, T.-H., and Tai, N.-H., “Fabrication and mechanical properties of multi-walled carbon nanotubes/epoxy nanocomposites,” *Materials Science and Engineering: A* vol.483-484, 2008, pp. 289-292.
- [89] Fraczek, A., and Blazewicz, S., “Effect of dispersion of carbon nanotubes in polyacrylonitrile matrix on mechanical and thermal behavior of nanocomposites,” *Journal of Physics: Conference Series* vol.146, Jan. 2009, p. 012005.
- [90] Chanteli, A., and Tserpes, K. I., “Finite element modeling of carbon nanotube agglomerates in polymers,” *Composite Structures* vol.132, 2015, pp. 1141-1148.

- [91] Byrne, M. T., and Gunko, Y. K., "Recent Advances in Research on Carbon Nanotube-Polymer Composites," *Advanced Materials* vol.22, 2010, pp. 1672-1688.
- [92] Wong, M., Paramsothy, M., Xu, X., Ren, Y., Li, S., and Liao, K., "Physical interactions at carbon nanotube-polymer interface," *Polymer* vol.44, 2003, pp. 7757-7764.
- [93] Sharma, K., and Shukla, M., "Three-Phase Carbon Fiber Amine Functionalized Carbon Nanotubes Epoxy Composite: Processing, Characterisation, and Multiscale Modeling," *Journal of Nanomaterials* vol.2014, 2014, pp. 1-10.
- [94] Villmow, T., Ptschke, P., Pegel, S., Hussler, L., and Kretzschmar, B., "Influence of twin-screw extrusion conditions on the dispersion of multi-walled carbon nanotubes in a poly(lactic acid) matrix," *Polymer* vol.49, 2008, pp. 3500-3509.
- [95] Schmid, C. F., and Klingenberg, D. J., "Mechanical Flocculation in Flowing Fiber Suspensions," *Physical Review Letters* vol.84, Oct. 2000, pp. 290-293.
- [96] Hwang, S.-H., Park, Y.-B., Han, K., and Suk, D., "Smart Materials and Structures Based on Carbon Nanotube Composites," *Carbon Nanotubes - Synthesis, Characterization, Applications*, 2011.
- [97] Munkhbayar, B., Nine, M. J., Jeoun, J., Bat-Erdene, M., Chung, H., and Jeong, H., "Influence of dry and wet ball milling on dispersion characteristics of the multi-walled carbon nanotubes in aqueous solution with and without surfactant," *Powder Technology* vol.234, 2013, pp. 132-140.

- 
- [98] Ayatollahi, M., Shadlou, S., Shokrieh, M., and Chitsazzadeh, M., "Effect of multi-walled carbon nanotube aspect ratio on mechanical and electrical properties of epoxy-based nanocomposites," *Polymer Testing* vol.30, 2011, pp. 548-556.
- [99] Kim, M., Rhee, K., Lee, J., Hui, D., and Lau, A. K., "Property enhancement of a carbon fiber/epoxy composite by using carbon nanotubes," *Composites Part B: Engineering* vol.42, 2011, pp. 1257-1261.
- [100] Geng, Y., Liu, M. Y., Li, J., Shi, X. M., and Kim, J. K., "Effects of surfactant treatment on mechanical and electrical properties of CNT/epoxy nanocomposites," *Composites Part A: Applied Science and Manufacturing* vol.39, 2008, pp. 1876-1883.
- [101] Kharisov, B. I., Kharissova, O. V., Gutierrez, H. L., and Mendez Ubaldo Ortiz, "Recent Advances on the Soluble Carbon Nanotubes," *Industrial Engineering Chemistry Research* vol.48, 2009, pp. 572-590.
- [102] Zhang, J., Zou, H., Qing, Q., Yang, Y., Li, Q., Liu, Z., Guo, X., and Du, Z., "Effect of Chemical Oxidation on the Structure of Single-Walled Carbon Nanotubes," *The Journal of Physical Chemistry B* vol.107, 2003, pp. 3712-3718.
- [103] Nogueira, S., Sahoo, S., Jarrosson, T., Serein-Spirau, F., Lre-Porte, J.-P., Moujaes, E., Marletta, A., Santos, A., Fantini, C., Furtado, C., and Silva, R., "A new designed conjugated molecule for stable single walled carbon nanotube dispersion in aqueous medium," *Journal of Colloid and Interface Science* vol.464, 2016, pp. 117-125.
- [104] Giordani, S., Bergin, S. D., Nicolosi, V., Lebedkin, S., Kappes, M. M., Blau, W. J., and Coleman, J. N., "Debundling of Single-Walled Nanotubes by Dilution: Observation of Large Populations of Individual Nanotubes

- 
- in Amide Solvent Dispersions,” *The Journal of Physical Chemistry B* vol.110, 2006, pp. 15708-15718.
- [105] Moore, V. C., Strano, M. S., Haroz, E. H., Hauge, R. H., Smalley, R. E., Schmidt, J., and Talmon, Y., “Individually Suspended Single-Walled Carbon Nanotubes in Various Surfactants,” *Nano Letters* vol.3, 2003, pp. 1379-1382.
- [106] Drzal, L. T., Rich, M. J., and Lloyd, P. F., “Adhesion of Graphite Fibers to Epoxy Matrices: I. The Role of Fiber Surface Treatment,” *The Journal of Adhesion* 16, 1983, pp. 1-30.
- [107] Kim, J.-K., and Mai, Y.-W., *Engineered Interfaces in Fiber Reinforced Composites*, “S.I. Elsevier”, 1998, pp 1-4.
- [108] Beg, M., and Pickering, K. “Mechanical performance of Kraft fibre reinforced polypropylene composites: Influence of fibre length, fibre beating and hygrothermal ageing”, *Composites Part A: Applied Science and Manufacturing*, vol.39 no. 11, 2008, pp. 1748-1755.
- [109] Ragoubi, M., Bienaime, D., Molinaa, S., Georgea, B., and Merlina A, “Impact of corona treated hemp fibres onto mechanical properties of polypropylene composites made thereof,” *Industrial Crops and Products* vol.31, no. 2, 2010, pp. 344-349.
- [110] Gassan, J. “Effects of corona discharge and UV treatment on the properties of jute-fibre epoxy composites”, *Composites Science and Technology* vol.60, no. 15, 2000, pp. 2857-2863.
- [111] Faruk, O., Bledzki, A. K., Fink, H.-P., and Sain, M., “Progress report on natural fiber reinforced composites”, *Macromolecular Materials and Engineering* vol.299, no. 1, 2013, pp. 9-26.

- 
- [112] Singh, B., Gupta, M., and Verma, A. "Influence of fiber surface treatment on the properties of sisal-polyester composites", *Polymer Composites* vol.17, no. 6, 1996, pp. 910-918.
- [113] Choi, J., Shin, H., Yang, S., and Cho, M., "The influence of nanoparticle size on the mechanical properties of polymer nanocomposites and the associated interphase region: A multiscale approach", *Composite Structures* vol.119, 2015, pp. 365-376.
- [114] Todo, M., Jar, P., and Takahashi, K. "Initiation of a mode-II interlaminar crack from an insert film in the end-notched flexure composite specimen." *Composites Science and Technology* vol.60, no. 2, 2000, pp. 263-272.
- [115] Gan, Yong. "Effect of interface structure on mechanical properties of advanced composite materials", *International Journal of Molecular Sciences* vol.10, no. 12, 2009, pp. 5115-5134.
- [116] Shahid, N., Villate, R., and Barron, A. "Chemically functionalized alumina nanoparticle effect on carbon fiber/epoxy composites", *Composites Science and Technology* vol.65, no. 14, 2005, pp. 2250-2258.
- [117] Odegard, G. "Constitutive modeling of nanotubereinforced polymer composites", *Composites Science and Technology* vol.63, no. 11, 2003, pp. 1671-1687.
- [118] Zhang, P., Qiu, D., Chen, H., Sun, J., Wang, J., Qin, C., and Dai, L. "Preparation of MWCNTs grafted with polyvinyl alcohol through Friedel-Crafts alkylation and their composite fibers with enhanced mechanical properties", *Journal of Materials Chemistry A* vol.3, no. 4, 2015, pp. 1442-1449.
- [119] Tasis, D., Tagmatarchis, N., Bianco, A. "Chemistry of Carbon Nanotubes." *ChemInform* vol.37, no. 24, 2006

- 
- [120] Gojny, F., Wichmann, M., Fiedler, B., Bauhofer, W., and Schulte, K. "Influence of nano-modification on the mechanical and electrical properties of conventional fibre-reinforced composites", *Composites Part A: Applied Science and Manufacturing* vol.36, no. 11, 2005, pp. 1525-1535.
- [121] Choi, J., Shin, H., Yang, S., and Cho, M. "Electrochemical Functionalization of Multi-Walled Carbon Nanotubes for Solvation and Purification", *Current Applied Physics* vol.2, no. 2, 2002, pp. 107-111.
- [122] Kim, K., Bae, D., Kim, J., Park, K., Lim, S., Kim, J., Choi, W., Park, C., and Lee, Y. "Modification of electronic structures of a carbon nanotube by hydrogen functionalization", *Advanced Materials* vol.14, no. 24, 2002, pp. 1818-1821.
- [123] Chua, T., Mariatti, M., Azizan, A., and Rashid, A. "Effects of surface-functionalized multi-walled carbon nanotubes on the properties of poly (dimethyl siloxane) nanocomposites", *Composites Science and Technology* vol.70, no. 4, 2010, pp. 671-677.
- [124] Jeon, I., Wook, D., Ashok, N., and Baek, J. "Functionalization of Carbon Nanotubes. Carbon Nanotubes" - *Polymer Nanocomposites*, 2011, pp. 91-110
- [125] Hill, D. E., Lin, Y., Rao, A. M., Allard, L. F., and Sun, Y.-P., "Functionalization of carbon nanotubes with polystyrene", *Macromolecules*, vol. 35, 2002, pp. 9466-9471.
- [126] Hill, D., Lin, Y., Rao, A., Allard, L., and Sun, Y. "Functionalization of carbon nanotubes with polystyrene", *Macromolecules* vol.35, no. 25, 2002, pp. 9466-9471.

- 
- [127] Xiao, K. Q., and L. C. Zhang. “Effective separation and alignment of long entangled carbon nanotubes in epoxy”, *Journal of Materials Science* vol.40, no. 24, May 2005, pp. 6513-6516.
- [128] Abbasi, S., Carreau, P., and Derdouri, A. “Flow induced orientation of multiwalled carbon nanotubes in polycarbonate nanocomposites: Rheology, conductivity and mechanical properties”, *Polymer* vol.51, no. 4, 2010, pp. 922-935.
- [129] Joshi, P., and Upadhyay, S. “Analysis of alignment effect on carbon nanotube layer in nanocomposites”, *Physica E: Low-Dimensional Systems and Nanostructures* vol.66, 2015, pp. 221-227.
- [130] Desai, A., and Haque, M., “Mechanics of the interface for carbon nanotubepolymer composites, Thin-Walled Structures”, vol.43, no. 11, 2005, pp. 1787-1803.
- [131] Fornes, T., Baur, J., Sabba, Y., and Thomas, E. “Morphology and properties of melt-spun polycarbonate fibers containing single-and multi-wall carbon nanotubes”, *Polymer* vol.47, no. 5, 2006, pp. 1704-1714.
- [132] Liu, Y.j., and X.l. Chen. “Continuum models of carbon nanotube-based composites using the boundary element method”, *Electronic Journal of Boundary Elements* vol.1, 2007
- [133] Jiang, Q., Wang, X., Zhu, Y., Hui, D., and Qiu, Y. “Mechanical, electrical and thermal properties of aligned carbon nanotube/polyimide composites”, *Composites Part B: Engineering* vol.56, 2014, pp. 408-412.
- [134] Frontera, P., Malara, A., Stelitano, S., Fazio, E., Neri, F., Scarpino, L., Antonucci, P., and Santangelo, S. “A new approach to the synthesis of titania nano-powders enriched with very high contents of carbon nanotubes

- 
- by electro-spinning”, *Materials Chemistry and Physics* vol.153, 2015, pp. 338-345.
- [135] Kannan, P., Eichhorn, S., and Young, R. “Deformation of isolated single-wall carbon nanotubes in electrospun polymer nanofibres”, *Nanotechnology* vol.18, no. 23, 2007, p. 235707.
- [136] He, B., Li, J., and Pan, Z. “Morphology and mechanical properties of MWNT/PMIA nanofibers by electrospinning”, *Textile Research Journal* vol.82, no. 13, 2012, pp. 1390-1395.
- [137] Ary Subagia, I.D.G Jiang, Zhe Tijing, Leonard Kim, Yonjig Pant, Hem Lim, Jae Kyoo. (2014). “Hybrid multi-scale basalt fiber-epoxy composite laminate reinforced with Electrospun polyurethane nanofibers containing carbon nanotubes”, *Fibers and Polymers*. vol.15, No.6, 2014, pp. 1295-1302.
- [138] Reneker, D. H., and Yarin, A. L. “Electrospinning jets and polymer nanofibers”, *Polymer* vol.49, no. 10, 2008, pp. 2387-2425.
- [139] Dong, Y., Marshall, J., Haroosh, H., Mohammadzadehmoghadam, S., Liu, D., Qi, X., and Lau, K. “Polylactic acid (PLA)/halloysite nanotube (HNT) composite mats: Influence of HNT content and modification”, *Composites Part A: Applied Science and Manufacturing* vol.76, 2015, pp. 28-36.
- [140] Formhals, A. Process and apparatus for preparing artificial threads. US Patent 1975504, 1934.
- [141] Taylor, G. “Electrically driven jets.” Proceedings of the Royal Society A: Mathematical, *Physical and Engineering Sciences* vol.313, no. 1515, Feb. 1969, pp. 453-475.

- 
- [142] Doshi, J., and D.h. Reneker. “Electrospinning process and applications of electrospun fibers”, *Conference Record of the 1993 IEEE Industry Applications Conference Twenty-Eighth IAS Annual Meeting*
- [143] Kaur, S., Rana, D., Matsuura, T., Sundarrajan, S., and Ramakrishna, S. “Preparation and characterization of surface modified electrospun membranes for higher filtration flux”, *Journal of Membrane Science* vol.390-391, 2012, pp. 235-242.
- [144] Ren, Z., and Gao, P.-X., “A review of helical nanostructures: growth theories, synthesis strategies and properties”, *Nanoscale* vol.6, no. 16, June 2014, p. 9366.
- [145] Jung, S., Yoon, G., Lee, H., and Shin, H. “Chitosan nanoparticle/PCL nanofiber composite for wound dressing and drug delivery”, *Journal of Biomaterials Science, Polymer Edition* vol.26, no. 4, Sept. 2015, pp. 252-263.
- [146] Yarin, A. L., Pourdeyhimi, B., and Ramakrishna, S., “Fundamentals and applications of micro and nanofibers”, *Cambridge, United Kingdom: University Printing House*, 2014, pp. 1-23.
- [147] Lubasova, D., Netravali, A., Parker, J., Ingel, B. “Bacterial filtration efficiency of green soy protein based nanofiber air filter”, *Journal of Nanoscience and Nanotechnology* vol.14, no. 7, Jan. 2014, pp. 4891-4898.
- [148] Liu, C., Feng, Y., He, H., Zhang, J., Sun, R., Chen, M. “Effect of carbonization temperature on properties of aligned electrospun polyacrylonitrile carbon nanofibers”, *Materials Design* vol.85, 2015, pp. 483-486.
- [149] Mehrasa, M., Asadollahi, M. A., Ghaedi, K., Salehi, H., Arpanaei, A. “Electrospun aligned PLGA and PLGA/gelatin nanofibers embedded with

- 
- silica nanoparticles for tissue engineering”, *International Journal of Biological Macromolecules* vol.79, 2015, pp. 687-695.
- [150] Li, Z., and Wang, C., “Effects of working parameters on electrospinning”, *Springer Briefs in Materials One-Dimensional nanostructures*, 2013, pp. 1528.
- [151] He, S., Li, S., Hu, Z., Yu, J., Chen, L., Zhu, J. “Effects of three parameters on the diameter of electrospun poly(ethylene oxide) nanofibers”, *Journal of Nanoscience and Nanotechnology* vol.11, no. 2, Jan. 2011, pp. 1052-1059.
- [152] Srivastava, V. K., and Shraddha Singh. “A Micro-Mechanical Model for Elastic Modulus of Multi-Walled Carbon Nanotube/Epoxy Resin Composites.” *International Journal of Composite Materials* vol.2, no. 2, 2012, pp. 1-6.
- [153] Gupta, P., Elkins, C., Long, T. E., Wilkes, G. L. “Electrospinning of linear homopolymers of poly(methyl methacrylate): exploring relationships between fiber formation, viscosity, molecular weight and concentration in a good solvent”, *Polymer* vol.46, no. 13, 2005, pp. 4799-4810.
- [154] Hekmati, A. H., Rashidi, A., Ghazisaeidi, R., Drean, J. “Effect of needle length, electrospinning distance, and solution concentration on morphological properties of polyamide-6 electrospun nanowebs”, *Textile Research Journal* vol.83, no. 14, Nov. 2013, pp. 1452-1466.
- [155] Zhang, C., Yuan, X., Wu, L., Han, Y., Sheng, J. “Study on morphology of electrospun poly (vinyl alcohol) mats”, *European Polymer Journal* vol.41, no. 3, 2005, pp. 423-432.

- 
- [156] Yuan, X., Zhang, Y., Dong, C., Sheng, J. “Morphology of ultrafine polysulfone fibers prepared by electrospinning”, *Polymer International* vol.53, no. 11, 2004, pp. 1704-1710.
- [157] Ki, C. S., Baek, D. H., Gang, K. D., Lee, K. H., Um, I. C., and Park, Y. H. “Characterization of gelatin nanofiber prepared from gelatinformic acid solution”, *Polymer* vol.46, no. 14, 2005, pp. 5094-5102.
- [158] Doustgani, Amir. “Effect of electrospinning process parameters of polycaprolactone and nanohydroxyapatite nanocomposite nanofibers”, *Textile Research Journal* vol.85, no. 14, 2015, pp. 1445-1454.
- [159] Deitzel, J., Kleinmeyer, J., Harris, D., and Tan, N. B. “The effect of processing variables on the morphology of electrospun nanofibers and textiles.” *Polymer* vol.42, no. 1, 2001, pp. 261-272.
- [160] Schoenmaker, B. D., Schueren, L. V. D., Zugle, R., Goethals, A., Westbroek, P., Kiekens, P., Nyokong, T., and Clerck, K. D. “Effect of the relative humidity on the fibre morphology of polyamide 4.6 and polyamide 6.9 nanofibres”, *Journal of Materials Science* vol.48, no. 4, Nov. 2012, pp. 1746-1754.
- [161] Nezarati, R. M., Eifert, M. B., and Cosgriff-Hernandez, E. “Effects of humidity and solution viscosity on electrospun fiber morphology”, *Tissue Engineering Part C: Methods* vol.19, no. 10, 2013, pp. 810-819.
- [162] Oulata, R. T., and Iolu, H. I., “Interaction between effects of ambient parameters and those of other important parameters on electrospinning of PEI/NMP solution”, *The Journal of The Textile Institute* vol.106, no. 1, 2014, pp. 57-66.
- [163] . Pauly, H. M., Kelly, D. J., Popat, K. C., Trujillo, N. A., Dunne, N. J., Mccarthy, H. O., and Donahue, T. L. H., “Mechanical properties and

- 
- cellular response of novel electrospun nanofibers for ligament tissue engineering: Effects of orientation and geometry”, *Journal of the Mechanical Behavior of Biomedical Materials* vol.61, 2016, pp. 258-270.
- [164] Liu, H.-Y., Xu, L., and Si, N. “Effect of magnetic intensity on diameter of charged jets in electrospinning”, *Thermal Science* vol.18, no. 5, 2014, pp. 1451-1454.
- [165] Li, D., Wang, Y., and Xia, Y., “Electrospinning of polymeric and ceramic nanofibers as uniaxially aligned arrays”, *Nano Letters* vol.3, no. 8, 2003, pp. 1167-1171.
- [166] Baji, A., Mai, Y.-W., Wong, S.-C., Abtahi, M., and Chen, P. “Electrospinning of polymer nanofibers: effects on oriented morphology, structures and tensile properties”, *Composites Science and Technology* vol.70, no. 5, 2010, pp. 703-718.
- [167] Luo, C. J., Stoyanov, S. D., Stride, E., Pelan, E., and Edirisinghe, M. “Electrospinning versus Fibre Production Methods: From Specifics to Technological Convergence.” *ChemInform* vol.43, no. 42, 2012
- [168] Zhu, Z., Chen, X., Huang, S., Du, Z., Zeng, J., Liao, W., Fang, F., Peng, D., and Wang, H. “The process of wavy fiber deposition via auxiliary electrodes in near-field electrospinning.” *Applied Physics A* vol.120, no. 4, July 2015, pp. 1435-1442.
- [169] Croisier, F., Duwez, A.-S., Jrme, C., Lonard, A., Werf, K. V. D., Dijkstra, P., and Bennink, M. “Mechanical testing of electrospun PCL fibers,” *Acta Biomaterialia* vol.8, no. 1, 2012, pp. 218-224.
- [170] Zhao, J., Liu, H., and Xu, L. “Preparation and formation mechanism of highly aligned electrospun nanofibers using a modified parallel electrode method,” *Materials Design* vol.90, 2016, pp. 1-6.

- 
- [171] Arras, M. M. L., Grasl, C., Bergmeister, H., and Schima, H. "Electrospinning of aligned fibers with adjustable orientation using auxiliary electrodes," *Science and Technology of Advanced Materials* vol.13, no. 3, 2012, p. 035008.
- [172] Zhou, Y., Hosur, M., Jeelani, S., and Mallick, P. K. "Fabrication and characterization of carbon fiber reinforced clay/epoxy composite", *Journal of Materials Science* vol.47, no. 12, 2012, pp. 5002-5012.
- [173] Sanchez, F., Garcia, J., Chinesta, F., Gascon, L., Zhang, C., Liang, Z., and Wang, B. "A process performance index based on gate-distance and incubation time for the optimization of gate locations in liquid composite molding processes", *Composites Part A: Applied Science and Manufacturing* vol.37, no. 6, 2006, pp. 903-912.
- [174] Lee, Y. J., Wu, J. H., Hsu, Y., and Chung, C. H. "A prediction method on in-plane permeability of mat/roving fibers laminates in vacuum assisted resin transfer molding," *Polymer Composites* vol.27, no. 6, 2006, pp. 665-670.
- [175] Gates, T., Odegard, G., Frankland, S., and Clancy, T. "Computational materials: Multi-scale modeling and simulation of nanostructured materials." *Composites Science and Technology* vol.65, no. 15-16, 2005, pp. 2416-2434.
- [176] McCartney, L. N. "Analytical micromechanical models for the prediction of multiple cracking in composites," *Le Journal De Physique IV* vol.03, no. C7, 1993
- [177] Hull, D., and T. W. Clyne. "An Introduction to Composite Materials." 1996

- 
- [178] Mori, T, and K Tanaka. “Average stress in matrix and average elastic energy of materials with misfitting inclusions”, *Acta Metallurgica* vol.21, no. 5, 1973, pp. 571-574.
- [179] Cox, H L. “The elasticity and strength of paper and other fibrous materials.” *British Journal of Applied Physics* vol.3, no. 3, 1952, pp. 72-79.
- [180] Tserpes, K., Papanikos, P., Labeas, G., and Pantelakis, S. “Multi-scale modeling of tensile behavior of carbon nanotube-reinforced composites”, *Theoretical and Applied Fracture Mechanics* vol.49, no. 1, 2008, pp. 51-60.
- [181] Mohammadpour, E., Awang, M., Kakooei, S., and Akil, H. M., “Modeling the tensile stress-strain response of carbon nanotube/polypropylene nanocomposites using nonlinear representative volume element”, *Materials Design* vol.58, 2014, pp. 36-42.
- [182] Ma, P.-C., Mo, S.-Y., Tang, B.-Z., and Kim, J.-K., “Dispersion, interfacial interaction and re-agglomeration of functionalized carbon nanotubes in epoxy composites,” *Carbon* vol.48, no. 6, 2010, pp. 1824-1834.
- [183] Li, Y, and G D Seidel. “Multiscale modeling of the effects of nanoscale load transfer on the effective elastic properties of unfunctionalized carbon Nanotube-Polyethylene Nanocomposites.” *Modelling and Simulation in Materials Science and Engineering* vol.22, no. 2, 2014, p. 025023.
- [184] Rahmandoust, M., and chsner, A., “On finite element modeling of single-walled and multi-walled carbon nanotubes,” *Journal of Nanoscience and Nanotechnology*, vol. 12, Jan. 2012, pp. 8129-8136.
- [185] Jiang, Q., Tallury, S. S., Qiu, Y., and Pasquinelli, M. A., “Molecular dynamics simulations of the effect of the volume fraction on unidirectional polyimide-carbon nanotube nanocomposites,” *Carbon* vol.67, 2014, pp. 440-448.

- 
- [186] Valavala, Pavan K., and Gregory M. Odegard. "Multiscale constitutive modeling of polymer materials." *Volume 1: Advances in Aerospace Technology*, 2007
- [187] Spanos, K., Georgantzinis, S., and Anifantis, N., "Investigation of stress transfer in carbon nanotube reinforced composites using a multi-scale finite element approach," *Composites Part B: Engineering* vol.63, 2014, pp. 85-93.
- [188] Pilehrood, M. K., Heikkil, P., and Harlin, A., "Preparation of carbon nanotube embedded in polyacrylonitrile (pan) nanofibre composites by electrospinning process", *Autex Research Journal*, vol. 12, Jan. 2012, pp. 1-6.
- [189] "AMT Composites", *AMT Composites*, Available: <http://www.amt-composites.co.za/>.
- [190] D. Cripps. netcomposites. com. 1999, [Online]. [http:// www.netcomposites.com/guide/glassfiberfiber/](http://www.netcomposites.com/guide/glassfiberfiber/) 32.
- [191] Bahr, J. L., and Tour, J. M., "Covalent chemistry of single-wall carbon nanotubes," *Journal of Materials Chemistry*, vol. 12, Jan. 2002, pp. 1952-1958.
- [192] Wu, X. L., and P. Liu. "Poly(vinyl chloride)-grafted multi-walled carbon nanotubes via friedel-crafts alkylation." *Express Polymer Letters*, vol. 4, no. 11, 2010, pp. 723-728.
- [193] Saito, R., Jorio, A., Filho, A. S., Grueneis, A., Pimenta, M., Dresselhaus, G., and Dresselhaus, M., "Dispersive Raman spectra observed in graphite and single wall carbon nanotubes," *Physica B: Condensed Matter* , vol. 323, no. 1-4, 2002, pp. 100-106.

- 
- [194] Wepasnick, K. A., Smith, B. A., Bitter, J. L., and Fairbrother, D. H., “Chemical and structural characterization of carbon nanotube surfaces, Analytical and Bioanalytical Chemistry,” *Analytical and Bioanalytical Chemistry*, vol. 396, no. 3, June 2010, pp. 1003-1014.
- [195] ASTM, ”ASTM Standard D638,” in Standard Test Method for Tensile Properties of Plastics. ASTM International, 2010.
- [196] Raman, C. V. “A New Radiation.” *Proceedings of the Indian Academy of Sciences - Section A* 37, no. 3, 1953, pp. 333-341.
- [197] S. Costa, E. Borowiak-Palen , M. Kruszynska, A. Bachmatiuk, R. J. Kalenczuk., “Characterization of carbon nanotubes by Raman spectroscopy”. *Materials. Science-Poland*, 2008, vol.26, no.2, pp.1-9.
- [198] Tuinstra, F., and J. L. Koenig. “Raman spectrum of graphite.” *The Journal of Chemical Physics* vol.53, no. 3, 1970, pp. 1126-1130.
- [199] Smith, B. C., *Fundamentals of Fourier transform infrared spectroscopy*, “Boca Raton, FL: CRC Press”, Second Edition. Sept. 2011.
- [200] Tamura, T., and Kawakami, H., “Aligned electrospun nanofiber composite membranes for fuel cell electrolytes”, *Nano Letters* vol.10, no. 4, 2010, pp. 1324-1328.
- [201] Li, P., Liu, D., Zhu, B., Li, B., Jia, X., Wang, L., Li, G., and Yang, X., “.Synchronous effects of multiscale reinforced and toughened CFRP composites by MWNTs-EP/PSF hybrid nanofibers with preferred orientation,” *Composites Part A: Applied Science and Manufacturing* vol.68, 2015, pp. 72-80.
- [202] Chou, T.-W., Gao, L., Thostenson, E. T., Zhang, Z., and Byun, J.-H., “An assessment of the science and technology of carbon nanotube-based

- 
- fibers and composites,” *Composites Science and Technology*, vol.70, no. 1, 2010, pp. 1-19.
- [203] Reneker, D. H., and Yarin, A. L., “Electrospinning jets and polymer nanofibers”, *Polymer* vol.49, no. 10, 2008, pp. 2387-2425.
- [204] Philip B., “Characterization of the structural properties of ECNT embedded PAN nanomat reinforced glass fiber hybrid composites (master’s degree)”. 2016, Retrieved from <http://wiredspace.wits.ac.za/handle/10539/21162>.
- [205] Isuru I. K. J., Electrospun Nano-mat strengthened sramid fibre hybrid composites: Improved mechanical properties by continuous nanofibres. 2016, Retrieved from <http://wiredspace.wits.ac.za/handle/10539/22603>.
- [206] Muthu, J., Bradley, P., Jinasena, I. I., Durbach, S., Moya, A., and Paskaramoorthy, R., “The effects of carbon nanofiber on the mechanical properties of glass/coir fiber reinforced polyester hybrid composites,” *Polymer Composites*, vol. 39, 2016, pp. 318-328.
- [207] Naraghi M., Chasiotis I., “Mechanics of PAN nanofibers.” *Major Accomplishments in Composite Materials and Sandwich Structures*, 2009, pp. 757-778.
- [208] Lachman, N., and Wagner, H. D., “Correlation between interfacial molecular structure and mechanics in CNT/epoxy nano-composites”, *Composites Part A: Applied Science and Manufacturing* vol.41, no. 9, 2010, pp. 1093-1098.
- [209] Paiva, M., Zhou, B., Fernando, K., Lin, Y., Kennedy, J., and Sun, Y.-P., “Mechanical and morphological characterization of polymer-carbon nanocomposites from functionalized carbon nanotubes,” *Carbon*, vol. 42, 2004, pp. 2849-2854.

- [210] Zuberi, M. J. S., and Esat, V., “Investigating the mechanical properties of single walled carbon nanotube reinforced epoxy composite through finite element modelling”, *Composites Part B: Engineering* vol.71, 2015, pp. 1-9.
- [211] Chabalala, V., Wagner, N., and Potgieter-Vermaak, S., “Investigation into the evolution of char structure using Raman spectroscopy in conjunction with coal petrography; Part 1,” *Fuel Processing Technology*, vol. 92, 2011, pp. 750-756.
- [212] Han, F., Azdoud, Y., and Lubineau, G., “Computational modeling of elastic properties of carbon nanotube/polymer composites with interphase regions. Part II: Mechanical modeling,” *Computational Materials Science*, vol. 81, 2014, pp. 652-661.
- [213] Zohdi, Tarek I., and Peter Wriggers. “An Introduction to Computational Micromechanics”, *Introduction to Computational Micromechanics Lecture Notes in Applied and Computational Mechanics*, pp. 1-6.
- [214] Tserpes, K., Papanikos, P., Labeas, G., and Pantelakis, S., “Multi-scale modeling of tensile behavior of carbon nanotube-reinforced composites,” *Theoretical and Applied Fracture Mechanics*, vol. 49, 2008, pp. 51-60.
- [215] Han, F., Azdoud, Y., and Lubineau, G., “Computational modeling of elastic properties of carbon nanotube/polymer composites with interphase regions. Part I: Micro-structural characterization and geometric modeling,” *Computational Materials Science*, vol. 81, 2014, pp. 641-651.
- [216] Hernandez-Prez, A., and Avils, F., “Modeling the influence of interphase on the elastic properties of carbon nanotube composites,” *Computational Materials Science*, vol. 47, 2010, pp. 926-933.

- 
- [217] Chowdhury, A. N. R., Wang, C. M., and Koh, S. J. A., “Continuum Shell Model For Buckling Of Armchair Carbon Nanotubes Under Compression Or Torsion,” *International Journal of Applied Mechanics*, vol. 06, 2014, p. 1450006.
- [218] Hu, N., Nunoya, K., Pan, D., Okabe, T., and Fukunaga, H., “Prediction of buckling characteristics of carbon nanotubes,” *International Journal of Solids and Structures*, vol. 44, 2007, pp. 6535-6550.
- [219] MUC, A., “Modelling of carbon nanotubes behaviour with the use of a thin shell theory.” *Journal of Theoretical and Applied Mechanics*, vol 49, no 2, 2011, pp. 531-540.
- [220] Ghavamian, A., Rahmandoust, M., and Ochsner, A., “On the determination of the shear modulus of carbon nanotubes,” *Composites Part B: Engineering*, vol. 44, 2013, pp. 52-59.
- [221] Muc, A., “Design and identification methods of effective mechanical properties for carbon nanotubes,” *Materials Design*, vol. 31, 2010, pp. 1671-1675.
- [222] Rahmandoust, M., and Ochsner, A., “Influence of Structural Imperfections and Doping on the Mechanical Properties of Single-Walled Carbon Nanotubes,” *Journal of Nano Research*, vol. 6, 2009, pp. 185-196.
- [223] A.K. Gupta, S.P. Harsha, “Analysis of mechanical properties of carbon nanotube reinforced polymer composites using multi-scale finite element modeling approach”, *Composites Part B: Engineering*, Vol. 95, 2016, pp. 172-178.
- [224] Li, C., and Chou, T.-W., “A structural mechanics approach for the analysis of carbon nanotubes,” *International Journal of Solids and Structures*, vol. 40, 2003, pp. 2487-2499.

- 
- [225] Tersoff, J., and Ruoff, R. S., “Structural Properties of a Carbon-Nanotube Crystal,” *Physical Review Letters*, vol. 73, Jan. 1994, pp. 676-679.
- [226] Reich, S., Thomsen, C., and Ordejn, P., “Elastic properties of carbon nanotubes under hydrostatic pressure,” *Physical Review B*, vol. 65, Mar. 2002.
- [227] Jones, J. E., “On the Determination of Molecular Fields. I. From the Variation of the Viscosity of a Gas with Temperature,” *Proceedings of the Royal Society A: Mathematical, Physical and Engineering Sciences*, vol. 106, Jan. 1924, pp. 441-462.
- [228] Treacy, M. M. J., Ebbesen, T. W., and Gibson, J. M., “Exceptionally high Youngs modulus observed for individual carbon nanotubes,” *Nature*, vol. 381, 1996, pp. 678-680.
- [229] Mohammadpour, E., Awang, M., Hashim, A. M., and Arora, V. K., “Predicting a Stretching Behavior of Carbon Nanotubes using Finite Element Method,” 2011.
- [230] Agrawal, P. M., Sudalayandi, B. S., Raff, L. M., and Komanduri, R., “A comparison of different methods of Youngs modulus determination for single-wall carbon nanotubes (SWCNT) using molecular dynamics (MD) simulations,” *Computational Materials Science*, vol. 38, 2006, pp. 271-281.
- [231] Yang, Y., Ramirez, C., Wang, X., Guo, Z., Tokranov, A., Zhao, R., Szlufarska, I., Lou, J., and Sheldon, B. W., “Impact of carbon nanotube defects on fracture mechanisms in ceramic nanocomposites,” *Carbon*, vol. 115, 2017, pp. 402-408..
- [232] Sakhaee-Pour, A., “Elastic properties of single-layered graphene sheet,” *Solid State Communications*, vol. 149, 2009, pp. 91-95.

- 
- [233] Li, C., “Elastic moduli of multi-walled carbon nanotubes and the effect of van der Waals forces,” *Composites Science and Technology*, vol. 63, 2003, pp. 1517-1524.
- [234] Yu, M., “Strength and Breaking Mechanism of Multiwalled Carbon Nanotubes Under Tensile Load,” *Science*, vol. 287, 2000, pp. 637-640.
- [235] Papkov, D., Zou, Y., Andalib, M. N., Goponenko, A., Cheng, S. Z. D., and Dzenis, Y. A., “Simultaneously Strong and Tough Ultrafine Continuous Nanofibers,” *ACS Nano*, vol. 7, 2013, pp. 3324-3331.
- [236] Sawai, D., Fujii, Y., and Kanamoto, T., “Development of oriented morphology and tensile properties upon superdrawing of solution-spun fibers of ultra-high molecular weight poly(acrylonitrile),” *Polymer*, vol.47, 2006, pp. 4445-4453.
- [237] Alian, A., Kundalwal, S., and Meguid, S., “Multiscale modeling of carbon nanotube epoxy composites,” *Polymer*, vol. 70, 2015, pp. 149-160.
- [238] Duan, W. H., Wang, Q., and Collins, F., “Dispersion of carbon nanotubes with SDS surfactants: a study from a binding energy perspective,” *Chemical Science*, vol. 2, 2011, p. 1407.

# Appendix A

## A.1 Tensile Tests Details

### A.1.1 Neat glassfibre composite (32% Vol)

TABLE A.1: 05 specimens batch tensile test results of neat glassfibre composite (32% Vol)

Batch:Neat glassfibre composite (32% Vol)				Tensile strength	L	$\Delta l$	Strain	Young Modulus
S.No.	Width. mm	Thickness. mm	Energy absorbed (N)	(MPa)	(mm)	(mm)	(mm/mm)	(MPa)
1	13.12	3.22	7235.342401	171.2653007	49.447967	0.703064	0.014218259	12045.44812
2	13.24	3.16	6264.048844	149.7200859	50.326784	0.640294	0.012722728	11767.9229
3	13.3	3.2	5339.42427	125.4563973	50.175137	0.573613	0.011432216	10973.93525
4	13.25	3.12	6716.79106	162.4768036	50.020554	0.617865	0.012352222	13153.64963
5	13.24	3.3	7588.279161	173.6766264	50.207933	0.801003	0.015953714	10886.28185
Average				156.5190428	50.035675	0.6671678	0.013335828	11765.44755

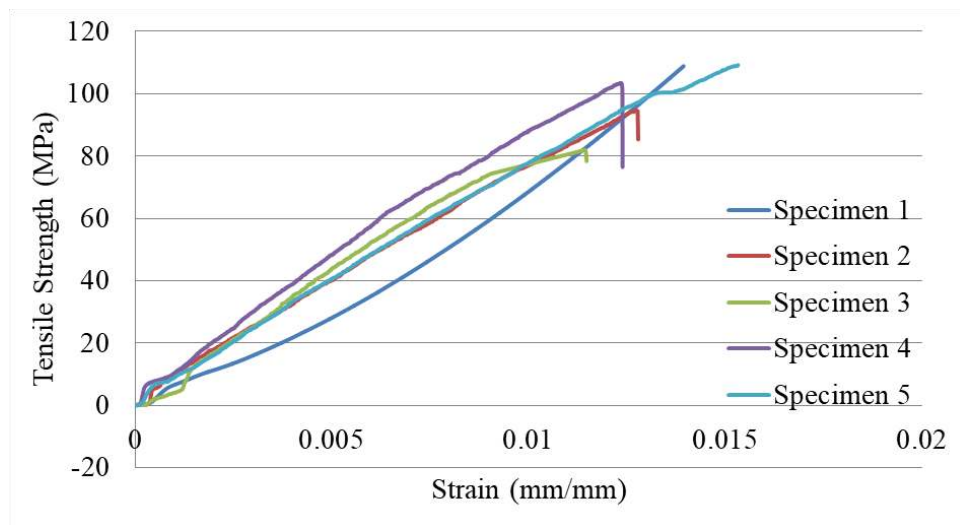


FIGURE A.1: Tensile strengths of glass fibre composite (32% vol) specimens

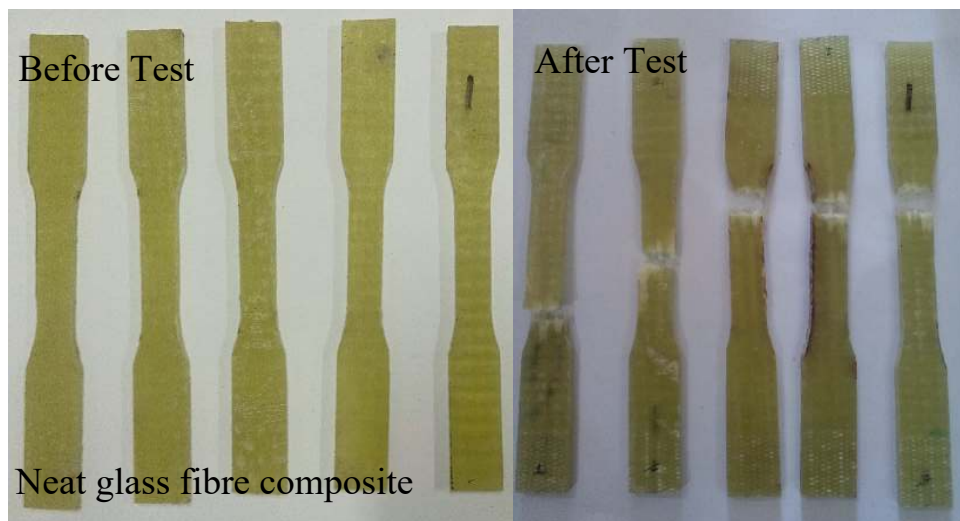


FIGURE A.2: Tested Tensile specimens of glass fibre composite (32% vol)

### A.1.2 Random nanofibres mat (0.1% Vol) strengthened hybrid composite

TABLE A.2: 05 specimens batch tensile test results of random nanofibres mat (0.1% Vol) strengthened hybrid composite

Batch: Random nanofibre mat (0.1% Vol)				Tensile strength	L	$\Delta l$	Strain	Young Modulus
S.No.	Width. mm	Thickness. mm	Energy absorbed (N)	(MPa)	(mm)	(mm)	(mm/mm)	(MPa)
1	13.25	3.25	9025.555	209.592	50.96188	0.747735	0.014672	14284.74
2	13.18	3.25	6820.584	159.2292	50.57686	0.670651	0.01326	12008.2
3	13.32	3.25	9101.966	210.2556	50.43639	0.928882	0.018417	11416.45
4	13.22	3.3	8043.498	184.3739	50.11241	0.828882	0.01654	11146.86
5	13.26	3.3	9092.064	207.7806	49.85392	1.02618	0.020584	10094.41
Average				194.2463	50.38829	0.840466	0.016695	11790.13

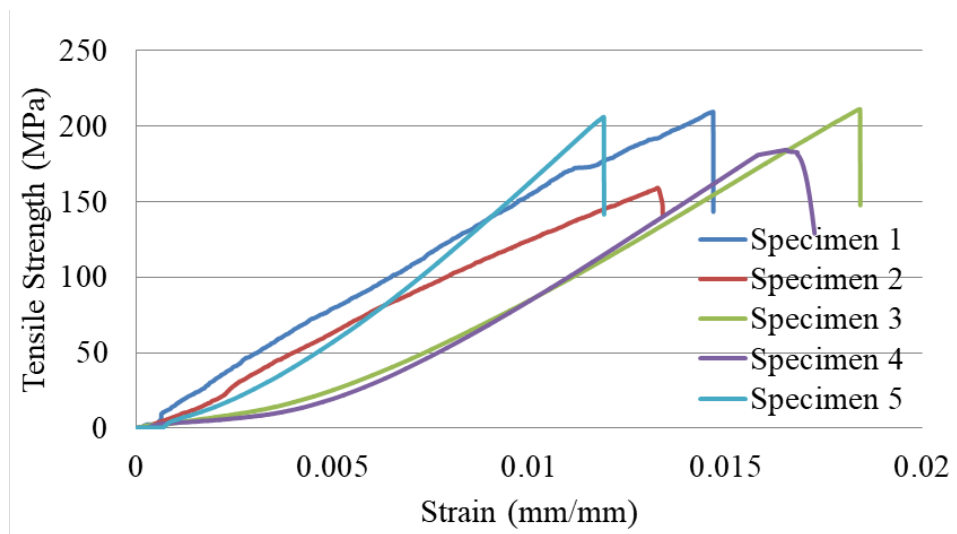


FIGURE A.3: Tensile strengths of random nanofibres mat (0.1% vol) strengthened hybrid composite specimens

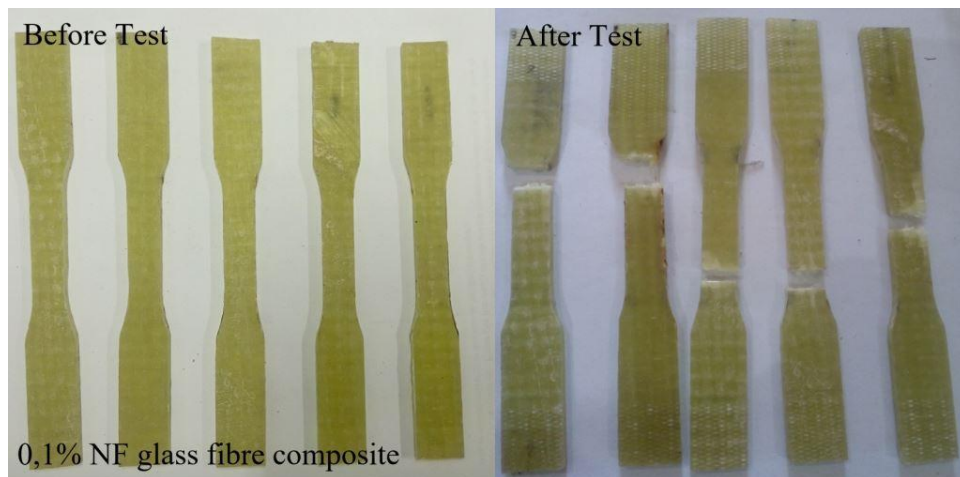


FIGURE A.4: Tested Tensile specimens of random nanofibres mat (0.1% vol) strengthened hybrid composite

### A.1.3 Random nanofibres mat (0.2% Vol) strengthened hybrid composite

TABLE A.3: 05 specimens batch tensile test results of random nanofibres mat (0.2% Vol) strengthened hybrid composite

Batch:Random nanofibre mat (0.2% Vol)				Tensile strength	L	$\Delta l$	Strain	Young Modulus
S.No.	Width. mm	Thickness. mm	Energy absorbed (N)	(MPa)	(mm)	(mm)	(mm/mm)	(MPa)
1	13.2	3.15	9622.5	231.4214	50.06851	1.111485	0.022199	10424.73
2	13.1	3.2	8956.583	213.6589	50.71304	0.780073	0.015382	13890.11
3	13	3.15	7579.076	185.0812	50.76105	0.729344	0.014368	12881.33
4	13.2	3.2	8916.495	211.0913	50.12697	0.926316	0.018479	11423.06
5	13.15	3.1	9234.85	226.5387	50.64922	0.931296	0.018387	12320.47
Average				213.5583	50.46376	0.895703	0.017763	12187.94

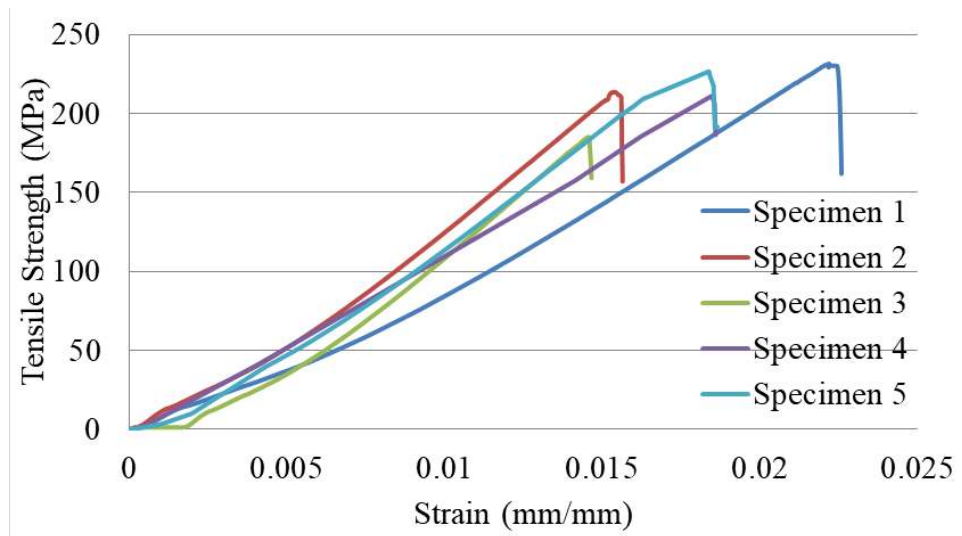


FIGURE A.5: Tensile strengths of random nanofibres mat (0.2% vol) strengthened hybrid composite specimens

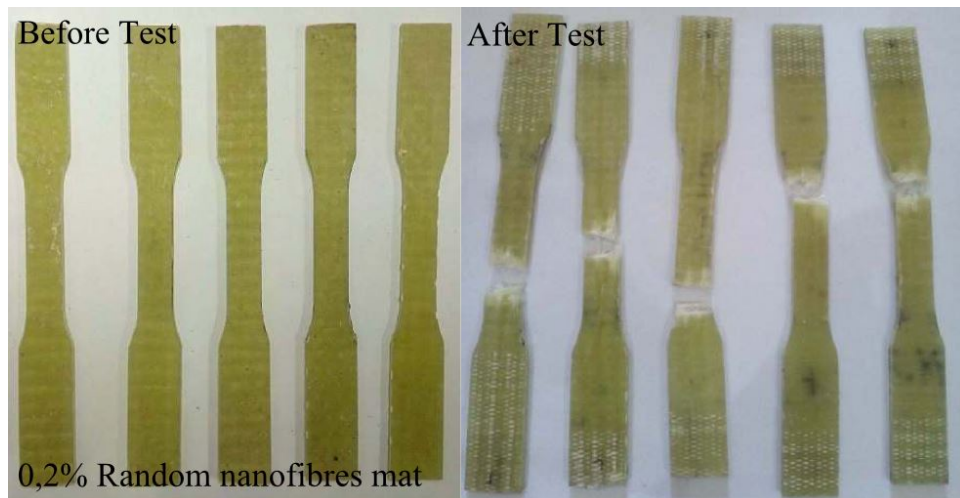


FIGURE A.6: Tested Tensile specimens of random nanofibres mat (0.2% vol) strengthened hybrid composite

### A.1.4 Random nanofibres mat (0.5% Vol) strengthened hybrid composite

TABLE A.4: 05 specimens batch tensile test results of random nanofibres mat (0.5% Vol) strengthened hybrid composite

Batch:Random nanofibre mat (0.5% Vol)				Tensile strength	L	$\Delta l$	Strain	Young Modulus
S.No.	Width. mm	Thickness. mm	Energy absorbed (N)	(MPa)	(mm)	(mm)	(mm/mm)	(MPa)
1	13.2	3.15	9276.182	223.0924	49.78658	0.720764	0.014477	15410.05
2	13.18	3.2	9023.502	213.9487	49.85303	0.786489	0.015776	13561.53
3	13.2	3.16	11595.94	278	50.87429	0.972237	0.019111	14546.92
4	13.1	3.2	11945.53	284.9601	49.21722	1.03944	0.021119	13492.79
5	13.1	3.18	12927.63	310.3277	50.22972	1.055109	0.021006	14773.52
Average				262.0658	49.99217	0.914808	0.018298	14356.96

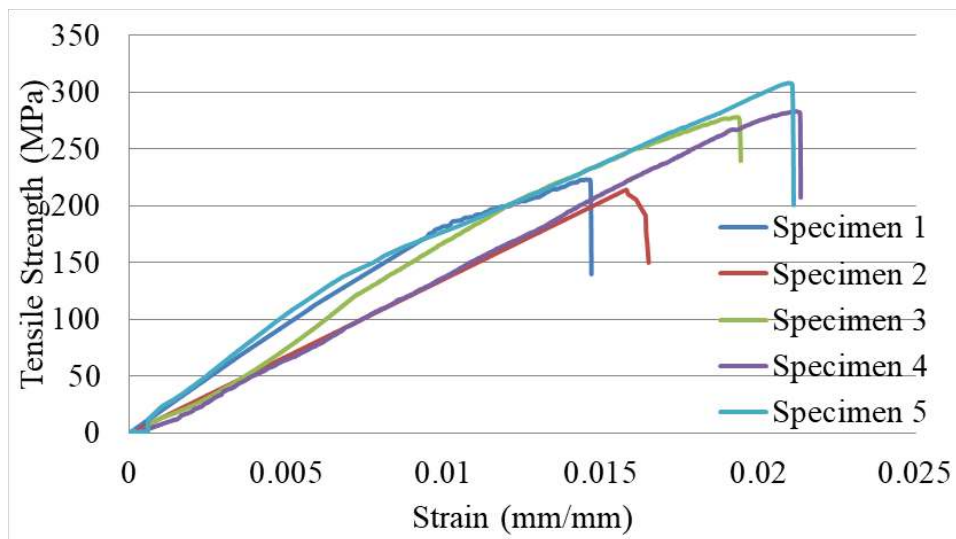


FIGURE A.7: Tensile strengths of random nanofibres mat (0.5% vol) strengthened hybrid composite specimens

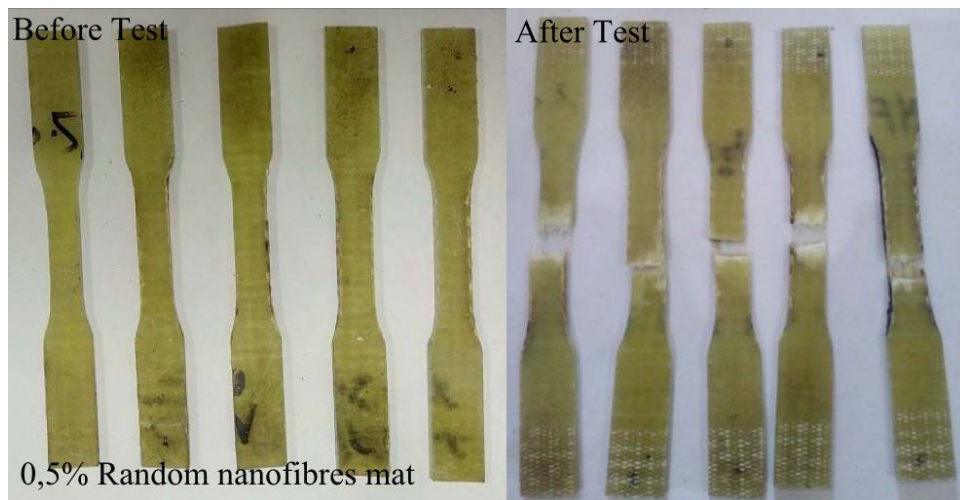


FIGURE A.8: Tested Tensile specimens of random nanofibres mat (0.5% vol) strengthened hybrid composite

### A.1.5 Random nanofibres mat (1% Vol) strengthened hybrid composite

TABLE A.5: 05 specimens batch tensile test of random nanofibres mat (1% Vol) strengthened hybrid composite

Batch:Random nanofibre mat (1% Vol)				Tensile strength (MPa)	L (mm)	$\Delta l$ (mm)	Strain (mm/mm)	Young Modulus (MPa)
S.No.	Width. mm	Thickness. mm	Energy absorbed (N)					
1	13.1	3.23	6180.582	146.0682	50.57679	0.68793	0.013602	10738.97
2	13.12	3.19	8143.929	194.585	49.34246	0.846954	0.017165	11336.28
3	13.18	3.25	5581.61	130.3049	50.81066	0.630996	0.012419	10492.74
4	13.1	3.2	7313.784	174.47	50.53449	0.823882	0.016303	10701.48
5	13.16	3.24	7170.091	168.1604	49.91237	0.738423	0.014794	11366.49
Average				162.7177	50.23535	0.745637	0.014857	10927.19

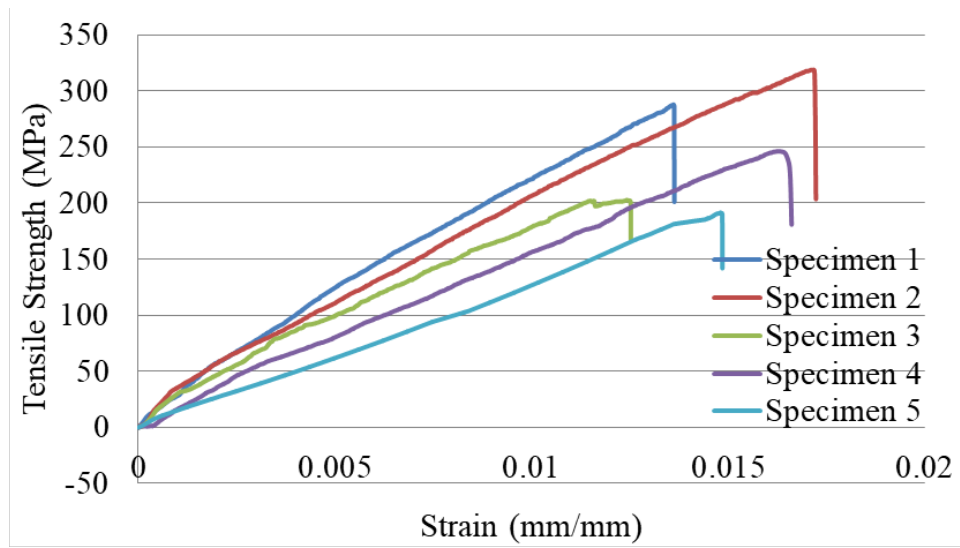


FIGURE A.9: Tensile strengths of random nanofibres mat (1% vol) strengthened hybrid composite specimens

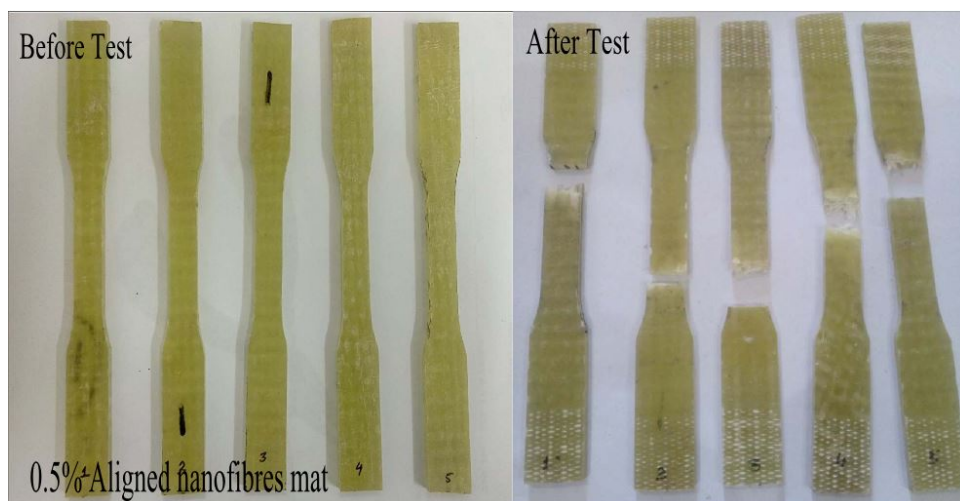


FIGURE A.10: Tested Tensile specimens of random nanofibres mat (1% vol) strengthened hybrid composite

### A.1.6 Aligned nanofibres mat (0.5% Vol) strengthened hybrid composite

TABLE A.6: 05 specimens batch tensile test of aligned nanofibres mat (0.5% Vol) strengthened hybrid composite

Batch: Aligned nanofibre mat (0.1% Vol)				Tensile strength	L	$\Delta l$	Strain	Young Modulus
S.No.	Width. mm	Thickness. mm	Energy absorbed (N)	(MPa)	(mm)	(mm)	(mm/mm)	(MPa)
1	13.15	3.18	10357.97	247.6976	49.47168	0.808933	0.016351	15148.37
2	13.12	3.12	10987.76	268.4235	49.98397	0.781953	0.015644	17158.16
3	13.2	3.2	10049.12	237.9054	49.92355	0.83954	0.016817	14147.13
4	13.1	3.16	9889.821	238.9076	50.38491	0.78287	0.015538	15375.91
5	13.2	3.14	13167.55	317.6885	50.1897	0.966859	0.019264	16491.22
Average				262.1245	49.99076	0.836031	0.016723	15664.16

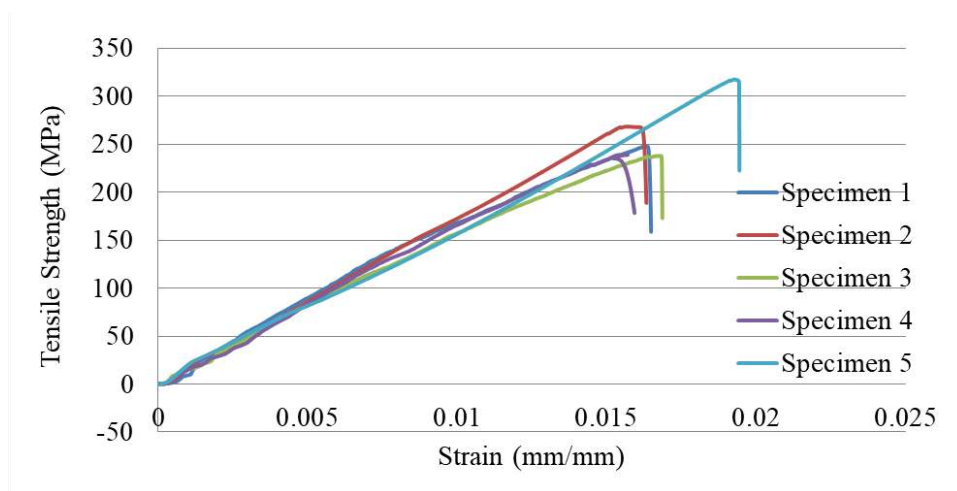


FIGURE A.11: Tensile strengths of aligned nanofibres mat (0.5% vol) strengthened hybrid composite specimens

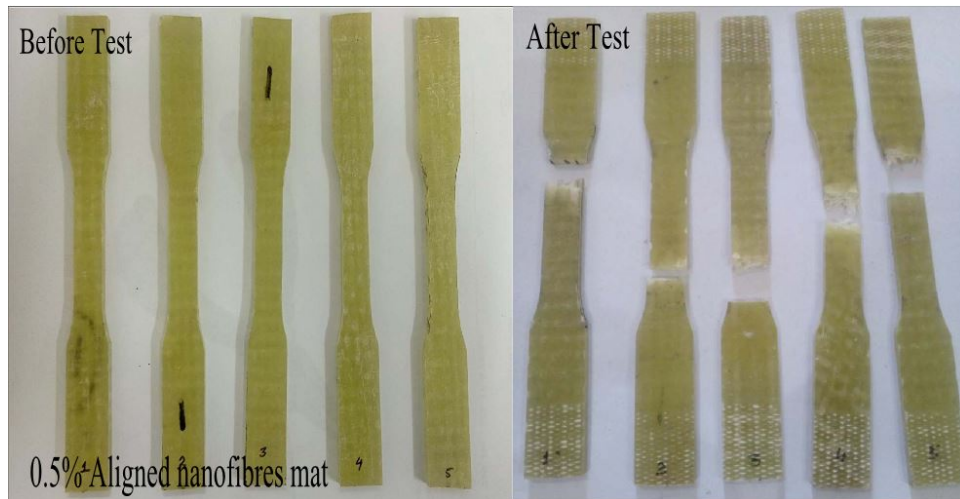


FIGURE A.12: Tested Tensile specimens of aligned nanofibres mat (0.5% vol) strengthened hybrid composite

### A.1.7 (0.25% Vol) p-SWCNTs doped aligned nanofibres mat strengthened hybrid composite

TABLE A.7: 05 specimens batch tensile test of (0.25% Vol) p-SWCNTs doped aligned nanofibres mat strengthened hybrid composite

Batch: (0.25% Vol) p-SWCNTs doped aligned nanofibre mat				Tensile strength	L	$\Delta l$	Strain	Young Modulus
S.No.	Width. mm	Thickness. mm	Energy absorbed (N)	(MPa)	(mm)	(mm)	(mm/mm)	(MPa)
1	12.6	3.16	12001.98	301.4362	50.69411	0.902071	0.017794	16939.95
2	12.7	3.18	11945.11	295.7736	49.21259	0.849828	0.017269	17127.91
3	12.8	3.15	13167.35	326.5713	50.18912	0.818465	0.016308	20025.69
4	12.6	3.2	11605.98	287.8468	50.77793	0.774035	0.015244	18883.21
5	12.7	3.18	10359.85	256.5209	50.46831	0.674024	0.013355	19207.3
Average				293.6297	50.26841	0.803685	0.015994	18436.81

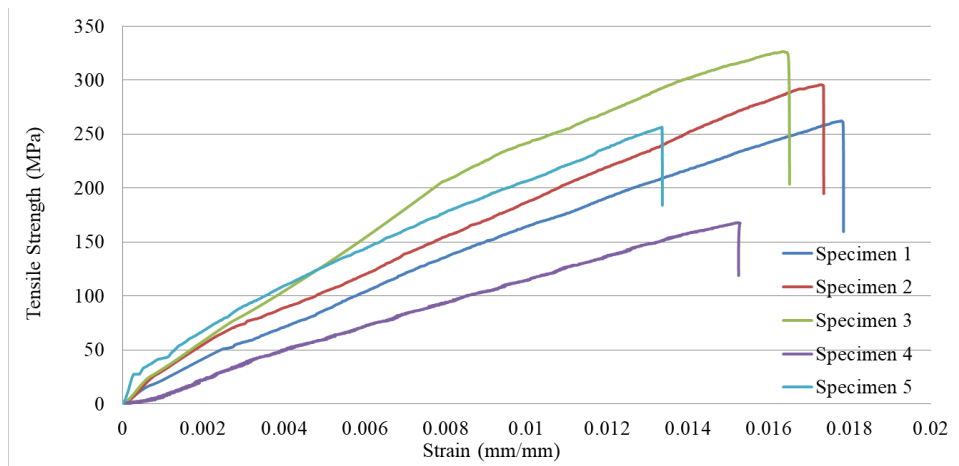


FIGURE A.13: Tensile strengths of p-SWCNTs (0.25% Vol) doped nanofibres mat (0.5% vol) strengthened hybrid composite specimens



FIGURE A.14: Tested Tensile specimens of p-SWCNTs (vol 0.25%) doped aligned nanofibres mat (0.5% vol) strengthened hybrid composite samples

### A.1.8 (0.25% Vol) f-SWCNTs doped aligned nanofibre mat strengthened hybrid composite

TABLE A.8: 05 specimens batch tensile test of (0.25% Vol) f-SWCNTs doped aligned nanofibre mat strengthened hybrid composite

Batch: (0.25% Vol) f-SWCNTs doped aligned nanofibre mat				Tensile strength	L	$\Delta l$	Strain	Young Modulus
S.No.	Width. mm	Thickness. mm	Energy absorbed (N)	(MPa)	(mm)	(mm)	(mm/mm)	(MPa)
1	12.9	3.1	12626.8	315.749	50.897	0.731159	0.014365	21979.73
2	13	3.2	13344.51	320.7815	49.92828	0.813339	0.01629	19691.75
3	13.08	3.1	12986.91	320.2849	49.8909	0.738441	0.014801	21639.24
4	12.8	3.16	13247.09	327.5091	50.8242	0.787865	0.015502	21127.21
5	13	3.12	14391.36	354.8166	50.1098	0.736293	0.014694	24147.69
Average				327.8282	50.33004	0.761419	0.01513	21717.12

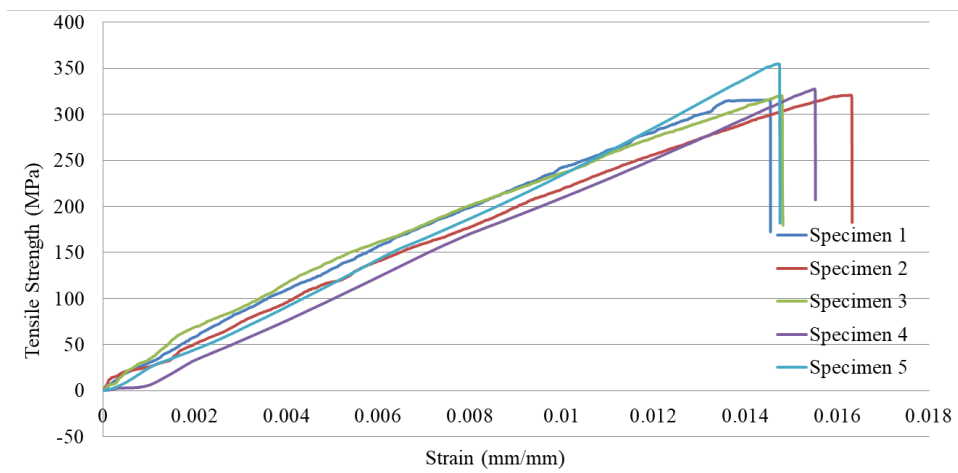


FIGURE A.15: Tensile strengths of f-SWCNTs (0.25% Vol) doped nanofibres mat (0.5% vol) strengthened hybrid composite specimens

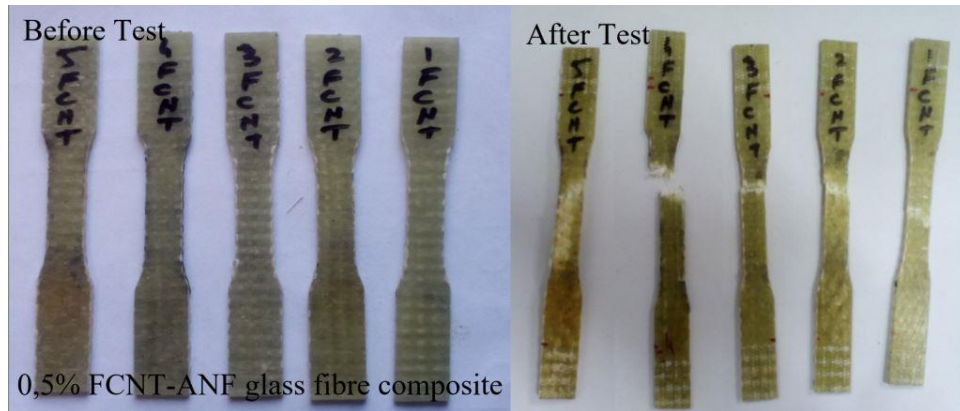


FIGURE A.16: Tested Tensile specimens of f-SWCNTs doped aligned nanofibres mat (0.5% vol) strengthened hybrid composite

## A.2 Flexural Test Details

### A.2.1 Neat glassfibre composite 32%

TABLE A.9: Flexural strength details of neat glassfibre specimens (32% Vol)

Batch: Neat glass fibre composite 32%				Flexural strength N/mm <sup>2</sup>	Strain Constant	Max Bending mm	Strain mm/mm	Flexure modulus N/mm <sup>2</sup>
S.No.	Width mm	Thickness mm	Force N (maximum)					
1	13.4	3.2	362.2535	249.4822	0.0048	5.3650	0.0260	9612.7974
2	13.45	3.22	368.7952	249.9097	0.0049	4.9550	0.0241	10361.2788
3	13.4	3.18	321.1252	223.9480	0.0048	4.8530	0.0233	9599.3016
4	13.4	3.22	386.5236	262.9004	0.0049	5.6550	0.0275	9550.6429
5	13.4	3.24	334.7522	224.8850	0.0049	5.2450	0.0257	8753.8644
Average			354.6899	242.2251	0.0049	5.2146	0.0253	9575.5770

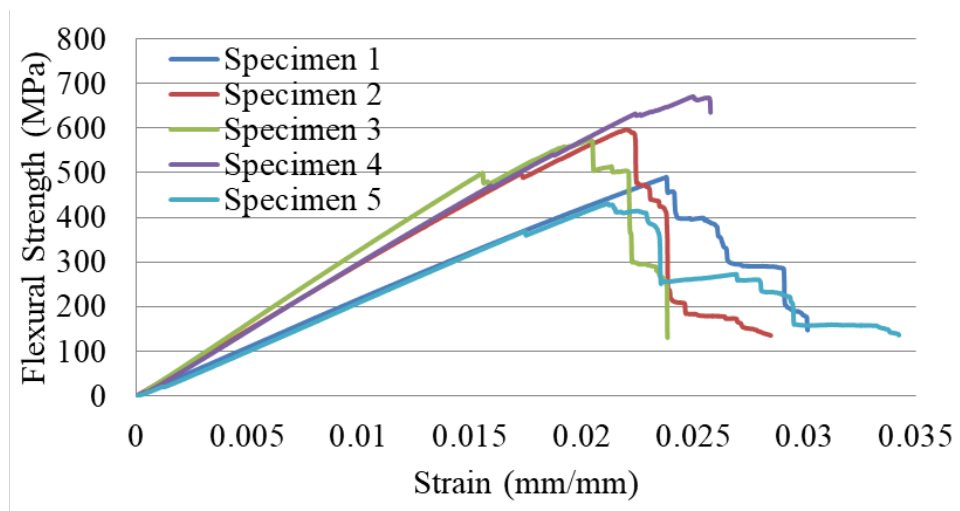


FIGURE A.17: Flexural strengths of glass fibre samples (32% Vol)

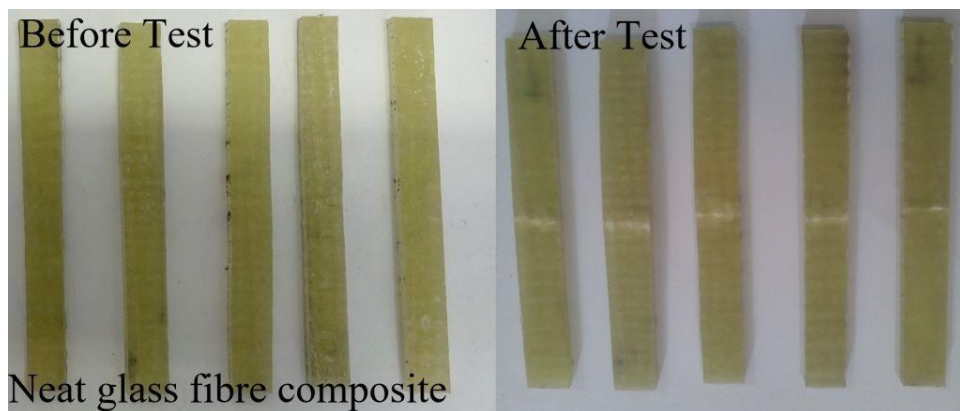


FIGURE A.18: Tested flexural specimens of glassfibre samples (32% Vol)

## A.2.2 Random nanofibres mat (0.1%) strengthened hybrid composite

TABLE A.10: Flexural strength details of Random nanofibres mat (0.1%) strengthened hybrid composite specimens

Batch:0.1% Random nanofibres mat				Flexural strength N/mm <sup>2</sup>	Strain Constant	Max Bending mm	Strain mm/mm	Flexure modulus N/mm <sup>2</sup>
S.No.	Width mm	Thickness mm	Force N (maximum)					
1	13.3	3.02	366.5235	285.5408	0.0046	5.7390	0.0262	10898.2003
2	13.25	3.3	402.8751	263.8508	0.0050	5.5760	0.0278	9485.3120
3	13.25	3.3	367.7518	240.8479	0.0050	4.6320	0.0231	10422.9395
4	13.3	3.2	437.3205	303.4450	0.0048	4.6010	0.0223	13633.5087
5	13.2	3.25	479.7524	325.1684	0.0049	4.9790	0.0245	13292.6826
Average			410.8446	283.7706	0.0049	5.1054	0.0248	11546.5286

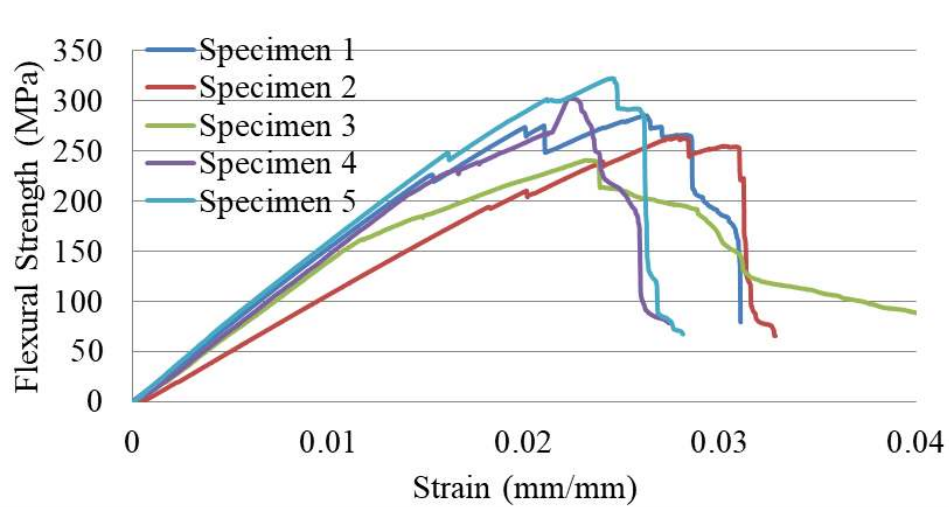


FIGURE A.19: Flexural strengths of Random nanofibres mat (0.1%) strengthened hybrid composite samples

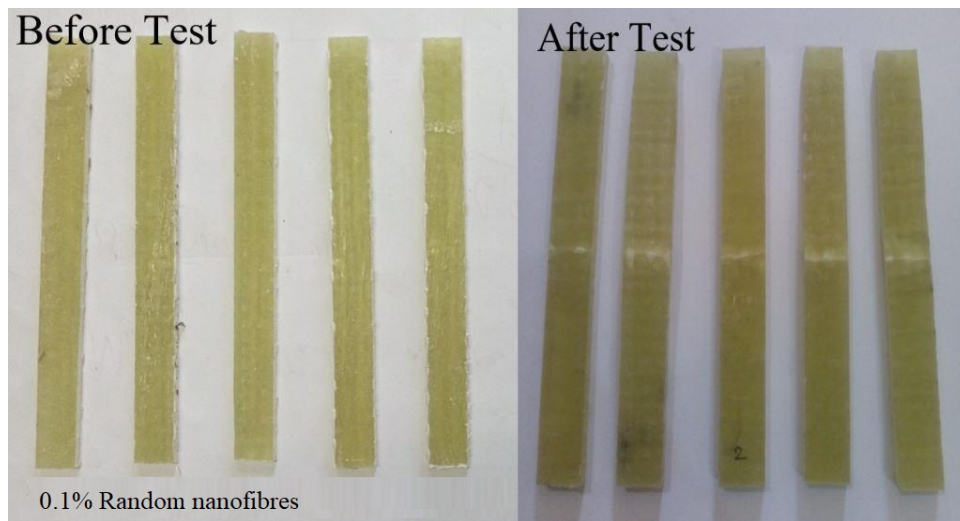


FIGURE A.20: Tested specimens of random nanofibres mat (0.1%) strengthened hybrid composite

### A.2.3 Random nanofibres mat (0.2%) strengthened hybrid composite

TABLE A.11: Flexural strength details of Random nanofibres mat (0.2%) strengthened hybrid composite specimens

Batch:0.2% Random nanofibres mat				Flexural strength N/mm <sup>2</sup>	Strain Constant	Max Bending mm	Strain mm/mm	Flexure modulus N/mm <sup>2</sup>
S.No.	Width mm	Thickness mm	Force N (maximum)					
1	13	3.1	352.8750	266.9230	0.0047	5.0320	0.0236	11319.1413
2	13.12	3.16	457.3750	329.9106	0.0048	4.9660	0.0237	13906.9624
3	13.2	3.24	350.6250	239.1172	0.0049	5.3710	0.0263	9089.5089
4	13.12	3.04	469.7500	366.1151	0.0046	5.5260	0.0254	14416.6043
5	13.1	3.2	505.9375	356.4162	0.0048	4.2860	0.0207	17190.3663
Average			427.3125	311.6964	0.0048	5.0362	0.0239	13184.5167

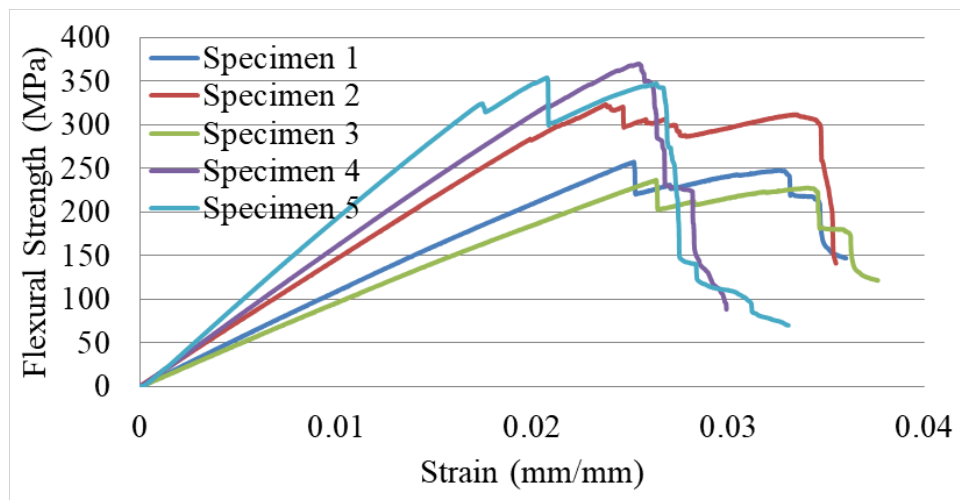


FIGURE A.21: Flexural strengths of Random nanofibres mat (0.2%) strengthened hybrid composite samples

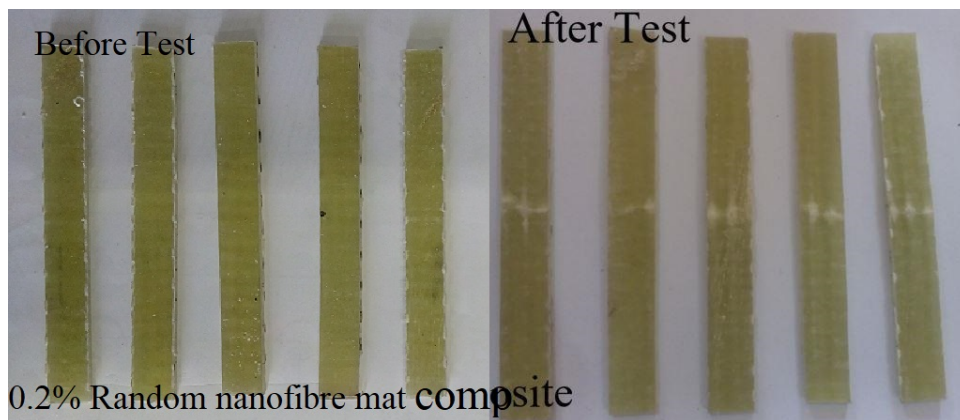


FIGURE A.22: Tested flexural random nanofibres mat (0.2%) strengthened hybrid composite samples

## A.2.4 Random nanofibres mat (0.5%) strengthened hybrid composite

TABLE A.12: Flexural strength details of random nanofibres mat (0.5%) strengthened hybrid composite specimens

Batch:0.5% Random nanofibres mat				Flexural strength	Strain Constant	Max Bending	Strain	Flexure modulus
S.No.	Width mm	Thickness mm	Force N (maximum)	N/mm2		mm		
1	13.2	3.15	583.1875	420.7702	0.0048	6.2330	0.0297	14176.4387
2	12.7	3	494.7890	409.0775	0.0045	4.7970	0.0218	18803.7509
3	13.34	3.2	602.6250	416.8916	0.0048	6.2920	0.0304	13696.6489
4	13.4	3.18	566.1252	394.8074	0.0048	5.7750	0.0278	14221.1919
5	13.4	3.3	591.1237	382.8049	0.0050	6.1340	0.0306	12509.7780
Average			567.5701	404.8703	0.0048	5.8462	0.0280	14681.5617

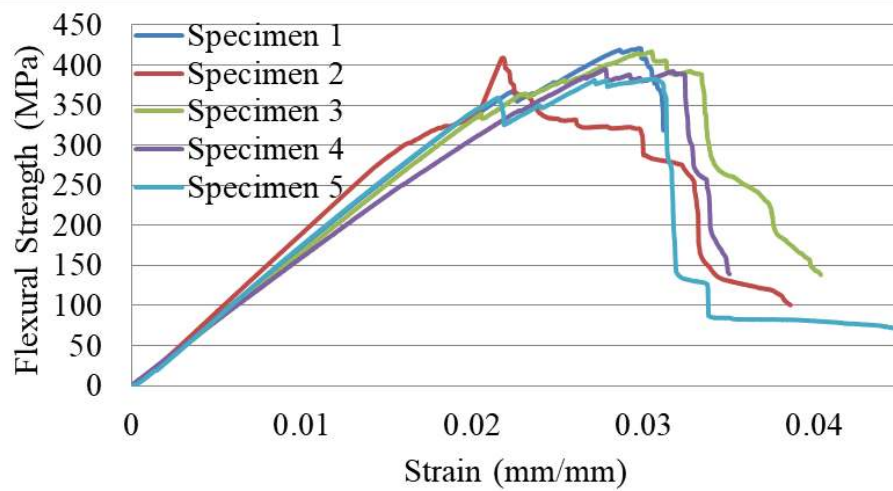


FIGURE A.23: Flexural strengths of random nanofibres mat (0.5%) strengthened hybrid composite samples

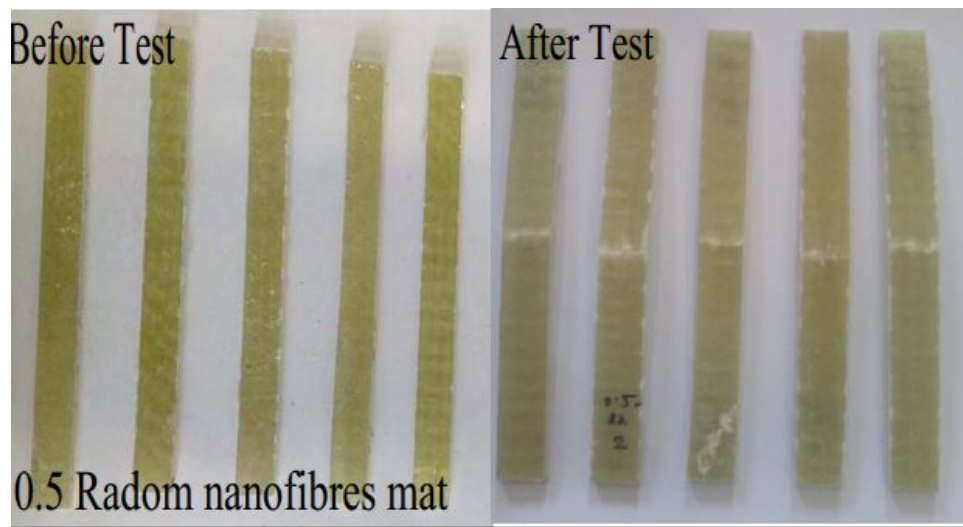


FIGURE A.24: Tested specimens of random nanofibres mat (0.5%) strengthened hybrid composite

### A.2.5 Random nanofibres mat (1%) strengthened hybrid composite

TABLE A.13: Flexural strength of random nanofibres mat (1%) strengthened hybrid composite specimens

Batch:1% random nanofibres mat				Flexural strength N/mm <sup>2</sup>	Strain Constant	Max Bending mm	Strain mm/mm	Flexure modulus N/mm <sup>2</sup>
S.No.	Width mm	Thickness mm	Force N (maximum)					
1	13.2	3.3	364.8750	239.8690	0.0050	5.7840	0.0289	8313.0756
2	13.2	3.28	353.1250	234.9842	0.0050	5.2440	0.0260	9037.1601
3	13.5	3.2	484.8750	331.4575	0.0048	4.6390	0.0224	14770.0979
4	13.3	3.3	545.6250	355.9972	0.0050	5.9300	0.0296	12033.9378
5	13.2	3.4	405.0000	250.8159	0.0051	4.4860	0.0231	10877.9417
Average			430.7000	282.6248	0.0050	5.2166	0.0260	11006.4426

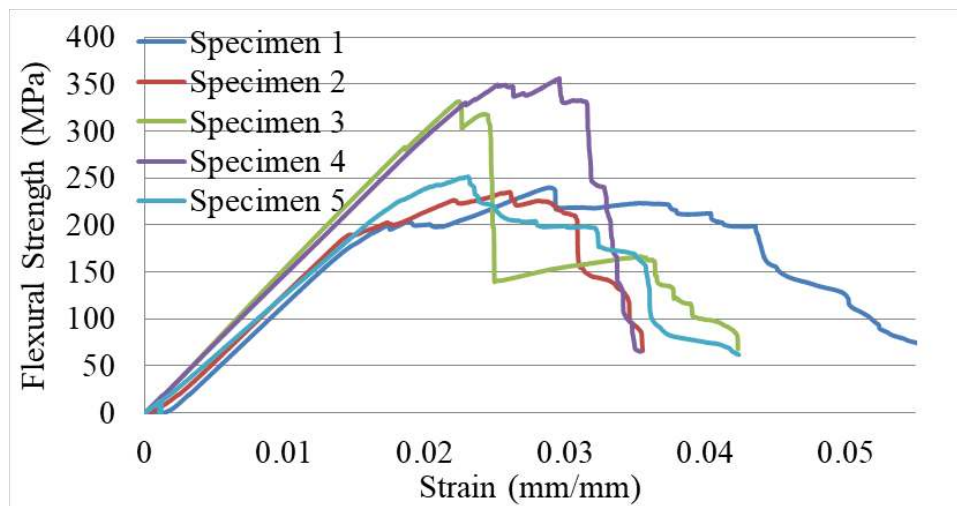


FIGURE A.25: Flexural strengths of random nanofibres mat (1%) strengthened hybrid composite samples

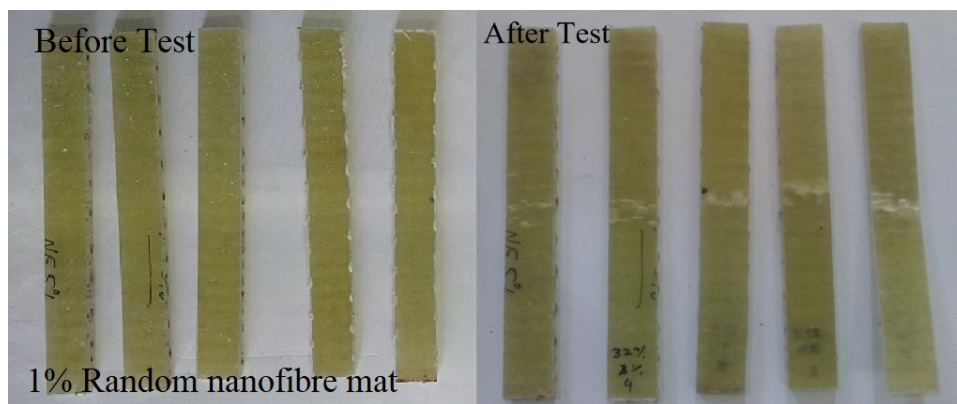


FIGURE A.26: Tested specimens of Flexural Random nanofibres mat (1%) strengthened hybrid composite

## A.2.6 Aligned nanofibres mat (0.5%) strengthened hybrid composite

TABLE A.14: Flexural strength details of Aligned nanofibres mat (0.5%) strengthened hybrid composite

Batch:0.5%Aligned nanofibres mat				Flexural strength	Strain Constant	Max Bending	Strain	Flexure modulus
S.No.	Width mm	Thickness mm	Force N (maximum)	N/mm2		mm		mm/mm
1	13.3	3.22	698.2500	478.4972	0.0049	5.2920	0.0258	18575.2005
2	13.36	3.08	614.3125	458.0504	0.0047	5.7320	0.0267	17162.7241
3	13.2	3.25	654.3750	443.5247	0.0049	5.2200	0.0256	17293.9357
4	13.26	3	625.3125	495.1570	0.0045	6.1030	0.0277	17889.9081
5	13.2	3.01	622.6250	491.9845	0.0046	6.2440	0.0284	17316.1723
Average			642.9750	473.4428	0.0047	5.7182	0.0268	17647.5881

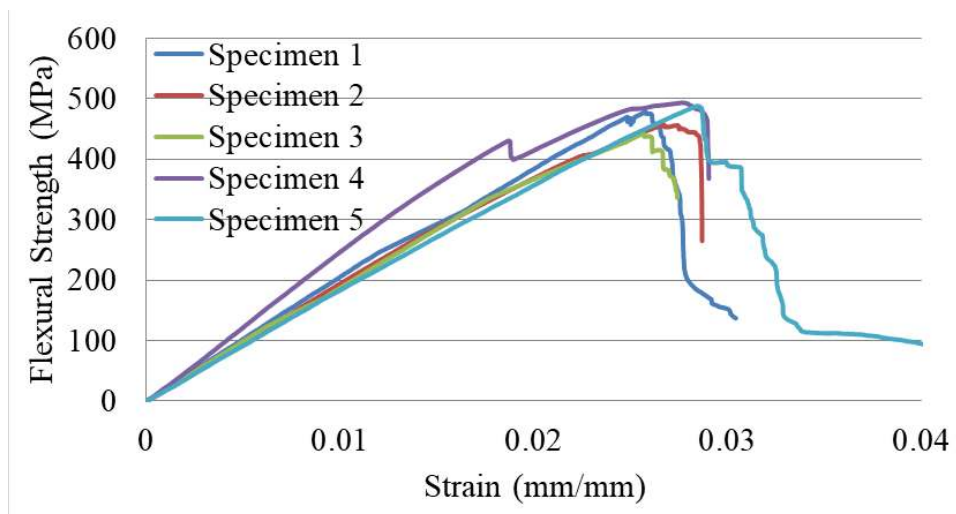


FIGURE A.27: Flexural strengths of aligned nanofibres mat (0.5%) strengthened hybrid composite samples

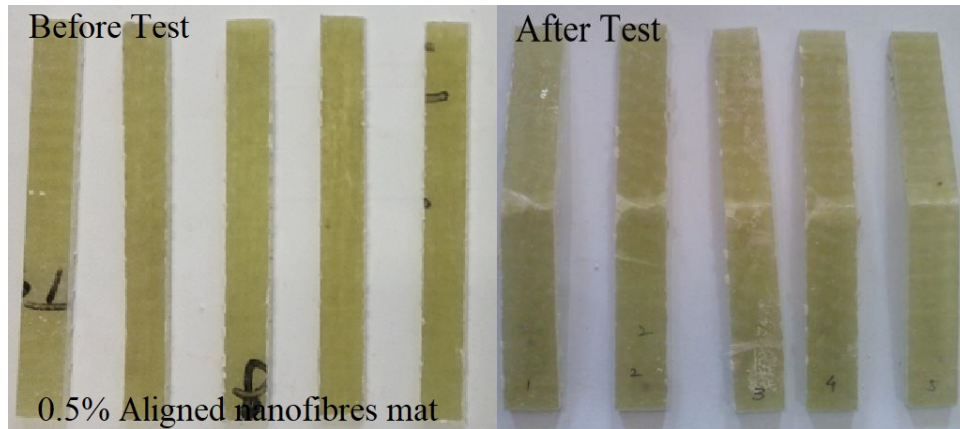


FIGURE A.28: Tested specimens of Aligned nanofibres mat (0.5%) strengthened hybrid composite samples

### A.2.7 0.25% vol p-SWCNTs doped aligned nanofibres mat (0.5%) strengthened hybrid composite

TABLE A.15: Flexural strength details of CNTs doped 0.5% aligned nanofibres mat

Batch: 0.25% vol p-SWCNTs doped aligned nanofibres mat (0.5%) strengthened hybrid composite				Flexural strength	Strain Constant	Max Bending	Strain	Flexure modulus
S.No.	Width mm	Thickness mm	Force N (maximum)	N/mm <sup>2</sup>		mm	mm/mm	N/mm <sup>2</sup>
1	13.24	3.1	624.6875	463.9629	0.0047	5.7690	0.0270	17161.3270
2	13.3	3.15	761.8125	545.5156	0.0048	5.7490	0.0274	19926.6430
3	13.12	3.04	648.6875	505.5759	0.0046	5.4160	0.0249	20312.5265
4	13.2	3.04	576.3125	446.4458	0.0046	4.7250	0.0217	20560.0043
5	13.14	3.06	686.6880	527.4157	0.0046	5.4170	0.0251	21047.6026
Average			659.6376	497.7832	0.0047	5.4152	0.0252	19801.6207

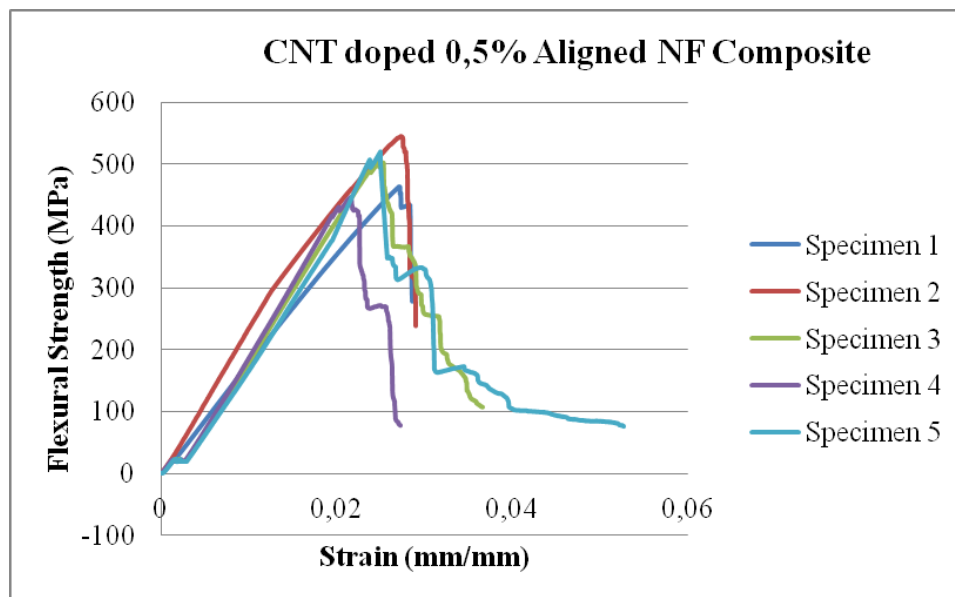


FIGURE A.29: Flexural strengths of 0.25% vol p-SWCNTs doped aligned nanofibres mat (0.5%) strengthened hybrid composite samples

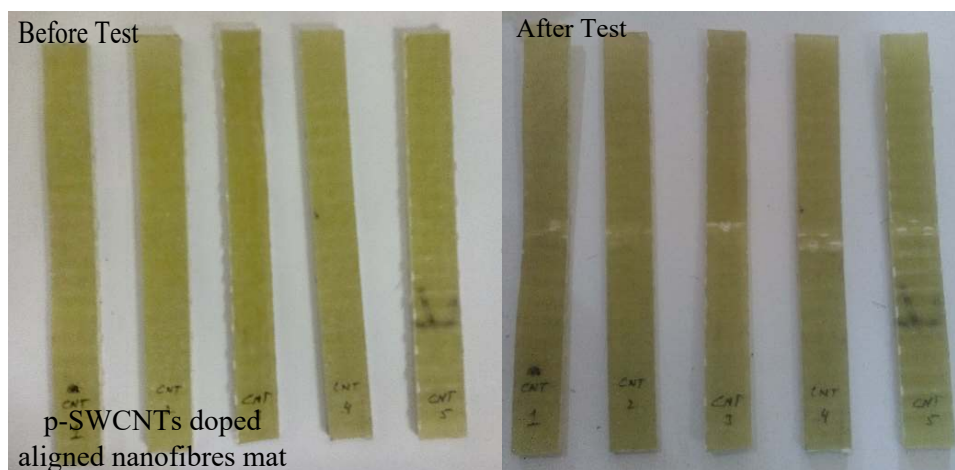


FIGURE A.30: Tested specimens of 0.25% vol p-SWCNTs doped aligned nanofibres mat (0.5%) strengthened hybrid composite

### A.2.8 0.25% vol f-SWCNTs doped aligned nanofibres mat (0.5%) strengthened hybrid composite

TABLE A.16: Flexural strength details of 0.25% vol f-SWCNTs doped aligned nanofibres mat (0.5%) strengthened hybrid composite

Batch: 0.25% vol f-SWCNTs doped aligned nanofibres mat				Flexural strength	Strain Constant	Max Bending	Strain	Flexure modulus
S.No.	Width mm	Thickness mm	Force N (maximum)	N/mm <sup>2</sup>		mm		N/mm <sup>2</sup>
1	13.04	3.2	836.4394	591.9551	0.0048	5.0179	0.0243	24386.5473
2	13.15	3.15	723.4375	523.9453	0.0048	4.8490	0.0231	22690.9707
3	13.16	3.1	661.8125	494.5241	0.0047	4.8370	0.0227	21816.2230
4	13.1	3.12	679.7535	503.7358	0.0047	4.8130	0.0227	22190.2490
5	13.15	3.12	698.5257	515.6787	0.0047	5.1180	0.0241	21362.6047
Average			719.9937	525.9678	0.0047	4.9270	0.0234	22489.3190

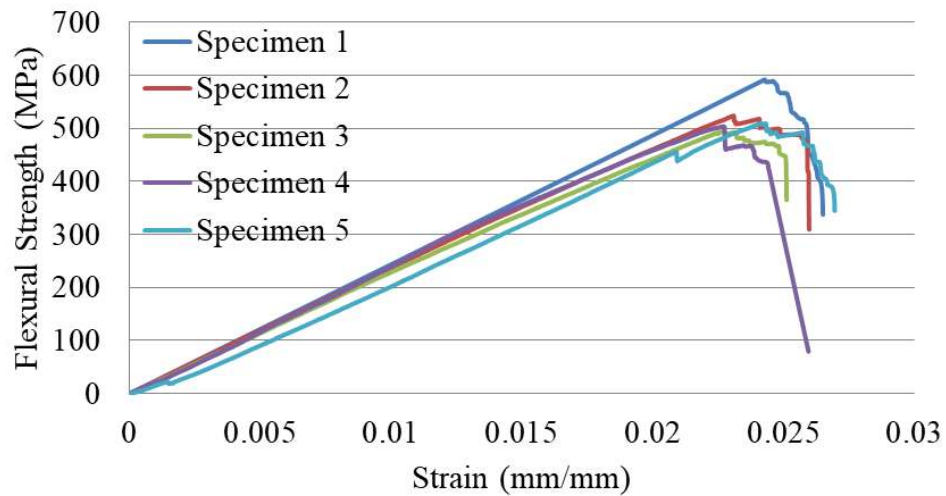


FIGURE A.31: Flexural strengths of 0.25% vol f-SWCNTs doped aligned nanofibres mat (0.5%) strengthened hybrid composite samples

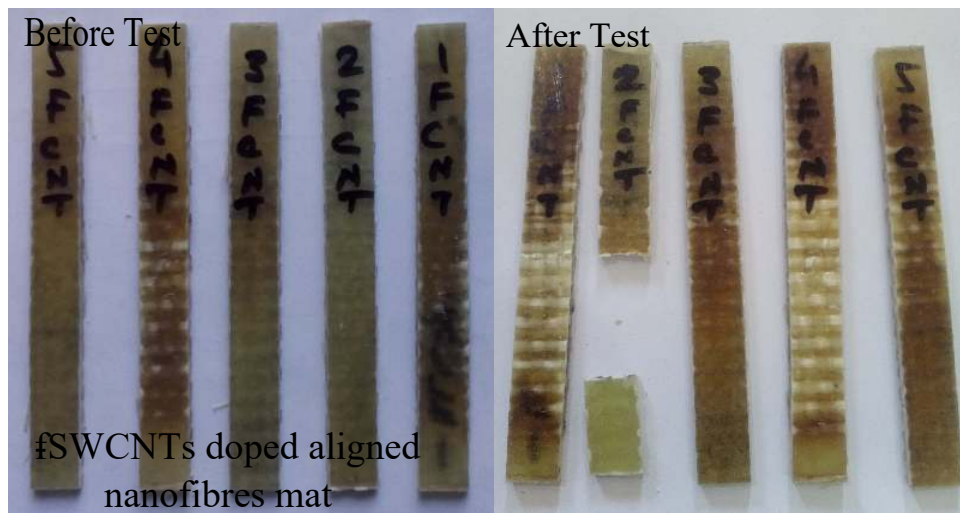


FIGURE A.32: Tested specimens 0.25% vol f-SWCNTs doped aligned nanofibres mat (0.5%) strengthened hybrid composite

## A.3 Impact Test Details

### A.3.1 Neat glassfibre composite 32%

TABLE A.17: Impact test specimen results for neat glass fibre composite 32 %

Batch: Neat glass fibre composite 32 %				
S.No.	Width. mm	Thickness. mm	Energy absorbed J	Fracture resistance Kj/m <sup>2</sup>
1	10.46	3.21	5.5	163.8045544
2	10.5	3.22	6	177.4622893
3	10.6	3.18	5.5	163.166014
4	10.8	3.25	5	142.4501425
5	11	3.24	5.5	154.3209877
Average			5.5	160.2407975



FIGURE A.33: Tested impact specimens of glass fibre composite (32% vol)

### A.3.2 Random nanofibres mat strengthened hybrid composite (0.1% Vol)

TABLE A.18: Impact test specimen results for 0.1% Random nanofibres mat strengthened hybrid composite

Batch:0.1% Random nanofibres mat				
S.No.	Width. mm	Thickness. mm	Energy absorbed J	Fracture resistance Kj/m <sup>2</sup>
1	10.5	3.1	6	184.3317972
2	10.5	3.22	5.5	162.6737652
3	10.5	3.2	6.5	193.452381
4	10.8	3.18	5.5	160.1444212
5	11	3.16	5	143.8434983
		Average	5.7	168.8891726



FIGURE A.34: Tested specimens of Random nanofibres mat (0.1% Vol) strengthened hybrid composite samples

### A.3.3 Random nanofibres mat (0.2% Vol) strengthened hybrid composite

TABLE A.19: Impact test specimens results for random nanofibres mat (0.2% Vol) strengthened hybrid composite

Batch:0.2% Random nanofibres mat				
S.No.	Width. mm	Thickness. mm	Energy absorbed J	Fracture resistance Kj/m <sup>2</sup>
1	10.5	3.12	5.8	177.045177
2	10.5	3.1	5.6	172.0430108
3	10.5	3.14	5.5	166.8183197
4	10.8	3.1	6.2	185.1851852
5	10.7	3	6.6	205.6074766
Average			5.94	181.3398339



FIGURE A.35: Tested impact specimens of random nanofibres mat (0.2% Vol) strengthened hybrid composite

### A.3.4 Random nanofibres mat (0.5% Vol) strengthened hybrid composite

TABLE A.20: Impact test specimens results for Random nanofibres mat (0.5% Vol) strengthened hybrid composite

Batch:0.5% Random nanofibres mat				
S.No.	Width. mm	Thickness. mm	Energy absorbed J	Fracture resistance Kj/m <sup>2</sup>
1	10.5	3.28	6.8	197.4448316
2	10.5	3.26	6.2	181.1276658
3	10.4	3.25	6.4	189.3491124
4	10.5	3.2	6.3	187.5
5	10.6	3.15	7.1	212.6385145
Average			6.56	193.6120249



FIGURE A.36: Tested impact specimens of Random nanofibres mat (0.5% Vol) strengthened hybrid composite

### A.3.5 Random nanofibres mat (1% Vol) strengthened hybrid composite

TABLE A.21: Impact test specimen results for (1% vol) random nanofibres mat glass fibre composite

Batch: Random nanofibres mat (1% Vol) strengthened hybrid composite				
S.No.	Width. mm	Thickness. mm	Energy absorbed J	Fracture resistance Kj/m <sup>2</sup>
1	11	3.15	7	198.8636364
2	10.5	3.25	6	178.5714286
3	10.5	3.3	6.5	193.452381
4	10	3.4	7	218.75
5	11	3.15	6	170.4545455
Average			6.5	192.0183983



FIGURE A.37: Tested impact specimens of Random nanofibres mat (1% Vol) strengthened hybrid composite

### A.3.6 0.5% (vol) aligned nanofibres mat strengthened hybrid composite

TABLE A.22: Impact test specimen results for 0.5% volume fraction aligned nanofibres mat

Batch:0.5% volume fraction aligned nanofibres mat				
S.No.	Width. mm	Thickness. mm	Energy absorbed J	Fracture resistance Kj/m <sup>2</sup>
1	10	3	7	233.3333333
2	10.5	3.1	8	245.7757296
3	11	3.1	7.5	219.941349
4	11	3.2	8.5	241.4772727
5	10.5	3.2	7.5	223.2142857
Average			7.7	232.7483941

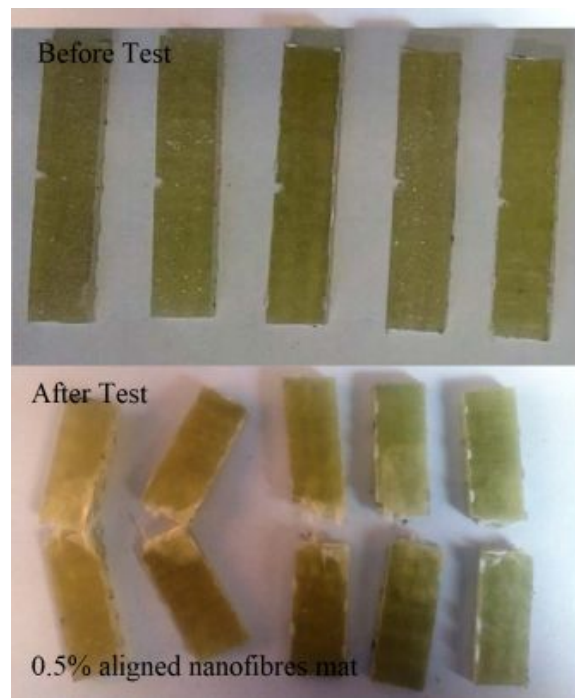


FIGURE A.38: Tested specimens of 0.5% aligned nanofibres mat glass fibre composite

### A.3.7 0.25% Vol) p-SWCNTs doped aligned nanofibres mat strengthened hybrid composite

TABLE A.23: Impact test specimen results for (0.25% Vol) p-SWCNTs doped aligned nanofibre mat strengthened hybrid composite

Batch:P-SWCNTs doped aligned nanofibres mat				
S.No.	Width, mm	Thickness. mm	Energy absorbed J	Fracture resistance Kj/m <sup>2</sup>
1	10.8	3.15	10.4	305.7025279
2	10.2	3.1	11.4	360.5313093
3	11.5	3.15	11.9	328.5024155
4	11	3.15	13.9	401.1544012
5	11	3.15	9.2	265.5122655
Average			11.36	332.2805839

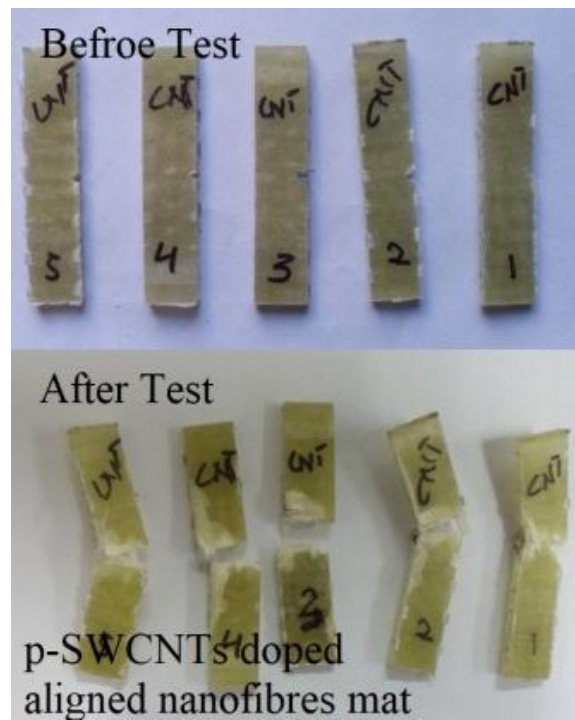


FIGURE A.39: Tested specimens of (0.25% Vol) p-SWCNTs doped aligned nanofibres mat strengthened hybrid composite

### A.3.8 (0.25% Vol) f-SWCNTs doped aligned nanofibres mat strengthened hybrid composite

TABLE A.24: Impact test specimen results for 0.25% Vol) f-SWCNTs doped aligned nanofibres mat strengthened hybrid composite

Batch:f-SWCNTs doped aligned nanofibres mat				
S.No.	Width. mm	Thickness. mm	Energy absorbed J	Fracture resistance Kj/m <sup>2</sup>
1	11.15	3.15	16.1	458.3956153
2	10.7	3.1	16.8	506.4817606
3	11	3.15	13.8	398.2683983
4	11.2	3.15	16	453.5147392
5	10.8	3.15	14.5	426.2198707
Average			15.44	448.5760768

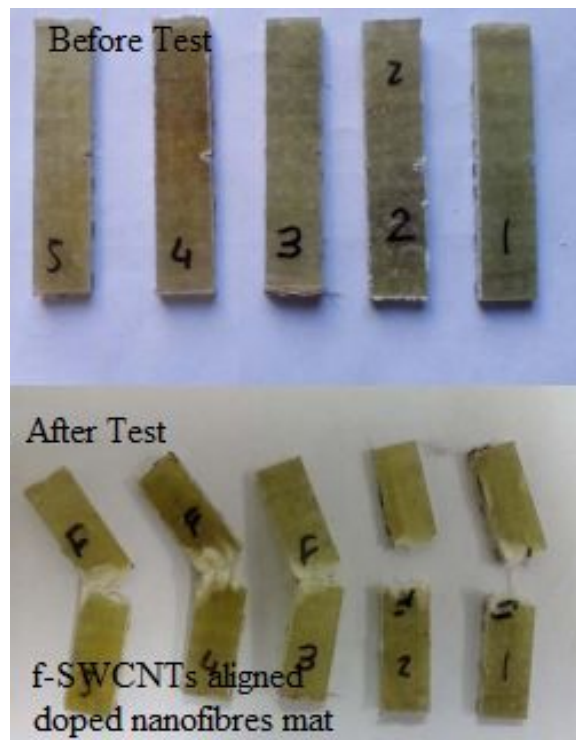


FIGURE A.40: Tested Impact specimens of f-SWCNTs doped aligned nanofibres mat strengthened hybrid composite



---

```
%number of elements

Ni = round(Ne);

number of elements to round of

if Ne < Ni

Ne = Ni + 1;

else

Ne = Ni;

end

Ne

theta = 360/Ne;

D = Le*Ne/pi(); circumference = number of elements into lengths

R = D/2;

a = R;

b = 0;

c = 0;

theta1 = 0;

m = 1;

mm = 1;

zzz = 0;

Pn = 1;
```

---

```
Cord = [Pn,Pn a b c];

Points(Pn,1) = Cord(1,1); store points data in matrix points

Points(Pn,2) = a;

Points(Pn,3) = b;

Points(Pn,4) = c;

Points(Pn,5) = theta1;

aa(www)= a;

www=www+1;

i = 1; t = 1; tt = 1; counter = 0;

while theta1 + theta j= 2600;

Pn = Pn + 1;

counter = counter +1;

if m|2

check if its the first element of the second

theta1 = theta1 + theta; first element theta1 is theta1 = theta

xxx = 1;

m=2;

else

theta1 = theta1 + 2*theta;

xx = 0;
```

```
m=1;

end

while t < 3

if counter < 8

counter = 1;

end

if mm < 1;

a = R*cos(pi()*theta1/180);

b = R*sin(pi()*theta1/180);

if counter < 4;

c = 2*Lh;

else

c = Lh;

end

Cord = [Pn,Pn a b c];

Points(Pn,1) = Pn;

Points(Pn,2) = a;

Points(Pn,3) = b;

Points(Pn,4) = c;

Points(Pn,5) = theta1;
```

```
aa(www)= a;

www=www+1;

mm = 2;

else

a = R*cos(pi()*theta1/180);

b = R*sin(pi()*theta1/180);

if counter < 4;

c = 0; else

c = -Lh;

end

Points(Pn,1) = Pn;

Points(Pn,2) = a

Points(Pn,3) = b;

Points(Pn,4) = c;

Points(Pn,5) = theta1;

aa(www)= a;

www=www+1;

mm = 0;

end

t = t + 1;
```

---

```
if t|3;

Pn = Pn + 1;

counter = counter +1;

end

end

t = 1;

theta1;

i = i + 1;

if 360 |theta1|=720

Pn = Pn + 1;

counter = counter +1;

if m|2

theta1 = theta1 + theta;

xxx = 1;

m=2;

else

theta1 = theta1 + 2*theta;

xx = 0;

m=1;

end
```

---

```
while t j 3

if counter j 8

counter = 1;

end

if mm j 1;

a = R*cos(pi()*theta1/180);

b = R*sin(pi()*theta1/180);

if counter j 4;

c = 6*Lh;

else

c = 5*Lh;

end

Cord = [Pn,Pn a b c];

Points(Pn,1) = Pn;

Points(Pn,2) = a

Points(Pn,3) = b;

Points(Pn,4) = c;

Points(Pn,5) = theta1;

aa(www)= a;

www=www+1;
```

```
mm = 2;

else

a = R*cos(pi()*theta1/180);

b = R*sin(pi()*theta1/180);

if counter  $\leq$  4;

c = 4*Lh;

else

c = 3*Lh;

end

Points(Pn,1) = Pn;

Points(Pn,2) = a

Points(Pn,3) = b;

Points(Pn,4) = c;

Points(Pn,5) = theta1;

aa(www)= a;

www=www+1;

mm = 0;

end

t = t + 1;

if t $\leq$ 3;
```

```
Pn = Pn + 1;

counter = counter +1;

end

end

t = 1;

theta1;

i = i + 1;

end

if 720;theta1;=1080

Pn = Pn + 1;

counter = counter +1;

if m;2

theta1 = theta1 + theta;

xxx = 1;

m=2;

else

theta1 = theta1 + 2*theta;

xx = 0;

m=1;

end
```

---

```
while t j 3

if counter j 8

counter = 1;

end

if mm j 1;

a = R*cos(pi()*theta1/180);

b = R*sin(pi()*theta1/180);

if counter j 4;

c = 10*Lh;

else

c = 9*Lh;

end

Cord = [Pn,Pn a b c];

Points(Pn,1) = Pn;

Points(Pn,2) = a

Points(Pn,3) = b;

Points(Pn,4) = c;

Points(Pn,5) = theta1;

aa(www)= a;

www=www+1;
```

---

```
mm = 2;

else

a = R*cos(pi()*theta1/180);

b = R*sin(pi()*theta1/180);

if counter < 4;

c = 8*Lh;

else

c = 7*Lh;

end

Points(Pn,1) = Pn;

Points(Pn,2) = a

Points(Pn,3) = b;

Points(Pn,4) = c;

Points(Pn,5) = theta1;

aa(www)= a;

www=www+1;

mm = 0;

end

t = t + 1;

if t<3;
```

```
Pn = Pn + 1;

counter = counter +1;

end

end

t = 1;

theta1;

i = i + 1;

end

if 1080;theta1;=1440

Pn = Pn + 1;

counter = counter +1;

if m;2

theta1 = theta1 + theta;

xxx = 1;

m=2;

else

theta1 = theta1 + 2*theta;

xx = 0;

m=1;

end
```

---

```
while t j 3

if counter j 8

counter = 1;

end

if mm j 1;

a = R*cos(pi()*theta1/180);

b = R*sin(pi()*theta1/180);

if counter j 4;

c = 14*Lh;

else

c = 13*Lh;

end

Cord = [Pn,Pn a b c];

Points(Pn,1) = Pn;

Points(Pn,2) = a

Points(Pn,3) = b;

Points(Pn,4) = c;

Points(Pn,5) = theta1;

aa(www)= a;

www=www+1;
```

```
mm = 2;

else

a = R*cos(pi()*theta1/180);

b = R*sin(pi()*theta1/180);

if counter < 4;

c = 12*Lh; else

c = 11*Lh;

end

Points(Pn,1) = Pn;

Points(Pn,2) = a

Points(Pn,3) = b;

Points(Pn,4) = c;

Points(Pn,5) = theta1;

aa(www)= a;

www=www+1;

mm = 0;

end

t = t + 1;

if t>3;

Pn = Pn + 1;
```

```
counter = counter +1;

end

end

t = 1;

theta1;

i = i + 1;

end

if 1440;theta1;=1800

Pn = Pn + 1;

counter = counter +1;

if m;2

theta1 = theta1 + theta;

xxx = 1;

m=2;

else theta1 = theta1 + 2*theta;

xx = 0;

m=1;

end

while t ; 3

if counter ; 8
```

```
counter = 1;

end

if mm  $\neq$  1;

a = R*cos(pi()*theta1/180);

b = R*sin(pi()*theta1/180);

if counter  $\leq$  4;

c = 18*Lh;

else

c = 17*Lh;

end

Cord = [Pn,Pn a b c];

Points(Pn,1) = Pn;

Points(Pn,2) = a

Points(Pn,3) = b;

Points(Pn,4) = c;

Points(Pn,5) = theta1;

aa(www)= a;

www=www+1;

mm = 2;

else
```

---

```
a = R*cos(pi()*theta1/180);
```

```
b = R*sin(pi()*theta1/180);
```

```
if counter < 4;
```

```
  c = 16*Lh;
```

```
else
```

```
  c = 15*Lh;
```

```
end
```

```
Points(Pn,1) = Pn;
```

```
Points(Pn,2) = a
```

```
Points(Pn,3) = b;
```

```
Points(Pn,4) = c;
```

```
Points(Pn,5) = theta1;
```

```
aa(www)= a;
```

```
www=www+1;
```

```
mm = 0;
```

```
end
```

```
t = t + 1;
```

```
if t<3;
```

```
  Pn = Pn + 1;
```

```
  counter = counter +1;
```

```
end

end

t = 1;

theta1;

i = i + 1;

end

if 18000 < theta1 <= 2200

Pn = Pn + 1;

counter = counter + 1;

if m < 2

theta1 = theta1 + theta;

xxx = 1;

m = 2;

else

theta1 = theta1 + 2*theta;

xx = 0;

m = 1;

end

while t < 3

if counter < 8
```

```
counter = 1;

end

if mm  $\neq$  1;

a = R*cos(pi()*theta1/180);

b = R*sin(pi()*theta1/180);

if counter  $\leq$  4;

c = 22*Lh;

else

c = 21*Lh;

end

Cord = [Pn,Pn a b c];

Points(Pn,1) = Pn;

Points(Pn,2) = a

Points(Pn,3) = b;

Points(Pn,4) = c;

Points(Pn,5) = theta1;

aa(www) = a;

www = www + 1;

mm = 2;

else
```

---

```
a = R*cos(pi()*theta1/180);
```

```
b = R*sin(pi()*theta1/180);
```

```
if counter < 4;
```

```
  c = 20*Lh;
```

```
else
```

```
  c = 19*Lh;
```

```
end
```

```
Points(Pn,1) = Pn;
```

```
Points(Pn,2) = a
```

```
Points(Pn,3) = b;
```

```
Points(Pn,4) = c;
```

```
Points(Pn,5) = theta1;
```

```
aa(www)= a;
```

```
www=www+1;
```

```
mm = 0;
```

```
end
```

```
t = t + 1;
```

```
if t<3;
```

```
  Pn = Pn + 1;
```

```
  counter = counter +1;
```

```
end

end

t = 1;

theta1;

i = i + 1;

end

end

aa;

Points;

surf(Points(:,2),Points(:,3),Points(:,4),Points(:,5))

Points(1:2,2:4)

plot3(Points(:,2),Points(:,3),Points(:,4))

colorbar;

xlabel('x');

ylabel('y');

zlabel('z');

csvwrite('arif',Points)

csvwrite('x',Points(:,2));

csvwrite('y',Points(:,3));

csvwrite('z',Points(:,4));

Points = cntarif; close all; [rows,cols] = size(Points);
```

---

```
totalp= rows;

pairind1=1;

for l=1:rows

for j= 1:rows

p1 = Points(l,2:4);

p2 = Points(j,2:4);

dist= arifdistance(p1,p2);

dist = sqrt((p2(1)-p1(1))2+(p2(2)-p1(2))2+(p2(3)-p1(3))2); distmat(l,j)=dist;

if(dist < 1.425) pairs1(pairind1,:)= [Points(l,1), Points(j,1)]; graph1=plot3([p1(1)
p2(1)], [p1(2) p2(2)], [p1(3) p2(3)]); ,'-ko',... 'LineWidth',3,... 'MarkerEdge-
Color','k',... 'MarkerFaceColor','k',... 'MarkerSize',5);

hold on;

pairind1=pairind1+1;

end

end csvwrite('pairs1.txt',pairs1)

end
```



---

```
m = 1;

mm = 1;

zzz = 0;

Pn = 1;

Cord = [Pn,Pn a b c];

Points(Pn,1) = Cord(1,1);

Points(Pn,2) = a;

Points(Pn,3) = b;

Points(Pn,4) = c;

Points(Pn,5) = theta1;

aa(www)= a;

www=www+1;

while theta1 + theta j=8640;

Pn = Pn + 1;

i=1:Ne-1;

theta1 = theta1 + theta;

a = R*cos(pi()*theta1/180);

b = R*sin(pi()*theta1/180);

Cord = [Pn,Pn a b c];

Points(Pn,1) = Cord(1,1); Points(Pn,2) = a;
```

---

```
Points(Pn,3) = b;

Points(Pn,4) = c;

Points(Pn,5) = theta1;

aa(www)= a;

www=www+1;

if theta1<360

a=R*cos(pi()*(theta1-theta/2)/180);

b = R*sin(pi()*(theta1-theta/2)/180);

c = Ls;

end

Points(Pn,1) = Cord(1,1); Points(Pn,2) = a;

Points(Pn,3) = b;

Points(Pn,4) = c;

Points(Pn,5) = theta1;

aa(www)= a;

www=www+1;

mm = 0;

if theta1<720;

a = R*cos(pi()*(theta1-theta/2)/180);

b = R*sin(pi()*(theta1-theta/2)/180);
```

---

```
c = Ls+Lb;

end

Points(Pn,1) = Cord(1,1); Points(Pn,2) = a;

Points(Pn,3) = b;

Points(Pn,4) = c;

Points(Pn,5) = theta1;

aa(www)= a;

www=www+1;

if theta1<1080;

a = R*cos(pi()*(theta1)/180);

b = R*sin(pi()*(theta1)/180);

c = 2*Ls+Lb;

end

Points(Pn,1) = Cord(1,1);

Points(Pn,2) = a;

Points(Pn,3) = b;

Points(Pn,4) = c;

Points(Pn,5) = theta1;

aa(www)= a; www=www+1;

mm = 0;
```

---

```
if theta1<1440;

a = R*cos(pi()*(theta1)/180);

b = R*sin(pi()*(theta1)/180);

c = 2*Ls+2*Lb; end

Points(Pn,1) = Cord(1,1); Points(Pn,2) = a;

Points(Pn,3) = b;

Points(Pn,4) = c;

Points(Pn,5) = theta1;

aa(www)= a;

www=www+1;

mm = 0;

if theta1<1800;

a = R*cos(pi()*(theta1-theta/2)/180);

b = R*sin(pi()*(theta1-theta/2)/180);

c = 3*Ls+2*Lb;

end

Points(Pn,1) = Cord(1,1); Points(Pn,2) = a;

Points(Pn,3) = b;

Points(Pn,4) = c;

Points(Pn,5) = theta1;
```

---

```
aa(www)= a;

www=www+1;

mm = 0;

if theta1<2160;

a = R*cos(pi()*(theta1-theta/2)/180);

b = R*sin(pi()*(theta1-theta/2)/180);

c = 3*Ls+3*Lb;

end

Points(Pn,1) = Cord(1,1); Points(Pn,2) = a;

Points(Pn,3) = b;

Points(Pn,4) = c;

Points(Pn,5) = theta1;

aa(www)= a;

www=www+1;

mm = 0;

if theta1<2520;

a = R*cos(pi()*(theta1)/180);

b = R*sin(pi()*(theta1)/180);

c = 4*Ls+3*Lb;

end
```

---

Points(Pn,1) = Cord(1,1); Points(Pn,2) = a;

Points(Pn,3) = b;

Points(Pn,4) = c;

Points(Pn,5) = theta1;

aa(www)= a;

www=www+1;

mm = 0;

if theta1<2880;

a = R\*cos(pi()\*(theta1)/180);

b = R\*sin(pi()\*(theta1)/180);

c = 4\*Ls+4\*Lb;

end

Points(Pn,1) = Cord(1,1); Points(Pn,2) = a;

Points(Pn,3) = b;

Points(Pn,4) = c;

Points(Pn,5) = theta1;

aa(www)= a;

www=www+1;

mm = 0;

if theta1<3240;

---

```
a = R*cos(pi()*(theta1-theta/2)/180);
b = R*sin(pi()*(theta1-theta/2)/180);
c = 5*Ls+4*Lb;

end

Points(Pn,1) = Cord(1,1); Points(Pn,2) = a;

Points(Pn,3) = b;

Points(Pn,4) = c;

Points(Pn,5) = theta1;

aa(www) = a; www=www+1;

mm = 0;

if theta1<3600;

a = R*cos(pi()*(theta1-theta/2)/180);
b = R*sin(pi()*(theta1-theta/2)/180);
c = 5*Ls+5*Lb;

end

Points(Pn,1) = Cord(1,1); Points(Pn,2) = a;

Points(Pn,3) = b;

Points(Pn,4) = c;

Points(Pn,5) = theta1;

aa(www) = a; www=www+1;
```

---

```
mm = 0;

if theta1 > 3960;

a = R*cos(pi()*(theta1)/180);

b = R*sin(pi()*(theta1)/180);

c = 6*Ls+5*Lb;

end

Points(Pn,1) = Cord(1,1); Points(Pn,2) = a;

Points(Pn,3) = b;

Points(Pn,4) = c;

Points(Pn,5) = theta1;

aa(www) = a;

www = www + 1;

mm = 0;

if theta1 > 4320;

a = R*cos(pi()*(theta1)/180);

b = R*sin(pi()*(theta1)/180);

c = 6*Ls+6*Lb;

end

Points(Pn,1) = Cord(1,1);

Points(Pn,2) = a;
```

---

```
Points(Pn,3) = b;

Points(Pn,4) = c;

Points(Pn,5) = theta1;

aa(www)= a; www=www+1;

mm = 0;

if theta1<4680;

a = R*cos(pi()*(theta1-theta/2)/180);

b = R*sin(pi()*(theta1-theta/2)/180);

c = 7*Ls+6*Lb;

end

Points(Pn,1) = Cord(1,1);

Points(Pn,2) = a;

Points(Pn,3) = b;

Points(Pn,4) = c;

Points(Pn,5) = theta1;

aa(www)= a;

www=www+1;

mm = 0;

if theta1<5040;

a = R*cos(pi()*(theta1-theta/2)/180);
```

---

```
b = R*sin(pi()*(theta1-theta/2)/180); c = 7*Ls+7*Lb;
```

```
end
```

```
Points(Pn,1) = Cord(1,1);
```

```
Points(Pn,2) = a;
```

```
Points(Pn,3) = b;
```

```
Points(Pn,4) = c;
```

```
Points(Pn,5) = theta1;
```

```
aa(www)= a;
```

```
www=www+1;
```

```
mm = 0;
```

```
if theta1<5400;
```

```
a = R*cos(pi()*(theta1)/180);
```

```
b = R*sin(pi()*(theta1)/180);
```

```
c = 8*Ls+7*Lb;
```

```
end
```

```
Points(Pn,1) = Cord(1,1);
```

```
Points(Pn,2) = a;
```

```
Points(Pn,3) = b;
```

```
Points(Pn,4) = c;
```

```
Points(Pn,5) = theta1;
```

---

```
aa(www)= a;

www=www+1;

mm = 0;

if theta1<5760;

a = R*cos(pi()*(theta1)/180);

b = R*sin(pi()*(theta1)/180);

c = 8*Ls+8*Lb;

end

Points(Pn,1) = Cord(1,1);

Points(Pn,2) = a;

Points(Pn,3) = b;

Points(Pn,4) = c;

Points(Pn,5) = theta1;

aa(www)= a;

www=www+1;

mm = 0;

if theta1<6120;

a = R*cos(pi()*(theta1-theta/2)/180);

b = R*sin(pi()*(theta1-theta/2)/180);

c = 9*Ls+8*Lb;
```

```
end

Points(Pn,1) = Cord(1,1);

Points(Pn,2) = a;

Points(Pn,3) = b;

Points(Pn,4) = c;

Points(Pn,5) = theta1;

aa(www)= a;

www=www+1;

mm = 0;

if theta1<6480;

a = R*cos(pi()*(theta1-theta/2)/180);

b = R*sin(pi()*(theta1-theta/2)/180);

c = 9*Ls+9*Lb;

end

Points(Pn,1) = Cord(1,1);

Points(Pn,2) = a;

Points(Pn,3) = b;

Points(Pn,4) = c;

Points(Pn,5) = theta1;

aa(www)= a; www=www+1;
```

---

```
mm = 0;

if theta1 > 6840;

a = R*cos(pi()*(theta1)/180);

b = R*sin(pi()*(theta1)/180);

c = 10*Ls+9*Lb;

end

Points(Pn,1) = Cord(1,1);

Points(Pn,2) = a;

Points(Pn,3) = b;

Points(Pn,4) = c;

Points(Pn,5) = theta1;

aa(www) = a; www=www+1;

mm = 0;

if theta1 > 7200;

a = R*cos(pi()*(theta1)/180);

b = R*sin(pi()*(theta1)/180);

c = 10*Ls+10*Lb;

end

Points(Pn,1) = Cord(1,1);

Points(Pn,2) = a;
```

---

```
Points(Pn,3) = b;

Points(Pn,4) = c;

Points(Pn,5) = theta1;

aa(www) = a; www=www+1;

mm = 0;

if theta1<7560;

a = R*cos(pi()*(theta1-theta/2)/180);

b = R*sin(pi()*(theta1-theta/2)/180);

c = 11*Ls+10*Lb;

end

Points(Pn,1) = Cord(1,1);

Points(Pn,2) = a;

Points(Pn,3) = b;

Points(Pn,4) = c;

Points(Pn,5) = theta1;

aa(www) = a; www=www+1;

mm = 0;

if theta1<7920;

a = R*cos(pi()*(theta1-theta/2)/180);

b = R*sin(pi()*(theta1-theta/2)/180);
```

---

```
c = 11*Ls+11*Lb;

end

Points(Pn,1) = Pn;

Points(Pn,2) = a;

Points(Pn,3) = b;

Points(Pn,4) = c;

Points(Pn,5) = theta1;

aa(www)= a;

www=www+1;

mm = 0; if theta1<8280;

a = R*cos(pi()*(theta1)/180);

b = R*sin(pi()*(theta1)/180);

c = 12*Ls+11*Lb;

end

Points(Pn,1) = Pn;

Points(Pn,2) = a;

Points(Pn,3) = b;

Points(Pn,4) = c;

Points(Pn,5) = theta1;

aa(www)= a;
```

```
www=www+1;

mm = 0;

end

aa;

Points;

xlabel('x');

ylabel('y');

zlabel('z');

csvwrite('arif',Points)

csvwrite('x',Points(:,2))

csvwrite('y',Points(:,3))

csvwrite('z',Points(:,4))

csvwrite('values',Points(:,5))

[rows,cols] = size(Points);

totalp= rows;

pairind=1;

pairind1=1;

for l=1:rows

for j= 1:rows

p1 = Points(l,2:4);
```

---

```
p2 = Points(j,2:4);

dist = sqrt((p2(1) - p1(1))^2 + (p2(2) - p1(2))^2 + (p2(3) - p1(3))^2);

distmat(l,j)=dist;

if(dist < 1.425)

pairs(pairind,:)= [Points(1,1:4),
Points(j,1:4)];

pairs1(pairind1,:)= [Points(1,1), Points(j,1)];

plot3([p1(1) p2(1)], [p1(2) p2(2)], [p1(3) p2(3)]);

hold on;

Dist=dist;

pairs(pairind,:)= [Points(1,1:4), Points(j,1:4)];

pairind=pairind+1;

pairind1=pairind1+1;

end

end end csvwrite('pairs.txt',pairs)

csvwrite('pairs1.txt',pairs1)

end
```

---

### B.3 Macro file (Pristine single wall zigzag) used as input to the ANSYS Mechanical APDL software

```
/prep7
```

```
/view,,-1,-2,-3
```

```
"k, 1, 2.74010461024631, 0, 0"
```

```
"k, 2, 1.70842728051467, 2.14230004954635, 0"
```

```
"k, 3, -0.609730637010011, 2.67140446682722, 0"
```

```
"k, 4, -2.46874894862781, 1.18888683386693, 0"
```

```
"k, 5, -2.46874894862781, -1.18888683386693, 0"
```

```
"k, 6, -0.609730637010009, -2.67140446682722, 0"
```

```
"k, 7, 1.70842728051467, -2.14230004954635, 0"
```

```
"k, 8, 2.46874894862781, -1.18888683386693, 0.7100000000000000"
```

```
"k, 9, 2.46874894862781, 1.18888683386693, 0.7100000000000000"
```

```
"k, 10, 0.609730637010009, 2.67140446682722, 0.7100000000000000"
```

```
"k, 11, -1.70842728051468, 2.14230004954635, 0.7100000000000000"
```

```
"k, 12, -2.74010461024631, -3.86070546300307e-15, 0.7100000000000000"
```

```
"k, 13, -1.70842728051467, -2.14230004954636, 0.7100000000000000"
```

```
"k, 14, 0.609730637010019, -2.67140446682722, 0.7100000000000000"
```

```
"k, 15, 2.46874894862782, -1.18888683386692, 2.1300000000000000"
```

```
"k, 16, 2.46874894862781, 1.18888683386693, 2.1300000000000000"
```

```
"k, 17, 0.609730637010008, 2.67140446682722, 2.1300000000000000"
```

```
"k, 18, -1.70842728051467, 2.14230004954635, 2.1300000000000000"
```

```
"k, 19, -2.74010461024631, -1.29243805251160e-14, 2.1300000000000000"
```

```
"k, 20, -1.70842728051467, -2.14230004954636, 2.1300000000000000"
```

---

"k, 21, 0.609730637010019, -2.67140446682722, 2.1300000000000000"

"k, 22, 2.74010461024631, -2.01339620416023e-15, 2.8400000000000000"

"k, 23, 1.70842728051467, 2.14230004954635, 2.8400000000000000"

"k, 24, -0.609730637009999, 2.67140446682722, 2.8400000000000000"

"k, 25, -2.46874894862781, 1.18888683386695, 2.8400000000000000"

"k, 26, -2.46874894862782, -1.18888683386691, 2.8400000000000000"

"k, 27, -0.609730637010042, -2.67140446682721, 2.8400000000000000"

"k, 28, 1.70842728051465, -2.14230004954637, 2.8400000000000000"

"k, 29, 2.74010461024631, -3.18889496627127e-14, 4.2600000000000000"

"k, 30, 1.70842728051470, 2.14230004954633, 4.2600000000000000"

"k, 31, -0.609730637009970, 2.67140446682723, 4.2600000000000000"

"k, 32, -2.46874894862780, 1.18888683386696, 4.2600000000000000"

"k, 33, -2.46874894862784, -1.18888683386687, 4.2600000000000000"

"k, 34, -0.609730637010071, -2.67140446682721, 4.2600000000000000"

"k, 35, 1.70842728051462, -2.14230004954639, 4.2600000000000000"

"k, 36, 2.46874894862778, -1.18888683386699, 4.9700000000000000"

"k, 37, 2.46874894862785, 1.18888683386685, 4.9700000000000000"

"k, 38, 0.609730637010100, 2.67140446682720, 4.9700000000000000"

"k, 39, -1.70842728051460, 2.14230004954641, 4.9700000000000000"

"k, 40, -2.74010461024631, 9.13044905457911e-14, 4.9700000000000000"

"k, 41, -1.70842728051474, -2.14230004954630, 4.9700000000000000"

"k, 42, 0.609730637009922, -2.67140446682724, 4.9700000000000000"

"k, 43, 2.46874894862778, -1.18888683386699, 6.3900000000000000"

"k, 44, 2.46874894862785, 1.18888683386686, 6.3900000000000000"

"k, 45, 0.609730637010063, 2.67140446682721, 6.3900000000000000"

"k, 46, -1.70842728051463, 2.14230004954639, 6.3900000000000000"

"k, 47, -2.74010461024631, 5.30363940931790e-14, 6.3900000000000000"

"k, 48, -1.70842728051471, -2.14230004954632, 6.3900000000000000"

---

"k, 49, 0.609730637009978, -2.67140446682723, 6.390000000000000"

"k, 50, 2.74010461024631, -2.41675387367066e-14, 7.100000000000000"

"k, 51, 1.70842728051469, 2.14230004954634, 7.100000000000000"

"k, 52, -0.609730637010006, 2.67140446682722, 7.100000000000000"

"k, 53, -2.46874894862781, 1.18888683386693, 7.100000000000000"

"k, 54, -2.46874894862782, -1.18888683386692, 7.100000000000000"

"k, 55, -0.609730637010016, -2.67140446682722, 7.100000000000000"

"k, 56, 1.70842728051468, -2.14230004954634, 7.100000000000000"

"k, 57, 2.74010461024631, 3.35701719762382e-14, 8.520000000000000"

"k, 58, 1.70842728051466, 2.14230004954636, 8.520000000000000"

"k, 59, -0.609730637010044, 2.67140446682721, 8.520000000000000"

"k, 60, -2.46874894862783, 1.18888683386690, 8.520000000000000"

"k, 61, -2.46874894862779, -1.18888683386697, 8.520000000000000"

"k, 62, -0.609730637009979, -2.67140446682723, 8.520000000000000"

"k, 63, 1.70842728051471, -2.14230004954632, 8.520000000000000"

"k, 64, 2.46874894862784, -1.18888683386687, 9.230000000000000"

"k, 65, 2.46874894862779, 1.18888683386698, 9.230000000000000"

"k, 66, 0.609730637009951, 2.67140446682724, 9.230000000000000"

"k, 67, -1.70842728051472, 2.14230004954631, 9.230000000000000"

"k, 68, -2.74010461024631, -8.12375095249899e-14, 9.230000000000000"

"k, 69, -1.70842728051459, -2.14230004954642, 9.230000000000000"

"k, 70, 0.609730637010090, -2.67140446682720, 9.230000000000000"

"k, 71, 2.46874894862786, -1.18888683386684, 10.650000000000000"

"k, 72, 2.46874894862777, 1.18888683386702, 10.650000000000000"

"k, 73, 0.609730637009894, 2.67140446682725, 10.650000000000000"

"k, 74, -1.70842728051475, 2.14230004954629, 10.650000000000000"

"k, 75, -2.74010461024631, -1.19505605977602e-13, 10.650000000000000"

"k, 76, -1.70842728051456, -2.14230004954644, 10.650000000000000"

---

"k, 77, 0.609730637010165, -2.67140446682719, 10.650000000000000"

"k, 78, 2.74010461024631, 1.28904847073742e-13, 11.360000000000000"

"k, 79, 1.70842728051456, 2.14230004954645, 11.360000000000000"

"k, 80, -0.609730637010175, 2.67140446682718, 11.360000000000000"

"k, 81, -2.46874894862788, 1.18888683386679, 11.360000000000000"

"k, 82, -2.46874894862776, -1.18888683386704, 11.360000000000000"

"k, 83, -0.609730637009867, -2.67140446682725, 11.360000000000000"

"k, 84, 1.70842728051480, -2.14230004954625, 11.360000000000000"

"k, 85, 2.74010461024631, 1.86642557786686e-13, 12.780000000000000"

"k, 86, 1.70842728051454, 2.14230004954646, 12.780000000000000"

"k, 87, -0.609730637010193, 2.67140446682718, 12.780000000000000"

"k, 88, -2.46874894862790, 1.18888683386674, 12.780000000000000"

"k, 89, -2.46874894862773, -1.18888683386709, 12.780000000000000"

"k, 90, -0.609730637009810, -2.67140446682727, 12.780000000000000"

"k, 91, 1.70842728051482, -2.14230004954624, 12.780000000000000"

"k, 92, 2.46874894862792, -1.18888683386670, 13.490000000000000"

"k, 93, 2.46874894862771, 1.18888683386714, 13.490000000000000"

"k, 94, 0.609730637009763, 2.67140446682728, 13.490000000000000"

"k, 95, -1.70842728051486, 2.14230004954621, 13.490000000000000"

"k, 96, -2.74010461024631, -2.53779509595771e-13, 13.490000000000000"

"k, 97, -1.70842728051449, -2.14230004954650, 13.490000000000000"

"k, 98, 0.609730637010258, -2.67140446682716, 13.490000000000000"

"k, 99, 2.46874894862793, -1.18888683386668, 14.910000000000000"

"k, 100, 2.46874894862769, 1.18888683386719, 14.910000000000000"

"k, 101, 0.609730637009745, 2.67140446682728, 14.910000000000000"

"k, 102, -1.70842728051490, 2.14230004954617, 14.910000000000000"

"k, 103, -2.74010461024631, -2.72577991788050e-13, 14.910000000000000"

"k, 104, -1.70842728051444, -2.14230004954653, 14.910000000000000"

---

"k, 105, 0.609730637010315, -2.67140446682715, 14.9100000000000"

"k, 106, 2.74010461024631, 2.81977232884190e-13, 15.6200000000000"

"k, 107, 1.70842728051444, 2.14230004954654, 15.6200000000000"

"k, 108, -0.609730637010324, 2.67140446682715, 15.6200000000000"

"k, 109, -2.46874894862796, 1.18888683386662, 15.6200000000000"

"k, 110, -2.46874894862766, -1.18888683386725, 15.6200000000000"

"k, 111, -0.609730637009718, -2.67140446682729, 15.6200000000000"

"k, 112, 1.70842728051492, -2.14230004954615, 15.6200000000000"

"k, 113, 2.74010461024631, 3.39714943597135e-13, 17.0400000000000"

"k, 114, 1.70842728051439, 2.14230004954658, 17.0400000000000"

"k, 115, -0.609730637010342, 2.67140446682715, 17.0400000000000"

"k, 116, -2.46874894862797, 1.18888683386660, 17.0400000000000"

"k, 117, -2.46874894862765, -1.18888683386727, 17.0400000000000"

"k, 118, -0.609730637009623, -2.67140446682731, 17.0400000000000"

"k, 119, 1.70842728051494, -2.14230004954614, 17.0400000000000"

"k, 120, 2.46874894862797, -1.18888683386660, 17.7500000000000"

"k, 121, 2.46874894862765, 1.18888683386728, 17.7500000000000"

"k, 122, 0.609730637009614, 2.67140446682731, 17.7500000000000"

"k, 123, -1.70842728051501, 2.14230004954609, 17.7500000000000"

"k, 124, -2.74010461024631, -4.45791123926885e-13, 17.7500000000000"

"k, 125, -1.70842728051431, -2.14230004954664, 17.7500000000000"

"k, 126, 0.609730637010407, -2.67140446682713, 17.7500000000000"

"k, 127, 2.46874894862800, -1.18888683386654, 19.1700000000000"

"k, 128, 2.46874894862762, 1.18888683386733, 19.1700000000000"

"k, 129, 0.609730637009558, 2.67140446682732, 19.1700000000000"

"k, 130, -1.70842728051505, 2.14230004954605, 19.1700000000000"

"k, 131, -2.74010461024631, -4.64589606119164e-13, 19.1700000000000"

"k, 132, -1.70842728051429, -2.14230004954665, 19.1700000000000"

---

"k, 133, 0.609730637010502, -2.67140446682711, 19.1700000000000000"

"k, 134, 2.74010461024631, 4.35049618694638e-13, 19.8800000000000000"

"k, 135, 1.70842728051432, 2.14230004954664, 19.8800000000000000"

"k, 136, -0.609730637010473, 2.67140446682712, 19.8800000000000000"

"k, 137, -2.46874894862803, 1.18888683386648, 19.8800000000000000"

"k, 138, -2.46874894862759, -1.18888683386739, 19.8800000000000000"

"k, 139, -0.609730637009530, -2.67140446682733, 19.8800000000000000"

"k, 140, 1.70842728051507, -2.14230004954603, 19.8800000000000000"

"k, 141, 2.74010461024631, 5.31726557928248e-13, 21.3000000000000000"

"k, 142, 1.70842728051427, 2.14230004954667, 21.3000000000000000"

"k, 143, -0.609730637010491, 2.67140446682711, 21.3000000000000000"

"k, 144, -2.46874894862805, 1.18888683386643, 21.3000000000000000"

"k, 145, -2.46874894862758, -1.18888683386741, 21.3000000000000000"

"k, 146, -0.609730637009512, -2.67140446682734, 21.3000000000000000"

"k, 147, 1.70842728051512, -2.14230004954600, 21.3000000000000000"

"k, 148, 2.46874894862807, -1.18888683386639, 22.0100000000000000"

"k, 149, 2.46874894862756, 1.18888683386745, 22.0100000000000000"

"k, 150, 0.609730637009465, 2.67140446682735, 22.0100000000000000"

"k, 151, -1.70842728051509, 2.14230004954602, 22.0100000000000000"

"k, 152, -2.74010461024631, -5.98863509737333e-13, 22.0100000000000000"

"k, 153, -1.70842728051422, -2.14230004954671, 22.0100000000000000"

"k, 154, 0.609730637010633, -2.67140446682708, 22.0100000000000000"

"k, 155, 2.46874894862808, -1.18888683386637, 23.4300000000000000"

"k, 156, 2.46874894862752, 1.18888683386754, 23.4300000000000000"

"k, 157, 0.609730637009447, 2.67140446682735, 23.4300000000000000"

"k, 158, -1.70842728051517, 2.14230004954596, 23.4300000000000000"

"k, 159, -2.74010461024631, -6.17661991929612e-13, 23.4300000000000000"

"k, 160, -1.70842728051414, -2.14230004954677, 23.4300000000000000"

---

"k, 161, 0.609730637010575, -2.67140446682709, 23.4300000000000"

"k, 162, 2.74010461024631, 5.88122004505086e-13, 24.1400000000000"

"k, 163, 1.70842728051423, 2.14230004954671, 24.1400000000000"

"k, 164, -0.609730637010470, 2.67140446682712, 24.1400000000000"

"k, 165, -2.46874894862801, 1.18888683386652, 24.1400000000000"

"k, 166, -2.46874894862763, -1.18888683386732, 24.1400000000000"

"k, 167, -0.609730637009609, -2.67140446682731, 24.1400000000000"

"k, 168, 1.70842728051498, -2.14230004954611, 24.1400000000000"

"l, 8, 1"

"l, 8, 7"

"l, 9, 1"

"l, 9, 2"

"l, 10, 2"

"l, 10, 3"

"l, 11, 3"

"l, 11, 4"

"l, 12, 4"

"l, 12, 5"

"l, 13, 5"

"l, 13, 6"

"l, 14, 6"

"l, 14, 7"

"l, 15, 8"

"l, 16, 9"

"l, 17, 10"

"1, 18, 11"

"1, 19, 12"

"1, 20, 13"

"1, 21, 14"

"1, 22, 15"

"1, 22, 16"

"1, 23, 16"

"1, 23, 17"

"1, 24, 17"

"1, 24, 18"

"1, 25, 18"

"1, 25, 19"

"1, 26, 19"

"1, 26, 20"

"1, 27, 20"

"1, 27, 21"

"1, 28, 15"

"1, 28, 21"

"1, 29, 22"

"1, 30, 23"

"1, 31, 24"

"1, 32, 25"

"1, 33, 26"

"1, 34, 27"

"1, 35, 28"

"1, 36, 29"

"1, 36, 35"

"1, 37, 29"

"1, 37, 30"

"1, 38, 30"

"1, 38, 31"

"1, 39, 31"

"1, 39, 32"

"1, 40, 32"

"1, 40, 33"

"1, 41, 33"

"1, 41, 34"

"1, 42, 34"

"1, 42, 35"

"1, 43, 36"

"1, 44, 37"

"1, 45, 38"

"1, 46, 39"

"1, 47, 40"

"1, 48, 41"

"1, 49, 42"

"1, 50, 43"

"1, 50, 44"

"1, 51, 44"

"1, 51, 45"

"1, 52, 45"

"1, 52, 46"

"1, 53, 46"

"1, 53, 47"

"1, 54, 47"

"1, 54, 48"

"1, 55, 48"

"1, 55, 49"

"1, 56, 43"

"1, 56, 49"

"1, 57, 50"

"1, 58, 51"

"1, 59, 52"

"1, 60, 53"

"1, 61, 54"

"1, 62, 55"

"1, 63, 56"

"1, 64, 57"

"1, 64, 63"

"1, 65, 57"

"1, 65, 58"

"1, 66, 58"

"1, 66, 59"

"1, 67, 59"

"1, 67, 60"

"1, 68, 60"

"1, 68, 61"

"1, 69, 61"

"1, 69, 62"

"1, 70, 62"

"1, 70, 63"

"1, 71, 64"

"1, 72, 65"

"1, 73, 66"

"1, 74, 67"

"1, 75, 68"

"1, 76, 69"

"1, 77, 70"

"1, 78, 71"

"1, 78, 72"

"1, 79, 72"

"1, 79, 73"

"1, 80, 73"

"1, 80, 74"

"1, 81, 74"

"1, 81, 75"

"1, 82, 75"

"1, 82, 76"

"1, 83, 76"

"1, 83, 77"

"1, 84, 71"

"1, 84, 77"

"1, 85, 78"

"1, 86, 79"

"1, 87, 80"

"1, 88, 81"

"1, 89, 82"

"1, 90, 83"

"1, 91, 84"

"1, 92, 85"

"1, 92, 91"

"1, 93, 85"

"1, 93, 86"

"1, 94, 86"

"1, 94, 87"

"1, 95, 87"

"1, 95, 88"

"1, 96, 88"

"1, 96, 89"

"1, 97, 89"

"1, 97, 90"

"1, 98, 90"

"1, 98, 91"

"1, 99, 92"

"1, 100, 93"

"1, 101, 94"

"1, 102, 95"

"1, 103, 96"

"1, 104, 97"

"1, 105, 98"

"1, 106, 99"

"1, 106, 100"

"1, 107, 100"

"1, 107, 101"

"1, 108, 101"

"1, 108, 102"

"1, 109, 102"

"1, 109, 103"

"1, 110, 103"

"1, 110, 104"

"1, 111, 104"

"1, 111, 105"

"1, 112, 99"

"1, 112, 105"

"1, 113, 106"

"1, 114, 107"

"1, 115, 108"

"1, 116, 109"

"1, 117, 110"

"1, 118, 111"

"1, 119, 112"

"1, 120, 113"

"1, 120, 119"

"1, 121, 113"

"1, 121, 114"

"1, 122, 114"

"1, 122, 115"

"1, 123, 115"

"1, 123, 116"

"1, 124, 116"

"1, 124, 117"

"1, 125, 117"

"1, 125, 118"

"1, 126, 118"

"1, 126, 119"

"1, 127, 120"

"1, 128, 121"

"1, 129, 122"

"1, 130, 123"

"1, 131, 124"

"1, 132, 125"

"1, 133, 126"

"1, 134, 127"

"1, 134, 128"

"1, 135, 128"

"1, 135, 129"

"1, 136, 129"

"1, 136, 130"

"1, 137, 130"

"1, 137, 131"

"1, 138, 131"

"1, 138, 132"

"1, 139, 132"

"1, 139, 133"

"1, 140, 127"

"1, 140, 133"

"1, 141, 134"

"1, 142, 135"

"1, 143, 136"

"1, 144, 137"

"1, 145, 138"

"1, 146, 139"

"1, 147, 140"

"1, 148, 141"

"1, 148, 147"

"1, 149, 141"

"1, 149, 142"

"1, 150, 142"

"1, 150, 143"

"1, 151, 143"

"1, 151, 144"

"1, 152, 144"

"1, 152, 145"

"1, 153, 145"

"1, 153, 146"

"1, 154, 146"

"1, 154, 147"

"1, 155, 148"

"1, 156, 149"

"1, 157, 150"

"1, 158, 151"

"1, 159, 152"

"1, 160, 153"

"1, 161, 154"

"1, 162, 155"

"1, 162, 156"

"1, 163, 156"

"1, 163, 157"

"1, 164, 157"

"1, 164, 158"

"1, 165, 158"

"1, 165, 159"

"1, 166, 159"

"1, 166, 160"

---

"l, 167, 160"

"l, 167, 161"

"l, 168, 155"

"l, 168, 161"

finish

## **B.4 Macro file (Defective single wall zigzag) used as input to the ANSYS Mechanical APDL software**

/prep7

/view,,-1,-2,-3

"k, 1, 2.74010461024631, 0, 0"

"k, 2, 1.70842728051467, 2.14230004954635, 0"

"k, 3, -0.609730637010011, 2.67140446682722, 0"

"k, 4, -2.46874894862781, 1.18888683386693, 0"

"k, 5, -2.46874894862781, -1.18888683386693, 0"

"k, 6, -0.609730637010009, -2.67140446682722, 0"

"k, 7, 1.70842728051467, -2.14230004954635, 0"

"k, 8, 2.46874894862781, -1.18888683386693, 0.7100000000000000"

"k, 9, 2.46874894862781, 1.18888683386693, 0.7100000000000000"

"k, 10, 0.609730637010009, 2.67140446682722, 0.7100000000000000"

"k, 11, -1.70842728051468, 2.14230004954635, 0.7100000000000000"

---

"k, 12, -2.74010461024631, -3.86070546300307e-15, 0.7100000000000000"

"k, 13, -1.70842728051467, -2.14230004954636, 0.7100000000000000"

"k, 14, 0.609730637010019, -2.67140446682722, 0.7100000000000000"

"k, 15, 2.46874894862782, -1.18888683386692, 2.1300000000000000"

"k, 16, 2.46874894862781, 1.18888683386693, 2.1300000000000000"

"k, 17, 0.609730637010008, 2.67140446682722, 2.1300000000000000"

"k, 18, -1.70842728051467, 2.14230004954635, 2.1300000000000000"

"k, 19, -2.74010461024631, -1.29243805251160e-14, 2.1300000000000000"

"k, 20, -1.70842728051467, -2.14230004954636, 2.1300000000000000"

"k, 21, 0.609730637010019, -2.67140446682722, 2.1300000000000000"

"k, 22, 2.74010461024631, -2.01339620416023e-15, 2.8400000000000000"

"k, 23, 1.70842728051467, 2.14230004954635, 2.8400000000000000"

"k, 24, -0.609730637009999, 2.67140446682722, 2.8400000000000000"

"k, 25, -2.46874894862781, 1.18888683386695, 2.8400000000000000"

"k, 26, -2.46874894862782, -1.18888683386691, 2.8400000000000000"

"k, 27, -0.609730637010042, -2.67140446682721, 2.8400000000000000"

"k, 28, 1.70842728051465, -2.14230004954637, 2.8400000000000000"

"k, 29, 2.74010461024631, -3.18889496627127e-14, 4.2600000000000000"

"k, 30, 1.70842728051470, 2.14230004954633, 4.2600000000000000"

"k, 32, -2.46874894862780, 1.18888683386696, 4.2600000000000000"

"k, 33, -2.46874894862784, -1.18888683386687, 4.2600000000000000"

"k, 34, -0.609730637010071, -2.67140446682721, 4.2600000000000000"

"k, 35, 1.70842728051462, -2.14230004954639, 4.2600000000000000"

"k, 36, 2.46874894862778, -1.18888683386699, 4.9700000000000000"

"k, 37, 2.46874894862785, 1.18888683386685, 4.9700000000000000"

"k, 38, 0.609730637010100, 2.67140446682720, 4.9700000000000000"

"k, 39, -1.70842728051460, 2.14230004954641, 4.9700000000000000"

"k, 40, -2.74010461024631, 9.13044905457911e-14, 4.9700000000000000"

---

"k, 41, -1.70842728051474, -2.14230004954630, 4.9700000000000000"

"k, 42, 0.609730637009922, -2.67140446682724, 4.9700000000000000"

"k, 43, 2.46874894862778, -1.18888683386699, 6.3900000000000000"

"k, 44, 2.46874894862785, 1.18888683386686, 6.3900000000000000"

"k, 45, 0.609730637010063, 2.67140446682721, 6.3900000000000000"

"k, 46, -1.70842728051463, 2.14230004954639, 6.3900000000000000"

"k, 47, -2.74010461024631, 5.30363940931790e-14, 6.3900000000000000"

"k, 48, -1.70842728051471, -2.14230004954632, 6.3900000000000000"

"k, 49, 0.609730637009978, -2.67140446682723, 6.3900000000000000"

"k, 50, 2.74010461024631, -2.41675387367066e-14, 7.1000000000000000"

"k, 51, 1.70842728051469, 2.14230004954634, 7.1000000000000000"

"k, 52, -0.609730637010006, 2.67140446682722, 7.1000000000000000"

"k, 53, -2.46874894862781, 1.18888683386693, 7.1000000000000000"

"k, 54, -2.46874894862782, -1.18888683386692, 7.1000000000000000"

"k, 55, -0.609730637010016, -2.67140446682722, 7.1000000000000000"

"k, 56, 1.70842728051468, -2.14230004954634, 7.1000000000000000"

"k, 57, 2.74010461024631, 3.35701719762382e-14, 8.5200000000000000"

"k, 58, 1.70842728051466, 2.14230004954636, 8.5200000000000000"

"k, 59, -0.609730637010044, 2.67140446682721, 8.5200000000000000"

"k, 60, -2.46874894862783, 1.18888683386690, 8.5200000000000000"

"k, 61, -2.46874894862779, -1.18888683386697, 8.5200000000000000"

"k, 62, -0.609730637009979, -2.67140446682723, 8.5200000000000000"

"k, 63, 1.70842728051471, -2.14230004954632, 8.5200000000000000"

"k, 64, 2.46874894862784, -1.18888683386687, 9.2300000000000000"

"k, 65, 2.46874894862779, 1.18888683386698, 9.2300000000000000"

"k, 66, 0.609730637009951, 2.67140446682724, 9.2300000000000000"

"k, 67, -1.70842728051472, 2.14230004954631, 9.2300000000000000"

"k, 68, -2.74010461024631, -8.12375095249899e-14, 9.2300000000000000"

---

"k, 69, -1.70842728051459, -2.14230004954642, 9.2300000000000000"

"k, 70, 0.609730637010090, -2.67140446682720, 9.2300000000000000"

"k, 71, 2.46874894862786, -1.18888683386684, 10.6500000000000000"

"k, 72, 2.46874894862777, 1.18888683386702, 10.6500000000000000"

"k, 73, 0.609730637009894, 2.67140446682725, 10.6500000000000000"

"k, 74, -1.70842728051475, 2.14230004954629, 10.6500000000000000"

"k, 75, -2.74010461024631, -1.19505605977602e-13, 10.6500000000000000"

"k, 76, -1.70842728051456, -2.14230004954644, 10.6500000000000000"

"k, 77, 0.609730637010165, -2.67140446682719, 10.6500000000000000"

"k, 78, 2.74010461024631, 1.28904847073742e-13, 11.3600000000000000"

"k, 79, 1.70842728051456, 2.14230004954645, 11.3600000000000000"

"k, 80, -0.609730637010175, 2.67140446682718, 11.3600000000000000"

"k, 81, -2.46874894862788, 1.18888683386679, 11.3600000000000000"

"k, 82, -2.46874894862776, -1.18888683386704, 11.3600000000000000"

"k, 83, -0.609730637009867, -2.67140446682725, 11.3600000000000000"

"k, 85, 2.74010461024631, 1.86642557786686e-13, 12.7800000000000000"

"k, 86, 1.70842728051454, 2.14230004954646, 12.7800000000000000"

"k, 87, -0.609730637010193, 2.67140446682718, 12.7800000000000000"

"k, 88, -2.46874894862790, 1.18888683386674, 12.7800000000000000"

"k, 89, -2.46874894862773, -1.18888683386709, 12.7800000000000000"

"k, 90, -0.609730637009810, -2.67140446682727, 12.7800000000000000"

"k, 91, 1.70842728051482, -2.14230004954624, 12.7800000000000000"

"k, 92, 2.46874894862792, -1.18888683386670, 13.4900000000000000"

"k, 93, 2.46874894862771, 1.18888683386714, 13.4900000000000000"

"k, 94, 0.609730637009763, 2.67140446682728, 13.4900000000000000"

"k, 95, -1.70842728051486, 2.14230004954621, 13.4900000000000000"

"k, 96, -2.74010461024631, -2.53779509595771e-13, 13.4900000000000000"

"k, 97, -1.70842728051449, -2.14230004954650, 13.4900000000000000"

---

"k, 98, 0.609730637010258, -2.67140446682716, 13.4900000000000"

"k, 99, 2.46874894862793, -1.18888683386668, 14.9100000000000"

"k, 100, 2.46874894862769, 1.18888683386719, 14.9100000000000"

"k, 101, 0.609730637009745, 2.67140446682728, 14.9100000000000"

"k, 102, -1.70842728051490, 2.14230004954617, 14.9100000000000"

"k, 103, -2.74010461024631, -2.72577991788050e-13, 14.9100000000000"

"k, 104, -1.70842728051444, -2.14230004954653, 14.9100000000000"

"k, 105, 0.609730637010315, -2.67140446682715, 14.9100000000000"

"k, 106, 2.74010461024631, 2.81977232884190e-13, 15.6200000000000"

"k, 107, 1.70842728051444, 2.14230004954654, 15.6200000000000"

"k, 108, -0.609730637010324, 2.67140446682715, 15.6200000000000"

"k, 109, -2.46874894862796, 1.18888683386662, 15.6200000000000"

"k, 110, -2.46874894862766, -1.18888683386725, 15.6200000000000"

"k, 111, -0.609730637009718, -2.67140446682729, 15.6200000000000"

"k, 112, 1.70842728051492, -2.14230004954615, 15.6200000000000"

"k, 113, 2.74010461024631, 3.39714943597135e-13, 17.0400000000000"

"k, 114, 1.70842728051439, 2.14230004954658, 17.0400000000000"

"k, 115, -0.609730637010342, 2.67140446682715, 17.0400000000000"

"k, 116, -2.46874894862797, 1.18888683386660, 17.0400000000000"

"k, 117, -2.46874894862765, -1.18888683386727, 17.0400000000000"

"k, 118, -0.609730637009623, -2.67140446682731, 17.0400000000000"

"k, 119, 1.70842728051494, -2.14230004954614, 17.0400000000000"

"k, 120, 2.46874894862797, -1.18888683386660, 17.7500000000000"

"k, 121, 2.46874894862765, 1.18888683386728, 17.7500000000000"

"k, 122, 0.609730637009614, 2.67140446682731, 17.7500000000000"

"k, 123, -1.70842728051501, 2.14230004954609, 17.7500000000000"

"k, 124, -2.74010461024631, -4.45791123926885e-13, 17.7500000000000"

"k, 125, -1.70842728051431, -2.14230004954664, 17.7500000000000"

---

"k, 126, 0.609730637010407, -2.67140446682713, 17.7500000000000"

"k, 127, 2.46874894862800, -1.18888683386654, 19.1700000000000"

"k, 128, 2.46874894862762, 1.18888683386733, 19.1700000000000"

"k, 129, 0.609730637009558, 2.67140446682732, 19.1700000000000"

"k, 130, -1.70842728051505, 2.14230004954605, 19.1700000000000"

"k, 131, -2.74010461024631, -4.64589606119164e-13, 19.1700000000000"

"k, 132, -1.70842728051429, -2.14230004954665, 19.1700000000000"

"k, 133, 0.609730637010502, -2.67140446682711, 19.1700000000000"

"k, 134, 2.74010461024631, 4.35049618694638e-13, 19.8800000000000"

"k, 135, 1.70842728051432, 2.14230004954664, 19.8800000000000"

"k, 136, -0.609730637010473, 2.67140446682712, 19.8800000000000"

"k, 137, -2.46874894862803, 1.18888683386648, 19.8800000000000"

"k, 138, -2.46874894862759, -1.18888683386739, 19.8800000000000"

"k, 140, 1.70842728051507, -2.14230004954603, 19.8800000000000"

"k, 141, 2.74010461024631, 5.31726557928248e-13, 21.3000000000000"

"k, 142, 1.70842728051427, 2.14230004954667, 21.3000000000000"

"k, 143, -0.609730637010491, 2.67140446682711, 21.3000000000000"

"k, 144, -2.46874894862805, 1.18888683386643, 21.3000000000000"

"k, 145, -2.46874894862758, -1.18888683386741, 21.3000000000000"

"k, 146, -0.609730637009512, -2.67140446682734, 21.3000000000000"

"k, 147, 1.70842728051512, -2.14230004954600, 21.3000000000000"

"k, 148, 2.46874894862807, -1.18888683386639, 22.0100000000000"

"k, 149, 2.46874894862756, 1.18888683386745, 22.0100000000000"

"k, 150, 0.609730637009465, 2.67140446682735, 22.0100000000000"

"k, 151, -1.70842728051509, 2.14230004954602, 22.0100000000000"

"k, 152, -2.74010461024631, -5.98863509737333e-13, 22.0100000000000"

"k, 153, -1.70842728051422, -2.14230004954671, 22.0100000000000"

"k, 154, 0.609730637010633, -2.67140446682708, 22.0100000000000"

---

"k, 155, 2.46874894862808, -1.18888683386637, 23.4300000000000000"  
"k, 156, 2.46874894862752, 1.18888683386754, 23.4300000000000000"  
"k, 157, 0.609730637009447, 2.67140446682735, 23.4300000000000000"  
"k, 158, -1.70842728051517, 2.14230004954596, 23.4300000000000000"  
"k, 159, -2.74010461024631, -6.17661991929612e-13, 23.4300000000000000"  
"k, 160, -1.70842728051414, -2.14230004954677, 23.4300000000000000"  
"k, 161, 0.609730637010575, -2.67140446682709, 23.4300000000000000"  
"k, 162, 2.74010461024631, 5.88122004505086e-13, 24.1400000000000000"  
"k, 163, 1.70842728051423, 2.14230004954671, 24.1400000000000000"  
"k, 164, -0.609730637010470, 2.67140446682712, 24.1400000000000000"  
"k, 165, -2.46874894862801, 1.18888683386652, 24.1400000000000000"  
"k, 166, -2.46874894862763, -1.18888683386732, 24.1400000000000000"  
"k, 167, -0.609730637009609, -2.67140446682731, 24.1400000000000000"  
"k, 168, 1.70842728051498, -2.14230004954611, 24.1400000000000000"

"l, 8, 1"

"l, 8, 7"

"l, 9, 1"

"l, 9, 2"

"l, 10, 2"

"l, 10, 3"

"l, 11, 3"

"l, 11, 4"

"l, 12, 4"

"l, 12, 5"

"l, 13, 5"

"1, 13, 6"  
"1, 14, 6"  
"1, 14, 7"  
"1, 15, 8"  
"1, 16, 9"  
"1, 17, 10"  
"1, 18, 11"  
"1, 19, 12"  
"1, 20, 13"  
"1, 21, 14"  
"1, 22, 15"  
"1, 22, 16"  
"1, 23, 16"  
"1, 23, 17"  
"1, 24, 17"  
"1, 24, 18"  
"1, 25, 18"  
"1, 25, 19"  
"1, 26, 19"  
"1, 26, 20"  
"1, 27, 20"  
"1, 27, 21"  
"1, 28, 15"  
"1, 28, 21"  
"1, 29, 22"  
"1, 30, 23"  
"1, 32, 25"  
"1, 33, 26"

"1, 34, 27"

"1, 35, 28"

"1, 36, 29"

"1, 36, 35"

"1, 37, 29"

"1, 37, 30"

"1, 38, 30"

"1, 39, 32"

"1, 40, 32"

"1, 40, 33"

"1, 41, 33"

"1, 41, 34"

"1, 42, 34"

"1, 42, 35"

"1, 43, 36"

"1, 44, 37"

"1, 45, 38"

"1, 46, 39"

"1, 47, 40"

"1, 48, 41"

"1, 49, 42"

"1, 50, 43"

"1, 50, 44"

"1, 51, 44"

"1, 51, 45"

"1, 52, 45"

"1, 52, 46"

"1, 53, 46"

"1, 53, 47"

"1, 54, 47"

"1, 54, 48"

"1, 55, 48"

"1, 55, 49"

"1, 56, 43"

"1, 56, 49"

"1, 57, 50"

"1, 58, 51"

"1, 59, 52"

"1, 60, 53"

"1, 61, 54"

"1, 62, 55"

"1, 63, 56"

"1, 64, 57"

"1, 64, 63"

"1, 65, 57"

"1, 65, 58"

"1, 66, 58"

"1, 66, 59"

"1, 67, 59"

"1, 67, 60"

"1, 68, 60"

"1, 68, 61"

"1, 69, 61"

"1, 69, 62"

"1, 70, 62"

"1, 70, 63"

"1, 71, 64"

"1, 72, 65"

"1, 73, 66"

"1, 74, 67"

"1, 75, 68"

"1, 76, 69"

"1, 77, 70"

"1, 78, 71"

"1, 78, 72"

"1, 79, 72"

"1, 79, 73"

"1, 80, 73"

"1, 80, 74"

"1, 81, 74"

"1, 81, 75"

"1, 82, 75"

"1, 82, 76"

"1, 83, 76"

"1, 83, 77"

"1, 85, 78"

"1, 86, 79"

"1, 87, 80"

"1, 88, 81"

"1, 89, 82"

"1, 90, 83"

"1, 92, 85"

"1, 92, 91"

"1, 93, 85"

"1, 93, 86"

"1, 94, 86"

"1, 94, 87"

"1, 95, 87"

"1, 95, 88"

"1, 96, 88"

"1, 96, 89"

"1, 97, 89"

"1, 97, 90"

"1, 98, 90"

"1, 98, 91"

"1, 99, 92"

"1, 100, 93"

"1, 101, 94"

"1, 102, 95"

"1, 103, 96"

"1, 104, 97"

"1, 105, 98"

"1, 106, 99"

"1, 106, 100"

"1, 107, 100"

"1, 107, 101"

"1, 108, 101"

"1, 108, 102"

"1, 109, 102"

"1, 109, 103"

"1, 110, 103"

"1, 110, 104"

"1, 111, 104"

"1, 111, 105"

"1, 112, 99"

"1, 112, 105"

"1, 113, 106"

"1, 114, 107"

"1, 115, 108"

"1, 116, 109"

"1, 117, 110"

"1, 118, 111"

"1, 119, 112"

"1, 120, 113"

"1, 120, 119"

"1, 121, 113"

"1, 121, 114"

"1, 122, 114"

"1, 122, 115"

"1, 123, 115"

"1, 123, 116"

"1, 124, 116"

"1, 124, 117"

"1, 125, 117"

"1, 125, 118"

"1, 126, 118"

"1, 126, 119"

"1, 127, 120"

"1, 128, 121"

"1, 129, 122"

"1, 130, 123"

"1, 131, 124"

"1, 132, 125"

"1, 133, 126"

"1, 134, 127"

"1, 134, 128"

"1, 135, 128"

"1, 135, 129"

"1, 136, 129"

"1, 136, 130"

"1, 137, 130"

"1, 137, 131"

"1, 138, 131"

"1, 138, 132"

"1, 140, 127"

"1, 140, 133"

"1, 141, 134"

"1, 142, 135"

"1, 143, 136"

"1, 144, 137"

"1, 145, 138"

"1, 147, 140"

"1, 148, 141"

"1, 148, 147"

"1, 149, 141"

"1, 149, 142"

"1, 150, 142"

"1, 150, 143"

"1, 151, 143"

"1, 151, 144"

"1, 152, 144"

"1, 152, 145"

"1, 153, 145"

"1, 153, 146"

"1, 154, 146"

"1, 154, 147"

"1, 155, 148"

"1, 156, 149"

"1, 157, 150"

"1, 158, 151"

"1, 159, 152"

"1, 160, 153"

"1, 161, 154"

"1, 162, 155"

"1, 162, 156"

"1, 163, 156"

"1, 163, 157"

"1, 164, 157"

"1, 164, 158"

"1, 165, 158"

"1, 165, 159"

"1, 166, 159"

"1, 166, 160"

"1, 167, 160"

"1, 167, 161"

"1, 168, 155"

"1, 168, 161"

finish

TABLE B.1: Properties of pristine and defective SWCNT of zigzag

n	m	Diameters obtained (Matlab)	Applied force	Elongation (Steel)	Elongation (SWCNT)	Young modulus of (SWCNT)	Angular defromation (Steel)	Angular defromation (SWCNT)	Shear modulus of (SWCNT)	Elongation in defective (SWCNT)	Young modulus of defective (SWCNT)	Deflection	Shear modulus of defective (SWCNT)
		Zigzag	uN	nm	nm	MPa	nm	nm	Pa	nm	Pa	nm	Pa
7	0	5.481		0.0096104	0.002501	7.68525E+11	0.0089854	0.0021582	3.202259E+11	0.0032554	2.60328E+11	0.0029365	1.04663E+11
11	0	8.61		0.006071	0.0015786	7.69163E+11	0.0037961	0.00090471	3.22764E+11	0.0019375	2.45471E+11	0.0010484	89140247372
14	0	10.96	500uN	0.00476	0.0012376	7.69231E+11	0.0023702	0.00056418	3.23164E+11	0.0014594	2.35844E+11	0.00064217	87556529671
20	0	15.657		0.0033327	0.00086514	7.70442E+11	0.0011724	0.00028166	3.20189E+11	0.00095246	2.20186E+11	0.00030608	83592245402
28	0	21.92		0.0023936	0.00061819	7.7439E+11	0.00060081	0.00014829	3.1166E+11	0.00064744	2.09463E+11	0.00013561	70345458426

TABLE B.2: Properties of pristine DWCNT of zigzag

n	m	Diameters obtained (Matlab)	Applied force	Elongation (Steel)	Elongation (DWCNT)	Young modulus (DWCNT)	Angular deformation (Steel)	Angular deformation (DWCNT)	Shear modulus (DWCNT)
		Zigzag	uN	nm	nm	MPa	nm	nm	Pa
7	0	5.481		0.0030431	0.00076603	7.94512E+11	0.0027681	0.00066492	3.20235E+11
11	0	8.61		0.0022022	0.00056228	7.83311E+11	0.0013562	0.00032323	3.22752E+11
14	0	10.96	500uN	0.0018037	0.0004683	7.70318E+11	0.00089727	0.00021348	3.23312E+11
20	0	15.657		0.0015945	0.00041869	7.61661E+11	0.00049557	0.00011604	3.28514E+11
28	0	21.92		0.0010126	0.00025886	7.82353E+11	0.00023565	0.000058215	3.11379E+11

TABLE B.3: Properties of MWCNT of zigzag

n	m	Diameters obtained (Matlab)	Applied force	Elongation (Steel)	Elongation (DWCNT)	Young modulus (DWCNT)	Angular deformation (Steel)	Angular deformation (DWCNT)	Shear modulus (DWCNT)
		Zigzag	uN	nm	nm	MPa	nm	nm	Pa
7	0	5.481	500uN	0.0014418	0.00037455	7.69884E+11	0.0015231	0.0003674	3.18893E+11
11	0	8.61		0.0011346	0.00029116	7.79365E+11	0.00070098	0.00016706	3.22767E+11
14	0	10.96	500uN	0.00097652	0.00025112	7.77732E+11	0.00048097	0.00011447	3.23208E+11
20	0	15.657		0.00078131	0.00019941	7.83622E+11	0.00027103	0.000064771	3.21879E+11
28	0	21.92		0.00061155	0.00015397	7.94376E+11	0.00013916	0.000034496	3.10314E+11

TABLE B.4: Properties of pristine and defective SWCNT of zigzag

n	m	Diameters obtained (Matlab)	Applied force	Elongation (Steel)	Elongation (SWCNT)	Young modulus of (SWCNT)	Angular defromation (Steel)	Angular deformation (SWCNT)	Shear modulus of (SWCNT)	Elongation in defective (SWCNT)	Young modulus of defective (SWCNT)	Deflection	Shear modulus of defective (SWCNT)
		Armchair	uN	nm	nm	MPa	nm	nm	Pa	nm	Pa	nm	Pa
4	4	5.424000467		0.0092978	0.0024623	7.55213E+11	0.0090133	0.0019118	3.62658E+11	0.0031719	2.57637E+11	0.0024323	97865787687
6	6	8.136		0.00627	0.0016606	7.55149E+11	0.0040911	0.00087414	3.60011E+11	0.0020005	2.40937E+11	0.001056	92926405381
8	8	10.84800093	500uN	0.00469	0.0012413	7.55659E+11	0.0023233	0.00049771	3.59075E+11	0.0014344	2.31113E+11	0.0005763	89069387595
11	11	14.91600128		0.0033836	0.00089056	7.59881E+11	0.0012435	0.00026677	3.58563E+11	0.00098548	2.21317E+11	0.00029485	85019854369
16	16	21.69600187		0.0023557	0.0006154	7.65583E+11	0.00060025	0.00012893	3.58125E+11	0.00070157	2.28005E+11	0.00014087	84046715349

TABLE B.5: Properties of DWCNT of Armchair

n	m	Diameters obtained (Matlab)	Applied force	Elongation (Steel)	Elongation (DWCNT)	Young modulus (DWCNT)	Angular defromation (Steel)	Angular deformation (DWCNT)	Shear modulus (DWCNT)
4	4	5.424000467		0.0027025	0.00071337	7.57671E+11	0.002823	0.00059203	3.66795E+11
6	6	8.136		0.0020618	0.00054755	7.531E+11	0.0013689	0.0002927	3.59754E+11
8	8	10.84800093	500uN	0.0017772	0.0004677	7.59974E+11	0.00088481	0.00018995	3.58317E+11
11	11	14.91600128		0.0013489	0.00035209	7.66225E+11	0.00048928	0.00010485	3.58959E+11
16	16	21.69600187		0.0010352	0.00026789	7.72855E+11	0.00025957	0.000055756	3.58112E+11

TABLE B.6: Properties of MWCNT of Armchair

n	m	Diameters obtained (Matlab)	Applied force	Elongation	Elongation	Young modulus (MWCNT)	Angular defromation	Angular deformation	Shear modulus (MWCNT)
				(Steel)	(MWCNT)		(Steel)	(MWCNT)	
		Armchair	uN	nm	nm	MPa	nm	nm	Pa
4	4	5.424000467	500uN	0.001386	0.000417	6.65E+11	0.001338	0.00034125	3.01516E+11
6	6	8.136		0.001079	0.00033	6.53E+11	0.000708	0.00018331	2.9713E+11
8	8	10.84800093		0.000973	0.000299	6.51E+11	0.000478	0.00012571	2.9226E+11
11	11	14.91600128		0.000769	0.000198	7.77E+11	0.000282	0.000060663	3.57688E+11
16	16	21.69600187		0.000623	0.000159	7.86E+11	0.000153	0.000032823	3.59668E+11

# Appendix C

## C.1 Paper1

CHARACTERIZATION OF CNT PROPERTIES USING SPACE-FRAME STRUCTURE, Muhammad Arif, Jacob Muthu

### Abstract

We studied the elastic properties of different carbon nanotubes (CNTs) i.e. Pristine and defective single wall (SWCNTs), double wall (DWCNTs), and multiwall (MWCNTs) for zigzag and armchair configurations. CNTs atomic geometry was replicated with an equivalent space frame structure (SFS). Coordinates definition of SFS of CNTs was developed in MATLAB code and transferred to the finite element analysis (FEA) software 'ANSYS'. The basic entity of SFS, C-C chemical bond was designed as a circular beam of orthotropic properties. The properties were determined by linking the energy equation of molecular mechanics to structural mechanics along with the parametric study. The van der Waals forces between inter-shell of DWCNTs and MWCNTs were modelled as linear elastic springs in a simplified way. The simplified model

avoided the problems due to nonlinear behaviour of van der Waals forces and improved the performance of the FEA software by computational resources. The effect of chirality, vacancy defects, different diameters and numbers of walls on elastic properties of CNTs were calculated, tabulated and compared with each other. The result of proposed SFS model with orthotropic properties was compared with other's result. The SFS model is found better than the equivalent shell model as the defects can be placed at exact location and a more realistic behaviour could be predicted. The SFS models could be developed with any type of defects, a number of walls, van der Waals and agglomerated forms with variable geometries. These models could be directly embedded in the matrix with designable interface region to predict tensile and torsional properties of future nanocomposites.

## **C.2 Paper2**

Improvement of Interlaminar Region Properties of Fibre Glass Composite by Incorporating Electrospun Aligned Nanofibres Mats, Muhammad Arif, Mkhululi Ncube, Jacob Muthu.

### **Abstract**

Polymer composite reinforced with conventional macro size fibres have taken a major role in various modern engineering applications and the demand for high performing composites is ever increasing due to their light weight and design flexibility. Various improvements in the methods, techniques and composition have been made over the years to produce better polymer composites

---

however one of the challenges limiting the performance of conventional polymer composites is their failure at the interlaminar region resulting in lower mechanical properties. A number of research attempts with little success have been made to rectify this problem. One of the potential methods expected to improve the strength of the interlaminar region is the incorporation of nanosize fillers such as electrospun Polyacrylonitrile (PAN) nanofibres mat as an interalia into the matrix rich interlaminar region of the conventional polymer composite. Controlling orientation of the PAN nanofibres during the chaotic electrospinning process is a major hurdle for this method. The random orientation of electrospun PAN nanofibres mat reduce their strengthening effect, moreover, different applications require a specific orientation of PAN nanofibres mat to design required material properties. The current study was carried out to design and improved technique produce and analyse the mechanical behaviour of random using general technique and aligned using improved technique PAN nanofibres mat, for both pristine and functionalized single walled carbon nanotubes (SWCNTs) doped PAN nanofibres mat strengthened hybrid composites. Experimentally developed composites were also modelled using multiscale modelling method for comparison of tensile properties. As part of the procedure, electric fields of general electrospinning technique was manipulated using two position adjustable auxiliary vertical electrodes (AVEs) to produce aligned nanofibres mat along with reduced diameter. AVEs were connected in series with multi-spinnerets and powered with same DC voltage. So as to optimise the electrospinning parameters, the effect of AVEs on the PAN nanofibres mat orientation, distribution and diameter were experimentally matrixed and analysed. The fractographic study showed that auxiliary vertical electrodes (AVEs) added to general electrospinning technique, reduced the diameter, enhance the alignment of the nanofibres and improved molecular orientation. Four different volume fractions, 0.1%, 0.2%, 0.5% and 1%

of randomly oriented PAN nanofibre mats were used with 32% glass fibre for manufacturing the PAN nanomats strengthened hybrid composites. Based on the mechanical properties, the volume fraction (0.5%) of PAN polymer with better properties was selected to manufacture aligned PAN nanofibres mat strengthened hybrid composite.

A series of tests showed that glass fibre composites (GFC) reinforced with the volume fraction of 0.5% aligned nanofibre mats were better than those of 0.5% random nanofibre mats. The aligned nanofibre mat with reduced diameter increased the tensile, flexural, and impact properties of glass fibre composite by 68.91%, 95.32% and 45.30% respectively. Compared to the random nanofibres mat, the same volume fraction of aligned nanofibre mat improved the tensile, flexural, and impact properties by 10.79%, 30.98% and 24.74% respectively. Aligned nanofibres mat was further utilised to align and disperse the pristine and functionalized SWCNTs into the interlaminar region of fibreglass composite. Alignment and the confinement of nanofibre into a thinner diameter of nanofibres helped in the better distribution and alignment of pristine SWCNTs (p-SWCNTs) which is reflected as an increase in tensile, flexural and impact resistance by 89.30%, 105.48% and 107.17% respectively. A nondestructive functionalization method (Friedel craft alkylation) was used to improve the interface bonding of SWCNTs with the host material 'nanofibre mat'. PVA chain attachment to the surface of the SWCNTs without damaging the wall was confirmed using FTIR and Raman spectroscopy. The effect of functionalized SWCNTs (f-SWCNTs) doped aligned nanofibre mat improved the properties of nano-hybrid composite up to 111.34%, 117.11% and 180.03% in tensile, flexural and impact resistance respectively.

Multiscale Modelling Analysis for Characterizing Multiscale Nanohybrid Composites, Muhammad Arif, Jacob Muthu.

## **Abstract**

In the current research, multiscale modelling was used to determine the properties of the multiscale nanohybrid composites (MNHCs) strengthened with random and aligned PAN nanofibre mats, PAN doped with p-SWCNTs and f-SWCNTs aligned nanofibres mats. In multiscale modelling, three length scales, such as nano, micro and macro scales were modelled. The nanoscale RVE of SWCNTs doped PAN nanofibre was modelled using space frame structures (SFS) of SWCNTs and PAN polymer matrix. Simulated results of nanoscale RVEs were used to determine the equivalent properties of p-SWCNTs and f-SWCNTs doped nanofibres which were further used in micro scale RVEs. Four micro scale RVEs were developed to represent the random, aligned, p-SWCNTs and f-SWCNTs doped aligned nanofibre mat in the epoxy matrix. Analyzed micro scale RVEs provided equivalent properties of interlaminar regions developed with random and aligned PAN nanofibre mats, PAN doped with p-SWCNTs and f-SWCNTs aligned nanofibres mats. At the macro scale, MNHCs were developed with equivalent interlaminar regions and analysed. The results of the simulated MNHCs were compared with experimentally tensile test results obtained in previous study. The research could serve in experimental and theoretical fields where smaller diameter, aligned nanofibre mat and better molecular orientation are required; e.g. SWCNTs doped nanofibres mat strengthened hybrid composites, medical field, and nano-electronics. Results of the multiscale modelling were in line with the experimental results which could be useful in extending the small-scale theoretical results to the real-life applications.